SURFACE AND CRUSTAL DEFORMATION MECHANISM OF THE DOBI GRABEN AND SURROUNDING AREA IN THE AFAR DEPRESSION, ETHIOPIA

By

ZELALEM SHIFERAW DEMISSIE

Bachelor of Science in Geology
Addis Ababa University
Addis Ababa, Ethiopia
2000

Master of Science in Geology and Geophysics
Addis Ababa University
Addis Ababa, Ethiopia
2005

Submitted to the Faculty of the
Graduate College of the
Oklahoma State University
in partial fulfillment of
the requirements for
the Degree of Geology
DOCTOR OF PHILOSOPHY
December, 2018

SURFACE AND CRUSTAL DEFORMATION MECHANISM OF THE DOBI GRABEN AND SURROUNDING AREA IN THE AFAR DEPRESSION, ETHIOPIA

Dissertation Approved:

Dissertation Adviser

Mohamed Abdelsalam, Ph.D. Chair

Daniel Lao-Davila, Ph.D.

Estella E. Atekwana, Ph.D

Amy Elizabeth Frazier, Ph.D.

ACKNOWLEDGEMENTS

I would first like to thank my advisor Dr. Mohammed Abdelsalam for his guidance and support throughout the project. I would also like to thank my committee members Dr. Estella Atekewana, Dr. Daniel Lao-Davila, and Dr. Amy Frazier for their valuable contributions. Dr. Kevin Mickus of Missouri State University (MSU), has gone through pains taking exercise of checking earlier version of the manuscript and have given important suggestions and valuable comments, which greatly helped in improving the quality of Paper III of this dissertation. I particularly express my gratitude to Mr. Shiferaw Demissie (my Father), his enthusiasm for my work and his support sustained me through my research. He also has spent much effort in creating a large network of scientific and social contacts that I am glad I was able to use. My research benefited much from it. I am grateful to the faculties and staff members of Boone Pickens School of Geology for their continued assistance in areas where I needed their corporation and help. I enjoyed the discussions I had with the Tectonic group of the school. I have special thanks to the Ethiopian Geological Survey for allowing me to access their archives. Special thanks to Mr. Befekadu Oluma and Mr. Gethaun Demissie. I am greatly indebted to my family for their wonderful advice, encouragement, endless support, love and for being on my side when things seemed to work out wrong. I am deeply grateful to the Boone Pickens School of Geology for the financial support of this research.

Name: ZELALEM SHIFERAW DEMISSIE

Date of Degree: DECEMBER, 2018

Title of Study: SURFACE AND CRUSTAL STRUCTURE DEFORMATION MECHANISM OF THE DOBI GRABEN AND SURROUNDING AREA IN THE AFAR DEPRESSION, ETHIOPIA

Major Field: GEOLOGY

Abstract: Our Study used the Advanced Synthetic Aperture Radar (ASAR), C- Band (λ = 5.6 cm) of the ENVISAT satellite ASAR data, Landsat Operational Land Imager (OLI), and Shuttle Radar Topography Mission (SRTM) digital elevation models, as well as the integration of geophysical ground base magnetic survey data, aeromagnetic, and Satellite gravity data, to investigate the time series surface deformation and crustal structure of the Dobi graben and surrounding area. Results from our fault population analysis using SRTM DEM aided by satellite imageries suggest that the direction of the faults' lateral propagations are highly influenced by the two regional volcanic rifts, the Red Sea Rift (RSR) and Gulf of Aden Rift (GAR). Additionally, the Dmax/Lmax ratio of the faults is calculated as ~0.03, which indicates the normal faults in the region can be characterized by the constant displacement fault growth model. Our fault population analysis also indicates that the possible presence of melt material in the lower crust likely acts as a barrier for lateral propagations of the faults. Results from our InSAR analysis suggest that an extension process with a creeping mechanism associated mainly with normal faulting presumably causes subsidence within the graben and uplifting in the rift shoulder. The abnormal, continuous uplifting in the horst area might be associated with the temporary reactivation of normal faulting in the region. Finally, our 2D magnetic and gravity forward modeling revealed the crust to be thinner beneath the Dobi graben, reaching a thickness of only ~23 km. We also found the boundary between the upper and lower crusts to be at depth of between 10 and 12 km. Additionally, we found two ~5 km wide zones where melt and mafic dike intrusions are possibly present within the lower crust. These zones are centered beneath a relay zone on the southwestern side of the Dobi graben and beneath a narrow (~2 km wide) graben just to the northeast of the Dobi graben. We propose that, while the upper crust beneath the Dobi graben is stretching mechanically, the lower crust is stretching ductily, aided by the presence of melt and the intrusion of mafic dikes.

PUBLICATION DISSERTATION OPTION

This dissertation has been organized in two sections. The first section gives a brief Outline of the dissertation and introduces the scientific question that we investigated in this research. The consecutive sections present two manuscripts that have been under review for publication and one published manuscript.

Paper 1: “Demissie, Z.S., Abera, R., Kiflu, H.G., 2018. The Influence of the Red Sea Rifts and the Gulf of Aden Rifts on the lateral propagations of faults in the Dobi graben and its surrounding, Afar Depression. This work been submitted to Journal of Structural Geology and is under review.

Paper 2: “Demissie, Z.S., Mullissa, A.G., 2018. Present day Kinematics of the Dobi graben from Surface time series Displacement analysis of ASAR data, Afar Depression in Ethiopia. This work been submitted to Tectonophysics Journal and is under review.

Paper 3: “Demissie, Z.S., Kevin M., Bridges, D., Abdelsalam, M.G., Atekwana, E.A., 2018. Upper lithospheric structure of the Dobi graben, Afar Depression from magnetic and gravity data. Journal of African Earth Sciences.
Doi.org/10.1016/j.jafrearsci.2018.06.012

TABLE OF CONTENTS

Chapter Page

LIST OF TABLES

PAPER I

Table Page

PAPER II

LIST OF FIGURES

PAPER I

Figure Page

Figure Page

Figure Page

PAPER II

Figure Page

PAPER III

Figure Page

SECTION I

GENERAL REVIEW

The Afar Depression (AD) in Ethiopia is unique area in which to study all stages of continental rifting as it is a stretched continental crust which is highly injected with mafic dikes. The concept that the AD crust is a stretched continental crust is of great interest to the geoscientific community (Markis and Gingburg, 1987; Bridges et al., 2012; Lewi et al., 2016). Many studies explain that in magma-assisted continental rifting, thermal softening of the lithosphere during the initiation of rifts is facilitated by the intrusion of mafic dikes sourced from shallow (~6 km deep) magma chambers (e.g., Daniel et al., 2014). Despite the obvious recent extensional features, there are no surface expressions of recent magmatic activity in certain areas in the AD. For example, what is observed in the Dobi graben and the surrounding area can be considered to be contrary to what is perceived in the Tendaho graben or other magma-assisted continental rifts. Nonetheless, it has been stated that the lack of surface magmatism does not imply the absence of sub-surface magma sources beneath magma-poor continental rifts such as the Dobi graben (Wolbern et al., 2012; Jakovlev et al., 2013). The absence of magma with which to initiate rifting through thermal softening of the lithosphere leads us to consider what other factors could be responsible for rift initiation. For instance, there is the possibility that the Dobi graben is opening through mechanical stretching, which is supported by the relatively high concentration of earthquakes throughout

the seismogenic depth within the graben compared to other parts of the AD (Hofstetter and Beyth, 2003). Therefore, it is important to investigate the surface deformations of the area which can be measured and used to constrain the subsurface crustal deformation (Doubre et al., 2016). Hence, an integrated investigation of both the surface deformation mechanism and crustal deformation on the embryonic spreading centers of AD should presumably establish an explanation as to what could be causing and controlling the extension across the area overlapping the Red Sea Rift (RSR) and the Gulf of Aden Rift (GAR). These are the problems which this research seeks to address. The subsurface geometry and deformation within the divergent diffused rifts boundaries of the AD can be addressed precisely if a combination of geophysical data and information derived from long-term geodetic data are used properly. More importantly, these data, even when used primarily for recording sudden deformation event processes, can serve as a significant constraint on the crustal deformation processes which are involved both in active rifting and transfer of the extensional deformation between spreading axes. Additionally, the techniques used in this study can be applied not only to the AD, but also to other tectonically active and deformed areas. In addition, having accurate knowledge of the crustal structures and surface rupturing is the first step in volcanic and earthquake hazard mitigation.

We have organized this study into three main parts. First, we conducted fault population analysis in the Dobi graben using a 30-meter Shuttle Rader Topography Mission (SRTM) Digital Elevation Model (DEM) and described displacement-length profiles along the strike direction of normal faults. Our first objective is then to investigate any systematic characterization of the normal faults and their role in surface deformation with respect to the RSR and GAR active volcanic rifts. Then, we conducted surface displacements

measurements within the Dobi graben and its surrounded area with Advanced Synthetic Aperture Radar (ASAR) data by employing Small Baseline Algorithm (SBA) and Quasi Permanent Scatterer (QPS) techniques. Our second approach will help us to understand more about the sources of deformation and to answer more fundamental questions about factors and parameters which control or facilitate the surface deformation processes. Finally, in order to determine the factors controlling the extension across the Dobi graben at crustal-scale depth, we collected and analyzed detailed, high-resolution ground magnetic data, which is supported by previous aeromagnetic data (Aeromagnetic Carta of Republic of Djibouti) and satellite gravity data (World Gravity Model 2012). Below we summarize the main contributions of this work:

1.1 Contributions

1. We design and implement a new SAS algorithm to identify the statistical pattern in the normal faults in the Dobi graben and its surrounding area and find that the regional strain transfer processes are highly controlled and influenced by the faults' tapering directions.
2. Based on the fault propagation termination styles, our faults population analysis shows that faults which exhibit half-restricted termination styles account for 85% of the 953 normal faults in our fault geo-database and that the Dmax/Lmax ratio of these faults is ~0.03, which is in accord with the constant displacement length fault growth model. We prepared a geo-metadatabase which provides propagation direction, dip direction, and the extended length and maximum displacement information for 953 faults. The total cumulative length of these faults is ~2000 km.

3. We found the crust to be thinner beneath the Dobi graben, reaching a thickness of only ~23 km, by employing 2D forward modeling of high-resolution ground magnetic, aeromagnetic, and satellite gravity data. We also found the boundary between the upper and lower crust to be at a depth between 10 and 12 km. Additionally, we found two ~5 km wide zones where melt and mafic dike intrusions are possibly present within the lower crust. These zones are centered beneath a relay zone on the southwestern side of the Dobi graben and beneath a narrow (~2 km wide) graben just to the northeast of the Dobi graben.

4. We propose that, while the upper crust beneath the Dobi graben is stretching mechanically, the lower crust is stretching in a ductile manner, aided by the presence of melt materials and intrusions of mafic dikes.

1.2 Thesis Road map

Chapters 2 to 4 (PAPER I, PAPER II, and PAPER III) of this dissertation are written as independent studies and structured as specific manuscripts. One of the manuscript has already been published in a scientific journal, and two manuscripts have been submitted to a separate journal and are currently under review. It is possible to read each chapter independently without the requisite of reading any previous chapters first. For each associated manuscript, there are multiple authors who contributed to and endorsed the contents of the manuscripts while partaking in intense discussions. Each chapter provides a brief overview of the kinematics and tectonic history of the AD, as is evident from previously published works.

Chapter 2 is concerned primarily with the characterization of normal faulting to provide a fault growth model and geo-spatial-database which isolates and extracts the fault length with respect to displacements based mainly on the elastic deformation theory (Cowie and Scholz, 1992a; Schlische et al., 1996; Manighetti et al., 2001a). Our results from fault population analysis using high resolution satellite imagery and SRTM DEM along the active Quaternary rift of the Dobi graben and the surrounding area provide a unique opportunity for understanding the influence of the regional strain transfer toward the East-Central Block (ECB) of the AD. This chapter is based on material which was submitted to the Journal of Structural Geology, which is published by Elsevier.

Chapter 3 describes a time series surface deformation mechanism for the Dobi graben and the surrounding area which utilized the Small Baseline Algorithm (SBA; Berardino et al., 2002) and Quasi Permanent Scatterer techniques (QPS; Perissin and Wang, 2012; Mullissa et al., 2018) independently. Using both descending and ascending orbit ASAR data from EnviSat®, respectively, we examined uplift and subsidence incidents of the graben for the period between June 2007 and October 2009. Results from the velocity, displacement maps, and time series analysis suggest that creeping is associated mainly with normal faulting and could be the primary tectonic deformation mechanism. The anomalous continuous uplifting exhibited at the rift shoulder and in the horst area might be associated with the temporary reactivation of normal faulting in the region. The continuous positive line of sight (LOS) signals observed oblique to the normal faults in different parts of the Dobi graben might serve as a proxy for understanding how strain is localized as normal faulting and transferred in the region in a distinct northeast direction, which is in accord with the northeast migration of the triple junction argument and the transfer of strain from the

southernmost RSR to the westernmost GAR (Doubre et al., 2016). This chapter is based on material which has been submitted to the Tectonophysics Journal published by Elsevier.

Chapter 4 describes the crustal structure of the Dobi graben and its surrounding area using non-unique potential data. In this chapter, a 2D forward model using high-resolution ground magnetic and satellite gravity data to produce the NE-SW trending crustal section is discussed in detail. We found the crust to be thinner beneath the graben, reaching a thickness of ~23 km. We also found the boundary between the upper and lower crust to be between 10 and 12 km. Additionally, we found two ~3.5 km wide zones where melt and mafic dike intrusions are possibly present within the lower crust. This chapter shows how it is possible to obtain a unique solution from non-unique potential data if it is used in conjunction with prior knowledge and constrained by other geophysical data. It has been submitted to and accepted for publication by the Journal of African Earth Sciences.

1.3 References

Berardino, P., Fornaro, G., Lanari, R., Sansosti, E., 2002. A new algorithm for surface deformation monitoring based on small baseline differential SAR interferograms. IEEE Trans. Geosci. Remote Sens. 40 (11), 2375–2383.

Bridges, D. L., Mickus, K., Gao, S. S., Abdelsalam, M. G., Alemu, A., 2012. Magnetic stripes of a transitional continental rift in Afar. Geology 40, 203–206, http://doi.org/10.1130/G32697.1.

Cowie, P.A., Scholz, C.H., 1992a. Physical explanation for the displacement-length relationship for faults using a post-yield fracture mechanics model. Journal of Structural Geology 14, 1133-1148.

Daniels, K., Bastow, I.D., Keir, D., Sparks, R.S.J., Menand, T., 2013. Thermal models of dyke intrusion during development of continent–ocean transition. Earth and Planetary Science Letters 385 145-153, doi: 10.1016/j.epsl.2013.09.018.

Doubre, C., Deprez, A., Masson, F., Socquet, A., Lewi, E., Grandin, R., Nercessian, A., Ulrich, P., Chabalier, D. J., Saad. I., Abayazid, A., Peltzer, G., Delorme, A., Calais, E., Wright, T., 2016. Current deformation in Central Afar and triple junction kinematics deduced from GPS and InSAR measurements. Geophysical Journal International 208, 936-953.

Hofstetter, R., Beyth, M., 2003. The Afar Depression: Interpretation of the 1960-2000 earthquakes. Geophysical Journal International 155, 715-732, doi: 10.1046/j.1365-246X.2003.02080.x.

Jakovlev, A., Rümpker, G., Schmeling, H., Koulakov, I., Lindenfeld, M., Wallner, H., 2013. Seismic images of magmatic rifting beneath the western branch of the East African rift. Geochemistry, Geophysics, Geosystems 14, 4906-4920, doi:10.1002/2013GC004939.

Lewi. E., Keir, D., Birhanu, Y., Blundy, J., Stuart, G., Wright, T, Calais, E., 2016. Use of a high-precision gravity survey to understand the formation of oceanic crust and the role of melt at the southern Red Sea rift in Afar, Ethiopia, in Magma-dominated rifting in the Afar triple junction, edited by Wright T., Ayele A., Ferguson, J., Kidane, T., Vye-Brown, C., Geological Society of London, Special Publications 420, 165-180, https://doi.org/10.1144/SP420.13.

Manighetti, I., King, G.C.P., Gaudemer, Y., Scholz, C.H., Doubre, C., 2001a. Slip accumulation and lateral propagation of active normal faults in Afar. Journal of Geophysical Research: Solid Earth 106, 13667-13696.

Makris, J. and Ginzburg, A., 1987. The Afar depression: transition between continental rifting and sea-floor spreading. Tectonophysics 141, 199–214, https://doi.org/10.1016/0040-1951(87)90186-7.

Mullissa, A.G., Perissin, D., Tolpekin, V.A. , Stein, A., 2018. Polarimetry based distributed scatterer processing method for PSI applications. IEEE Trans. Geosci. Remote Sens.

Perissin, D., and Wang, T., 2012. Repeat-pass SAR interferometry with partially coherent targets. IEEE Trans. Geosci. Remote Sens., vol. 50, no. 1, pp. 271–280.

Schlische, R.W., Young, S.S., Ackermann, R.V., Gupta, A., 1996. Geometry and scaling relations of a population of very small rift-related normal faults. Geology 24, 683–686.

Wölbern, I., Rümpker, G., Link, K., Sodoudi, F., 2012. Melt infiltration of the lower lithosphere beneath the Tanzania craton and the Albertine rift inferred from S receiver functions. Geochemistry, Geophysics, Geosystems 13, doi: 10.1029/2012GC004167.

PAPER I

THE INFLUENCE OF THE RED SEA RIFTS AND THE GULF OF ADEN RIFTS ON THE LATERAL PROPAGATIONS OF FAULTS IN THE DOBI GRABEN AND ITS SURROUNDING AREA IN THE AFAR DEPRESSION

2.0 Abstract

The Dobi graben is a NW-trending, Quaternary continental rift found within the East-Central Block (ECB) of the Afar Depression (AD) in northeastern Ethiopia. Extension occurs on steeply dipping faults, where the ratio of maximum displacement to traced fault length extends to four orders of magnitude. We conducted fault population analysis in the Dobi graben using a 30 m resolution Shuttle Rader Topography Mission (SRTM) Digital Elevation Model (DEM). We traced a total of 953 faults. We used the fault displacement length profiles' tapering directions and the different types of the fault propagations' termination styles to characterize the fault kinematics pattern. Our population analysis results show that ~45% of the normal faults in the Dobi graben are tapering towards the southeast in a manner similar to the Red Sea Rift (RSR) regional strain gradient. On the other hand, our analysis showed that ~40% of the faults in the Dobi graben are tapering towards the northwest direction in a manner similar to the Gulf of Aden Rift (GAR)

regional strain gradient. We found the statistical regression correlation coefficients (R-square value) for both the southeast and the northwest tapering faults to be ~0.7. Therefore, we suggest that ~85% of the lateral propagation of the 953 faults in the Dobi graben is highly influenced by the regional strain transfer of the RSR and GAR. Additionally, based on the fault propagation termination styles, our faults population analysis shows that faults which exhibit the half-restricted termination style account for 85% of the 953 faults. The maximum displacement over maximum length (Dmax/Lmax) ratio of these faults is 0.03, which is in accord with the constant displacement length fault growth model.

Key Words: Afar Depression**,** Displacement-length scaling**,** Fault growth model**,** Strain distribution and localization

Research Highlights

- 953 faults are traced using Shuttle Radar Topography Mission (SRTM) Digital Elevation Model (DEM).
- Extension is accommodated by normal faulting and block tilting in the Dobi graben.
- Faults displacement is linearly related to fault length indicating constant growth model.
- Fault propagations is arrested with geological heterogeneities in the graben.
- Regional strain transfer influences the faults tapering directions.

2.1 Introduction

The Afar Depression (AD) is an ideal place to study the spatial heterogeneity of both lateral and vertical fault growth since the prevalently arid climate has preserved the different types of fault geometries produced by active extensional tectonism. The area provides us with a good opportunity to investigate faults growth trends in terms of strain transfer to the east-central AD when two regional volcanic rifts, such as the RSR and GAR, propagate towards each other. The AD is the northern terminus of the East Africa Rift System (EARS) (Fig. 1A), and it is situated where the Main Ethiopian Rift, RSR, and GAR form a diffuse rift-rift-rift triple junction (Fig. 1B; Tapponnier et al., 1990; Manighetti et al., 2001; Kidane et al., 2003; Beyene and Abdelsalam, 2005; Doubre et al., 2016). This diffused junction of the three rifts generates a wide zone of heterogeneous and distributed deformation. Additionally, the two volcanic branches of the RSR and GAR enclose large areas in the east-central AD consisting of a series of magmatic horst and grabens. For example, to the east of the southern segment of the RSR, the AD is characterized by a series of relatively narrow, non-volcanic grabens, such as the Dobi, Hanle, Derale, and Gumma – Kambourta grabens, which localize the strain transfer from the southernmost RSR to the westernmost GAR (Fig. 1C; Tapponnier et al., 1990; Manighetti et al., 1997; Tesfaye, 2005; Tesfaye et al., 2008). All of these non-volcanic, narrow grabens manifest heterogeneous deformations, due mainly to normal faulting. The normal faults in the region show both asymmetric and symmetric slip profiles (henceforth, displacement length profiles). Understanding the pattern in these profiles is important in terms of not

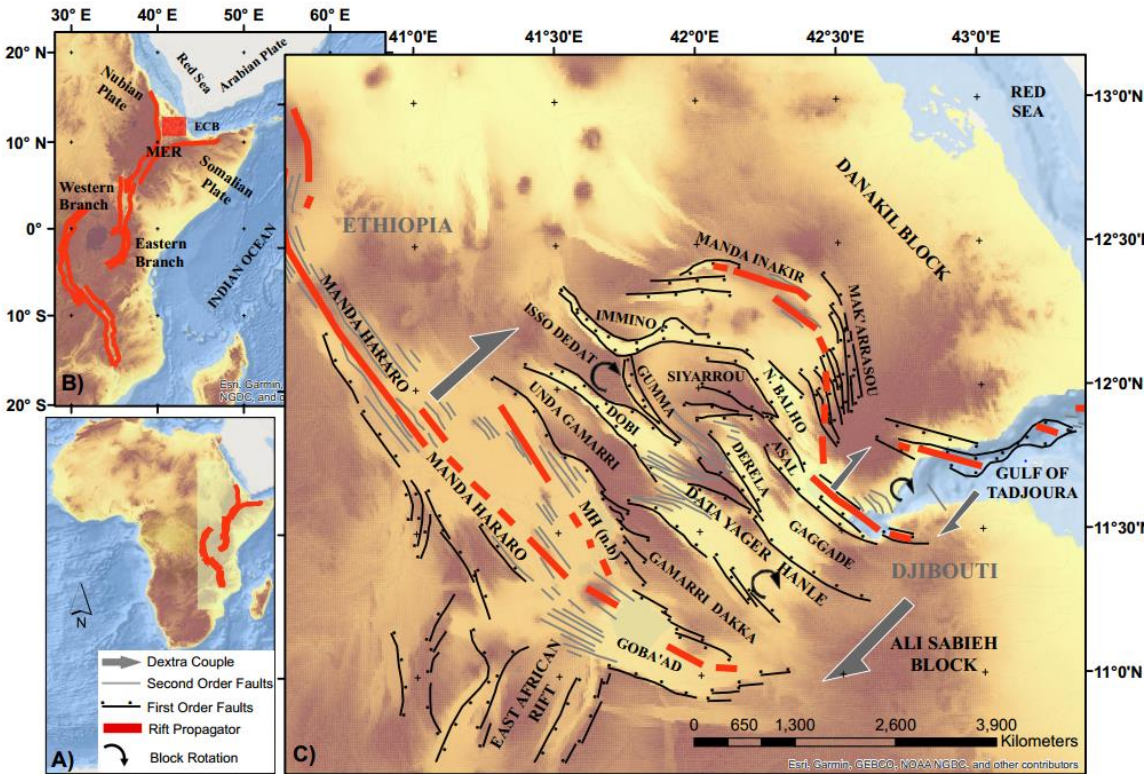

Figure 1: (A) Digital Elevation Model (DEM) of Africa. The mint color area represents the region affected by the East Africa Rift System (EARS) and the small red polygon in the Horn of Africa represents the Afar Depression (AD); (B) The EARS. The northern tip is the Ad which comprises the East Central Block (ECB) in the center. The eastern and the western branch of the EARS exist south of MER; (C) The tectonic framework of the Afar depression (AD) shown in Shuttle Radar Topographic Mission (SRTM) referred as Digital Elevation Model (DEM). Solid red lines indicate major rift propagators (Dobure et al., 2016) mainly the Red Sea Rifts (RSR) and Gulf of Aden Rifts (GAR). The element of rifts and blocks structures in the AD is represented by black lines and second-order faults with gray lines, respectively (Manighetti et al., 2001a). Clockwise rotation of the NW-trending blocks (Kidane et al., 2003) displayed with black curve arrow lines, and both NE and SW-directed dextral strike-slip shear couples are indicated with broad, gray, arrow lines.

only how these normal faults have been growing, but also in helping us to understand the mechanical behavior of the area's crust. Therefore, we employed a fault population

analysis approach for investigating the tectonic and structural influences of both the localized RSR and GAR on the overlapping zone, particularly in the Dobi graben and its surroundings. Fault population analysis is an effective approach for understanding the mechanics of faulting, fault growth processes, and fault propagation directions. An investigation into the mechanics of faulting can be accomplished by examining the natural exposure of a fault's surface, such as the fault traced length and displacement, which are measured along the slip direction. Additionally, understanding the processes of fault growth and propagation direction in normal faults in the earliest stages of continental rifting will give us a better insight into the different mechanisms of tectonic deformation, including strain transfer among fault segments and adjacent rift basins.

Fault population analysis has been used in the last three decades to understand fault growth models (Pollard and Segall, 1987; Walsh and Watterson, 1988; Cowie and Scholz, 1992a; Dawers et al., 1993; Cowie et al., 1998; Schultz and Fossen, 2002; Manighetti et al., 2001a, 2004, 2007, 2015), study fault geometries (Pickering et al., 1997; Manighetti et al., 2001a; Walsh et al., 2003; Soliva and Benedicto, 2004, Tesfaye et al., 2005), and comprehend displacement (strain) transfer among segmented faults and adjacent rift geometries (e.g., Gupta and Scholz, 2000a; Manighetti et al., 2001a; Tesfaye et al., 2005). Most fault population analyses have documented fault displacement variability along the fault traced length and predicted what ought to be the maximum displacement at the center of the fault and zero displacement at the fault tips (e.g., Pollard and Segall, 1987; Cowie and Scholz, 1992a; Manighetti et al., 2001a, 2001b; Scholz and Fossen, 2002; Dumont et al., 2016). However, these fault displacement profiles exhibit various different shapes, largely asymmetric (Muraoka and Kamata, 1983; Peacock and

Sanderson, 1991; Dawers and Anders, 1995; Nicol et al., 1996, 2010; Manighetti et al., 2001a, 2004, 2015; Davis et al., 2005; Roche et al., 2012; Nixon et al., 2014; Tibaldi et al., 2016; Dumont et al., 2016). These different asymmetric shapes of the fault displacement profile are either governed by adjacent fault segment coalesces which lead to the growth of a larger fault as a result of fault segment linkage (Cartwright et al., 1995; Dawers and Anders, 1995; Nicol et al., 1996, 2010; Fossen and Rotevatn, 2016) or interactions between faults and crustal heterogeneities, which arrest their propagation (Aki, 1979; King, 1986; Manighetti et al., 2001a, 2004). Whenever there is a barrier, lateral propagations would be affected and accompanied consequently by vertical fault growth (Aki, 1979; King, 1986; Manighetti et al., 2001a, 2004).

The primary purpose of this paper is to measure the displacement-length profiles across the strike direction of normal faults in the Dobi graben and to give insights into the fault propagation directions with respect to the regional strain distribution kinematics of the central AD. To achieve our goal, we used WorldView-2 satellite images and the 30 m resolution Shuttle Radar Topography Mission (SRTM) Digital Elevation Model (DEM). We first identified and traced the faults using the satellite imageries and then verified that they were topographical offsets using the SRTM DEM. Nine-hundred and fifty-three individual faults with a cumulative fault traced length of ~2000 km were identified and mapped. This was followed by measurements of vertical throws or scarp heights (fault displacement measurements) at 30 m intervals along strike direction for each of the 953 faults. The results from our analysis along the active rift of the Dobi graben and surrounding area provide a unique opportunity for understanding the influence of the regional strain transfer toward the central-east AD, specifically to the Dobi graben and

the surrounding area. We used the fault displacement data and traced lengths to characterize the fault growth model by implementing a statistical double normalization of the displacement-length profile shapes. Characterizations of the displacement-length profile shapes also help us to understand the nature of fault movements, such as their lateral propagation directions.

2.2.Tectonic Setting

The AD is the northern terminus of the EARS, which is an active, ~2,000-km-long continental rift. The AD occurs where three rift zones form a triple junction. The three branches include the RSR, GAR, and the Main Ethiopian Rift, which trends south through Ethiopia (Fig. 1A). The EARS is a divergent plate boundary where the African plate is in the process of splitting at the rate of 6.5 mm/year into two tectonic plates, the Somali and the Nubian plates, as observed in the vicinity of the AD (Fernandes et al., 2004; Ebinger, 2005; Moungenot et al., 2006).

The central part of the AD is dissected highly by normal faults which form a series of horsts and grabens (Fig. 1C). It can be divided into northern, east-central, and southwestern regions on the basis of similar structural trends (Hayward and Ebinger, 1996). Of importance to this paper is the ECB, which is bounded by the SE-propagating RSR and NW-propagating GAR (Beyene and Abdelsalam, 2005), with a special emphasized on the NW-trending narrow rift of the Dobi graben. The propagation of the RSR and GAR is believed to have induced dextral strike-slip shearing which has caused clockwise rotation of the ECB due to differential spreading (Courtillot et al., 1984; Acton et al., 1991, 2000). Approximately 11^{o} of rotation in the clockwise direction has been

estimated for the ECB in the past 2 Ma. Acton et al. (2000) determined that the ECB rotation has terminated but that small rotations might take place in the future if further rift localizations occur within the RSR (Fig. 1C). The clockwise rotation of the ECB has, in turn, induced sinistral strike-slip shearing on the reactivated NW-trending normal faults (Courtillot, 1980, 1982; Courtillot et al., 1984; Tapponnier et al., 1990; Sigmundsson, 1992; Manighetti et al., 2001). Tapponnier et al. (1990) and Manighetti et al. (2001) proposed the book shelf faulting model as a deformation mechanism for the ECB.

Despite the manifestation of a diffused tectonic extension within the ECB, the extension is localized in narrow rifts, such as the Dobi graben. The Dobi graben is characterized by NW-trending, high-angle normal faults and low-angle, layer-parallel slip faults, which might have prompted a subsequent crustal extension due to mechanical deformation in the brittle zone.

2.2.1 Surface deformation mechanism of the central Afar

The crustal stretching rates across the AD are constrained by GPS and InSAR geodesy (Nooner et al., 2009; McClusky et al., 2010; Pagli et al., 2014; Doubre et al., 2017) and the late Quaternary surface deformation (Manighetti et al., 2001a; Jacques et al., 2011). The geodetic observations explain the comprehensive short term (∼10–20 year) stretching rate, whereas the late Quaternary fault slip rates measure the long term stretching rate on large faults (Polun et al., 2018). Those observations have also revealed the presence of sudden deformation across the magmatic segments related to the intrusion of large volumes of dyke and mafic melts material (e.g. Nooner et al., 2009; Doubre et al., 2017). For example, Amelung et al. (2000) used the European Remote Sensing (ERS)

to study the Gada'Ale volcanism and discussed about deformation mechanism due to deflation by magma movements that causes normal faulting displacement. Doubre and Peltzer (2007) also used the Canadian Space Agency (CSA) to characterize the nature of faulting in the GAR and, documented the kinematics as either due to creeping or sudden slip related to an increase in seismic activities between 1997 and 2005. Of the importance of this work, Pagali et al. (2014) and Doubre et al. (2016) revealed higher strain accommodation and considered the Southern part of Dobi as PBZ (Plate Boundary zone) that extends 150 to 200 Km including (Gardori, an area just north of Tendaho) and Immino Graben based on studies constrained by GPS and InSAR geodesy.

2.2.2 Crustal structure of the central Afar

The crust within the AD has been modified by intense thinning and magmatic intrusion, as receiver function studies were used to determine the V_p/V_s ratios of the AD crust (Barberi and Santacroce, 1980; Makris and Ginzburg, 1987; Hammond et al., 2011; Reed et al., 2014). Regional gravity observations and active-source refraction seismology indicates that the crust thins from approximately 30 km in the western Afar margin to less than 20 km on the RSR (Makris and Ginzburg, 1987). Additional information about the presence of melt and mafic dike intrusions within the crust of the AD is obtained from magnetic and gravity data (Bridges et al. 2012; Lewi et al., 2016, Demissie et al., 2018). For example, Demissie et al. (2018) analyzed high-resolution ground magnetic data collected along a ~24 km long profile across the Dobi graben together with satellite gravity data, to develop a 2D forward model showing that the crust to be thinner beneath the Dobi graben reaching a thickness of only ~23 km. Demissie et al. (2018) also found

the boundary between the upper and lower crust to be at depth between 10 and 12 km. Additionally, they found two ~5 km wide zones where melt and mafic dike intrusions are possibly present within the lower crust. Seismic receiver function results also show that the crust is 17 km thick within the axis of Tendaho graben and increases to ~23 km thick near Dobi graben (Reed et al., 2014). Other receiver function studies indicate that the average crustal thickness in the central Afar is likely 25–30 km (Berckhemer et al., 1975; Makris and Ginzburg, 1987; Dugda and Nyblade, 2006; Hammond et al., 2011).

2.2.3 Magmato-tectonic and the bulk Crustal properties effects on the Faults in the AD

The magmato-tectonic interactions which have been considered as a decisive factors and accountable for sudden deformation effects such as mafic dike intrusions were explained using radar geodesy together with field observations (Wright et al., 2006; Rowland et al., 2007; Grandin et al., 2009, 2010b; Hamling et al., 2009). Yet, along the RSR and the GAR, magmato-tectonic interactions have been active for the last hundred thousand years in the AD (Lahitte et al., 2003a, b; Vye-Brown et al., 2012; Ferguson et al., 2013; Medynski et al., 2013; 2015, 2016).

In the AD, Manighetti et al. (2001) is the first to have performed a detailed investigation about the effects of Magmato-tectonic on slip accumulation and lateral propagation trends on the active normal faults associated with GAR (Asal-Ghoubbet rift). According to Manighetti et al. (2001), most faults have slip length profiles tapering northwestward. Conferring fault cumulative slip decreases in the same direction as the regional extensional strain gradient Manighetti et al. (2001). This result from the counterclockwise rotation of both the Danakil microplate and the Arabia plate with

respect to Africa (e.g., Sichler,1980; Chu and Gordon,1998; Manighetti et al., 2001). Likewise, Nico et al (1996), Peacock and Sanderson (1996), and Manighetti et al. (2001) have explained that the linear profiles typically mimic the propagation history of the faults, tapering in the direction of fault propagation. Dumont et al. (2016) also suggest that lateral propagation of faults is easier away from areas where magma has been stored for a long time at crustal depth, thus modifying the thermo-mechanical properties of the host rock.

2.2.4 Geology of the Dobi Graben

The Dobi graben is located in the center of the intensely dissected ECB, northeast of the southern terminus of the RSR (Fig. 1C; Manighetti et al., 2001; Jacques et al., 2011). The width of the graben is variable and ranges from ~6 km wide in the Dobi-Hanle accommodation zone to the northwest to ~16 km wide in the southeast portion of the graben (Fig. 2 and 3; Jacques et al., 2011). The Dobi graben is composed of asymmetrical half grabens, which are composed mainly of extensional imbrication fans which widen southeastward towards the Gammarri tear zone (Figs. 2 and 3; Tesfaye, 2008). The Dobi graben occupies an area of ~600 km^2, extending in a NW-SE direction and presenting as a right-stepping, northwestern continuation of the Data Yagar-Hanle accommodation zone (Figs. 1C and 2; Tesfaye, 2008). The graben is connected to the Immino graben in the north through the Gumma graben (Figs. 1C, 2and 3). Adjacent to the northwestern and southeastern ends of the Dobi graben are the Isso Dedat and Unda Gamarri horsts, respectively ((Figs. 1C, 2and 3).

The Dobi graben is underlain by intensely faulted basaltic flows which are collectively known as the Afar Stratoid Series (Varet, 1978). In places, the basaltic flows attain an exposed thickness in excess of ~1500 m (Varet, 1978). The K/Ar geochronological studies by Kidane et al. (2003) indicated that the age of the Afar Stratoid Series in the vicinity of the Dobi graben is 1.6 - 2 Ma.

The basalts are commonly scoriaceous, vesicular, and rubble-forming where lateritized agglomerates separate these laterally continuous flows from one another locally (Geological Survey of Ethiopia, 2013; Fig 2). The lateral persistence of the lava flows is visible along the graben bounding escarpments (Tesfaye, 2005).

The top layers of the basalt are characteristically sub-horizontal compared to the more tilted base layers, indicating the progressive tilting of older layers with time (Varet, 1978). However, locally, some younger blocks are tilted substantially due to faulting. In some cases, stratigraphic marker horizons of less than 1 Ma in age are tilted by up to 35° (Hayward and Ebinger, 1996; Figs. 2, and3). Together with the Stratoid basalts, thin trachytic flows and lateritic horizons occur within the Dobi graben. The graben's floor is underlain by alluvial and lacustrine sediments and volcanic talus (Figs. 2 and 3; Varet, 1978; Hayward and Ebinger, 1996; Acton et al., 2000).

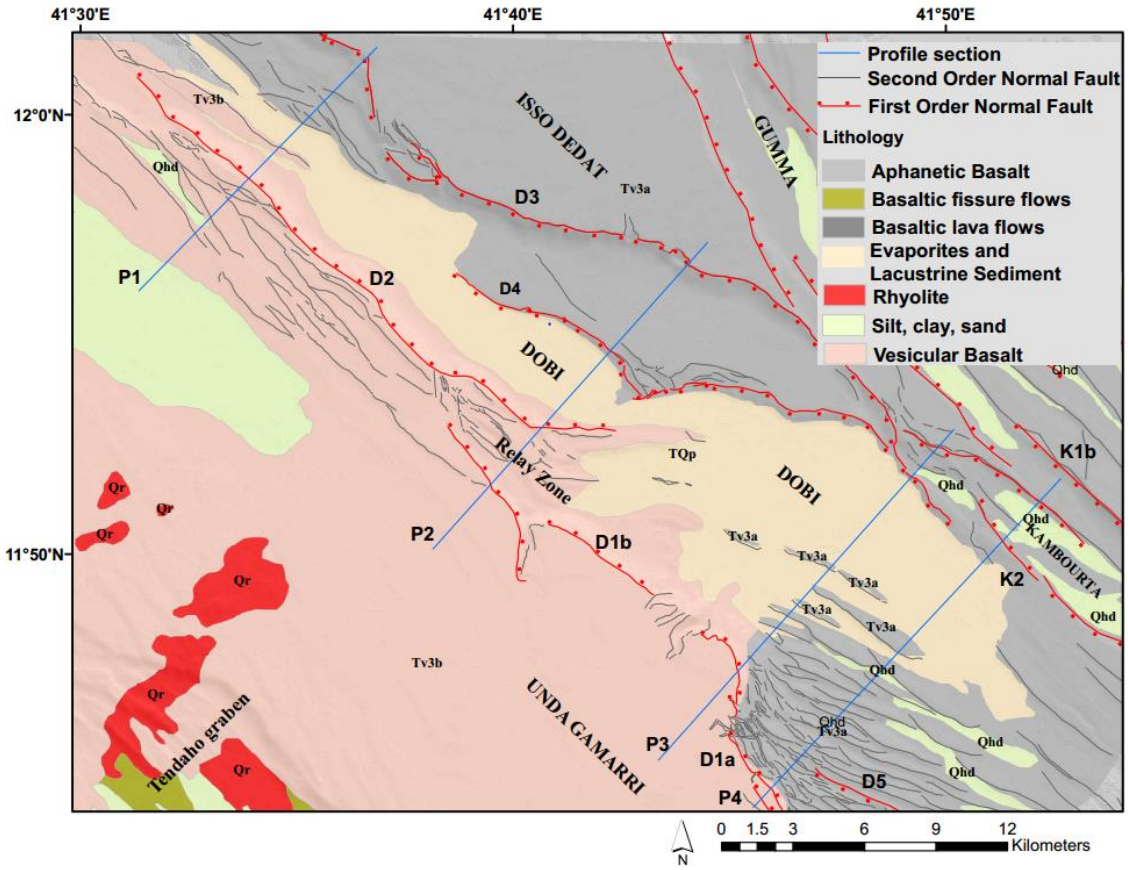

Figure 2: Geological map of the Dobi graben and its surrounding derived from supervised classification of Landsat ETM+ and field geological ground validation.

2.3 Data and Methods

2.3.1 Data used for the identification and mapping of faults

In this work, adopting Willemse et al.'s (1996) definition, we define an 'individual fault' as the longest horizontal or sub-horizontal continuous linear or sub-linear feature in map view and its lateral dimension as Lmax. Conversely, we consider "fault height" or "cross-sectional trace profile" as the "fault scarp height" or "displacement, d." The maximum fault scarp height obtained or measured across the entire traced length of the faults is referred to as the maximum displacement (Dmax).

We used integrated remote sensing and Geographic Information System (GIS) mapping techniques for the identification and mapping of the faults and their geometries. We then used WorldView-2 satellite images to identify and trace the faults. The WorldView-2 satellite images have 8 multi-spectral bands at 1.84 m spatial resolution and collect panchromatic bands at 0.46 m simultaneously. Additionally, we used 30.6 m spatial resolution 30 meter SRTM DEM to determine throw across faults (the exposed topographic escarpment of the fault) and extract topographic profiles. The SRTM DEM provides an overall absolute vertical accuracy expressed as the root mean square error (RMSE) of 2.44 meters.

We have analyzed 224 faults in the Dobi imbrication zone, 73 individual faults were traced in the high-linkage ramp zone, 101 in the Dobi relay zone, 124 faults in the Derelafault zone, 170 faults in the Dobi-Hanle accommodations zones, and 261 in the Dobi fault termination zone (Fig. 2). Only 953 faults which were longer than the spatial resolution of the SRTM data were selected for analysis. These criteria helped us avoid oversampling of the small fault scarps and traced fault lengths (even if the samples exist in the system) due to imaging resolution (Pickering et al., 1995). Observations which are not considered in the statistical analyses due to scale resolution limitations are described as being included in the data truncation. Moreover, doing this helped us to eliminate automatically those outliers in our Log Dmax to Log Lmax scatter plot which would cause a higher degree of scattering. Additionally, most of the small faults are located within the floor of the Dobi graben and mostly covered by the graben fill sediments; hence, they are prone to being under-sampled. Generally, setting threshold criteria to

consider only faults longer than 30 m allowed us to avoid misinterpretation of their displacement-length profile.

We prepared our database by implementing elevation profiles acquired from the SRTM DEM as a representation for structural cross-sections. Therefore, considering the minimal amount of erosion in the AD, we used the SRTM DEM to extract elevation profiles by following the top and base of each scarp.

Additionally, the border fault scarps in the AD are steeper than 70^{o} at the surface, meaning that the measured 'cross-sectional trace profile' or 'fault scarp height' are nearly the same as the down dip fault throws (Chabalier and Avouac, 1994; Manighetti et al, 2001a). From these profiles, we calculated the variation in vertical displacement as a function of distance along the faults' strike directions. This methodology was adopted from Manighetti et al. (2001a) and Dumont et al. (2016).

The short cross-sectional trace profiles (fault displacement, d) are spaced by ~30 m, and the total number of profiles for each fault depends on the maximum length of the fault. Each short, cross-sectional trace profile (fault displacement, d) measurement and their corresponding traced length (l) were normalized by their maximum displacement (D/Dmax) and their cumulative traced length (L/Lmax) for each individual fault, respectively. We then plotted the Dmax and Lmax to examine the different displacement profile shapes and to further classify them according to Manighetti et al. (2001a). These authors identified eight different types of displacement profiles based on their shape. Manighetti et al. (2001a) and Dumont et al. (2016) classified further the eight displacement profiles into three main subgroups: unrestricted, restricted, and elliptical profiles (Fig. 4). The criteria they used for fault growth consider the fault nucleation

point, where slip starts, and the presence of barriers, where propagation is arrested by various spatial structural heterogeneity and geological conditions. In this work, we classified all the 953 traced faults into tip unrestricted, tip restricted, and half restricted, but we did not incorporate double tip restricted in line with Manighetti et al. (2001a) since faults of this type were negligible in number. Furthermore, the geological map of the Dobi graben and its surrounding is derived from supervised classification of Landsat ETM+ and field geological ground validation.

2.4 Results

2.4.1 Structural Architecture of the Dobi graben

The Plio-Pleistocene flood basalts exposed within the Dobi graben are faulted intensively by normal faults, and the blocks between the faults are tilted strongly. Typically, a series of faults striking in a northwest direction govern the general architecture of the graben, and, in the southeastern border fault of the Dobi graben, antithetic faults are common (Fig. 3).

Given the need to classify and describe the geometry of the boundary faults, their visible scarp heights (termed as faults displacement, D), and their spatial heterogeneities in different damaged zones, we found Jacques et al. (2011) fault nomenclatures manner is helpful. Therefore, the boundary faults of the Dobi graben and the surrounding area is named as Dobi Fault-one (D1a, D1b), Dobi-Fault-two (D2), Dobi-Fault-three (D3), Dobi-Fault-four (D4), Dobi-Fault-five (D5), Kambourta- Fault (K1a, K1b, K2) embracing Jacques et al. (2011) work.

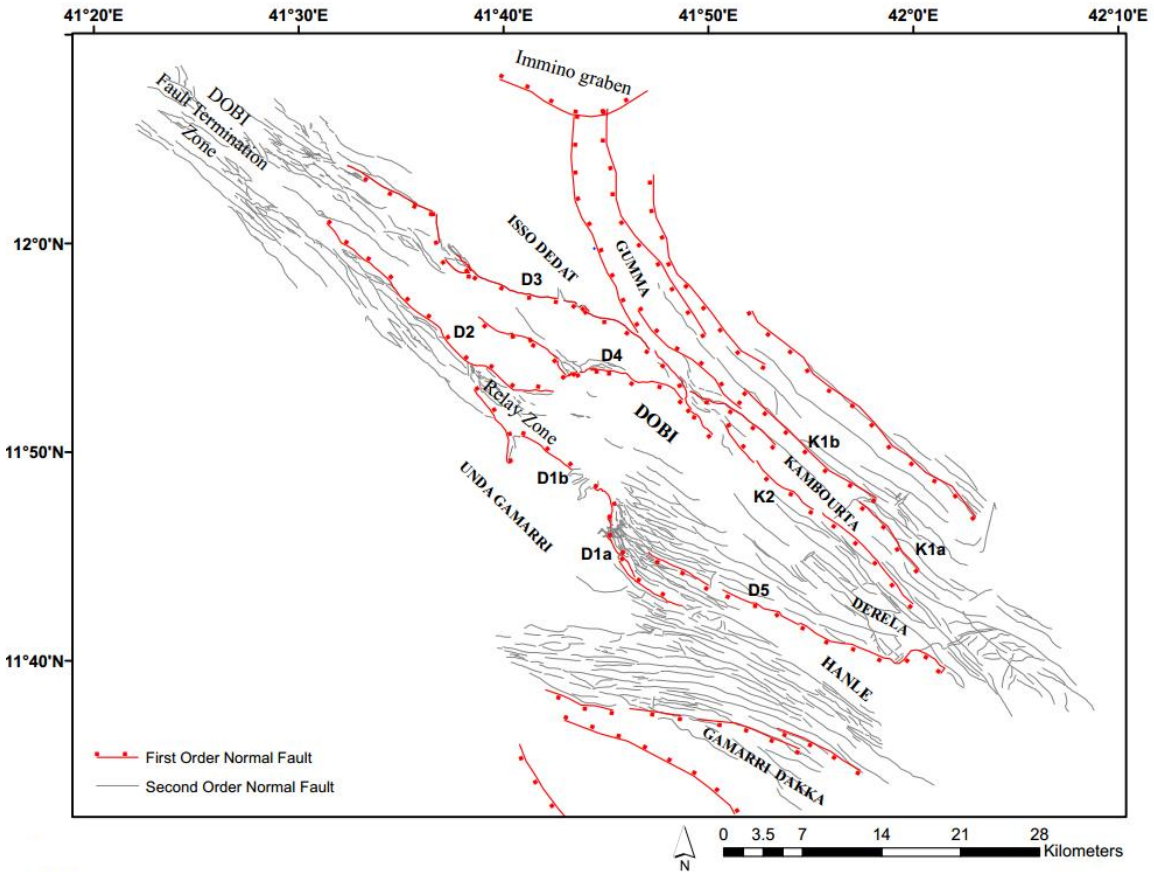

Figure 3: Structural map of the Dobi graben produced from a 0.46 m spatial resolution panchromatic images acquired by Worldview-2 satellite and 30 m Shuttle Radar Topography Mission (SRTM) Digital Elevation Model (DEM).

The southeastern border fault of the graben is composed of at least four sub-curvilinear, first-order faults arranged in an echelon pattern, and these faults are referred to collectively as D1a (Figs. 2 and 3; Jacques et al., 2011). In the northwest section of the imbrication zone, D1a has an orientation of ~N175^{o}E. However, as it approaches its southeastern tip, it rotates in a counterclockwise direction, resulting in a mean strike of N125^{o}E. All of the D1a faults have dips of ~70^{o} in the northeast direction (Figs. 2 and 3). Northeast of D1a, there are a number of low angle normal faults antithetic to D1a which

form an imbrication zone with strikes of N105°E to N115°E. These faults form southwest-facing scarps, and they are between 5 and 9 km long, and have vertical throws varying between ~20 m and ~150 m (Fig. 3). Southeast of D1a, the southwest-dipping D5 has a strike ranging between N130^{o}E and N115^{o}E (Fig. 3; Jacques, et al., 2011). D5 represents the northeastern boundary of the Dobi-Hanle accommodation zone (Fig. 2). It extends for ~40 km and has a maximum vertical throw of ~600 m in its southeastern part (Fig. 3), which decreases to a few tens of meters when approaching D1a in the northwest (Fig. 3).

The middle part of the Dobi graben is dominated by a fault relay zone due to the overlap of zones D2 and D1b. D1b and D2 are linked by numerous steep, southwest-dipping, sub-curvilinear, low angle normal faults. This zone is ~4.2 km in width and is dissected by second-order faults into crescent-shape basaltic blocks which are ~2.5 km long and 0.5 km wide (Figs. 2 and 3).

Similar to D1b and D2, two other first-order, southwest dipping boarder faults, D3 and D4 also fully overlap in the north-central part of the graben to form another relay zone in the northeastern border fault of the graben. This relay zone is bounded by an outer northwest-trending border fault (D3) and an inner E-W trending to northwest trending synthetic fault (D4) (Figs. 2 and 3). D3 branches into numerous second-order faults in the northwest as it merges into the fault termination zone of the Dobi graben.

The southwest dipping D4 has a ramp with a 225 m vertical throw which extends from the top of the Stratoid basaltic layer down to the lacustrine deposit starting from the southeastern end of D3 (Fig. 3). K1b and K1a are situated southeast of D3. South of K1a and K1b, there is a northeast-dipping fault named K2 (Fig. 3). K1b, K1a, and K2 are all

major boundary faults found on the flank of a Kambourta graben which is situated northeast of the Dobi graben (Figs. 2 and 3).

The northern portion of the Dobi graben is defined as the fault termination zone and forms a symmetrical graben (Figs. 2 and 3). This zone is composed of numerous smaller intra-rift faults (the second-order faults located in the graben's floor) striking $120^{o} \pm 10^{o}$, which overlap in echelon style. In this zone, individual faults exhibit a horsetail, fish tail-ended fault system which is propagating mainly toward the northwest.

2.4.2 Spatial locations of barriers and the different geometries of displacement length fault profiles

Based on the initiation point, where slip starts, and where barriers arrested the propagations of the fault, we classified the faults as having elliptical slip profiles (both tips unrestricted) or asymmetrical fault length-displacement profiles. In the case of an elliptical slip profile, fault growth evolution shows both vertical development and a bilateral propagation and exhibits an elliptical displacement length profile (Fig. 2). However, through time, the elliptical faults cease propagation (Dumont et al., 2016). Our fault population analysis showed that, out of the 953 faults traced in the Dobi graben and its surrounding area, only 66 of the traced faults (cumulative length of ~129 km) are tapered to zero at both fault tips (both tip unrestricted or elliptical faults). These elliptical faults represent only ~6% of the total cumulative traced fault lengths (Table 1). Our results showed that ~42% of the elliptical faults mark a distinct boundary between the Dobi imbrication zone's faults and the Derela domain faults and extend in an echelon manner to the southern sections of the Dobi relay zone (Fig. 4).

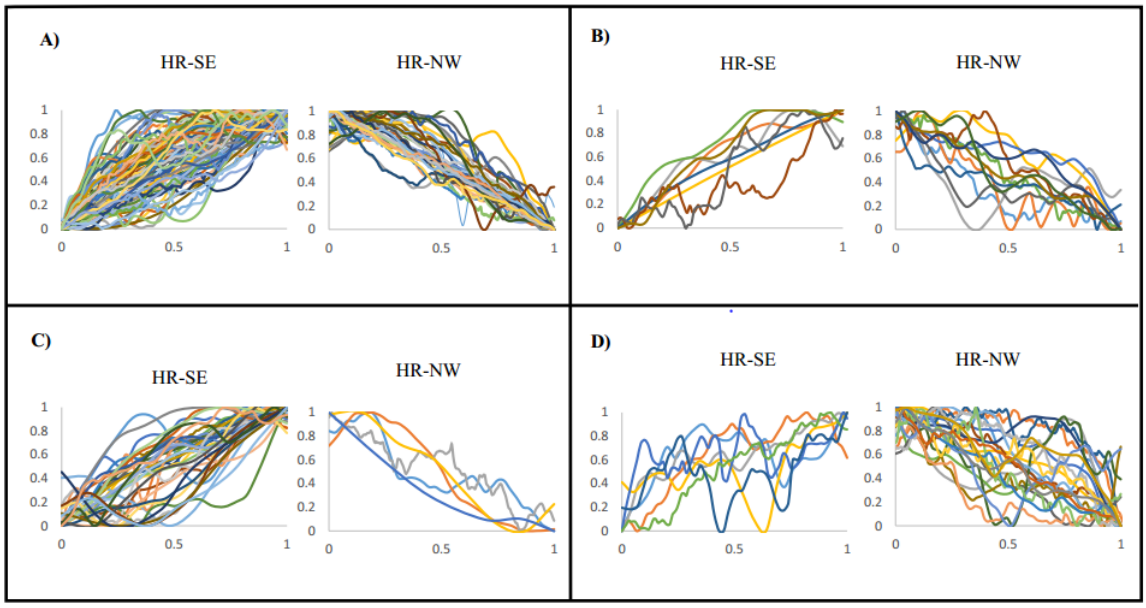

Figure 4 The termination styles and tapering direction of representative examples of the fault in the four different spatial locations. The abbreviation HR-SE for half restricted and tapering to southeast whereas HR-NW for half restricted and tapering toward northwest. The X-axis is the normalized fault traced length of the form (l/Lmax) and the y-axis is the normalized fault displacement of the form (D/Dmax). A) Imbrication fault zone; B) High linkage ramp zone; C) Dobi relay zone; D) Fault termination zone. For comprehensive profile shapes, see Manighetti et al. (2001a) and Dumont et al. (2016).

Additionally, ~18% of the elliptical faults are found in the Dobi-Hanle fault zone, where the majority of them are found at the northeastern edges of the fault zone. In addition, ~12% of these faults are found also at the southeastern boundary of the Derale fault zone; whereas, 18% of the elliptical faults are identified in the Dobi relay zone. Eleven of the 66 elliptical faults are found in the termination zone, but they represent

only ~9% of the total traced lengths of the elliptical faults since they exhibit a mean traced length of only ~1 km (Table 1; Fig. 5).

To the contrary, faults exhibit an asymmetrical displacement length profile when a barrier is encountered along either side of the fault tips and practically arrests the propagation of the fault during fault growth evolution. We noticed two major asymmetrical slip profiles in the Dobi graben, the half restricted and the tip restricted. The half restricted profiles are produced when a barrier is encountered along one of the fault's tips and when a displacement length ratio value of ~0.50 or more is calculated at the point where the barrier and the restricted tip are encountered (Figs. 4 and 5). We designated the displacement length profiles as tip restricted profiles when a displacement length ratio of ~0.49 or less was calculated at the point at which the restricted tip and the barrier were met (Figs. 4 and 5). We considered both tip restricted and half restricted faults as propagating unilaterally, and their steep gradients reflect an early arresting of lateral growth. The fault population analysis results show that ~8% (cumulative traced length of ~162 km) of the 953 faults are tip-restricted. However, ~85% (cumulative traced length of ~1699 km) of the faults in the Dobi graben revealed half-restricted displacement-length profiles, in which the Derela zone, the imbrication, and the Dobi-Hanle zone accounted for ~60% of the total traced length in this category (Table 1 and Fig. 5). To identify the spatial barriers and understand their relationships with the crustal structure and

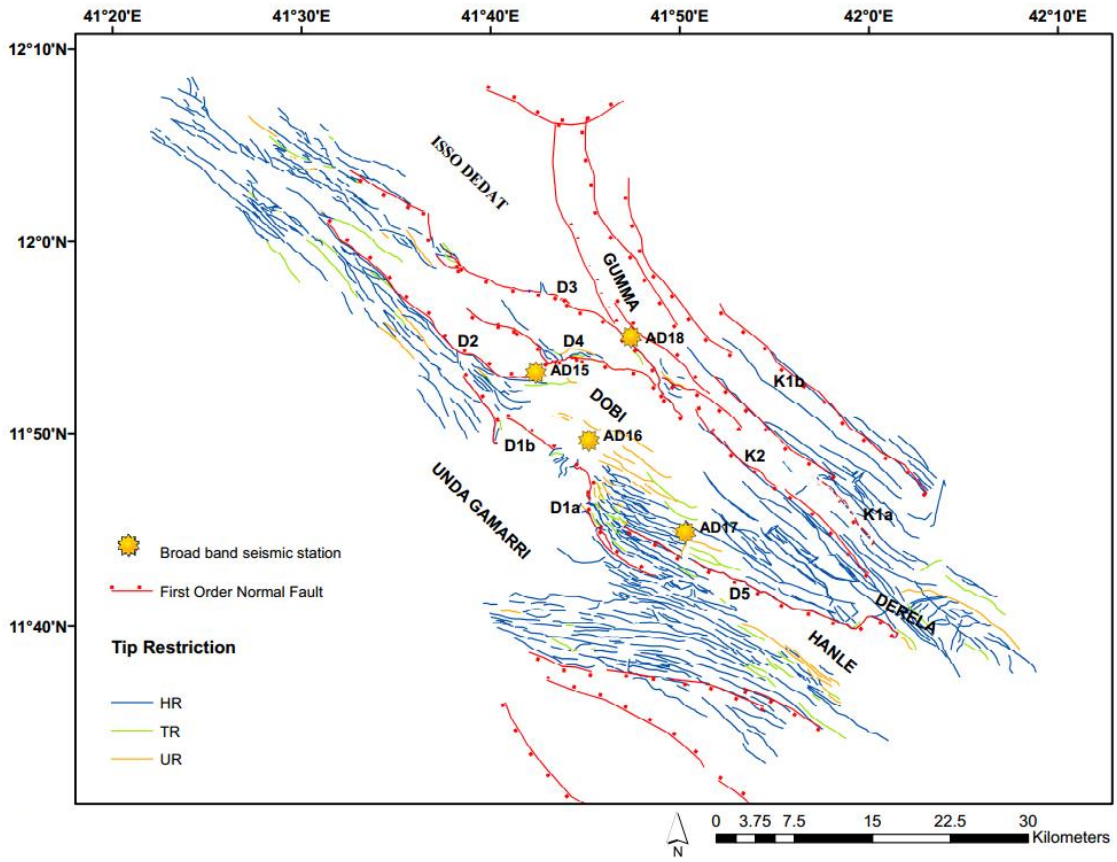

Figure 5: The structural map of the Dobi graben that are traced in Figure 2 is classified based on the manner on which faults propagations are arrested. HR is corresponding to a half restricted, TR is stands for tip restricted and UR is for unrestricted. The Broad band seismic stations represented by the yellow sunny symbol interpreted as presences of melts in the lower crust Reed at al. (2014).

understand the mechanical behavior of the crust in the area beneath the elastic deformation zone, we digitized over as point features the four broadband receiver stations (Reed et al., 2014) in the Dobi graben. We found that there is a clear spatial correlation between the different types of fault termination styles and the location of the broadband stations which exhibit a Vp/Vs ratio greater than 1.85. We observed that the faults' lateral

propagations are arrested at the four different locations where Reed et al.'s (2014) broadband receiver stations were installed, at AD15, AD16, AD17, and AD18. As indicated in Figure 6, at the southeast tip of the fault labelled D2 there exists a broadband receiver station, AD15, with a Vp/Vs ratio of 1.87. We also observed that station AD16, with a Vp/Vs ratio of 1.89, is located at the northwestern tips where the bilateral faults are extinct, particularly in the region between the Dobi relay and the imbrication fault zones. Station AD17, with a Vp/Vs value of 1.96, is also situated at breach faults which separate the southeast tapering imbrication zone faults and the northwest tapering imbrication zones. The outer boundary fault of the Dobi ramp zone, designated as D3, is broken down into multiple fault segments (Figs. 2, 5, and 6). We noticed that in two of D3's the southeastern segments, there are two fault segments which exhibit the half restricted fault termination style and the tip restricted fault termination style. Additionally, at the point where these two different fault termination styles come in contact, maximum displacement is displayed and overlapped at station AD18, which has a Vp/Vs value of 1.91.

Table 1. Different types of fault propagations arrest style with respect to their spatial populations in the different structural heterogeneity of the Dobi Graben

Type of restrictions	Spatial location	Number of traced faults	Length, Cumulative Sum (Km)	mean, Length (Km)	S.D, Length (Km)	Minimum Length (Km)	Maximum Length (Km)	Percentage W.R.T. Spatial Domain (%)	Percentage W.R.T. The total traced length (%)
Half Restricted (HR)	Derale	116	458	3.9	4.5	0.183	23	26.96	23.02
	Dobi-Hanle	146	424	2.9	2.7	0.107	19	24.96	21.31
	Dobi Ramp zone	54	55	1	1.1	0.039	6.2	3.24	2.76
	Imbrication zone	176	301	1.7	2.5	0.047	23	17.72	15.13
	Dobi Relay zone	85	125	1.4	2.4	0.05	17	7.36	6.28
	Fault termination Zone	233	336	1.7	1.7	0.052	11	19.78	16.89
HR Total		***810***	***1699***	***2***	***2.8***	***0.039***	***23***	100.00	**85.39**
Tip Restricted (TR)	Derale	6	19	3.1	1.8	0.861	6.9	11.80	0.95
	Dobi-Hanle	16	28	1.8	1.3	0.288	5.7	17.39	1.41
	Dobi Ramp zone	10	25	2.5	2.6	0.105	8.7	15.53	1.26
	Imbrication zone	22	39	1.7	1.7	0.21	5.9	24.22	1.96
	Dobi Relay zone	9	12	1.4	1.6	0.157	5	7.45	0.60
	Fault termination Zone	16	35	2.2	2.3	0.102	7.9	21.74	1.76
TR Total		***79***	***161***	***2***	***2***	***0.102***	***8.7***	100.00	**8.09**
Both tips Unrestricted (elliptical)	Derale	2	15	7.6	5.5	2.05	13.2	11.57	0.75
	Dobi-Hanle	8	24	2.9	2.1	0.456	6.5	18.50	1.21
	Dobi Ramp zone	8	15	1.9	1.3	0.362	4.1	11.57	0.75
	Imbrication zone	26	45	1.7	1.5	0.168	5.7	34.70	2.26
	Dobi Relay zone	7	19	2.7	1.6	1.1	5.9	14.65	0.95
	Fault termination Zone	9	11	1.2	1.3	0.127	4.1	8.48	0.55

elliptical Total		***60***	***129.7***	***2.1***	***2.2***	***0.127***	***13.2***	100.00	**6.52**
Total traced faults		953	1989.7						**100.00**

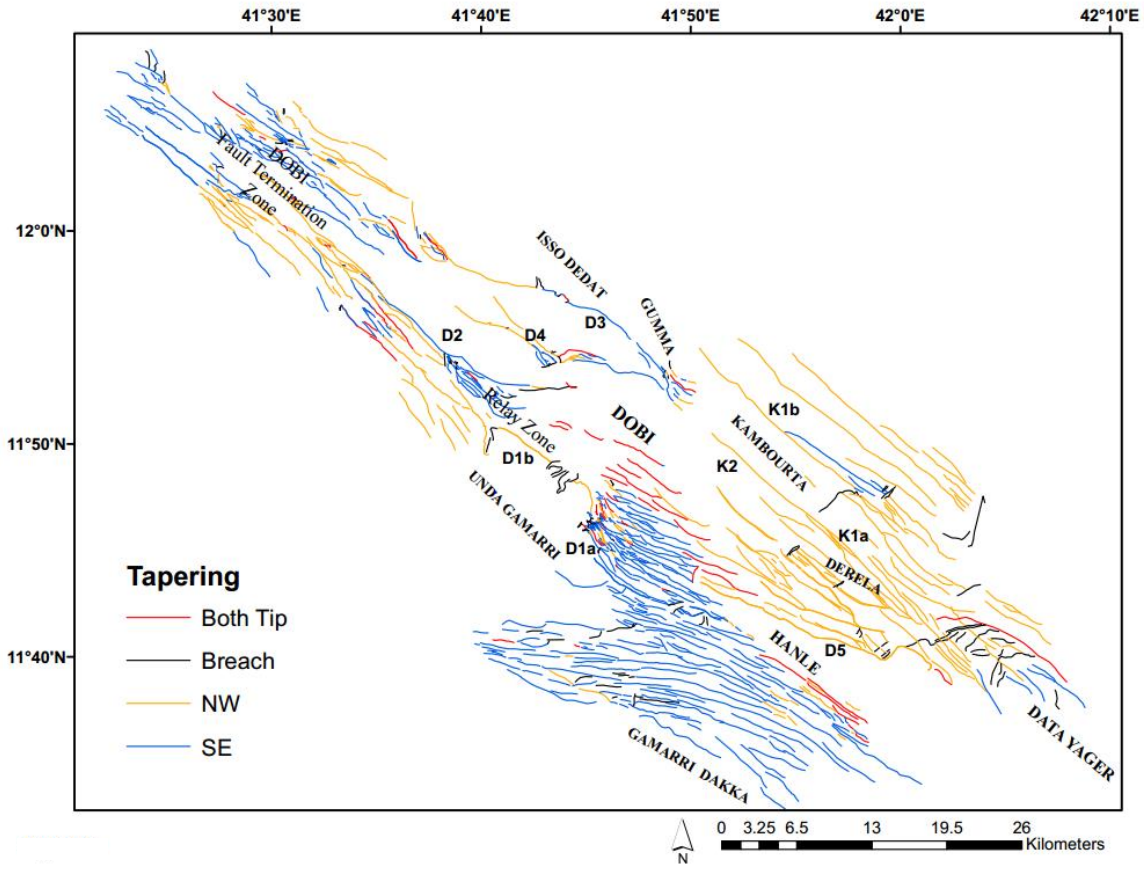

Figure 6: Structural map showing the different tapering directions of the faults in the Dobi graben and its surrounding.

2.4.3 Fault tapering direction

The overall spatial distribution of the fault displacement-length profiles indicates that ~40% of the cumulative fault traced lengths are northwest tapering, whereas ~45% of the total traced lengths are southeast tapering (Table 2; Figs. 4 and 6). Our fault population analysis also revealed that ~6% of the total traced fault lengths are tapering orthogonal to either northwest or southeast tapering faults, which are classified as breach

faults in this research. Additionally, we detected that ~7% of the traced faults are tapering toward both tips of the fault.

In this section, we focus on those faults which are tapering toward the northwest and southeast directions since they account for ~85% of the faults. The Derela fault zone contains ~46% of the faults which are tapering toward the northwest direction, the fault termination zone contains ~20% of these faults, and the imbrication zone accounts for ~17% of the northwest tapering population. Whereas, in the case of those faults which are tapering toward the southeast direction, the Dobi-Hanle fault zone accounts for ~45% of the southeast tapering fault system, following by the fault termination zone and the imbrication zone, which account for ~22% and ~18%, respectively (Table 2; Fig. 6).

Additionally, we noticed that the northwest tapering faults surround the southeast tapering faults at both sides of the rift shoulders and are forcing them to remain at the rift axial of the Dobi fault termination zones (Fig. 6). Similarly, the northwest portion of the Dobi ramp zone is dominated by the northwest tapering faults spatially, while the remaining southeast portion of the ramp zone is dominated by the southeast tapering faults. The spatial heterogeneities of these two tapering styles is also distinct in the Dobi relay zone and the southwest shoulder faults also taper northwest, but most of the faults in the graben floor show a southeast tapering direction.

Table 2. Different types of fault tapering direction and their population size in terms of percentages

Type of Tapering	Spatial location	Number of traced faults	Length, Cumulative Sum (Km)	mean, Length (Km)	S.D, Length (Km)	Minimum Length (Km)	Maximum Length (Km)	Percentage W.R.T. Spatial Domain (%)	Percentage W.R.T. The total traced length (%)
Both Tips (BT)	Derale	2	15.2	7.6	5.5	2.05	13.2	10.45	0.76
	Dobi-Hanle	8	23.7	2.9	2.1	0.456	6.5	16.29	1.18
	Dobi Ramp zone	8	15.2	1.9	1.3	0.362	4.1	10.45	0.76
	Imbrication zone	26	55.6	1.9	1.6	0.168	5.6	38.21	2.78
	Dobi Relay zone	8	22.9	2.8	1.6	1.11	5.9	15.74	1.14
	Fault termination	11	12.6	1.1	1.2	0.127	4.1	8.66	0.63
BT Total		***66***	***145.5***	***2.2***	***2.1***	***0.127***	***13.2***	***100.00***	***7.27***
Breach	Derale	37	60	1.6	1.1	0.242	5.2	46.08	3.00
	Dobi-Hanle	20	22	1.1	0.8	0.107	3.4	16.90	1.10
	Dobi Ramp zone	16	7.2	0.4	0.3	0.106	1	5.53	0.36
	Imbrication zone	29	18.8	0.65	0.5	0.047	2.3	14.44	0.94
	Dobi Relay zone	15	12.2	0.81	1.1	0.089	5	9.37	0.61
	Fault termination	20	9	0.45	0.36	0.047	1.5	6.91	0.45
Breach Total		***137***	***130.2***	***0.95***	***0.96***	***0.183***	***5.2***	***100.00***	***6.51***
NW	Derale	75	380	5	5.2	0.288	23.5	46.51	18.99
	Dobi-Hanle	18	23.4	1.3	0.75	0.299	3	2.86	1.17
	Dobi Ramp zone	22	38.5	1.7	1.8	0.167	8.7	4.71	1.92
	Imbrication zone	50	142.5	2.8	3.8	0.06	23.4	17.44	7.12
	Dobi Relay zone	30	63.7	2.1	2.3	0.056	8.1	7.80	3.18
	Fault termination	92	167.8	1.8	1.8	0.287	11.6	20.54	8.39
NW Total		***287***	***817***	***2.8***	***3.6***	***0.056***	***23.5***	***100.00***	***40.83***
SE	Derale	10	35.2	3.5	2.7	0.392	10.3	3.88	1.76
	Dobi-Hanle	124	407.3	3.3	2.9	0.274	19.2	44.85	20.36

	Dobi Ramp zone	27	44.3	1.6	2.1	0.039	8.7	4.88	2.21
	Imbrication zone	116	167.2	1.4	1.7	0.055	8.2	18.41	8.36
	Dobi Relay zone	48	58.5	1.2	2.6	0.05	17	6.44	2.92
	Fault termination Zone	138	195.6	1.4	1.75	0.052	7.9	21.54	9.78
SE Total		***463***	***908.2***	***1.9***	***2.3***	***0.039***	***19.2***	***100.00***	***45.39***
Total traced faults		**953**	**2000.9**						**100.00**

2.4.4 Correlation of the fault maximum displacement with its traced length, Dmax and Lmax, (R^2)

The relationship between the maximum fault scarp height, also referred to as maximum displacement (Dmax), and the fault traced length (Lmax) has been studied in detail for each fault zones and for all 953 traced faults. The results show that our Dmax/Lmax gradient ratios span three to four magnitudes, ranging from $1.00e^{-4}$ to $1.00e^{0}$, causing them to became highly scattered and poorly correlated, even in the Log-Log plot (Fig. 7A, Appendices 1, 2 and 3).

The common statistical values for "c" for the different types of faults and fault systems have been already documented in the literature, and c is approximately 0.03 for an extensional regime such as the AD (Schlische et al., 1996; Schultz and Fossen, 2002). When the faults are classified by fault termination style (the different kinds of mechanisms responsible for arresting fault propagation), we notice that the faults which have half-restricted termination styles or are unrestricted (elliptical) exhibit a relatively high R-square value, ~0.60 and ~0.67, respectively (Figs. 7B and D). Whereas those faults that have tip- restricted termination styles have an R-square value of 0.54 (Fig. 7C). Additionally, those faults which exhibit a half-restricted termination style account for 85% of the total traced lengths of the 953 traced faults. The Dmax/Lmax ratio of these faults is 0.03, and it is in accord with the vertical displacement gradient which is documented in the literature (Appendices 2 and 3). When considering tapering directions, those faults classified as tapering toward the northwest, tapering toward the southeast, and those faults tapering at both fault tips exhibit an R-square value of ~0.65 (Figs. 8A,

C, and D, Appendices 2 and 3). However, those faults which are classified as a breach in this research have a relatively lower R-square value of 0.42 (Fig. 8B).

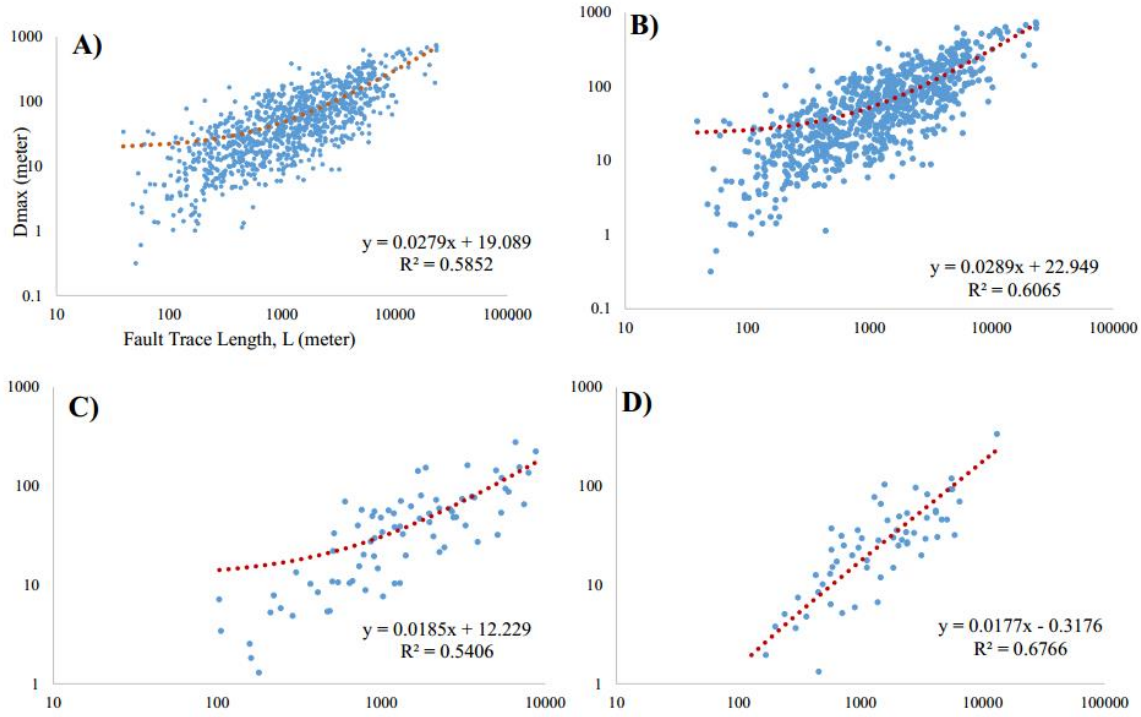

Figure 7: (A) Log-Log plots of Dmax in meter (Vertical axis) to traced length in kilometer (Horizontal axis) of all 953 traced faults of the Dobi graben and its surrounding; (B) Log-Log plots of Dmax to Lmax of those faults that exhibited the termination style of half restricted, HR; (C) Log-Log plots of Dmax to Lmax of those faults that exhibited the termination style of tip restricted, TR; and (D) Log-Log plots of Dmax to Lmax of those faults that exhibited unrestricted, UR

Comparing our vertical displacement gradient (c) with the Dmax/Lmax ratio value in the literature (e.g., Schlische et al., 1996) reveals that those faults classified as

tapering toward the northwest and tapering toward the southeast exhibit a Dmax/Lmax ratio of ~0.03. Whereas, those tapering at fault tips exhibit a Dmax/Lmax ratio of 0.016, which is 2 times less than the value documented in the literature (Appendices 1, 2, and 3).

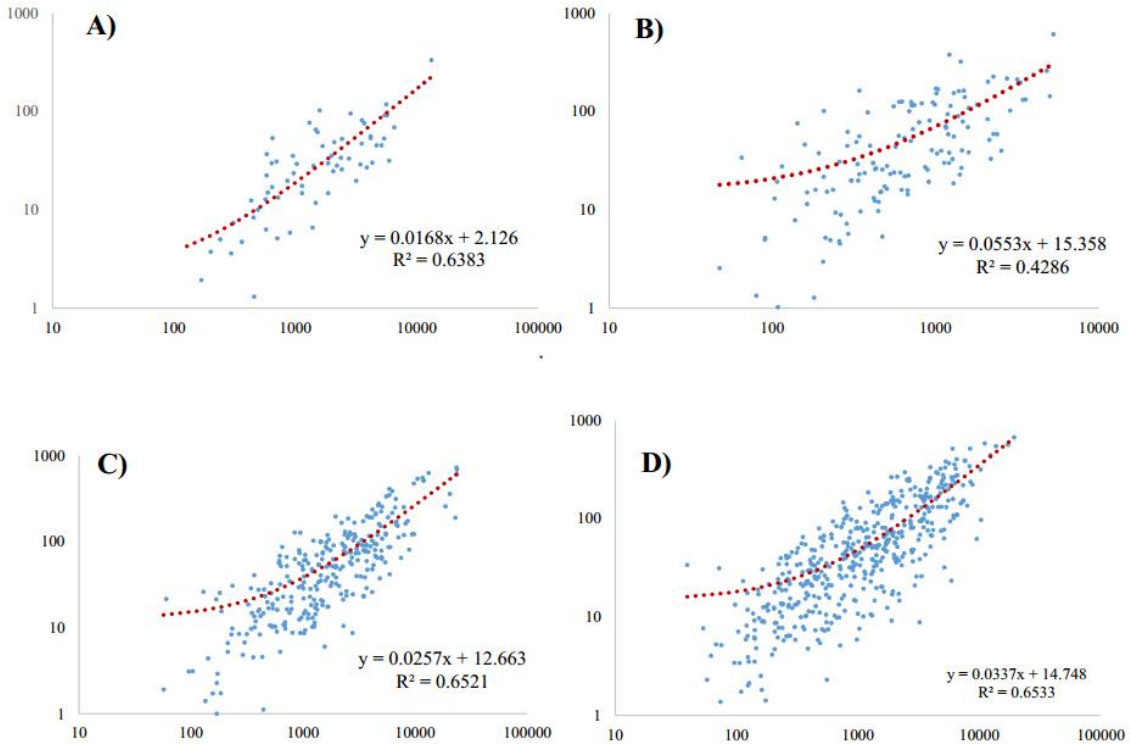

Figure 8: Log-Log plots of Dmax in meter (Vertical axis) to traced length in kilometer (Horizontal axis). (A) Corresponding to faults that propagating in two directions and tapering at both tips; (B) Faults that propagating orthogonal to faults that have a northwest striking direction and considered as a breach; (C) Corresponding to faults that tapering in northwest direction and (D) Corresponding to faults that tapering in southeast direction

2.5 Discussion

Our analysis of the fault population data suggested that there exist two different types of fault tapering directions in the Dobi graben and its surrounding area, in which ~40% of the fault traced lengths are northwest tapering, and ~45% of the total traced lengths are southeast tapering (Table 2; Figs. 5 and 7). Therefore, the cumulative traced lengths of faults account for more than 85% of the 953 faults traced in this study resembled the strain directions of either RSR or GAR. This is in accord with Manighetti et al. (2001) observations that most faults in the Asal rifts have slip length profiles tapering northwestward. Likewise, Nico et al (1996), Peacock and Sanderson (1996), and Manighetti et al. (2001) have explained that the linear profiles typically mimic the propagation history of the faults, tapering in the direction of fault propagation similar to our fault population analysis. Our analysis gives insight into the existence of two different types of fault tapering within the Dobi graben and the surrounding area which support the propagation direction of the traced faults being in the direction of the regional strain gradient of either the RSR or the GAR. Our findings showed that ~45% of the normal faulting in the Dobi graben is tapering towards the southeast, resembling the RSR regional strain gradient, whereas ~40% of the faults in the Dobi graben and the surrounding area mimic the GAR regional strain gradient, with ~0.7 regression correlation coefficients (R-square values). Therefore, we suggest that ~85% of the lateral propagations of the 953 traced faults in the Dobi graben and its surrounding area is influenced highly by the regional strain transfer gradients of the RSR and GAR.

Additionally, this study provides a deeper insight into the deformation mechanism in the southeastern part of the Dobi graben, particularly in the Dobi-Hanle fault zone,

Dobi imbrication, and Derela fault zone. Figure 5 and Table 2 indicate that ~46% of the faults in the Derela fault zone propagate northwest, whereas ~63% of the faults in the Dobi imbrication zone, and Dobi-Hanle fault zone propagate in a southeastern direction. The location of these two oppositely propagating fault systems demonstrates that the northwest tapering is parallel to the southwest tapering faults. Presumably both fault systems taper to zero at the point of contact in the form of a left lateral strike-slip system. Contrarily, despite the 1969 Serdo strike-slip event earthquake (Kebede et al., 1989), most repeated episodes of earthquakes recorded in the past 40 years released tensile stresses in the central AD, such as the November, 1978 Asal Rift earthquakes (Abdallah et al., 1979; Jacques et al., 1996) and the August, 1989 Dobi earthquakes (Braunmiller and Nabelek, 1990; Dziewonski et al., 1990; Sigmundsson, 1992; Jacques, 1995; Jacques et al., 2011), indicating that crustal extension is accommodated mainly by normal faulting. However, based on interpretations of satellite imageries, Mohr (1971) suggested the presence of left lateral strike-slip shearing in the Dobi graben. From slickensides analysis performed at several points in the Dobi rift and at its shoulders, Abbate et al. (1995) also reported the existence of strike-slip faults with NNE to ENE (rift transversal) strikes. Furthermore, Hofstetter and Beyth, (2003) also illustrated a strike-slip seismic pitch with the fault planes striking WNW–ESE to NW–SE at the Dobi ramp zone around 42◦E and 12◦N, just ~ 3 km northwest of the strike-slip component reported by Abbate et al. (1995). This is also in accord with the strike-slip strain rate tensor value reported in the present- day kinematic synthesis of the central AD by Dobure et al. (2016), which was derived from geodetic data.

Similarly, our fault population analysis research discovered that at the inter-rift faults in D1a (Figs. 2, 3, 5, and 6), there exist a small component of dextral strike-slip produced by the intra-rift faults. This small component of dextral strike-slip accounts for ~17% of the total fault population traced in the Dobi imbrication zone and ~7% of the 953 faults traced in the Dobi graben and its surrounding area (Table 2 and Fig. 6). Similar findings were presented in Jacques et al. (2011), explaining the existence of small components of dextral strike-slip present along the SW-dipping, N110°E ± 10°-striking normal faults in the southeastern part of the Dobi graben. Jacques et al. (2011) termed the kinematics in the southeastern Dobi local bookshelf faulting as strain transfer between the stepping, NW- trending Dobi and Hanle grabens. Additionally, Paleomagnetic and tectonic studies (Manighetti et al., 2001; Kidane et al., 2003) also explained the existence of a counterclockwise rotation in the Dobi and the surrounding area, within which NW-trending faults are, in turn, involved in clockwise bookshelf faulting at a larger regional scale. This is in accord with the bookshelf faulting model proposed by Tapponnier et al. (1990), in which the RSR and GAR act as two spreading propagators, leading to a large zone of dextral strike-slip shear and the clockwise rotation which activated a left lateral strike slip along the NW-striking elongated blocks.

Additionally, a strong correlation between the melt material presence in the lower crust, which was reported by Reed et al. (2014), and the arresting of fault lateral propagation was observed. For example, Figure 6 indicates that lateral propagations are arrested at the four locations indicated by Reed et al. (2014): AD15, AD16, AD17, and AD18. Utilizing a broadband passive seismic receiver function, Reed et al. (2014) reported high V_p/V_s ratios of 1.85 or more within the lower crust beneath the Dobi

graben, which implies the presence of melt (Fig. 5). Dumont et al. (2016) also suggest that lateral propagation of faults is easier away from areas where magma has been stored for a long time at crustal depth, thus modifying the thermo-mechanical properties of the host rock. The spatial correlation between the melt zones identified by Reed et al. (2014) and the fault lateral propagation arrest shown in this research is presumably due to the thermo-mechanical heterogeneities within the brittle crust which stimulate the initiation of faults. Additionally, they also act as barriers to fault propagation, as demonstrated by the faults labeled D2 and D3 in Figure 5 as well as many of the intra-rift faults found in the low angle short normal faults located in the Dobi relay, fault termination, and imbrication zones (Figs. 2 and 5; Manighetti et al., 2004, Dumont et al., 2016). In addition, the inelastic deformation due to the highly damaged crust located at the fault tips, as demonstrated in the fault termination zone, is susceptible to preventing the lateral propagation of the faults (Manighetti et al., 2004).

2.6 Conclusion

Results from our fault population analysis using SRTM DEM within the Dobi graben aided by satellite imageries suggest that the directions of faults propagation are highly influenced by the two regional volcanic rifts, RSR and GAR. Our fault population analysis also indicates the possible presence of melt in the lower crust which acts as a barrier for fault lateral propagations. A small-scale, local bookshelf faulting model may best explain the deformation mechanism in the southeastern part of Dobi graben. Our results also suggest a constant fault growth model for the normal faulting in the Dobi

graben and adjacent area, as a 0.03 Dmax/Lmax ratio was exhibited for ~85% of the traced faults.

2.7 Acknowledgments

We thank our colleagues from Oklahoma State University and Addis Ababa University who provided insight and expertise that greatly assisted the research and for comments that greatly improved the manuscript. The SAS program script code for the regression analysis is performed in collaboration with Mr. Abdul Kelil. This is Oklahoma State University Boone Pickens School of Geology contribution # 2018-xx.

2.8 References

Abbate, E., Passerini, P., and Zan, L., 1995. Strike-slip faults in a rift area: a transect in the Afar Triangle, East Africa: Tectonophysics 241, p. 67-97.

Acton, G.D., Stein, S. & Engeln, J., 1991. Block rotation and continental extension in Afar: a comparison to oceanic microplate systems. Tectonics 10, 501–526.

Acton, G.D., Tessema, A., Jackson, M. & Bilham, R., 2000. The tectonic and geomagnetic significance of paleomagnetic observations from volcanic rocks from central Afar, Africa. Earth and planetary Sciense Letter 180, 225–241.

Aki, K., 1979. Characterization of barriers on an earthquake fault. Journal of Geophysical Research: Solid Earth 84, 6140-6148.

Amelung, F., Oppenheimer, C., Segall, P., and Zebker, H., 2000. Ground Deformation near Gada'Ale Volcano, Afar, observed by Radar Interferometry: Geophysical Research Letters, v. 27, p. 3093-3096.

Audin, L. et al., 2004. Paleomagnetism and K-Ar and 40Ar/39Ar ages in the Ali Sabieh area (Republic of Djibouti and Ethiopia): constraints on the mechanism of Aden ridge propagation into southeastern Afar during the last 10 Myr. Geophysical Journal International 158, 327–345.

Barberi, F., Santacroce, R., 1980. The Afar Stratoid Series and the magmatic evolution of the East Africa rift system. Bulletin Societe Geologique de France 22, 891–899.

Beyene, A., and Abdelsalam, M. G., 2005. Tectonics of the Afar Depression: A review and synthesis: Journal of African Earth Sciences 41, 41-59.

Berckhemer, H., Baier, B., Bartelsen, H., Behle, A., Burkhardt, H., Gebrande, H., Makris, J., Menzel, H., Miller, H., Vees, R., 1975. Deep seismic soundings in the Afar region and on the highland of Ethiopia. Afar Depression of Ethiopia 1, 89–107.

Braunmiller, J., and J. Nabelek., 1990. The 1989 Ethiopia earthquake sequence, Eos Trans. American Geophysical Union 71, 1480.

Bridges, D.L., Mickus, K., Gao, S.S., Abdelsalam, M.G., Alemu, A., 2012. Magnetic stripes of a transitional continental rift in Afar. Geology 40, 203–206.

Cartwright, J.A., Trudgill, B.D., Mansfield, C.S., 1995. Fault growth by segment linkage: an explanation for scatter in maximum displacement and trace length data from the Canyonlands Grabens of SE Utah. Journal of Structural Geology 17, 1319–1326.

Courtillot, V., Achache, J., Landre, F., Bonhommet, N., Montigny, R. & Feraud, G., 1984. Episodic spreading and rift propagation: new paleomagnetic and geochronologic data from the Afar nascent passive margin, Journal of geophysical Research 89, 3315–3333.

Courtillot, V., Armijo, R. & Tapponnier, P., 1987. The Sinai triple junction revisited, Tectonophysics, 141, 181–190.

Cowie, P.A., Scholz, C.H., 1992a. Physical explanation for the displacement-length relationship for faults using a post-yield fracture mechanics model. Journal of Structural Geology 14, 1133-1148.

Cowie, P. A., 1998. Normal fault growth in three dimensions in continental and oceanic crust, in Faulting and Magmatism at Mid-Ocean Ridges, Geophys. Monogr. Ser., vol. 106, edited by R. Buck et al., pp. 325 – 348, AGU, Washington, D. C.

Davis, K., Burbank, D.W., Fisher, D., Wallace, S., Nobes, D., 2005. Thrust-fault growth and segment linkage in the active Ostler fault zone, New Zealand. Journal of Structural Geology 27, 1528-1546.

Dawers, N.H., Anders, M.H., Scholz, C.H., 1993. Growth of normal faults: displacement-length scaling. Geology 21, 1107-1110.

Dawers, N.H., Anders, M.H., 1995. Displacement-length scaling and fault linkage. Journal of Structural Geology 17, 607-614. Dawers, N.H., Anders, M.H., Scholz, C.H., 1993. Growth of normal faults: displacement–length scaling. Geology 21, 1107–1110.

Demissie, Z.S., Kevin M., Bridges, D., Abdelsalam, M.G., Atekwana, E.A., 2018. Upper lithospheric structure of the Dobi graben, Afar Depression from magnetic and gravity data. Journal of African Earth Sciences. Doi.org/10.1016/j.jafrearsci.2018.06.012

Doubre, C., Deprez, A., Masson, F., Socquet, A., Lewi, E., Grandin, R., Nercessian, A., Ulrich, P., Chabalier, D. J., Saad. I., Abayazid, A., Peltzer, G., Delorme, A., Calais, E., Wright, T., 2016. Current deformation in Central Afar and triple junction kinematics deduced from GPS and InSAR measurements. Geophysical Journal International 208, 936-953.

Dugda, M.T., Nyblade, A.A., 2006. New constraints on crustal structure in eastern Afar from the analysis of receiver functions and surface wave dispersion in Djibouti. Geol. Soc., Lond., Spec. Publ. 259, 239–251.

Dumont, S., Socquet, A., Grandin, R., Doubre, C., Klinger, Y., Jacques, E., 2016. Magma influence on propagation of normal faults: Evidence from cumulative slip profiles along Dabbahu-Manda-Hararo rift segment (Afar, Ethiopia). Journal of Structural Geology 95, 48-59.

Dziewonski, A. M., G. Ekstrom, J. H. Woodhouse, and G. Zwart, 1990. Centroid moment tensor solutions for July-September 1989. physics Earth planetary 62, 529-532.

Ferguson, D.J., Calvert, A.T., Pyle, D.M., Blundy, J.D., Yirgu, G., Wright, T.J., 2013. Constraining timescales of focused magmatic accretion and extension in the Afar crust using lava geochronology. Nat. Commun. 4, 1416.

Fossen, H., Rotevatn, A., 2016. Fault linkage and relay structures in extensional settingsda review. Earth-Science Review 154, 14-28.

Gupta A. and Scholz H. C., 2000. Brittle strain regime transition in the Afar depression: Implications for fault growth and seafloor spreading. Geology 28, 1087-1090.

Grandin, R., Socquet, A., Binet, R., Klinger, Y., Jacques, E., de Chabalier, J.B., ..., Pinzuti, P., 2009. September 2005 Manda Hararo-Dabbahu rifting event, Afar

(Ethiopia): constraints provided by geodetic data. J. Geophys. Res. Solid Earth 114 (B8).

Hammond, J.O.S., Kendall, J.M., Stuart, G.W., Keir, D., Ebinger, C., Ayele, A., Belachew, M., 2011. The nature of the crust beneath the Afar triple junction: evidence from receiver functions. G-cubed 12.

Hamling, I.J., Ayele, A., Bennati, L., Calais, E., Ebinger, C.J., Keir, D., ..., Yirgu, G., 2009. Geodetic observations of the ongoing Dabbahu rifting episode: new dyke intrusions in 2006 and 2007. Geophys. J. Int. 178 (2), 989e1003.

Hayward, N. J., and Ebinger, C. J., 1996. Variations in the along-axis segmentation of the Afar Rift system: Tectonophysics, 15, 244-257.

Hofstetter, R., Beyth, M., 2003. The Afar Depression: interpretation of the 1960–2000 earthquakes. Geophys. J. Int. 155, 715–732.

Jacques, E., Ruegg, J.C., Lepine, J.C., Tapponnier, P., King, G.C.P., and Omar, A., 1999. Relocation of M>2 events of the 1989 Dobi seismic sequence in Afar: Evidence for earthquake migration: Geophysical Journal International 138, 447-469.

Jacques, E. ; Kidane, T. ; Tapponnier, P. ; Manighetti, I. ; Gaudemer, Y. ; Meyer, B. ; Ruegg, J. C. ; Audin, L. ; Armijo, R., 2011. Normal Faulting during the August 1989 Earthquakes in Central Afar: Sequential Triggering and Propagation of Rupture along the Dobi Graben. Bulletin of the Seismological Society of America 101, 994-1023.

Kidane, T., Courtillot, V., Manighetti, I., Audin, L., Lahitte, P., Quidelleur, X., Gillot, P.Y., Gallet, Y., Carlut, J., and Haile, T., 2003. New paleomagnetic and geochronologic results from Ethiopian Afar: Block rotations linked to rift overlap

and propagation and determination of a ~2 Ma reference pole for stable Africa: Journal of Geophysical Research 108, 2102.

King, G.C.P., 1986. Speculations on the geometry of the initiation and termination processes of earthquake rupture and its relation to morphology and geological structure. Pure Applied Geophysics 124, 567-585.

Lahitte, P., Gillot, P.Y., Courtillot, V., 2003a. Silicic central volcanoes as precursors to rift propagation: the Afar case. Earth Planet. Sci. Lett. 207 (1), 103e116.

Lahitte, P., Gillot, P.Y., Kidane, T., Courtillot, V., Bekele, A., 2003b. New age constraints on the timing of volcanism in central Afar, in the presence of propagating rifts. J. Geophys. Res. Solid Earth 108 (B2).

Lewi, E., Keir, D., Birhanu, Y., Blundy, J., Stuart, G., Wright, T., Calais, E., 2016. Use of a high-precision gravity survey to understand the formation of oceanic crust and the role of melt at the southern Red Sea rift in Afar, Ethiopia. Geol. Society, Lond., Spec. Publ. 420, 165–180.

Manighetti, I., P. Tapponnier, V. Courtillot, S. Gruszow, and P.Y. Gillot., 1997. Propagationof rifting alongthe ArabiaSomalia plate boundary: The Gulfs of Aden and Tadjoura, Journal of Geophysical Research: Solid Earth 102, 2681-2710.

Manighetti, I., Tapponnier, P., Gillot, P.Y., Jacques, E., Courtillot, V., Armijo, R., Ruegg, J.-C., and King, G., 1998. Propagation of rifting along the Arabia-Somalia plate boundary: Into Afar: Journal of Geophysical Research: Solid Earth 103, 947-4974.

Manighetti, I., King, G.C.P., Gaudemer, Y., Scholz, C.H., Doubre, C., 2001a. Slip accumulation and lateral propagation of active normal faults in Afar. Journal of Geophysical Research: Solid Earth 106, 13667-13696.

Manighetti, I., Tapponnier, P., Courtillot, V., Gallet, Y., Jacques, E., Gillot, P.Y., 2001b. Strain transfer between disconnected, propagating rifts in Afar. Journal of Geophysical Research: Solid Earth 106, 13613-13665.

Manighetti, I., King, G., Sammis, C.G., 2004. The role of off-fault damage in the evolution of normal faults. Earth Planet. Sci. Lett. 217 (3), 399e408. Manighetti, I., Campillo, M., Bouley, S., Cotton, F., 2007. Earthquake scaling, fault segmentation, and structural maturity. Earth and Planetary Science Letters 253, 429-438.

Manighetti, I., Caulet, C., Barros, L., Perrin, C., Cappa, F., Gaudemer, Y., 2015. Generic along-strike segmentation of Afar normal faults, East Africa: implications on fault growth and stress heterogeneity on seismogenic fault planes. Geochemistry Geophysics Geosystem 16 2, 443-467.

Makris, J., Ginzburg, A., 1987. The Afar Depression: transition between continental rifting and sea-floor spreading. Tectonophysics 141, 199–214.

Medynski, S., Pik, R., Burnard, P., Williams, A., Vye-Brown, C., Ferguson, D., ..., Calvert, A., 2013. Controls on magmatic cycles and development of rift topography of the Manda Hararo segment (Afar, Ethiopia): insights from cosmogenic 3 He investigation of landscape evolution. Earth Planet. Sci. Lett. 367, 133e145.

Medynski, S., Pik, R., Burnard, P., Vye-Brown, C., France, L., Schimmelpfennig, I., …, Yirgu, G., 2015. Stability of rift axis magma reservoirs: spatial and temporal evolution of magma supply in the Dabbahu rift segment (Afar, Ethiopia) over the past 30 kyr. Earth Planet. Sci. Lett. 409, 278e289.

Medynski, S., Pik, R., Burnard, P., Dumont, S., Grandin, R., Williams, A., Blard, P.-H., Schimmelpfennig, I., Vye-Brown, C., France, L., Ayelew, D., Benedetti, L., Yirgu, G., ASTER team, 2016. Magmatic cycles pace tectonic and morphological expression of rifting (Afar depression, Ethiopia). Earth Planet. Sci. Lett. 446, 77e88. http://dx.doi.org/10.1016/j.epsl.2016.04.014

McClusky, S., Reilinger, R., Ogubazghi, G., Amleson, A., Healeb, B., Vernant, P., Sholan,J., Fisseha, S., Asfaw, L., Bendick, R., Kogan, L., 2010. Kinematics of the southern Red Sea-Afar triple junction and implications for plate dynamics. Geophys. Res. Lett. 37 (n/a-n/a).

Mitku, B., Amassu, E., Arefayne, T., Gichila, B., 2013. Geological Map of Serdo Map Sheet (NC 37-4), Federal Democratic Republic of Ethiopia Ministry of Mines Geological Survey of Ethiopia.

Morton, W. H., and Black, R., 1975. Afar Depression of Ethiopia, *in* Pilger, A., and Rosler, A., eds., Afar Depression of Ethiopia, Proceedings of an International Symposium on the Afar Region and Rift Related Problems, Bad Bergzabren, Germany, 1974, Volume 1.

Muraoka, H., Kamata, H., 1983. Displacement distribution along minor fault traces. Journal of Structural Geology 5, 483–495.

Nicol, A., Watterson, J., Walsh, J.J., Childs, C., 1996. The shapes, major axis orientations and displacement patterns of fault surfaces. Journal of Structural Geology 18, 235–248.

Nicol, A., Walsh, J.J., Villamor, P., Seebeck, H., Berryman, K.R., 2010. Normal fault interactions, paleoearthquakes and growth in an active rift. Journal of Structural Geology 8, 1101-1113.

Nixon, C.W., Sanderson, D.J., Dee, S.J., Bull, J.M., Humphreys, R.J., Swanson, M.H., 2014. Fault interactions and reactivation within a normal-fault network at Milne Point, Alaska. American Associsation of Petroluem Geology Bulltien 98 (10), 2081-2107.

Nooner, S.L., Bennati Laura, L., Calais, E., Buck, W.R., Hamling, I., Wright, T., Lewi, E.,2009. Post-rifting relaxation in the Afar region, Ethiopia. Geophys. Res. Lett. 36, L21308.

Pagli, C., Wang, H., Wright, T.J., Calais, E., Lewi, E., 2014. Current plate boundary deformation of the Afar rift from a 3-D velocity fi eld inversion of InSAR and GPS. J. Geophys. Res.: Solid Earth 119, 8562–8575.

Peacock, D.C.P., Sanderson, D.J., 1991. Displacement and segment linkage and relay ramps in normal fault zones. Journal of Structural Geology 13, 721–733.

Pickering, G., Peacock, D.C.P., Sanderson, D.J., Bull, J.M., 1997. Modelling tip zones to predict the throw and length character- istics of faults. Bulletin of American Association of Petroleum Geologists 81, 82- 99.

Pollard, D.D., and P. Segall, 1987. Theoretical displacements and stresses near fractures in rock: With applications to faults, joints, veins,dikes,and solution surfaces, in

Fracture Mechanics of Rock, edited by B.K. Atkinson, pp.277-350, Academic Press,San Diego, Calif.

Polun, S.G., Gomez, F., Tesfaye, S., 2018. Scaling properties of normal faults in the central Afar, Ethiopia and Djibouti: Implications for strain partitioning during the final stages of continental breakup. Journal of Structural Geology 115 (2018) 178–189.

Reed, C.A., Almadani, S., Gao, S.S., Elsheikh, A.A., Cherie, S., Abdelsalam, M.G., Thurmond, A.K., Liu, K.H., 2014. Receiver function constraints on crustal seismic velocities and partial melting beneath the Red Sea rift and adjacent regions, Afar Depression. J. Geophys. Res.: Solid Earth 119, 2138–2152.

Schlische, R.W., Young, S.S., Ackermann, R.V., Gupta, A., 1996. Geometry and scaling relations of a population of very small rift-related normal faults. Geology 24, 683–686.

Schultz, R.A., Fossen, H., 2002. Displacement–length scaling in three-dimensions: the importance of aspect ratio and application to deformation bands. Journal of Structural Geology 24, 1389-1411.

Soliva, R., and A. Benedicto., 2004. A linkage criterion for segmented normal faults, Journal of Structural Geology, 26, 2251-2267.

Roche, V., Homberg, C., Rocher, M., 2012. Fault displacement profiles in multilayer systems: from fault restriction to fault propagation. Terra Nova 24 (6), 499-504.

Rowland, J.V., Baker, E., Ebinger, C.J., Keir, D., Kidane, T., Biggs, J., Hayward, N., Wright, T.J., 2007. Fault growth at a nascent slow-spreading ridge: 2005 Dabbahu rifting episode, Afar. Geophys. J. Int. 171, 1226–1246.

Tapponnier, P., Armijo, R., Manighetti, I., and Courtillot, V., 1990. Bookshelf faulting and horizontal block rotations between overlapping rifts in Southern Afar: Geophysical Research Letters 17, 1-4.

Tesfaye, S., 2005. Fault population investigation and estimating magnitude of extension in Guma Graben, Central Afar, Ethiopia, Journal of African Earth Sciences. 437–444.

Tesfaye, S., M.G.Rowan, K.Mueller, Trudgill, B. D., and Harding, D. J., 2008. Relay and accommodation zones in the Dobe and Hanle grabens, central Afar, Ethiopia and Djibouti, Journal of the Geological Society, London, 535–547.

Tibaldi, A., Bonali, F.L., Einarsson, P., Hjartardottir, A.R., Mariotto, F.P., 2016. Partitioning of Holocene kinematics and interaction between the Theistareykir Fissure Swarm and the Husavik-Flatey fault, North Iceland. Journal of Structural Geology 83, 134-155.

Vellutini, P. J., 1990. The Manda-Inakir Rift, Republic of Djibouti: a comparison with the Asal Rift and its geodynamic interpretation: Tectonophysics, 172, 141-153.

Vye-Brown, C., Medynski, S., Smith, K.B., Field, L., Wright, T., 2012. Geological Map of the Dabbahu (Manda-hararo) Rift, North, 1: 100,000 Scale (British Geological Survey).

Walsh, J.J., Watterson, J., 1988. Analysis of the relationship between the displacements and dimensions of faults. Journal of Structural Geology 10, 239–247.

Walsh, J.J., Bailey, W.R., Childs, C., Nicol, A., Bonson, C.G., 2003a. Formation of segmented normal faults: a 3-D perspective. Journal of Structural Geology 25, 1251– 1262.

Willemse, E.J.M., Pollard, D.D., Aydin, A., 1996. Three-dimensional analyses of slip distributions on normal fault arrays with consequences for fault scaling. Journal of Structural Geology 18, 295–309.

Wright, T.J., Sigmundsson, F., Pagli, C., Belachew, M., Hamling, I.J., Brandsdottir, B., Keir, D., Pedersen, R., Ayele, A., Ebinger, C., Einarsson, P., Lewi, E., and Calais, E., 2012. Geophysical constraints on the dynamics of spreading centres from rifting episodes on land: Nature Geoscience, v. 5, p. 242-250.

PAPER II

CURRENT DEFORMATION MECHANISM OF THE DOBI GRABEN FROM SURFACE TIME SERIES DISPLACEMENT ANALYSIS OF InSAR, AFAR DEPRESSION IN ETHIOPIA

3.0 Abstract

The Dobi graben is a Quaternary, NW-trending, continental rift found within the East-Central Block (ECB) of the Afar Depression (AD) in Ethiopia. The AD might be the only place where three active rifts meet on land. This diffused rift-rift-rift triple junction in the ECB comprises the overlap zone between the Red Sea and the Gulf of Aden propagators. Rifting is ongoing in the Dobi graben as evidenced by the August 1989 earthquakes of magnitude ($5.7 < Ms < 6.2$). This study carried out a surface displacement time series analysis to examine the kinematics of the Dobi graben and the surrounding area using 24 descending orbit scenes (between November 2003 and January 2010) along Track 6 of the Advanced Synthetic Aperture Radar (ASAR), C-band ($\lambda = 5.6$ cm) acquired by the Environmental Satellite (ENVISAT). We utilized the Small Baseline Algorithm (SBA) and Quasi Permanent Scatterer techniques, which were implemented independently to generate line of sight (LOS) displacement maps, LOS velocity maps, LOS time series maps and profile curves.

Results from the velocity and displacement maps and time series analysis suggest that creeping is associated mainly with normal faulting and could be the primary tectonic deformation mechanism. The anomalous continuous uplifting exhibited at the rift shoulder and in the horst area might be associated with the presence of temporary reactivation of normal faulting in the region. The oblique, positive LOS signals observed in different parts of the Dobi graben might serve as a proxy for understanding how strain is localized as normal faulting and transferred in the region in a distinct northeast direction. This explanation supports both the arguments for the northeast migration of the triple junction and the transfer of strain from the southernmost Red Sea Rift (RSR) to the westernmost Gulf of Aden Rift (GAR).

Keywords: **Afar Depression, Dobi graben, SBA, QPS, Strain localization and transfer, Time series analysis**

RESEARCH HIGLIGHTS

- SBA and QPS are used independently to study the deformation mechanism.
- Extension is caused by normal faulting in the Dobi graben.
- Time series displacement analysis is indicating deformation by creeping.
- Fault propagations is arrested with geological heterogeneities running in the northeast direction.

3.1 Introduction

Rifting of the Continental Lithosphere is a fundamental process which describes the thinning of the entire lithosphere and leads to the rupturing of the continents. It eventually controls the growth of continents and the birth of new ocean. Two comprehensive rifting mechanisms, magma-rich rifting (Buck, 1991, 2004, 2006; Corti et al., 2003; Grandin et al., 2010; Ebinger et al., 2013) and magma-poor rifting, are well exhibited in the East African Rift System (EARS) (Jacques, et al., 2011, Demissie et al., 2018; Fig. 1A). The Afar Depression (AD) is the northern tip of the EARS and considered as a divergent plate boundary where the African plate is in the process of splitting into two tectonic plates called the Somali and Nubian plates. These two plates are moving away from each other and also away from the Arabian plate to the north. However, the three plates diffusely meet in the AD of Ethiopia and form what is referred to as a rift-rift-rift (RRR) triple junction (Fig. 1B). The present day horizontal plate scale spreading velocities across the three plate boundaries in Afar have been widely accepted as ~6 mm yr^{-1} between the Nubia and Somalia plates, ~18 mm yr^{-1} along the NE direction for the Nubia and Aribia plates and ~16 mm yr^{-1} for the Somalia and Arabia plates (Jestin et al., 1994; Vigny et al., 2006; ArRajehi et al., 2009; McClusky et al., 2010; Deprez et al., 2013, 2015, Saria et al., 2014).

With the exception of the most recent studies by Doubre and Peltzer (2007), Pagali et al. (2014) and Doubre et al. (2016), which performed dense measurements of the present-day deformation in Central Afar, most studies have focused on either the regional scale strain transfers between the overlapping RSR and the GAR (e.g., Fig. 1C; Tapponnier et al., 1990; Manighetti et al. 1997, 1998, 2001); or investigated the extension

accommodated by far-field tectonic stresses created by the slab-pull of Arabia under Eurasia (Lahitte et al., 2003; Garfunkel and Beyth, 2006).

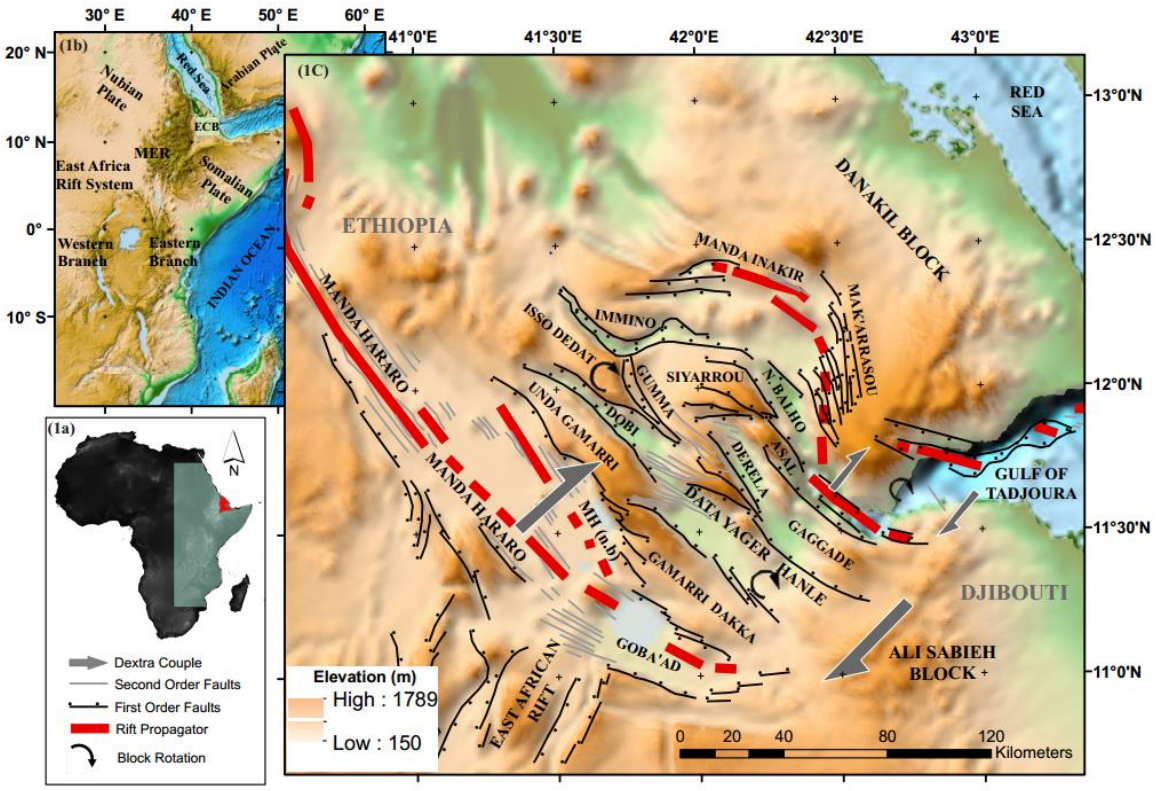

Figure 1: (A) Digital Elevation Model (DEM) of Africa. The mint color area represents the region affected by the East Africa Rift System (EARS) and the small red polygon in the Horn of Africa represents the Afar Depression (AD); (B) The EARS. The northern tip is the Ad which comprises the East Central Block (ECB) in the center. The eastern and the western branch of the EARS exist south of MER; (C) The tectonic framework of the Afar depression (AD) shown in Shuttle Radar Topographic Mission (SRTM) referred as Digital Elevation Model (DEM). Solid red lines indicate major rift propagators (Dobure et al., 2016) mainly the Red Sea Rifts (RSR) and Gulf of Aden Rifts (GAR). The element of rifts and blocks structures in the AD is represented by black lines and second-order faults with gray lines, respectively (Manighetti et al., 2001a). Clockwise rotation of the NW-trending blocks (Kidane et al., 2003) displayed with black curve arrow lines, and both NE and SW-directed dextral strike-slip shear couples are indicated with broad, gray, arrow lines.

Additionally, the recent investigations into the kinematics of Central Afar also relied mainly on dense GPS data from selected sites and 1-dimensional line of sight (LOS) measurements (Doubre and Peltzer,2007; Doubre et al., 2016). However, measurements along LOS present basically displacement along one direction. Even though, Doubre et al. (2016) used a dense network of GPS data inversion, they failed to investigate time series deformations. Moreover, Doubre et al. (2016) argue that the InSAR velocity field, mainly consistent with vertical displacements, does not allow the identification of clear, shallow creeping structures. On the other hand, Pagali et al. (2014) conducted the first continuous 3-D velocity field of the AD and the surrounding plateau by averaging 10 geocoded neighboring pixels to ~900 m resolution in all interferograms to reduce both the noise and the number of data points. Yet, Pagali et al.'s (2014) approach missed the slow slip motion along the northwest-trending, narrow grabens in the ECB and failed to point out any shallow structures creeping at a rate exceeding a few mm/year in the region. Consequently, details of strain accommodation by a slow slip with respect to continuous time series events in the ECB remain unclear.

The primary purpose of this paper is to focus on the recent tectonic deformation with particular emphasis given to obtaining insights into: (1) the slow slip displacement role of the present day Dobi graben kinematics, and (2) time series subsidence and uplift trends in the Dobi graben and their role in the propagation trends of the faults in the graben. To achieve our goal, we used the ascending and descending Track 6 of the ASAR ENVISAT images acquired during the 2003 to 2010 period (Fig. 2).

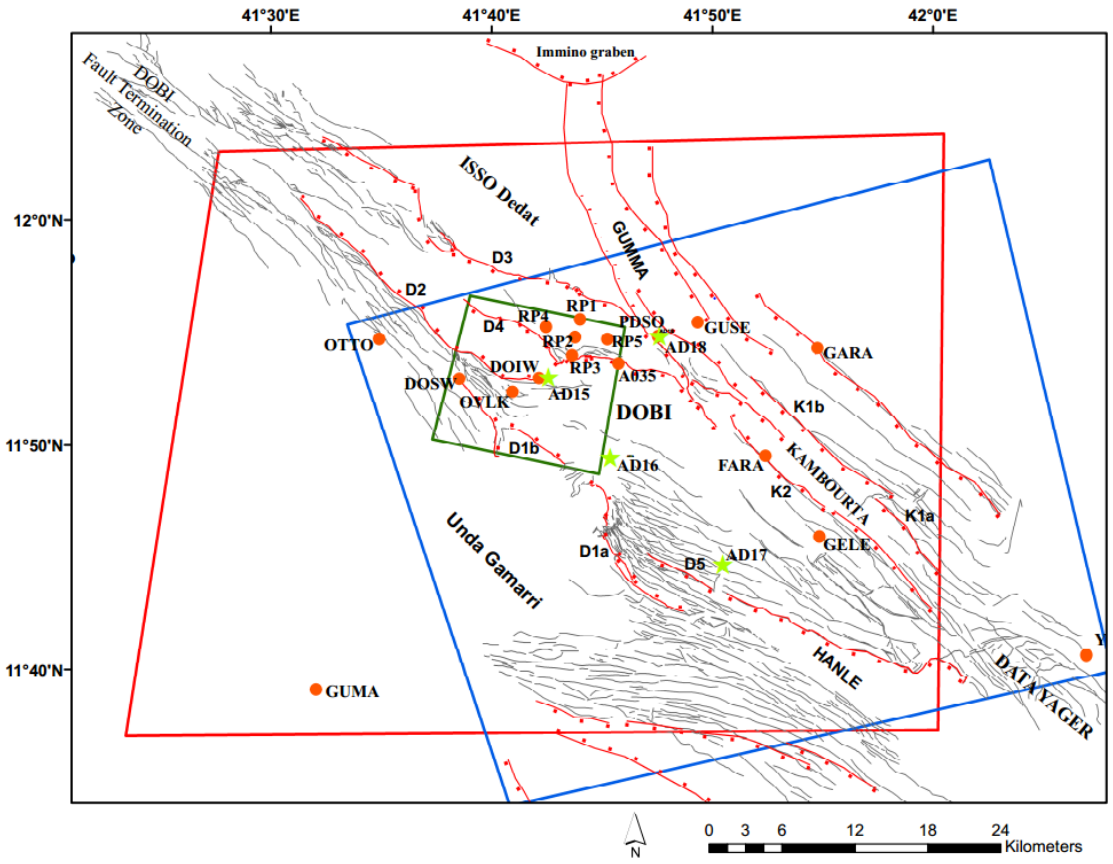

Figure 2. Normal faults interpreting for SRTM DEM. The red lines with suture marks represent the boarder faults. The grey lines represent intra basin normal faults. The orange circles are corresponding to GPS locations installed by Dobure et al. (2016) with in the Dobi graben and surrounding. The green stars reveled the broad band receiver function locations studied by Reed et al. (2014). The red rectangle represents the ASAR descending orbit track 6 used for SBA and the blue rectangle represent the ascending orbit ASAR used in the QPS technique. The small green rectangle represents the PS techniques which is present in the appendences.

We first identified the cumulative displacement and velocities of the surface along the LOS of the ENVISAT platform. This was followed by time series displacement analysis, aimed at resolving the slow slip displacements along with the uplift and subsidence movements caused by the normal faults. We employed two different InSAR

generation techniques independently, the Small Baseline Algorithm (SBA) and Quasi Permanent Scatterer (QPS). Results from SBA and QBS suggest the Dobi graben and surrounding area deformed mainly by fault creeping influenced by the two regional volcanic rifts. The creeping is associated mainly with normal faulting, which causes subsidence within the graben but uplifting in the rift shoulder. The abnormal continuous uplifting in the horst area might be associated with the presences of the temporary reactivation of normal faulting in the region.

3.1.1 Kinematics of the East Central Block (ECB)

Different models have been proposed to explain the kinematics of the RRR triple-junction with in the AD. For example, rigid plates (Mc Kenzie et al., 1970), microplates (Barberi and Varet, 1970; Acton et al., 1991; Eagles et al., 2002), progressive tearing (Courtillot, 1980), and crank arm tectonics (Souriot and Brun, 1992) are among the models which have been proposed to explain the deformation mechanism of the AD. Additionally, it has also been proposed that the slab-pull of Arabia under Eurasia has created a far-field stress that caused the Danakil block to rotate counter-clockwise (Collet et al., 2000; Eagles et al., 2002). It has also suggested that this counter-clockwise rotation of the Danakil block is the cause of rifting in the ECB (Lahitte et al., 2003; Garfunkel and Beyth, 2006).

Manighetti et al. (2001) argue that all of these models could be relevant in certain respects and are applicable to the AD at the proper scale. For instance, at the regional scale, the kinematics of this RRR junction have been defined by the Neogene-Pliocene

deformation and explained mainly by the overlapping propagating axes of the RSR and GAR. In this model, the RSR and GAR create an east-north-east trending dextral shear, generating a clockwise rotation of the northwest striking blocks separated by left lateral northwest striking faults—this is referred to as bookshelf faulting (Tapponnier et al., 1990; Manighetti et al., 1997, 1998, 2001).

However, with the exception of the 1969 Serdo strike-slip event earthquake (Kebede et al. 1989), most repeated episodes of earthquakes which released tensile stresses recorded in the past 40 years in the central AD, such as the November, 1978 Asal Rift earthquake (Abdallah et al., 1979; Jacques et al., 1996) and the August, 1989 Dobi earthquake (Braunmiller and Nabelek, 1990; Dziewonski et al., 1990; Sigmundsson, 1992; Jacques, 1996; Jacques et al., 1999, 2011) indicates crustal extension is accommodated mostly by normal faulting.

Although the classical diffused crustal extension by normal faulting and block tilting is emphasized more for the region, there are few reports which explain the existence of the left lateral strike faults, particularly in the northwest-trending Dobi graben. For example, Mohr (1971) states that there is a sinstral shearing presence in the Dobi graben based on the interpretation of satellite images. Abbate et al. (1995) also reports the existence of strike-slip faults with a NNE to ENE (rift transversal) strike from a slickensides analysis performed at several points in the Dobi graben and at the graben rift shoulders. Hofstetter and Beyth, (2003) also illustrated a strike slip seismic pitch with the fault planes striking WNW–ESE to NW–SE at the Dobi ramp zone around 42◦E and 12◦N, just ~ 3 Km northwest of the strike slip component reported by Abbate et al. (1995). This is also in accord with the strike slip strain rate tensor value reported in the

present day kinematic synthesis of the Central Afar by Dobure et al. (2016) derived from geodetic data.

3.1.2 Present day crustal deformation in the Central Afar

Plate spreading in the Central Afar is either through episodic intrusion diking events, such as in Dabbahu and Asal-Ghoubbet, or diffuse crustal extension and normal faulting in areas not yet manifesting any surface volcanic activity, as in the Dobi, Hanle, Immuno, Derale, and Gumma – Kambourta grabens (Fig. 1C). This is also consistent with the seismicity of the area showing normal faulting mechanisms (Keir et al., 2013; Sigmundsson, 1992) as well as a thick crust and lower Vp/Vs ratio, which suggest a lower degrees of melt as compare to the area affected directly by the Afar rift segments (Hammond et al., 2011, Reed et al., 2014). Similarly, Bridges et al. (2012) used detailed ground-based magnetic data across the Tendaho graben, which represents the southern segment of the Red Sea rift within the AD (Fig. 1C), to demonstrate that the Tendaho graben had an extension rate of ~0.64 cm/year from 2.0 Ma to 0.78 Ma and an extension rate of ~1.96 cm/year from 0.78 Ma to present. Bridges et al. (2012) explains that this as an indication that the extension across the Tendaho graben is slowing down and proposes that the boundary between the Arabian and Nubian plates within the AD may be developing within the ECB, possibly within the Dobi graben in the central part of the block (Fig. 1C and Fig. 2).

Additionally, the tectonic, seismic, and geodetic measurements explaining the crustal extension in the AD are concentrated mainly along the rift segments and accommodated mainly by transient magmatic intrusions within the crust, which allow

the plate-splitting mechanisms or processes in the region (Doubre et al., 2016). The current deformation in Afar has been studied extensively using dense measurements of geodetic data, such as GPS and InSAR analysis, focusing on the rift segments of MH-D and AG (Fig. 1C) since they were affected by active rifting sequences in 2005–2010 and 1978, respectively (e.g., Abdallah et al., 1979; Ruegg and Kasser, 1987; Wright et al., 2006; Vigny et al., 2007; ArRajehi et al., 2009; Grandin et al., 2009, Doubre and Peltzer, 2007; McClusky et al., 2010; Kogan et al., 2012; Pagali et al., 2014; Dobure et al., 2016).

Furthermore, in addition to the strain transfer from the two volcanic rifts to the region, the presence of partial melts beneath the northwest-trending narrow graben also plays a major role in strain accommodations and distributions. For example, Dugda et al. (2005) and Hammond et al. (2011) determine the crustal V_p/V_s ratios to be between 1.92 and 2.1 near the southwestern margin of the ECB, which is also suggestive of the presence of melt within the lower crust. Additionally, Reed et al. (2014) predict high Vp/Vs ratios of up to 1.92 within the lower crust beneath the Dobi graben, which implies the presence of melt and presumably indicates that strain accommodations in the lower crust are quite different from those in the upper crust.

3.2 Data and Methods

To estimate the LOS deformation, we employed two different techniques, the SBA (Berardino et al., 2002) and the QPS (Mullissa et al., 2018).

3.2.1 Small Baseline Algorithm (SBA)

The SBA technique was developed for generating time series deformations for non-urban areas (Berardino et al., 2002). Therefore, it is ideal to implement in an arid, non-vegetated area, such as the Dobi graben and the surrounding area. We proceeded with an image co-registration with a reference to DEM (1-arcsecond SRTM) to reduce the topographic contribution. We focused the raw level-0 SAR data into single complex images (SLC) by considering similar Doppler centroids and data obtained from DORIS (See ENVI SarScape®). The algorithm automatically selected an appropriate master image using both temporal and spatial baselines criteria set by the system (Figs. 3). Additionally, any differences in Doppler centroids are used to maximize the correlation between the images (Hooper et al., 2007). We utilized 720 days of small baseline temporal limits with reference to the image acquired on August 21, 2007, respectively, of the SAR image of descending Track 6. Our small temporal baseline caused the separation of the SLC into different subsets, which suppressed the effects of noise generated from incoherent pixels (Figs. 3). Next, by measuring the distance difference between a point on the Earth and the sensor position of the two different acquisition times, the phase difference (ϕ) was generated between master and slaves complex, co-registered SAR images. We produced 10 interferograms for the data sets from 2007 to 2009. In order to obtain the mean velocity field, cumulative displacement, and respective time series, deformation stacks were computed for the 10 interferograms. The stacking procedures

also helped us to mitigate the effect of the turbulent atmospheric noise (e.g., Peltzer et al., 2001).

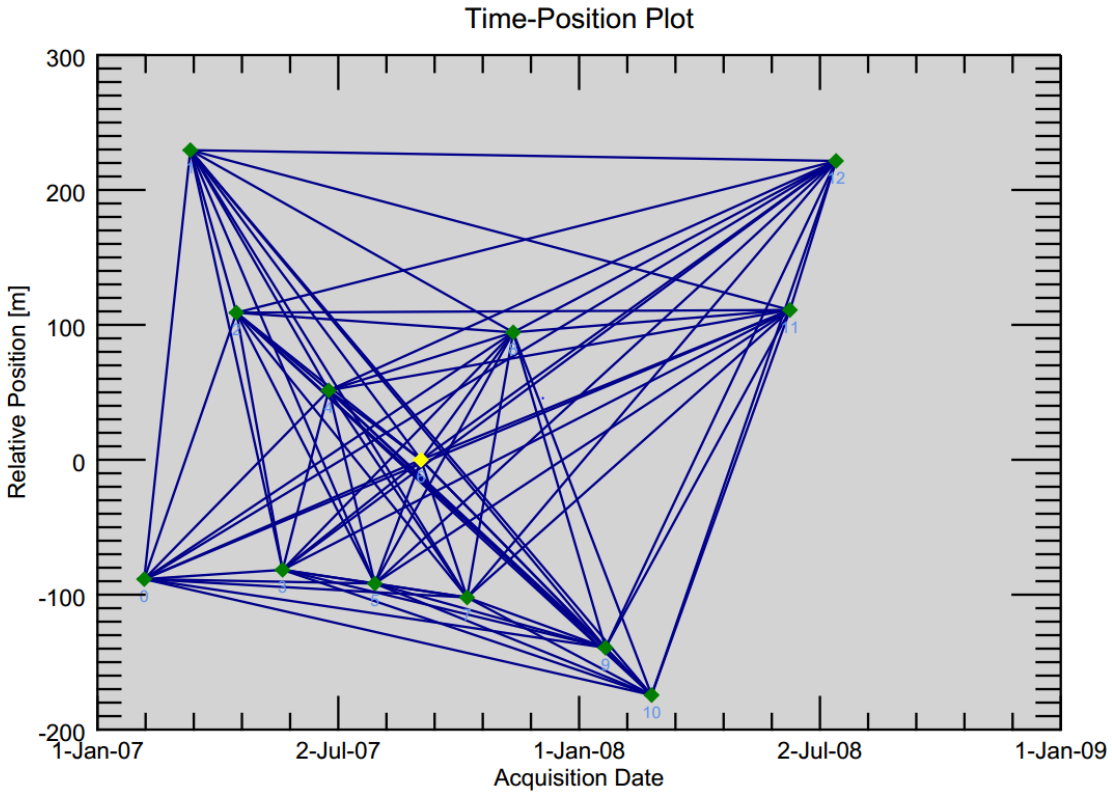

Figure 3. A) The time position plot chart showing a specific acquisition date with a normal perpendicular baseline used in SBA techniques to determine the coherencies of the imageries.

Additionally, interferograms flattening was performed using a 1-arcsecond SRTM input reference. We then spatially unwrapped the interferograms by adopting the unwrapped phase for a generic pixel of the interferogram, as in Hanssen (2001). We also unwrapped the interferograms utilizing the Goldstein adaptive algorithm, derived directly from the power spectrum of the fringes (Goldstein et al., 1988). This unwrapping phase was

followed by low- pass filtering, which we used to improve significantly fringe visibility and reduce the noise introduced by temporal or perpendicular baseline-related decorrelation. At this step, incoherent areas were filtered out and discarded while reducing the level of noise. Additionally, after the phase unwrapping step, the low-pass component of the deformation signal and topographic error were estimated for each coherent pixel (Berardino et al., 2002). This step helped us to estimate the residual topography and low-pass deformation. Later, for estimating the atmospheric propagation effects, a low-pass filtering was performed in the spatial domain (after removing the estimated low-pass deformation, see ENVI SarScape®), followed by a high-pass filtering in the time domain, since the atmospheric phase components exhibited a high spatial correlation, but a low temporal correlation. The atmospheric noise filtering that we applied in this research is similar to the QPS and PS approach used to screen the phase differences generated by the atmosphere (Ferretti et al., 2000; Ferretti et al., 2001).

3.2.2 Quasi-permanent scatterer (QPS)

To estimate the LOS deformation, we used 14 ENVISAT ASAR images in the ascending orbit and 13 ENVISAT ASAR images in the descending orbit over the period 2007-2010. We used the QPS multi-temporal InSAR processing method to estimate the linear deformation rate (Perissin and Wang, 2012; Mullissa et al., 2018). The only difference between QPS and permanent scatterer interferometry (PSI) is that images are not forced to create an interferogram with a common master image (Ferretti et al., 2001). In addition, the interferograms are filtered to improve the signal to noise ratio over

distributed scatterers. We used a Goldstein adaptive filter to derive the filtered interferograms (Goldstein and Werner, 1998). Finally, coherence was used as a weight to increase the influence of high coherence points in the deformation estimate. In this analysis, we used a full-image graph configuration to create 91 and 78 interferograms in the ascending and descending orbits, respectively. The phase contribution from the flat earth was estimated using the orbital information and reference ellipsoid parameters, and the phase contribution from the topographic variations was estimated from a 90m SRTM DEM. We estimated the atmospheric phase component by selecting pixels which exhibited high average coherence in all interferograms and connecting these coherent pixels in a spatial arc. We then integrated per arc to estimate the parameters in which the atmospheric variation between adjacent pixels was assumed to be very small. Once the APS (atmospheric phase screen) was estimated, we subtracted it from individual images and re-estimated the parameters of interest (i.e., linear velocity) again. As a quality parameter, we used temporal coherence to filter out noisy pixels. Temporal coherence is a metric introduced in Ferretti and Werner (1998) to show the correlation between the observed phases and the applied deformation model. For high temporal coherence, the deformation estimate is more reliable, whereas, in low temporal coherence pixels, we have a less reliable deformation estimate.

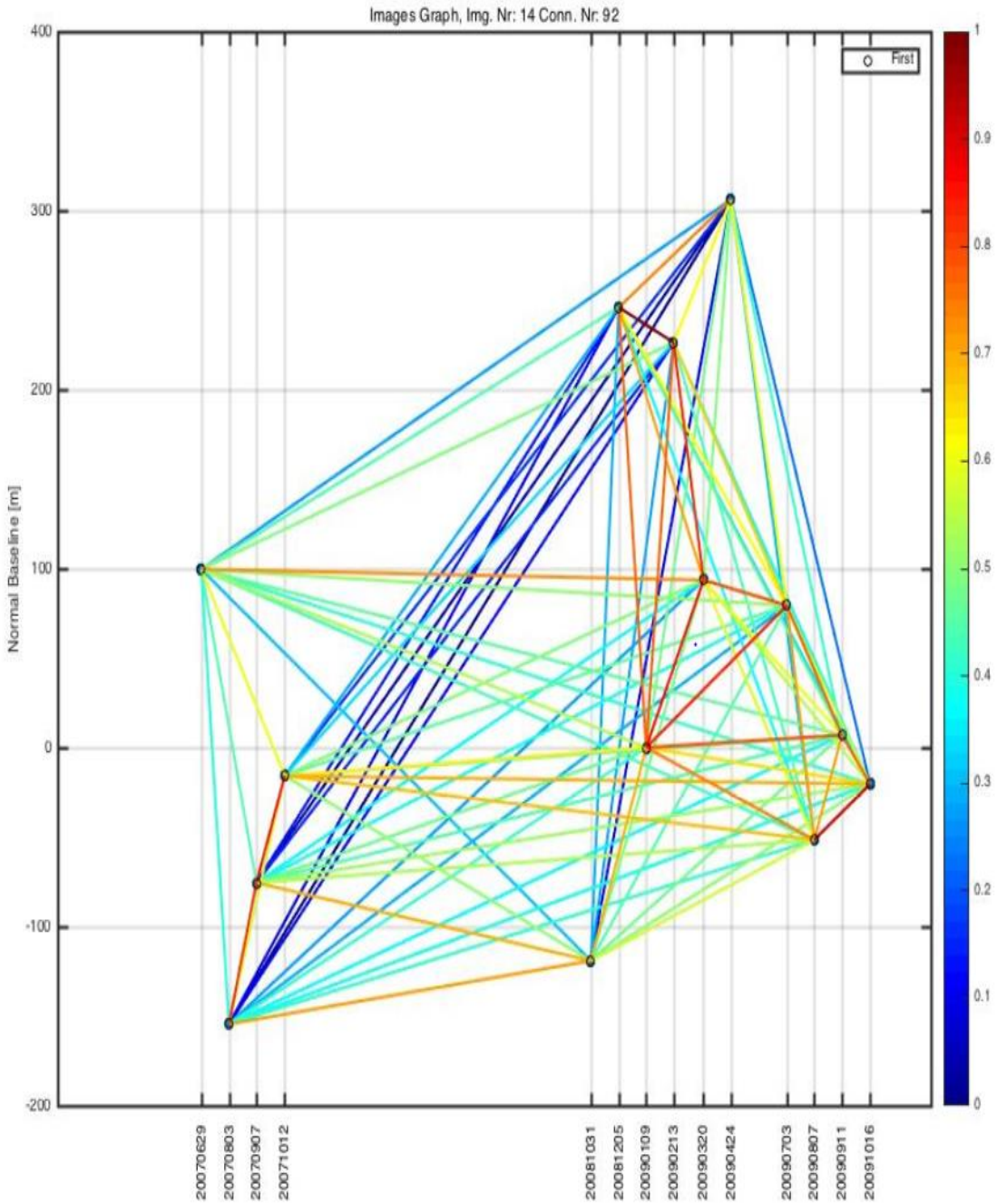

Figure 3. B) The time position plot chart showing a specific acquisition date with a normal perpendicular baseline used in QPS connection graph indicating Normal baseline with acquisition date.

3.3 Results

3.3.1 Interpretation of the results obtained using SBA techniques

Coherence information was generated during the Goldstein filtering process which we utilized to evaluate the phase noise. Our results indicate that of the August 21, 2007 to January 27, 2009 imageries, based on the small temporal baseline criteria of 525 days' worth of images, only images acquired on August 21, 2007, October 30, 2007, November 11, 2008, December 23, 2008, and the January 27, 2009 remained coherent with the master image. The phase coherent is represented by values ranging between 0 and 1 (Ferretti et al., 2007). A value of 0 indicates complete loss of coherence between the Master and Slave images, while a value of 1 indicates no phase noise or complete coherence between the Master and Slave images. Considering only the points which had a coherence value of 0.9 or more, a total of 1,414,227 LOS displacement points for the Dobi graben and the surrounding area were obtained using t the SBA technique (Berardino et al., 2002).

The results from the SBA revealed a significant loss of coherence in the LOS deformations which were observed in most of the Dobi graben and in the southeastern part of the Unda Gamarri horst. The former is perhaps due to the swing in unconsolidated sediments movements, whereas the latter is due presumably to changes in elevation attributed to frequent uplift or subsidence in the region. Additionally, the result exhibited a negative LOS in millimeters in the Gumma graben, Siyarrou horst, Isso Dedat horst, and Unda Gamarri horst (Fig. 4A). For example, the time series deformation analyses performed on both the previously installed GPSs locations (10 different spatial locations,

namely, near OTTA, DOSW, OVLK, DOIW, AO35, GARA, FARA, PDSO, GUSE and GELE selected by Doubre et al. (2016)) and on the locations of the broadband seismic stations (near four different spatial locations, such as the AD15, AD16, AD17, and AD18 installed by Reed et al. (2014)) are presented here in Figure 4B.

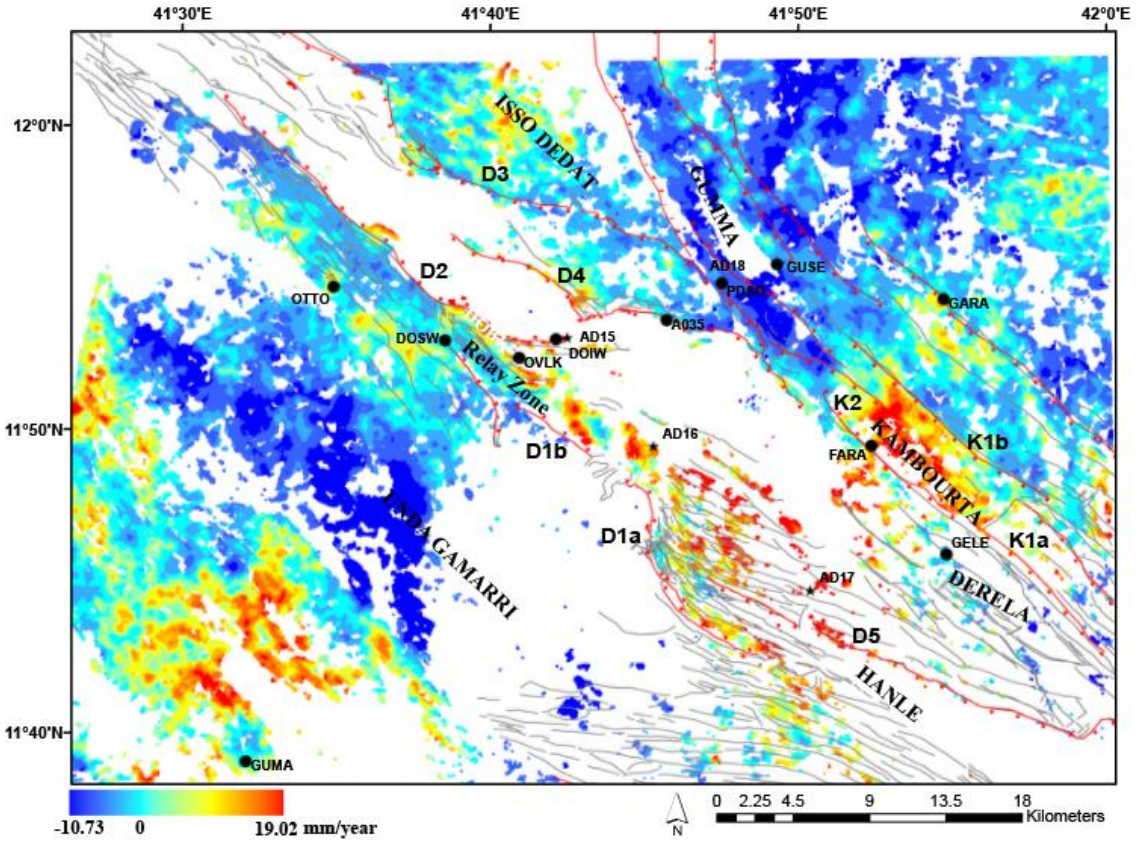

Figure 4A. Line of sight velocity map in mm/year (LOS) of the Dobi graben and surrounding area from August 2007 to September 2009 after unwrapping errors and artifacts cause by tropospheric lengthening are removed. Pixels with coherence value of 0.89 or less are masked out. The blue color ramp scale corresponding movements toward the LOS and the red color indicates movement away from the LOS.

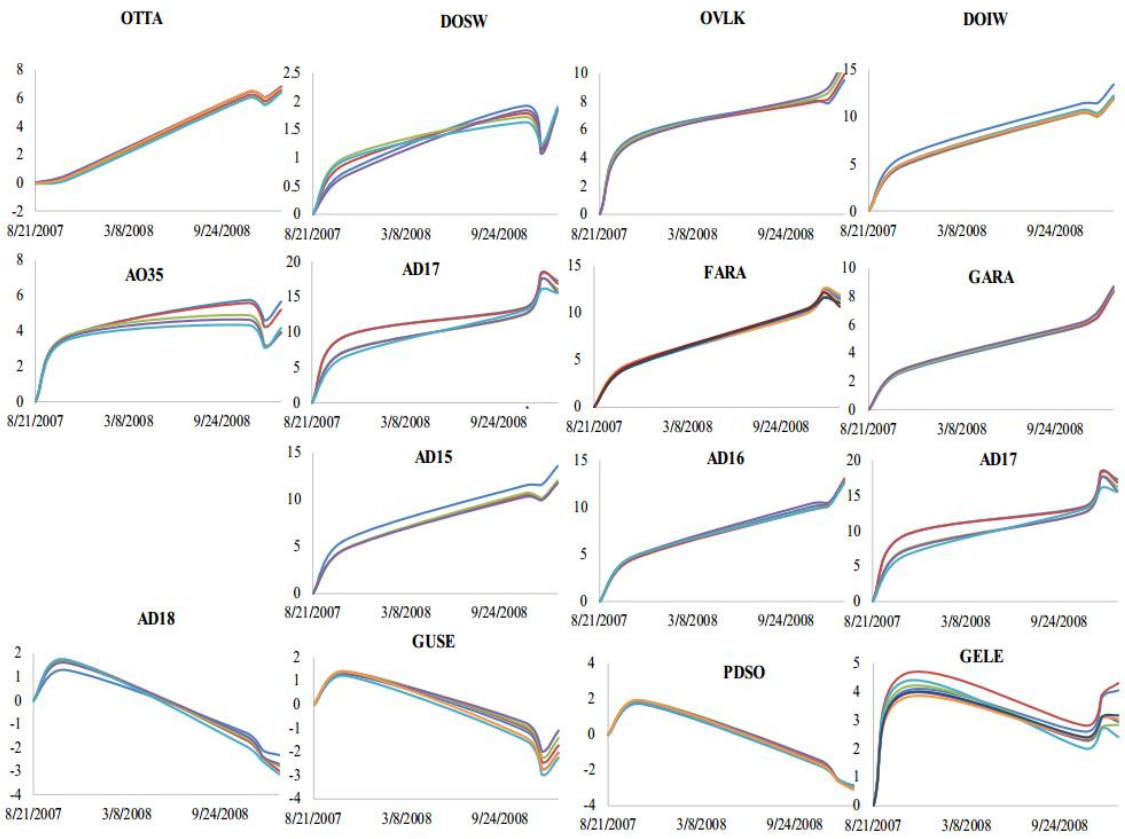

Figure 4B. Time series displacements for fifteen representative points in the Dobi graben and surrounding area from 2007 to 2009 period. The locations of representative samples are plotted in Figure 2 and 4A and their corresponding stations names are labeled at the top of each chart.

The time series analysis performed for representative samples near eight previously installed GPS locations, particularly at OTTA, DOSW, OVLK, DOIW, AO35, GARA, FARA, and GELE, showed a positive increment in LOS cumulative deformation and velocity in the LOS direction from August 21, 2007 to January 27, 2009. We noticed a similar scenario for the representative time series LOS deformation measurements near the AD15, AD16, and AD17 broadband seismic stations. This positive LOS can be

interpreted as the presence of continuous subsidence up to ~20 mm/year. The maximum LOS velocity is exhibited near AD17 in the Dobi imbrication fault zone. Additionally, the style of the LOS deformation profile curve produced from InSAR time series analysis exhibited an apparent tri-modal creep behavior when we plotted the LOS displacement (strain) against the image acquisition time. However, both LOS velocity and the time series deformation analysis for our representative samples near the PDSO and GUSE GPS locations and AD18 broadband seismic station showed a decrease in the LOS cumulative deformation and exhibited a negative LOS after November 18, 2018 (Fig. 4B). The negative LOS of up to -10.3 mm/year can be attributed to the presence of continuous uplifting in the Gumma graben. Additionally, near the southeastern corner of the Unda Gamarri horst (Fig. 4A), the InSAR signal exhibited a higher negative LOS, creating a large circular subset area. This negative LOS displacement is due perhaps to a high surface disturbance, which itself is due presumably to the turbulent tropospheric content in this region which is not compensated by the low number of interferograms used for the calculation of the mean velocity. Therefore, the region was filtered out of further time series analysis. Yet, Figure 4C, with a coherent pixel value of 0.6 or more, revealed an anomalously negative LOS displacement for this area. Furthermore, the style of the LOS deformation profile curve for these representative samples at the PDSO and GUSE GPS locations and AD18 broadband seismic station exhibited an inverse tri-modal creep behavior when we plotted the LOS displacement (strain) against the image acquisition time.

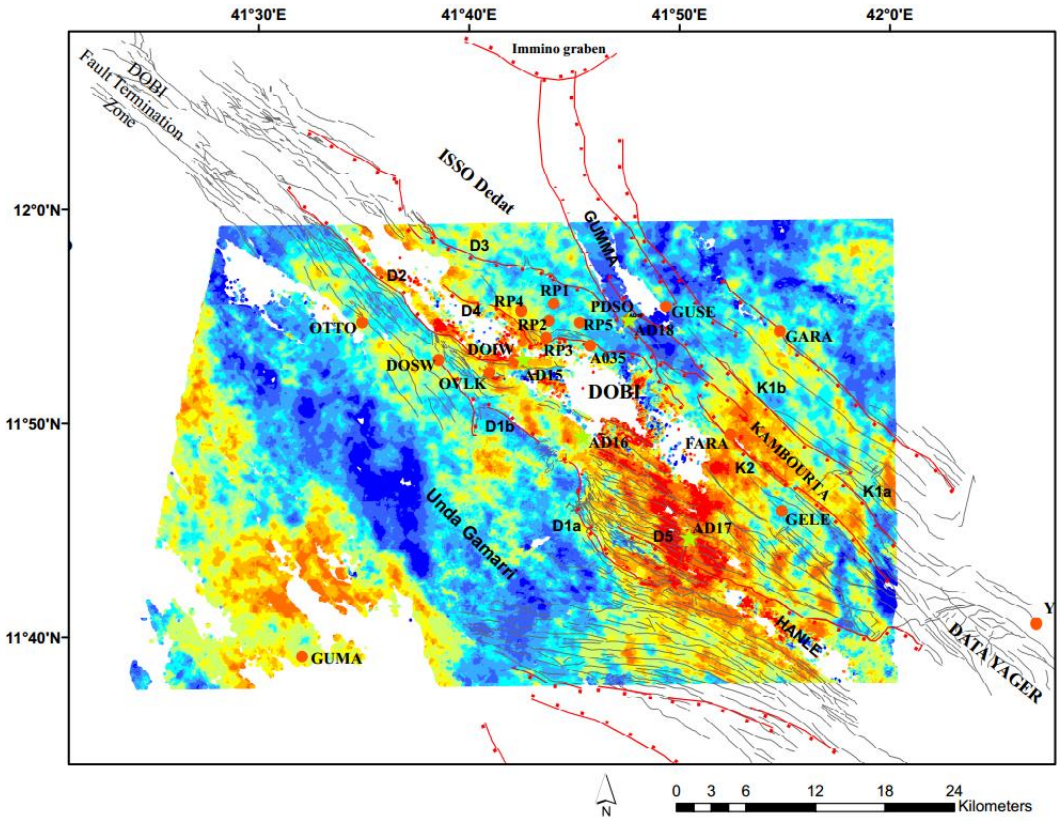

Figure 4C. Line of sight displacement map in mm (LOS) of the Dobi graben and surrounding area from August 2007 to January 2009 after unwrapping errors and artifacts cause by tropospheric lengthening are removed using SBA technique. Pixels with coherence value of 0.59 or less are masked out. The blue color ramp scale corresponding movements toward the LOS and the red color indicates movement away from the LOS.

3.3.2 Interpretation the result obtained using QPS techniques

We evaluated the QPS time series LOS displacements for fourteen ENVISAT images which were acquired at different times from June 29, 2007 to October 16, 2010. Each image had a total of 21,283 pixels which were used to produce an LOS velocity map, cumulative LOS displacement map, and time series maps. The pixels in each image

displayed a coherence value of 0.85 or more, and pixels with a coherence value of less than 0.85 were masked out to avoid the effect of sudden events in the displacement maps. Similar to those exhibited by the SBA technique, the results from QPS also exhibited a significant loss in coherence in most of the Dobi graben, Hanle graben, and southeastern part of the Kambourta graben. The red color or positive LOS in Figure 5A indicates motion towards the satellite and is mostly associated with the major boundary faults, Dobi Relay zone, southeast of the Imbrication zone, Kambourta graben, and northeast of the Hanle graben. Whereas, the blue color indicates motion away from the satellite and reveals a negative LOS velocity in the Gumma graben, Siyarrou horst, Isso Dedat horst, and Unda Gamarri horst (Fig. 5A). Additionally, in the southeastern part of the Dobi graben, particularly at the imbrication zone and the region which is found southeast of the imbrication zone, a negative LOS velocity is observed running parallel to the positive LOS velocity in the north-northeast (NNE) trending direction. These distinct, abrupt LOS changes from positive value to negative run shoulder to shoulder and orthogonal to the northwest-striking directions of the faults.

The time series deformation analysis performed showed a negative linear LOS deformation for 105 consecutive days from June 29, 2007 to October 12, 2007 (Fig. 5B). However, we noticed that the representative time series in these selected regions revealed a positive LOS deformation for 385 days from October 12, 2007 to October 10, 2008. Additionally, the deformation rate revealed a positive sinusoidal nonlinear growth trend after October 10, 2008 which lasted until October 16, 2009. To the contrary, the LOS displacement pixels near AD18, AO35, PDSO, GUSE, GARA, and GELE encompassed a continuous linear decay, similar to an inverse creep profile curve, from June 29, 2007

up to October 31, 2008 (Fig. 5B). However, from October 31, 2008 to October 16, 2009, the deformation rate revealed a negative sinusoidal nonlinear trend.

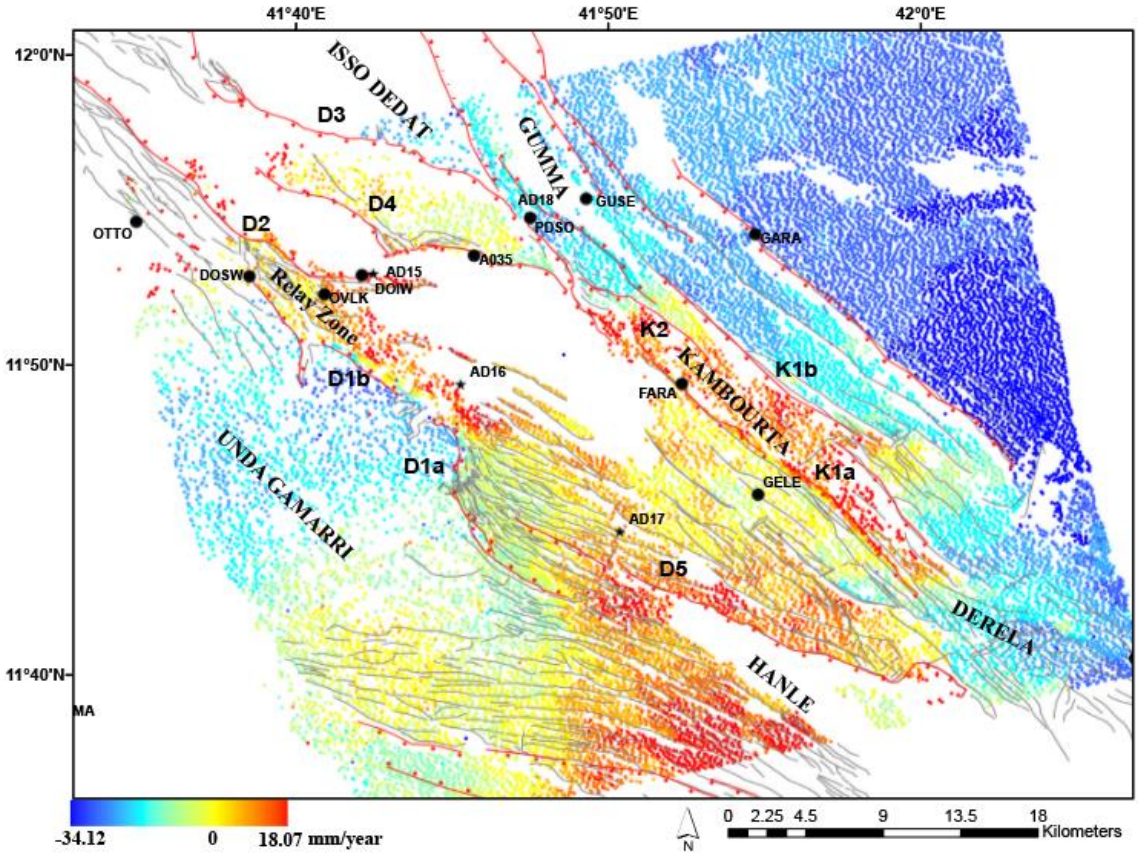

Figure 5A. Line of sight velocity map in mm/year (LOS) of the Dobi graben and surrounding area from June 2007 to October 2009 after unwrapping errors and artifacts cause by tropospheric lengthening are removed using QPS technique. Pixels with coherence value of 0.745 or less are masked out. The blue color ramp scale corresponding movements toward the LOS and the red color indicates movement away from the LOS.

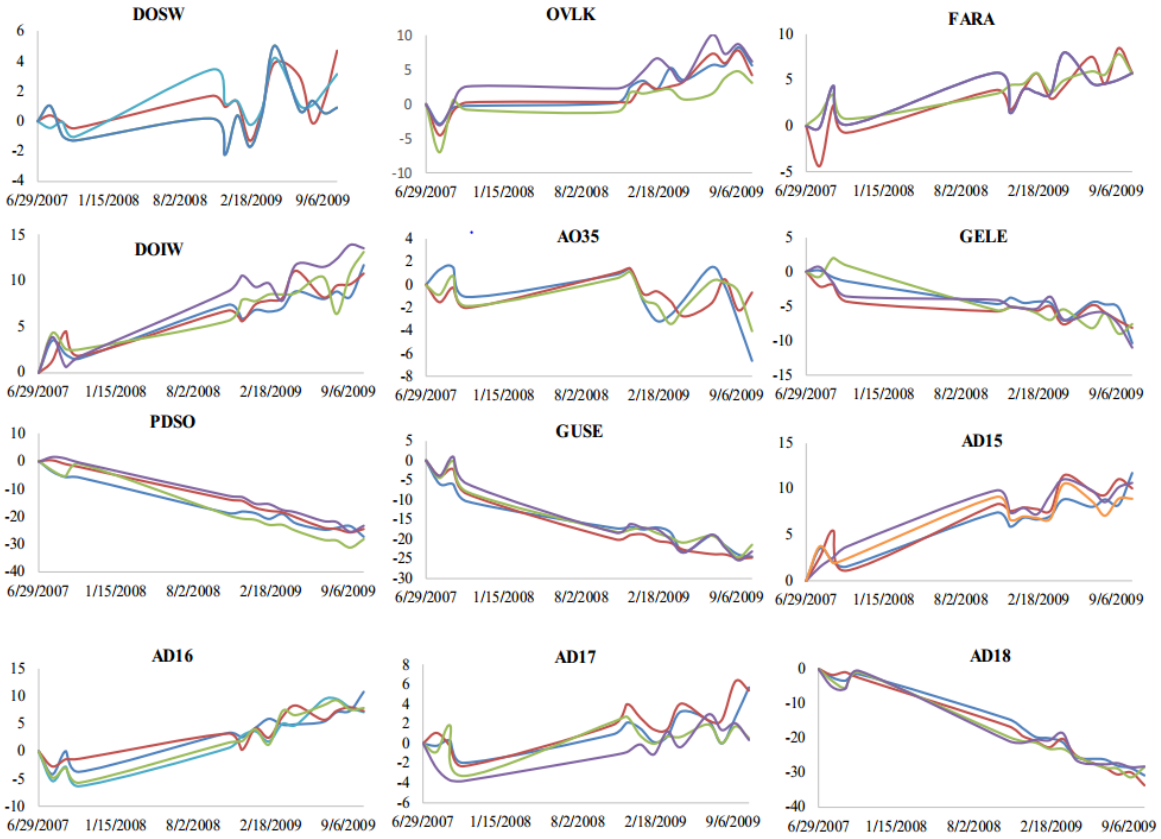

Figure 5B. Time series displacements for fifteen representative points in the Dobi graben and surrounding area from 2007 to 2009 period. The locations of representative samples are plotted in Figure 2 and 5A and their corresponding stations names are labeled at the top of each chart.

3.4 Discussion

Our SBA and QPS algorithm performed independently with respect to the geometry of the ASAR acquisitions (descending and ascending; Fig. 2) and, either in maps or profiles of the ground deformation, indicated the surface subsidence and uplifting in the Dobi graben and the surrounding area. This is consistent with the earliest displacement measurements from radar imageries in the AD conducted by Amelung et al.

(2000) and Doubre and Peltzer (2007). For example, the positive LOS velocity and positive time series displacement trends, confined as patches of signal mainly in the relay zone, imbrication zone, and Kambourta graben, embrace the localization of surface deformation in the regions which are essentially found to be associated with normal faults (Figs. 4A, 4C, 5A; Appendices 2 and 3). For example, we noticed that the rate of displacement reaches only up to few mm/year even though the current extension of the narrow grabens is accommodated mostly by normal faulting. Yet, due to the lack of sharp gradients in the InSAR data and the regular, low horizontal velocity gradient from the southwest to the northeast, Dobure et al. (2016) point out that no shallow structure is creeping at a rate exceeding a few mm/year. Dobure et al. (2016) further argue that the InSAR velocity field, mainly consistent with vertical displacements, does not allow the identification of clear shallow creeping structures. However, creeping could be presumably can be considered to be the prominent deformation mechanism, as most of our representative time series results revealed in Figure 4B and Figure 5B exhibited a conventional creep profile geometry (Dobure and Peltzer, 2007). For example, a detailed investigation of the LOS deformation profile curves produced by InSAR time series analysis revealed an apparent tri-modal creeping behavior when we plotted the LOS displacement (strain) against the image acquisition time. The creeping is presumably highly influenced by the two regional volcanic rifts, RSR and GAR, which build up differential stress in the Dobi and its surrounding area (Courtillot et al., 1980, 1982; Tapponnier et al., 1990; Sigmundsson, 1992; Souriot and Brun, 1992; Hayward and Ebinger, 1996; Manighetti et al., 1998; Gupta and Scholz, 2000; Manighetti et al., 2001).

Additionally, when we emphasized, in detail, the positive LOS displacement observed in the imbrication zone (southeast of the Dobi graben), in the Dobi relay zone, and near the fault designated as D1b (Figs. 2, 4A, 5B), the LOS signals are shown to accentuate the generally positive LOS trending pattern, which is oblique to the strikes of the faults. Moreover, these north-northeast trending, positive LOS signals also exhibited a relatively distinct LOS high and low stripping pattern (Figs. 4C, 5A, and Appendices 2 and 3). The relatively maximum positive LOS is found to be mostly associated with the imbrication zone, which is characterized by numerous closely-spaced, but relatively small, offset faults. These small faults are distributed across the imbrication zone with fault profile geometries showing maximum displacement at the points where their lateral propagation is arrested. The maximum displacements of these faults, which are marked by the LOS and found to be oblique to the faults, are consistent with the explanation provided for these narrow, non-volcanic grabens, such as the Dobi, Hanle and Guma grabens, which is presumably transfer strain from the southernmost RSR to the westernmost Gulf of Aden (Manighetti et al., 1997; Souriot and Brun, 1992; Tapponnier et al., 1990; Tesfaye, 2005; Tesfaye et al., 2008). Additionally, the general, northeast-trending maximum displacement signal traced from our LOS time series analysis is also consistent with a number of deformational mechanisms which have been proposed to describe the evolution of the Dobi graben and other northwest-trending grabens in the ECB (Courtillot et al., 1980, 1982; Tapponnier et al., 1990; Sigmundsson, 1992; Souriot and Brun, 1992; Hayward and Ebinger, 1996; Manighetti et al., 1998; Gupta and Scholz, 2000; Manighetti et al., 2001). All of these models consider that a northeast to southeast diffused crustal extension is presumably responsible for the present day deformation of

the northwest-trending Dobi graben. They also assume crustal thinning and extension are associated with normal faulting which reactivated through repeated episodes of tensile stress releases and responsible for the ongoing deformation.

Conversely, with a mean negative LOS rate of ~2 mm/year indicating that the uplift process is accommodated in the northwest localities of the Unda Gamarri horst and in the Gumma graben, particularly at the selected representative pixels, such as PSDO, GUSE, and AD18, we observed the presence of an inverse steady state creep profile. One possible explanation for this abnormal uplift in the extension regime might be a temporary reactivation of the graben's normal faults. For example, Abbate et al. (1995) report the existence of such a fault inversion in the ECB. This could be associated with local compressional stress within the region due to RSR and GAR propagating one to the other. Such compressional stress is presumably favored by the positioning of the northwest-trending narrow grabens, which are nearly parallel to the two volcanic rift segments which might force the grabens to act as a transient enclosure region during the clockwise rotation of the ECB. It is also noteworthy that the relatively negative LOS displacement in mm/year observed within the northwest Unda Gamarri region abruptly changes to a relatively positive LOS in mm/year near the southeast of the Dobi imbrication bordering the Hanle graben (Fig. 4C). This region is dominated by the Gamarri tear zone (Manighetti et al., 2001), where individual blocks are rotating clockwise around vertical axes (Courtillot et al., 1984; Manighetti et al., 2001; Tapponnier et al., 1990). These abrupt signal polarizations from a negative to positive LOS coincide with an area proposed to have an overall clockwise rotation of the ECB, as first suggested by Tapponnier et al.'s (1990) conceptual model and subsequently

confirmed by paleomagnetic data (Acton and Stein, 1991; Manighetti et al., 2001; Kidane et al., 2003). These scenarios cause the damaged zone to become unstable and unable to accommodate higher stress. Hence, this zone is subjected to distributing the stress by interaction with the nearby oblique or parallel faults. Thus, the stress can be either localized as a displacement or transfer the displacement, which might cause faults to grow in length (Fig. 4C, 5A and Appendix). Therefore, our time series analyses (Figs. 4A, 5A, and Appendices 2 and 3) are consistent and in agreement when showing a general northeast triple junction migration of the AD, as proposed by Keir et al. (2013) and Dobure et al. (2016).

3.5 Conclusions

Results from our InSAR analyses suggest that the extension process which is influenced by the two regional volcanic rifts dominates in the region. Creeping associated mostly with normal faulting causes subsidence in the graben but uplifting in the rift shoulder. The abnormal continuous uplifting in the horst area might be associated with the presence of temporary reactivation of normal faulting in the region. Our study yields a plausible, if not unique, scenario for the oblique, positive LOS signals observed in different parts of the Dobi graben which are associated with faults, indicating that strain is localized as a fault displacement (subsidence). Additionally, a continuous, traced pattern of the positive LOS oblique to the normal faults, which are observed striking uninterruptedly in the northeast direction, might be an indication of the transfer of strain as a distribution of deformation from the southernmost RSR to the westernmost Gulf of

Aden, which is also supported by the northeast migration of the triple junction's argument. Therefore, our results from our analyses using high-resolution ASAR data along the active rift of the Dobi graben and the surrounding area provide a unique opportunity to understand the role of the weak slip strain on the present-day Dobi graben and the surrounding area deformation.

3.6 Acknowledgments

We thank Prof. Tim Wright and anonymous review for providing their insights about the radar signal processing and how to improve noise associated with the images. We are grateful to our colleagues from Oklahoma State University and Addis Ababa University who provided insight and expertise that greatly assisted the research and for comments that greatly improved the manuscript. This is Oklahoma State University Boone Pickens School of Geology contribution # 2018-xx.

3.7 References

Abbate, E., Passerini, P., and Zan, L., 1995. Strike-slip faults in a rift area: a transect in the Afar Triangle, East Africa: Tectonophysics 241, p. 67-97.

Abdallah, A., V. Courtillot, M. Kasser, A. Y. Le Dain, J. C. Lépine, B. Robineau, J. C Ruegg, P. Tapponnier, and A. Tarantola (1979). Afar seismicity and volcanism: Relevance to the mechanics of accreting plate boundaries, Nature 282, 17–23.

Acton, G.D., Stein, S. and Engeln, J., 1991. Block rotation and continental extension in Afar: a comparison to oceanic microplate systems. Tectonics 10, 501–526.

Amelung, F., Oppenheimer, C., Segall, P., and Zebker, H., 2000, Ground Deformation near Gada'Ale Volcano, Afar, observed by Radar Interferometry: Geophysical Research Letters, v. 27, p. 3093-3096.

ArRajehi, A. et al., 2009. Geodetic constraints on present-day motion of the Arabian Plate: implications for Red Sea and Gulf of Aden rifting, Tectonics, 29, doi:10.1029/2009TC002482.

Barberi, F. & Varet, J., 1970. The Erta Ale volcanic range (Danakil depression, northern Afar, Ethiopia), Bull. Volc., 36, 848–917.

Baud, P. and P. G. Meredith, 1997. Damage accumulation during triaxial creep of Darley Dale sandstone from pore volumometry and acoustic emission, Int. J. Rock Mech. Min. Sci., 34:3-4, Paper No. 024.

Berardino, P., Fornaro, G., Lanari, R., Sansosti, E., 2002. A new algorithm for surface deformation monitoring based on small baseline differential SAR interferograms. IEEE Trans. Geosci. Remote Sens. 40 (11), 2375–2383.

Braunmiller, J., and J. Nabelek., 1990. The 1989 Ethiopia earthquake sequence, Eos Trans. AGU 71, 1480.

Bridges, D. L., Mickus, K., Gao, S. S., Abdelsalam, M. G., Alemu, A., 2012. Magnetic stripes of a transitional continental rift in Afar. Geology 40, 203–206, http://doi.org/10.1130/G32697.1.

Buck, W. R. (1991), Modes of continental lithospheric extension, J. Geophys. Res., 96(B12), 20,161–20,178, doi:10.1029/91JB01485.

Buck, W. R. (2004), Consequences of asthenospheric variability on continental rifting, in Rheology and Deformation of the Lithosphere at Continental Margins, vol. 62, pp. 1–30, Columbia Univ. Press.

Buck, W. R. (2006), The role of magma in the development of the Afro-Arabian Rift System, Geol. Soc. London Spec. Publ., 259(1), 43–54.

Chu, D. & Gordon, R., 1999. Evidence for motion between Nubia and Somalia along the Southwest India ridge, Nature, 398, 64–67.

Collet, B., Taud, H., Parrot, J.F., Bonavia, F., and Chorowicz, J., 2000, A new kinematic approach for the Danakil block using a Digital Elevation Model representation: Techtonophysics, v. 316, p. 343-357.

Corti, G., M. Bonini, S. Conticelli, F. Innocenti, P. Manetti, and D. Sokoutis (2003), Analogue modelling of continental extension: A review focused on the relations between the patterns of deformation and the presence of magma, Earth Sci. Rev., 63(3-4), 169–247, doi:10.1016/ S0012-8252(03)00035-7

Courtillot E. V., 1980. Opening of the Gulf of Aden and Afar by progressive tearing. Physics of the Earth and Planetary Interiors. Volume 21, Issue 4, March 1980, Pages 343-350.

Deprez, A., Doubre, C., Masson, F. & Ulrich, P., 2013. Seismic and aseismic deformation along the East African Rift System from a reanalysis of the GPS velocity field of Africa, Geophys. J. Int., 193, 1353–1369.

Deprez, A., Doubre, C., Masson, F. & Ulrich, P., 2015. Erratum: Seismic and aseismic deformation along the East African Rift System from a reanalysis of the GPS velocity field of Africa, Geophys. J. Int., 200, 556.

Doubre, C., Deprez, A., Masson, F., Socquet, A., Lewi, E., Grandin, R., Nercessian, A., Ulrich, P., Chabalier, D. J., Saad. I., Abayazid, A., Peltzer, G., Delorme, A., Calais, E., Wright, T., 2016. Current deformation in Central Afar and triple junction kinematics deduced from GPS and InSAR measurements. Geophysical Journal International 208, 936-953.

Doubre, C. & Peltzer, G., 2007. Fluid-controlled faulting process in the Asal Rift, Djibouti, from 8 yr of radar interferometry observations, Geology, 35, 69–72.

Dziewonski, A. M., G. Ekstrom, J. H. Woodhouse, and G. Zwart, 1990. Centroid moment tensor solutions for July-September 1989, phys. Earth planet. In 62, 529-532.

Dugda, M., Nyblade, A., Julia, J., Langston, C., Ammon, C. ,Simiyu, S., 2005. Crustal structure in Ethiopia and Kenya from receiver function analysis. Journal of Geophysical Research 110, doi.org/10.1029/2004JB003065

Eagles, G., Gloaguen, R. & Ebinger, C., 2002. Kinematics of the Danakil microplate, Earth planet. Sci. Lett., 203, 607–620.

Ebinger, C. J., J. van Wijk, and D. Keir (2013), The time scales of continental rifting: Implications for global processes, Geol. Soc. Am. Spec. Publ., 500, 371–396

Ferretti, A., Prati, C., and Rocca, F., 2001. Permanent scatterers in SAR interferometry, IEEE Trans. Geosci. Remote, 39(1), 8–20.

Ferretti, A., Monti-Guarnieri A., Prati, C., Rocca, F., Massonnet ,D., 2007.InSAR Principles: Guidelines for SAR Interferometry Processing and Interpretation. ESA Publications, TM-19. ISBN 92-9092-233-8.

Garfunkel, Z. & Beyth, M. (2006). Constraints on the structural development of Afar imposed by the kinematics of the major surrounding plates, in The Afar Volcanic Province within the East African Rift System, eds Yirgu, G., Ebinger, C.J.& Maguire, P.K.H., Geological Society of London, Special Pub. 259, pp. 23-42.

Goldstein, R.M., Zebker, H.A., Werner, C.L., 1988. Satellite radar interferometry: two dimensional phase unwrapping. Radio Sci. 23 (4), 713–720.

Goldstein, R.M., Werner, C.L. , 1998. Radar interferogram filtering for geophysical applications. Geo- phys. Res. Lett., vol. 25, no. 21, pp. 4035–4038.

Grandin, R., A. Socquet, E. Jacques, N. Mazzoni, J.-B. de Chabalier, and G. C. P. King (2010), Sequence of rifting in Afar, Manda-Hararo rift, Ethiopia, 2005–2009: Time-space evolution and interactions between dikes from interferometric synthetic aperture radar and static stress change modeling, J. Geophys. Res., 115, B10413, doi:10.1029/2009JB000815.

Gupta A. and Scholz H. C., 2000. Brittle strain regime transition in the Afar depression: Implications for fault growth and seafloor spreading. Geology 28, 1087-1090.

Hammond, J. O. S., Kendall, J. M., Stuart, G. W., Keir, D., Ebinger, C., Ayele, A. & Belachew, M., 2011. The nature of the crust beneath the Afar triple junction: evidence from receiver functions. Geochemistry, Geophysics, Geosystems 12, 1525–2027.

Hanssen, R., 2001. Radar interferometry Ed. Kluwer Academic Publishers, Dordrecht (The Netherlands) (2001)

Hayward, N. J., Ebinger, C. J., 1996. Variations in the along-axis segmentation of the Afar Rift system. Tectonics 15, 244-257, doi: 10.1029/95TC02292.

Hoffstetter, R., and Beyth, M., 2003, The Afar Depression: interpretation of the 1960-2000 earthquakes: Geophysical Journal International, v. 155, p. 715-732.

Jacques, E., (1995). Fonctionnement sismique et couplage élastique des failles en Afar, Master's Thesis, Université Paris, 7-IPGP, December 1995, 485 pp. (in French).

Jacques, E., C. Monaco, P. Tapponnier, L. Tortorici, and T. Winter (2001). Faulting and earthquake triggering during the 1783 Calabria seismic sequence, Geophys. J. Int. 144, 147, 499–516.

Jacques, E., J. C. Ruegg, J. C. Lépine, P. Tapponnier, G. C. P. King, and A. Omar (1999). Relocation of M ≥ 2 events of the 1989 Dôbi seismic sequence in Afar: Evidence for earthquake migration, Geophys. J. Int. 138, 447–469.

Jacques, E. et al., 2011. Normal faulting during the August 1989 earthquakes in Central Afar: sequential triggering and propagation of rupture along the Dobi Graben, ˆ Bull. Seism. Soc. Amer., 101, 994–1023.

Jestin, F., Huchon, P. & Gaulier, J.-M., 1994. The Somalia plate and the East African Rift System: present day kinematics, Geophys. J. Int., 116, 637–654.

Kebede, F., W. Kim, and O. Kulhanek (1989). Dynamic source parameters of the March–May 1969 Serdo earthquake sequence in Central Afar, Normal Faulting during the

August 1989 Earthquakes in Central Afar Ethiopia, deduced from teleseismic body waves, J. Geophys. Res. 94, 5603–5614.

Keir, D., I. D. Bastow, C. Pagli, and E. L. Chambers (2013), The development of extension and magmatism in the Red Sea rift of Afar, Tectonophysics, 607, 98–114, doi:10.1016/j.tecto.2012.10.015.

Kidane, T., V. Courtillot, I. Manighetti, L. Audin, P. Lahitte, X. Quidelleur, P.-Y. Gillot, Y. Gallet, J. Carlut, and T. Haile (2003), New paleomagnetic and geochronologic results from Ethiopian Afar: Block rotations linked to rift overlap and propagation and determination of a ∼2 Ma reference pole for stable Africa, J. Geophys. Res., 108(B2), 2102, doi:10.1029/2001JB000645.

Kogan, L., Fisseha, S., Bendick, R., Reilinger, R., McClusky, S., King, R. & Solomon, T., 2012. Lithospheric strength and strain localization in continental extension from observations of the east African Rift, J. geophys. Res., 117, doi:10.1029/2011JB008516.

Lahitte, P., Gillot, P.-Y., Kidane, T., Courtillot, V. & Bekele, A., 2003. New age constraints on the timing of volcanism in central Afar, in the presence of propagating rifts, J. geophys. Res., 108, 2123, doi:10.1029/2001JB001689.

Lockner, D., 1993. Room temperature creep in saturated granite, J. Geophys. Res., 98, 475-487.

Main, I. G., 2000. A damage mechanics model for power-law creep and earthquake aftershock and foreshock sequences Geophys. J. Int., 142, 151-161.

Manighetti, I., P. Tapponnier, V. Courtillot, S. Gruszow, and P.Y. Gillot., 1997. Propagationof rifting alongthe ArabiaSomalia plate boundary: The Gulfs of Aden and Tadjoura, Journal of Geophysical Research: Solid Earth 102, 2681-2710.

Manighetti, I., Tapponnier, P., Gillot, P.Y., Jacques, E., Courtillot, V., Armijo, R., Ruegg, J.-C., and King, G., 1998. Propagation of rifting along the Arabia-Somalia plate boundary: Into Afar: Journal of Geophysical Research: Solid Earth 103, 947-4974.

Manighetti, I., King, G.C.P., Gaudemer, Y., Scholz, C.H., Doubre, C., 2001a. Slip accumulation and lateral propagation of active normal faults in Afar. Journal of Geophysical Research: Solid Earth 106, 13667-13696.

Manighetti, I., Tapponnier, P., Courtillot, V., Gallet, Y., Jacques, E., Gillot, P.Y., 2001b. Strain transfer between disconnected, propagating rifts in Afar. Journal of Geophysical Research: Solid Earth 106, 13613-13665.

McClusky, S., Reilinger, R., Ogubazghi, G., Amleson, A., Healeb, B., Vernant, P. & Kogan, L., 2010. Kinematics of the southern Red Sea-Afar Triple Junction and implications for plate dynamics, Geophys. Res. Lett., 37, doi:10.1029/2009GL041127.

McKenzie, D. P., D. Davies, and P. Molnar (1970). Plate tectonics of the Red Sea and East Africa, Nature 226, 243–248.

Mullissa, A.G., Perissin, D., Tolpekin, V.A. , Stein, A., 2018. Polarimetry based distributed scatterer processing method for PSI applications. IEEE Trans. Geosci. Remote Sens.

Pagli, C., Wang, H., Wright, T.J., Calais, E. & Lewi, E., 2014. Current plate boundary deformation of the Afar rift from a 3-D velocity field inversion of InSAR and GPS, J. geophys. Res., 119, 8562–8575.

Perissin, D., and Wang, T., 2012. Repeat-pass SAR interferometry with partially coherent targets. IEEE Trans. Geosci. Remote Sens., vol. 50, no. 1, pp. 271–280.

Reed, C. A., Almadani, S., Gao, S., Elsheikh, A.A. , Cherir, S. , Abdelsalam, M.G., Thurmond, A.K., Liu, K.H., 2014. Receiver function constraints on crustal seismic velocities and partial melting beneath the Red Sea rift and adjacent regions, Afar Depression. Journal of Geophysics. Research 119, 2138-2152, Doi:10.1002/2013JB010719.

Ruegg, J.C. & Kasser, M., 1987. Deformation across the Asal-Ghoubbet Rift, Djibouti, uplift and crustal extension 1979–1986, Geophys. Res. Lett., 14, 745–748.

Saria, E., Calais, E., Stamps, D., Delvaux, D. & Hartnady, C., 2014. Present-day kinematics of the East African Rift, J. geophys. Res., 119, 3584–3600

Sichler, B., 1980. La biellette danakile: un modele pour l' ` evolution ´geodynamique de l'Afar, ´ Bull. Soc. Geol. Fr., ´ 22, 925–932.

Sigmundsson, F., 1992. Tectonic implication of the 1989 Afar earthquake sequence, Geophys. Res. Let. 19, 877-880.

Souriot, T. & Brun, J.P., 1992. Faulting and block rotation in the Afar triangle: the Danakil "crank arm" model, Geology, 20, 911–914.

Tapponnier, P., Armijo, R., Manighetti, I., and Courtillot, V., 1990. Bookshelf faulting and horizontal block rotations between overlapping rifts in Southern Afar: Geophysical Research Letters 17, 1-4.

Tesfaye, S., 2005. Fault population investigation and estimating magnitude of extension in Guma Graben, Central Afar, Ethiopia, Journal of African Earth Sciences. PP 437–444.

Tesfaye, S., M.G.Rowan, K.Mueller, Trudgill, B. D., and Harding, D. J., 2008. Relay and accommodation zones in the Dobe and Hanle grabens, central Afar, Ethiopia and Djibouti, Journal of the Geological Society, London, pp. 535–547.

Vigny, C., Huchon, P., Ruegg, J.-C., Khanbari, K. & Asfaw, L.M., 2006. Confirmation of Arabia plate slow motion by new GPS data in Yemen, J. geophys. Res., 111, B02402, doi:10.1029/2004JB003229.

Vigny, C., Huchon, P., Ruegg, J.-C., Khanbari, K. & Asfaw, L.M., 2006. Confirmation of Arabia plate slow motion by new GPS data in Yemen, J. geophys. Res., 111, B02402, doi:10.1029/2004JB003229.

Wright, T.J., Ebinger, C., Biggs, J., Ayele, A., Yirgu, G., Keir, D. & Stork, A., 2006. Magma-maintained rift segmentation at continental rupture in the 2005 Afar dyking episode, Nature, 442, 291–294.

PAPER III

UPPER LITHOSPHERIC STRUCTURE OF THE DOBI GRABEN, AFAR DEPRESSION FROM MAGNETICS AND GRAVITY DATA

4.0 ABSTRACT

We employed high-resolution ground magnetic, aeromagnetic and satellite gravity data to image the upper lithospheric structure beneath the Dobi graben and surroundings. This graben is located in the East Central Block (ECB) of the Afar Depression (AD) which is enclosed between the Red Sea and the Gulf of Aden rifts. Our aim is to understand the styles of crustal extension beneath the Dobi graben. We used two-dimensional (2D) radially-averaged power spectral analysis of both the aeromagnetic and the satellite gravity data to image deeper magnetic and density sources. We used the spectral analysis to estimate the depth to the boundary between the upper and lower crust, and the depth to Moho. Subsequently, we performed 2D forward modeling using the high-resolution ground magnetic and the satellite gravity data to produce a NE-SW trending model for the upper lithosphere beneath the Dobi graben and surroundings. We found the crust to be thinner beneath the Dobi graben reaching a thickness of only ~23 km. We also found the boundary between the upper and lower crust to be at depth between 10 and 12 km. Additionally, we found two ~5 km wide zones where melt and mafic dikes are possibly

present within the lower crust. These zones are centered beneath a relay zone on the southwestern side of the Dobi graben and beneath a narrow (~2 km wide) graben just to the northeast of the Dobi graben. Our model agrees with previous findings, especially V_p/V_s ratios of 1.85 or higher calculated from broadband passive seismic receiver function studies, which indicate the presence of melt in the lower crust beneath the graben. Because of this and the occurrence of earthquakes above ~15 km deepth seismogenic zone, we propose that, while the upper crust beneath the Dobi graben is mechanically stretching, the lower crust is ductily stretching aided by the presence of melt and the intrusion of mafic dikes.

KEYWORDS

Afar Depression, Dobi graben, Magnetic and gravity analysis, Upper lithospheric structure, Presence of melt and mafic dikes

RESEARCH HIGHLIGHTS

- We imaged upper lithosphere of the Dobi graben, Afar with magnetic and gravity data.
- We found shallower Moho (~23 km) and 10-12 km thick upper crust beneath the graben.
- We also found two, ~5 km wide zones of melt and mafic dikes in the lower crust.
- We propose the upper crust beneath the Dobi graben is mechanically-stretching.
- We also propose that the lower crust beneath the graben is ductily-stretching.

4.1 Introduction

The Afar Depression (AD) is the northern termination of the East Africa Rift System (EARS) (Fig. 1A) and it is an optimal natural laboratory to study continental rifting transitioning into seafloor spreading. It is situated where the continental Main Ethiopian Rift, and the oceanic Red Sea and the Gulf of Aden rifts form a diffuse rift-rift-rift triple junction juxtaposing the Arabian, Nubian and Somalian plates (Fig. 1A; Tapponnier et al., 1990; Manighetti et al., 2001; Kidane et al., 2003; Beyene and Abdelsalam, 2005). Within the AD, there are no sharp lithospheric boundaries between these plates. Rather, the SE-propagating Red Sea rift and the NW-propagating Gulf of Aden rift enclose a ~120 km long and ~100 km wide overlap zone characterized by distributed extension and this overlap zone is referred to as the East Central Block (ECB) (Fig. 1B). This block is dominated by the alternation of NW-trending graben and horst structures (Fig. 1B; Tapponnier et al., 1990; Sigmundsson, 1992; Manighetti et al., 1998; Kidane et al., 2003; Beyene and Abdelsalam, 2005).

A consensus now exists that the AD crust is a stretched continental crust that is highly injected by mafic dikes (Breckhemer, 1975; Markis and Gingburg, 1987; Bridges et al., 2012; Lewi et al., 2016). Many studies explained that in magma-assisted continental rifting, thermal softening of the lithosphere during the initiation of rifts is facilitated by the intrusion of mafic dikes sourced from shallow (~6 km deep) magma chambers (e.g., Daniel et al., 2014). These shallow magma chambers are fed from a deeper source possibly in the form of an ascending asthenosphere or a mantle plume (Benoit et al., 2006; Bastow et al., 2008; Rooney et al., 2012, 2013, 2016; Stab et al., 2016).

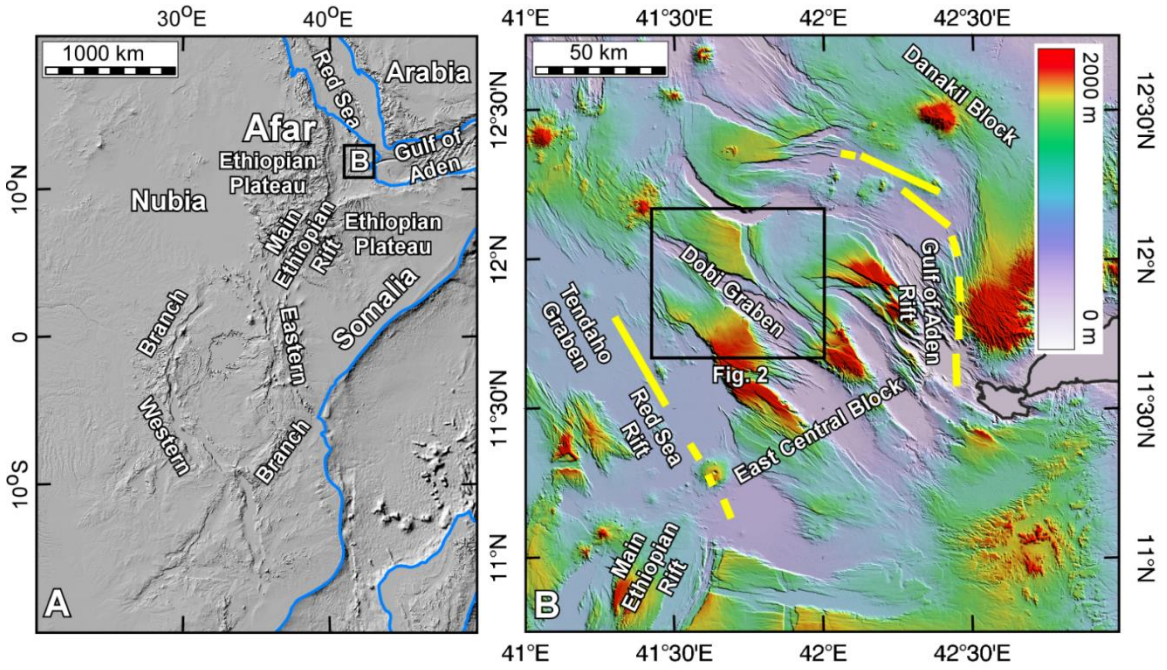

Figure 1: (A) Earth Topography 1 arc minute (ETOPO 1) Digital elevation model (DEM) showing the major segments of East Africa Rift System (EARS). (B) Shuttle Radar Topography Mission (SRTM) DEM of the East Central Block (ECB). Yellow lines indicate the location of the Red Sea and Gulf of Aden rifts.

The spatial extent of lava flows suggests that recent volcanism in the AD is localized within narrow magmatic segments similar to those observed in the Main Ethiopian Rift (Wolfenden et al., 2005; Ayalew et al., 2006). Over time, the locus of extension and magmatism has shifted eastward from the western border fault of the AD to the Red Sea rift (Wolfenden et al., 2005; Ayalew et al., 2006; Keir et al., 2011). This suggests that the younging direction of magmatism is towards the Quaternary–Recent axial magmatic segments, where faulting and magmatism are now localized (e.g., Barberi and Varet 1977; Manighetti et al., 2001). Bridges et al. (2012) used detailed land-based magnetic data across the NW-trending Tendaho graben, which represents the southern segment of the Red Sea rift within the AD (Fig. 1B), to demonstrate the presence of

magnetic stripes similar in pattern and amplitude to those found at mid-ocean ridges. Additionally, Bridges et al. (2012) modeled the Tendaho graben as being dominated by a ~10 km wide central zone characterized by normal polarity and this zone is flanked on each side by ~20 km wide regions characterized by reverse polarity. Bridges et al. (2012) noted that the Tendaho graben started opening ~2 Ma and the that latest polarity reversal event occurred ~0.78 Ma. Using this we can estimate that the extension rate of the Tendaho graben between ~2.0 Ma and ~0.78 Ma was ~1.6 cm/year and between 0.78 Ma and present is ~0.6 cm/year. Hence, we explain these extension rates as an indication that the extension across the Tendaho graben is slowing down and the boundary between the Arabian and Nubian plates within the AD might be developing within the ECB, possibly within the Dobi graben in the central part of the block (Fig. 1B).

Despite the obvious recent extensional features, there are no surface expression of recent magmatic activity within the Dobi graben analogous to that observed in the Tendaho graben or other magma-assisted continental rifts. Nonetheless, it has been debated that the lack of surface magmatism does not imply the absence of sub-surface magma sources beneath magma-poor continental rifts such as the Dobi graben (Wolbern et al., 2012; Jakovlev et al., 2013). The absence of magma to initiate rifting through thermal softening of the lithosphere leads us to consider other factors responsible for rift initiation. For instance, the possibility that the Dobi graben is opening through mechanical stretching is supported by the relatively high concentration of earthquakes within the graben compared to other parts of the AD (Hofstetter and Beyth, 2003). This is best illustrated by the 1989 earthquake sequences within the graben where most of the damage was caused by earthquake events that occurred only above the ~15 km deep

seismogenic zone (Sigmundsson, 1992, Jacques et al., 2011). Therefore, brittle deformation seems to be the dominant mechanism of extension in the upper crust beneath the graben. However, using broadband passive seismic receiver function studies (henceforth receiver function studies), Reed et al. (2014) documented high V_p/V_s ratios of up to 1.92 within the lower crust beneath the Dobi graben, which implies the presence of melt. Additionally, Dugda et al. (2005) and Hammond et al (2011) determined lower crustal V_p/V_s ratios between 1.92 and 2.1 near the southwestern margin of the ECB, which is also suggestive of the presence of melt.

In order to determine the factors controlling the extension across the Dobi graben at crustal-scale depth, we collected and analyzed high resolution ground magnetic data (Cyan line in Fig. 2) supported by previous aeromagnetic data (Aeromagnetic map of Republic of Djibouti) (Courtillot et al., 1980) and satellite gravity data (World Gravity Model 2012 (WGM 2012, Balmino et al., 2011)). Our magnetic and gravity study is constrained by previous active-source seismic refraction studies (Berckhemer et al., 1975; Makris and Ginzburg 1987), receiver function studies (Reed et al., 2014), and magnetic and gravity studies (Bridges et al., 2012; Lewi et al., 2016). Our analysis aims at imaging the upper lithospheric structure beneath the Dobi graben and surroundings. This includes determining the depth to the boundary between the surface formations and the upper crust, the depth to the boundary between the upper and lower crust, and the depth to the Moho representing the boundary between the lower crust and the sub-continental lithospheric mantle (SCLM). We also aim at imaging possible locations and the extent of zones where melt and mafic dikes are possibly present in the lower crust. We first determined the depth to the boundary between the upper and lower crust by analyzing the

aeromagnetic and satellite gravity data using the two-dimensional (2D) radially-average power spectral method (henceforth spectral analysis). We subsequently constrained the boundary between the lower crust and the SCLM using the Reed et al. (2014) receiver function studies results and our own results from the spectral analysis of the aeromagnetic and the satellite gravity data. We ended with using the high-resolution ground magnetic data and the satellite gravity data to produce a NE-SW trending 2D forward upper lithospheric model (henceforth the 2D model) across the Dobi graben and surroundings.

4.2 Tectonic Setting

4.2.1 The East-Central Block (ECB)

Based on similarity in structural trends, the AD can be divided into a northern block, an ECB, and a southwestern block (Hayward and Ebinger, 1996). Of importance to our study is the ECB, which encloses the NW-trending Dobi graben and is bounded in the southwest by the SE-propagating Red Sea rift and in the northeast by the NW-propagating Gulf of Aden rift (Fig 1B; Beyene and Abdelsalam, 2005). The most recent Global Positioning System (GPS) study in the Red Sea and Gulf of Aden rifts, and in the enclosed ECB revealed a rate of displacement within the ECB ranging between 6 and 11 mm/year in a N-direction and between 8 and 19 mm/year in an E-direction (Kogan et al., 2012). Additionally, Kogan et al. (2012) indicated that the overall displacement of the ECB is in an ENE-direction away from the Nubian plate, whereas the displacement increases towards the Gulf of Aden rift. Kogan et al. (2012) explained the pattern of displacement in the ECB as due to diffused extension across the AD, possibly because of

the presence of a relatively thin lithosphere. However, despite the general domination of the diffused extension within the ECB, localized extension within narrow grabens such as the Dobi graben (Fig. 1B) seems to be present. These zones of localized extension are characterized by the presence of NW-trending high-angle normal faults that might have facilitated extension through mechanical stretching in the brittle upper crust.

4.2.2 Geology of the Dobi Graben

The Dobi graben is a NW-trending graben in the center of the intensely dissected ECB and occupies an area of ~600 km^2 (Fig. 2). It is located to the northeast of the Tendaho graben, the southeastern termination of the Red Sea rift. It is also located to the southwest of the Gulf of Aden rift (Fig. 1B). The width of the graben varies from ~16 km in the Dobi-Hanle accommodation zone in the southeast to ~6 km in the Dobi termination zone to the northwest (Fig. 2). It is bounded in the northeast by the Isso Dedat horst and in the southwest by the Unda Gamarri horst (Fig. 2). The northeastern side of the southeastern end of the Dobi graben merges with the Kambourta graben, which is located in the southwestern side of the Siyarrou horst (Fig. 2).

The Dobi graben is underlain by the dominantly intensely faulted basaltic flows of the Afar Stratoid Series (henceforth the Afar basalts) (Varet, 1978). In places, the Afar basalts attain an exposed thickness in excess of 1.5 km (Varet, 1978). K/Ar geochronological studies by Kidane et al. (2003) indicated that the age of the Afar basalts near the Dobi graben is between 2.0 and 1.6 Ma. The basalts are variably weathered and are commonly scoriaceous, vesicular and rubble-forming where lateritized agglomerates locally separate these laterally continuous flows from one another. The lateral persistence

of the basaltic flows is visible along the escarpments of the graben's border faults (Tesfaye, 2005).

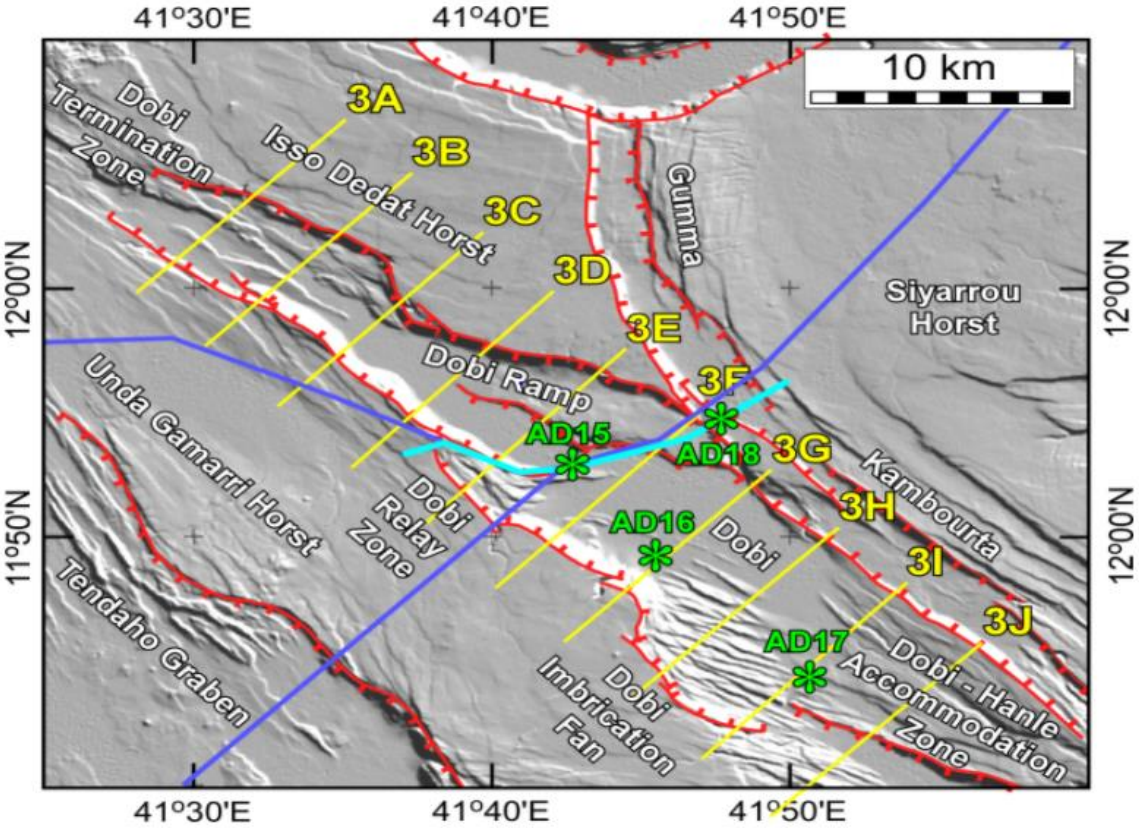

Figure 2: Shuttle Radar Topography Mission (SRTM) Digital Elevation Model (DEM) showing major structural features of the Dobi graben. See Figure 1B for location. Blue lines show the location of the active-source seismic refraction studies of Berckhemer et al. (1975) and Makris and Ginzburg (1987). Green stars represent the location of the broadband passive seismic stations of Reed et al. (2014). Yellow lines show the location of the geological cross-sections shown in Figure 3. Cyan line shows the location of the two-dimensional (2D) forward magnetic and gravity model shown in Figure 9D.

The top layers of the basalt are characteristically sub-horizontal (Fig. 3) compared to the more tilted base layers indicating progressive tilting of the older layers with time (Varet, 1978). However, locally some younger blocks are substantially tilted due to

faulting. In some cases, basaltic flows of less than 1 Ma age are tilted by up to 35° (Hayward and Ebinger, 1996). Together with the basalts, trachytic volcanic flows are also found within the Dobi graben, especially within what we identified as the Dobi relay zone (Fig. 2). Rhyolitic volcanic flows are also present in the northwestern tip of the Dobi graben. The graben is filled with Pleistocene – Recent lacustrine, evaporate and eolian sediment (henceforth graben sediment fill) (Fig. 3; Hayward and Ebinger, 1996; Acton et al., 2000).

4.2.3 Architecture of the Dobi Graben

The Dobi graben shows significant along-strike variation in its geometry as illustrated by the series of NE-SW cross-sections shown in Figure 3. The northwestern part of the graben is dominated by the ~6 km wide Dobi termination zone, which has NW-trending down-dropping blocks ending with ~1 km wide central graben (Figs. 2, and 3A and B). The escarpments of the northeastern and the southwestern border faults of the graben become progressively better developed southeastward reaching ~350 m in relief (Figs. 3A and B). Southeast of its termination zone, the Dobi graben attains a full graben geometry with a width of ~6 km bounded by NW-trending border faults with escarpments as high as ~600 m (Figs. 2, and 3C and D). Further southeast, the graben widens to reach a width of ~10 km (Figs. 2 and 3E).

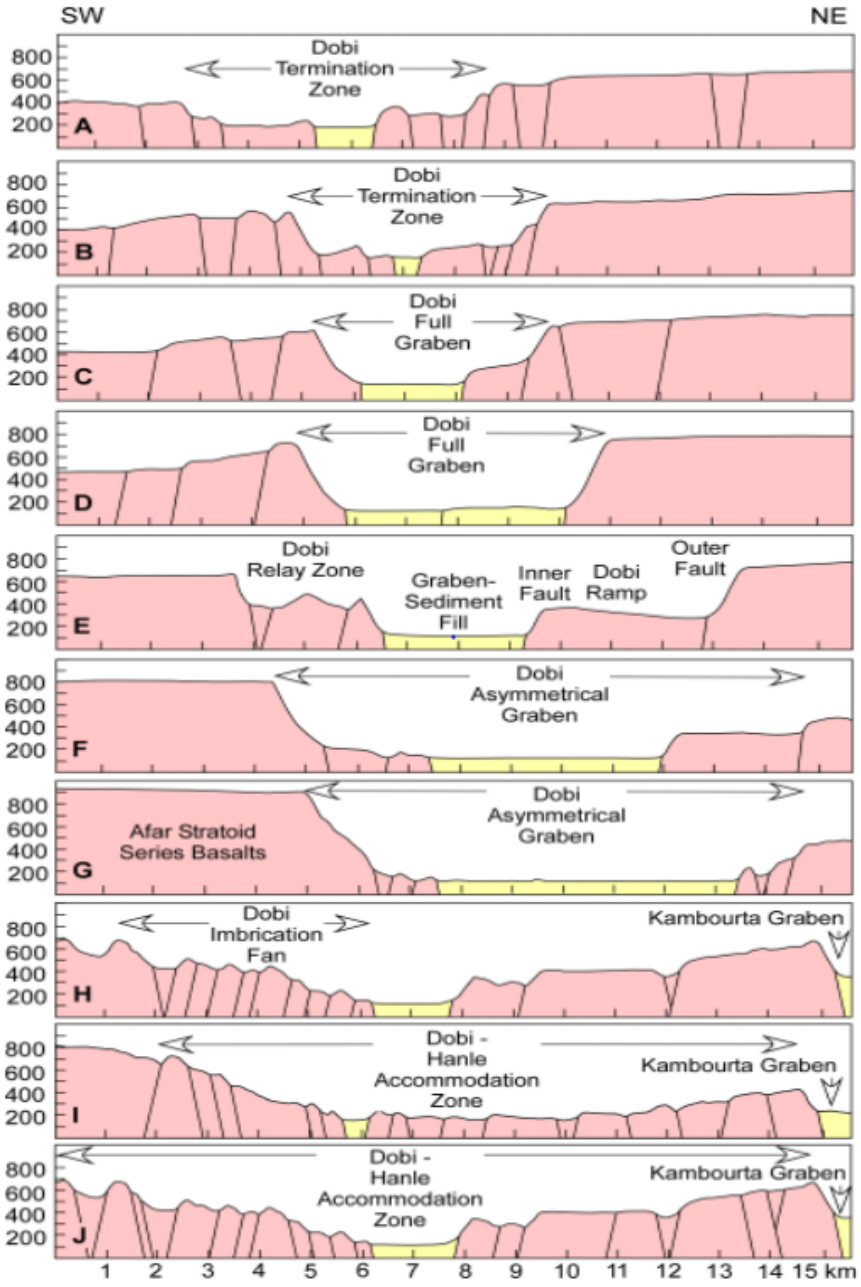

Figure 3: Schematic NE-SW-trending geological sections (Fig. 2) across the Dobi graben. See Figure 2 for the location of the cross-sections.

In this part of the Dobi graben, the NW-trending northeastern border fault is in the form of an outer fault that down-drop the Afar basalts. A topographic escarpment that reaches ~ 450 m high defines this outer border fault (Fig. 3E). To the southwest of the

outer border fault there exists an inner fault that is striking E-W (Fig. 2) and it is defined by ~250 m high escarpment that extends from the Afar basalts to the graben sediment fill (Fig. 3E). Here, the southwestern side of the graben forms a relay zone (the Dobi relay zone) bounded between NE-dipping outer and inner border faults (Fig. 3E). In the Dobi relay zone, the Afar basalts are dissected by a series of SW-dipping antithetic faults (Figs. 2 and 3E). The central part of the Dobi graben forms a ~10 km wide highly asymmetrical graben with the escarpment of the southwestern border fault reaching a height of ~800 m. Differently, the escarpment of the northeastern border fault is only cumulatively (cumulative height of the escarpments of the outer and inner border faults) ~300 m high (Figs. 2, and 3F and G). Further southeast, the southwestern border fault of the Dobi graben is poorly defined and lacks the development of an escarpment of any significant height (Figs. 2 and 3H). However, the hanging-wall of this border fault is defined by a ~5 km wide imbrication fan in which ~0.5 km wide, NE-dipping blocks of the Afar basalts are bounded by SW-dipping antithetic faults (Figs. 2 and 3H). There is no well-defined northeastern border fault in this part of the graben and the escarpment of the NE-dipping southwestern border fault of the Kambourta graben defines its width (Figs. 2 and 3H). The southeastern-most end of the Dobi graben is dominated by the ~12 km to ~16 km wide Dobi-Hanle accommodation zone, which is characterized by a series of ~1 km wide, NW-trending grabens and horst structures (Figs. 2, and 3I and J).

4.2.4 Lithospheric Structure

The lithospheric structure of the AD has been examined by a number of geophysical studies. These include active-source seismic refraction studies (Ruegg, 1975;

Berckhemer et al., 1975; Makris & Ginzburg 1987), gravity and magnetic studies (Makris et al., 1975; Mammo, 2004; Tiberi et al., 2005; Bridges et al., 2012; Lewi et al., 2016), and receiver function studies (Dugda et al., 2005; Dudga and Nyblade, 2006; Hammond et al., 2011; Reed et al., 2014). Below we summarize results of some of these studies relevant of our current study.

Berckhemer et al. (1975) acquired a seismic refraction profile that crossed the AD (including the Dobi graben; Blue line in Fig. 2) from the eastern escarpment of the Ethiopian plateau to the Red Sea coast. Berckhemer (1975) suggested that the crustal thickness decreases from ~38 km in the Ethiopian plateau to between 26 km and 16 km beneath the AD and further east towards the Red Sea. Based on V_p values ranging between 6.6 km/s and 6.8 km/s, Berckhemer et al. (1975) interpreted the AD crust to be of continental nature but it is accreted by mafic dikes, hence resulting in it being a transition between continental and oceanic crust. The transitional nature of the AD crust was further supported by Makris and Ginzburg (1987) who re-interpreted the above active-source seismic refraction data in connection with the gravity data of Makris et al. (1975). Makris and Ginzburg (1987) suggested that the AD has an attenuated transitional crust with low V_p values that range between the velocities of continental and oceanic crust and estimated a thickness of ~26 km in the central AD that gradually decreases towards the Red Sea to ~14 km. Additionally, Makris and Ginzburg (1987) identified a 2.5 km thick layer with V_p value of 2.2 km/s that thins towards the east and interpret this as sediment layer that overlies the Afar basalts. Furthermore, Makris and Ginzburg (1987) estimated the thickness of the upper crust to be ~11 km. Based on receiver function studies, Dugda et al. (2005) estimated that the crust beneath the Tendaho graben

to the southwest of the Dobi graben to be ~25 km thick. Also, based on receiver function studies, Reed et al. (2014) estimated the crust beneath the Tendaho and Dobi grabens to be between ~17 km and ~30 km with the thinnest crust beneath the Tendaho graben.

Receiver function studies were also used to determine the V_p/V_s ratios of the AD crust. Dugda et al. (2005) and Hammond et al. (2011) found the V_p/V_s ratios measured in broadband seismic stations within the southwestern footwall of the Tendaho graben (Fig. 1B) to range between 1.9 and 2.1. Reed et al. (2014) documented high V_p/V_s ratios ranging between 1.85 and 2.40 for stations within the ECB. Four stations within the Dobi graben gave V_p/V_s ratios ranging between 1.94 and 2.01 (Shown as green stars in Fig. 2).

Additional information about the presence of melt and mafic dikes within the crust of the AD is obtained from magnetic and gravity data (Bridges et al. 2012; Lewi et al., 2016). Analyzing high-resolution ground magnetic data collected along a ~50 km long profile across the Tendaho graben (Fig. 1B), Bridges et al. (2012) documented symmetrical magnetic anomalies, the scale, shape and magnitude of which resembles those found within seafloor spreading centers. Bridges et al. (2012) used these data, together with high resolution ground gravity data, to develop a 2D forward model showing the upper crustal structure to a depth of ~10 km beneath the Tendaho graben. Bridges et al. (2012) found that this upper crust hosts a ~10 wide zone of mafic dikes. Additionally, Bridges et al. (2012) indicated that the central part of this zone of mafic dikes is characterized by high heat flow possibly due to presence of melt. Subsequently, Lewi et al (2016) used high-resolution ground gravity data to create a 2D upper lithopsheric model across the Tendaho graben. In this model, Lewi et al. (2016) proposed that the lower crust beneath the central part of the Tendaho graben host an up to 15 km

wide zone where melt is present. Also, in this model, Lewi et al. (2016) proposed the Moho to be only ~25 km deep beneath the central part of the graben and that the boundary between the upper and lower crust extends uniformly at depth of ~12 km beneath the entire graben

4.3 Data and Methods

4.3.1 Magnetic Data

We acquired high resolution ground magnetic data through surveys carried out in 2008 and 2009 across the Dobi and Gumma - Kambourta grabens (Cyan line in Fig. 2). The survey utilized a cesium optically pumped magnetometer coupled with a Global Positioning System (GPS) on a backpack frame. We collected the data by walking across the grabens with the data being collected every 5 seconds. We also collected base station readings using a proton precession magnetometer at a stationary location to correct for diurnal variations.

Additionally, we obtained aeromagnetic data by digitizing the Aeromagnetic map of Republic of Djibouti that was published in 1980 (Courtillot et al., 1980). These data cover the Republic of Djibouti and surroundings, including the Dobi graben. The original data were collected at a ~200 m flight height, with a total of 54 lines oriented N-S and spaced ~5 km apart. Additional data were acquired with 9 cross or tie lines spaced ~25 km apart. The data were presented as a regional contour map, which we digitized and re-gridded into a 1250 m X 1250 m grid (Fig. 4).

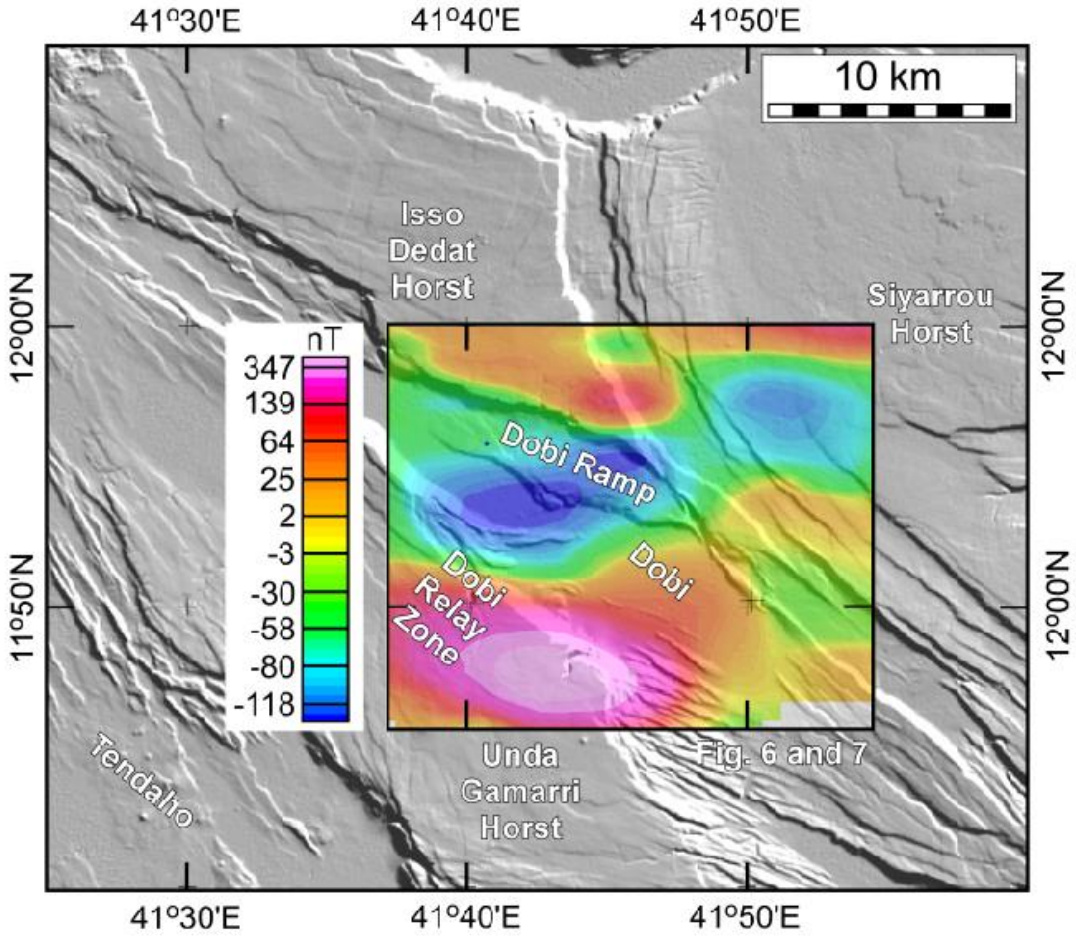

Figure 4: Aeromagnetic map of the Dobi graben draped onto Shuttle Radar Topography Mission (SRTM) Digital Elevation (DEM). The map is generated from the Aeromagnetic map of Republic of Djibouti (Courtillot et al., 1980).

We obtained the Bouguer gravity anomaly data (Fig. 5) from the International Gravity Bureau, which maintains the WGM 2012 (Balmino et al., 2011). The WGM 2012 Bouguer gravity anomalies were calculated using the Earth Gravity Model 2008 (EGM 2008) satellite gravity and the Earth Topography 1 arc-minute (ETOPO1) database for topography and bathymetry. This is to provide harmonic coefficients for a spherical

harmonic expansion up to an order of 10,800 to produce the Earth's Topography derived Gravity model at 1' X 1' resolution (ETOPG1) model (Balmino et al., 2011).

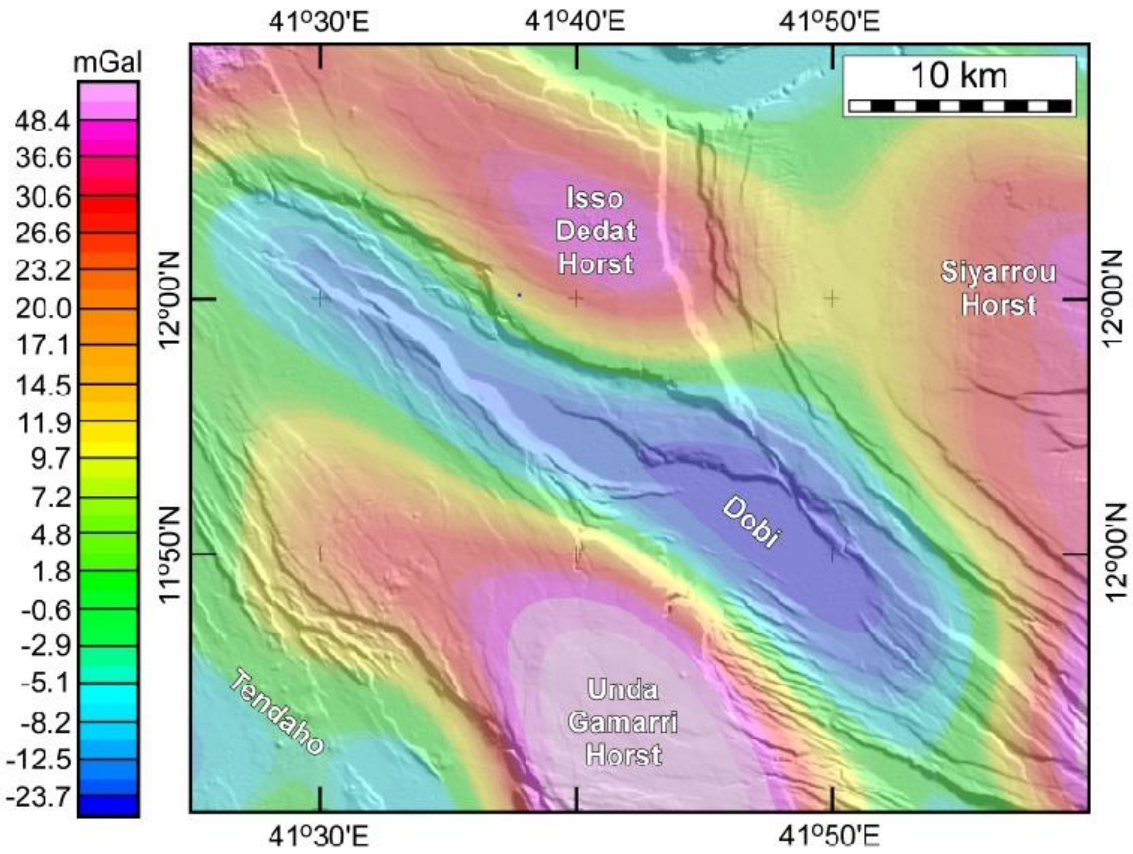

Figure 5: Bouguer gravity anomaly map of the Dobi graben generated from the World Gravity Model 2012 (WGM 2012) and draped onto Shuttle Radar Topography Mission (SRTM) Digital Elevation Model (DEM).

4.3.2 Magnetic Data Reduction

In the ground magnetic survey XYZ data files, we corrected for the missing readings that were introduced because of dropout of recording during the data acquisition. To correct for diurnal variations of the magnetic field, we used two base stations, one installed within the survey area and the second at the magnetic observatory

at Addis Ababa University. In addition to the correction of the data dropouts, we also removed the data outside the time ranges and high frequency spikes. After averaging data from the two base stations, we added the average of the differences of the magnetic readings to remove the diurnal effect from the field data to obtain the diurnal corrected magnetic data. To obtain the residual magnetic field data that we used in our analysis, we removed the 2005 International Geomagnetic Reference Field (IGRF) from the field magnetic data.

4.4 Analysis of Aeromagnetic and Satellite Gravity Data

4.4.1 Aeromagnetic and Gravity Data Enhancement

4.4.1.1 Vertical, Horizontal and Tilt Aeromangetic Derivatives

The aeromagnetic data revealed a magnetic minimum within the Dobi relay zone as well as at the central part of the graben (Fig. 4). Differently, the data highlighted magnetic maxima to the north and south of the magnetic minima, particularly within the southern part of the Isso Dedat horst and the northeastern side of the Unda Gamarri horst (Fig. 4). In order to enhance the edges of these magnetic anomalies, we determined the vertical (Fig. 6A) and the horizontal derivatives (Fig. 6B) from the aeromagnetic data. Each derivative provides different information about the location of the magnetic sources, as horizontal derivatives are suited to enhance the edge of the source (Cordell, 1979; Blakely and Simpson, 1986), while vertical derivatives are useful in narrowing determining the width of the source bodies (Marson and Klingele, 1993; Cooper and Cowan, 2004;).

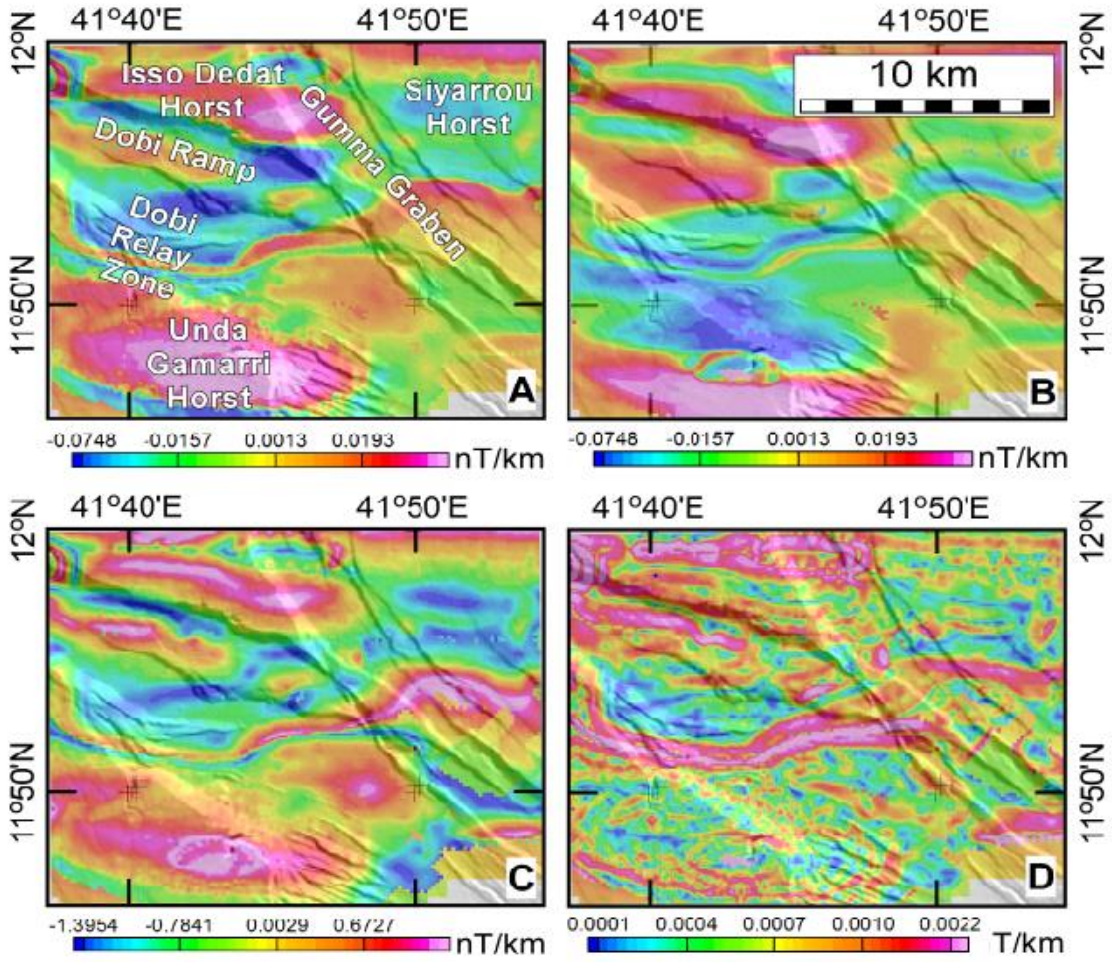

Figure 6: Magnetic derivative maps of the Dobi graben obtained from the aeromagnetic data in Figure 4. The magnetic derivatives are draped onto Shuttle Radar Topography Mission (SRTM) Digital Elevation Model (DEM). (A) Vertical magnetic derivative. (B) Horizontal magnetic derivative. (C) Magnetic tilt derivative. (D) Horizontal tilt derivative.

Additionally, vertical derivatives may enhance shallower density sources better than horizontal derivatives (Marson and Klingele, 1993). This is evident in Figure 6A, which shows that within the Dobi relay zone, the shallower graben sediment fill are resolved better than the NW-trending blocks of the Afar basalts. Figure 6A also shows

that the vertical derivative is positive over the edges of the Dobi ramp zone and within the Isso Dedat horst. This indicates that the vertical derivative detects the shallower graben sediment fill, which dominates the center of the graben as well as a few narrow regions within the relay zone. In contrast, Figure 6B shows horizontal gradient maxima over the edges of the Dobi ramp zone (both near the E-W trending normal fault (Fig. 2) and the NW-trending border fault, which is found between the Dobi ramp zone and the Isso Dedat horst). This horizontal gradient is zero over the Dobi ramp zone itself. However, in both cases if there exist more than one source for this anomaly, the shallower sources will be well resolved, but the deeper ones with shallower gradients may not be as apparent because the effective measure is the gradient amplitude (Askari et al., 2014).

According to Askari et al (2014), the presence of multiple sources can cause a considerable dynamic range in the size of the horizontal and/or vertical gradients, implying that either profiles or maps cannot provide enough signal so that the different sources can be identified. However, the tilt angle overcomes this problem by using the ratio of the vertical derivative to the horizontal gradient (Fig. 6C and D). Both the vertical derivative and the horizontal derivatives show lower amplitude values for the deeper sources. Therefore, the ratio of the two will be large over the source. Positive tilt angle values represent tilt variations within a magnetic source, while negative angle values quantify the tilt variation outside the magnetic source, and the zero values lie over the edges of the magnetic source (Salem et al., 2007). By expressing these values as a tilt angle rather than a ratio, they will always be in the range of $-90° < TILT < +90°$. The tilt angle is relatively insensitive to the depth of the source and it is capable of resolving

shallow and deep sources equally. For instance, the tilt angle maps show variations within NW-trending magnetic sources in the Dobi ramp zone and within the Isso Dedat horst and appears positive in the tilt angle images (Figs. 6C and D). However, a negative ratio is shown extending from the Dobi relay zone to the Dobi ramp zone in an almost orthogonal direction to the trend of the graben. Additionally, south of the Dobi relay zone, there is a higher tilt angle and extends in an ENE direction over the Gumma graben into the southern part of the Siyarrou horst (Fig. 6C and D).

4.4.1.2 Upward Continuation of Satellite Gravity Data

The Bouguer gravity anomaly map (Fig. 5) indicates a gravity minimum where the graben sediment fill are exposed. The Bouguer gravity anomaly map also indicates a gravity maximum over the Isso Dedat, Unda Gamarri and Siyarrou horsts. We applied upward continuation to the Bouguer gravity anomaly data to estimate the possible maximum depth the effect of the graben sediment fill has on the Bouguer gravity anomaly (Fig. 7). The upward continuation involves mathematically continuing the gravity field from a specific shallower depth to a specific deeper depth, in order to remove the effect of near surface and shorter wavelength anomalies (Jacobsen, 1987; Zeng et al., 2007). Jacobsen (1987) used upward continuation of the gravity field to a specific height (Z) where the depths of the sources are at or below half the continuation depth. Accordingly, we continued the Bouguer gravity anomaly data (Fig. 7A) to the heights of 5 km (Fig. 7B), 7 km (Fig. 7C), and 10 km (Fig. 7D).

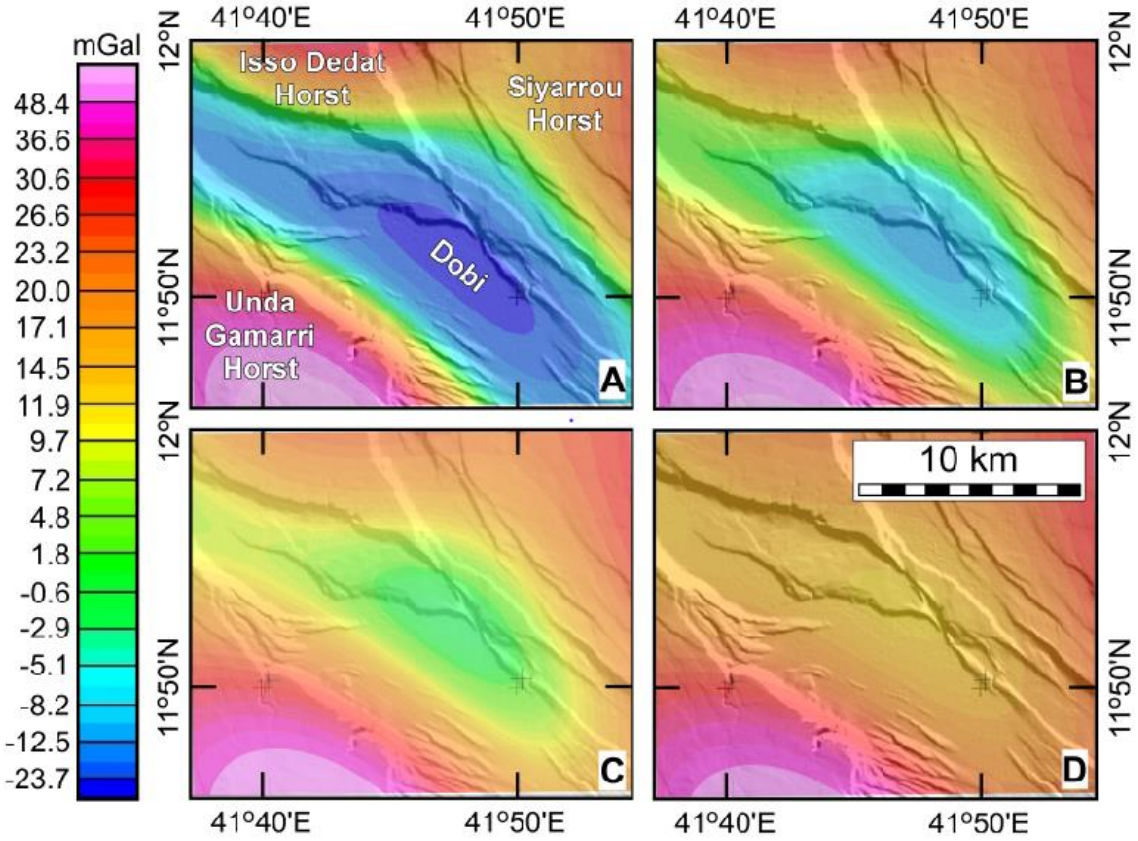

Figure 7: Upward continued maps of the Bouguer gravity anomaly data of the Dobi graben obtained from the World Gravity Model 2012 (WGM 2012) and draped onto Shuttle Radar Topography Mission (SRTM) Digital Elevation Model (DEM). (A) Original Bouguer gravity anomaly map. (B) Bouguer gravity anomaly map upward continued to 5 km. (C) Bouguer gravity anomaly data upward continued to 7 km. (D) Bouguer gravity anomaly data upward continued to 10 km.

Although estimates of the exact depth may not be reliable, the sources of the anomalies for these various maps can be approximated to at or below the depths of 2.5 km, 3.5 km and 5 km, respectively. The 5 km and 7 km continuation heights maps revealed gravity minima that are indicative of the presence of graben sediment fill or other less dense sedimentary rocks to depths of ~2.5 km and 3.5 km, respectively (Figs.

7B and C). However, the 10 km upward continuation did not show a gravity minimum related to the graben sediment fill, but rather a broad gravity high (Fig. 7D). Given geological constraints, we doubt that the graben sediment fill of the Dobi graben are as thick as ~2.5 km. For example, it is estimated that the graben sediment fill of the much wider (~50 km) Tendaho graben to the southwest of the Dobi graben to be only 1.6 km (Abbate et al., 1995). Hence, we take these results to only indicate that the thickness of the graben sediment fill of the Dobi graben is less than 2.5 km.

4.4.2 Spectral Analysis of Aeromagnetic and Satellite Gravity Data

Spectral analysis of magnetic and gravity data has been commonly used to deduce first-order depth estimates to magnetic susceptibility and density interfaces (e.g., Dorman and Lewis, 1970; Karner and Watts, 1983; Tselentis et al., 1988). To estimate the depth to sub-surface boundaries beneath the Dobi graben and surroundings, we performed a spectral analysis using both the aeromagnetic and satellite gravity data using the spectral analysis method described by Tanaka et al. (1999).

4.4.2.1 Depth to the Magnetic Sources

Using the total intensity of the aeromagnetic data covering the Dobi graben and surroundings, we calculated the 2D spectrum for 0.5° x 0.5° (~55 km × ~55 km) window. The window has been extended by 50% to allow for the computation of the magnetic susceptibility sources near the edges and to avoid Gibb's phenomena (edge effect) when using the Fast Fourier Transform. The depths to the top of the magnetic interfaces is based on breaks of the slope a logarithmic plot of the 2D spectral curve (Fig. 8A; Tanaka

et al., 1999). The region between the slope breaks can then be estimated by a linear segment, the slope of which is related to magnetic interfaces.

The selection of the linear segments depends on the user visually determined breaks in the slope of the 2D spectral curve. We estimated a number of slopes using different ranges of radial angular frequencies and we then determined the deviation between these linear segments and the actual data using the Linest function in Excel, which is based on the least squares best fit method. We used the average slope from these slope estimates to calculate the depth to the magnetic magnetic interface. To determine the potential error in our depth estimates, we used an error estimation method describe by Chiozzi et al. (2005) and Trifonova et al. (2009) where the error is defined by the ratio of the standard deviation of the linear fit to the range of the wavenumbers that are used when determining the slopes for each interface from the 2D spectral curves. The 2D spectral curve in Figure 8A suggests the presence of magnetic boundaries at depths of 22.9 km, 11.8 km and 2.7 km which correspond to low (~0.05 – ~0.25 radian/km), intermediate (~0.25 – ~0.35 radian/km) and high (~0.35 – 0.45 radian/km) radial angular frequency, respectively. The standard deviation and statistical error for these boundaries are 2.46 and 2.59 for the depth of 22.9 km, 2.84 and 2.25 for the depth of 11.8 km and 1.74 and 1.55 for the depth of 2.6 km. The 22.9 km depth is in good agreement with the depth to the Moho estimated from a receiver function study (Reed et al., 2014).

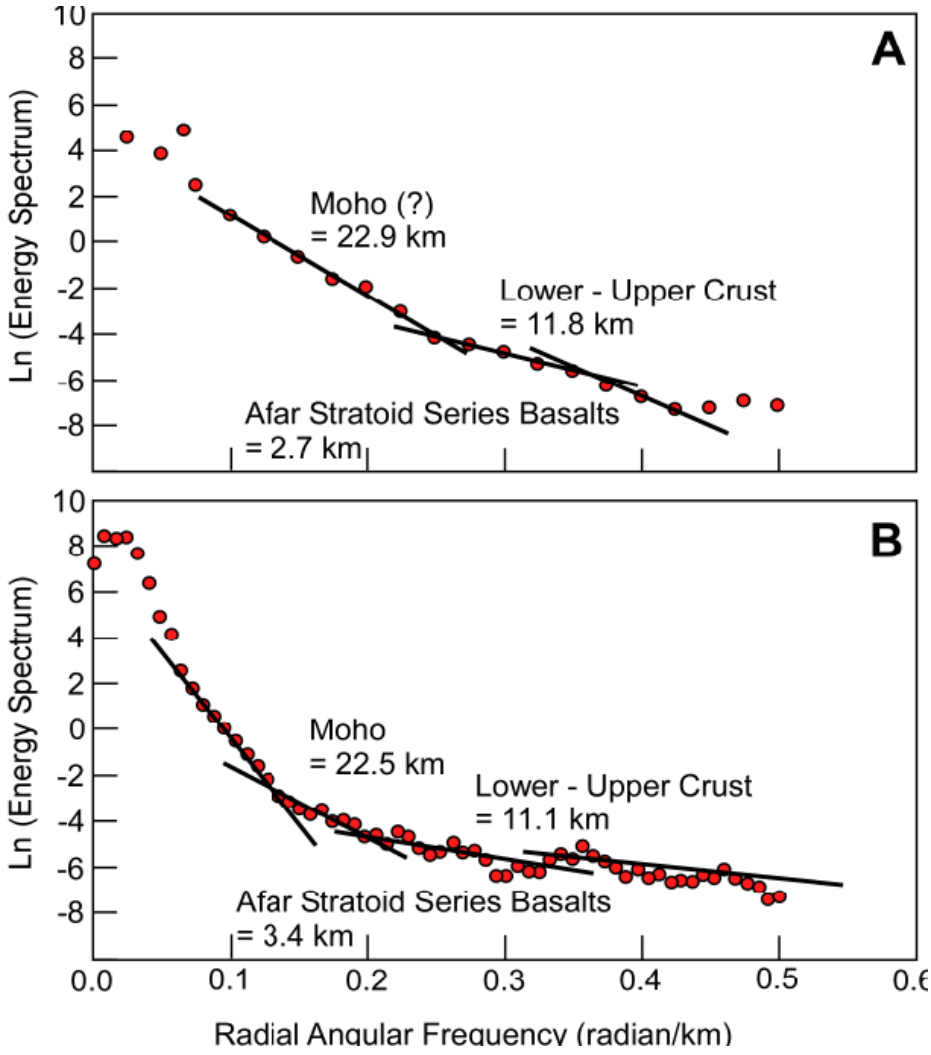

Figure 8: (A) Magnetic spectral curve obtained from 0.5° X 0.5° sub-area window of the aeromagnetic data shown in Figure 4 and used to estimate depths to magnetic susceptibility boundaries. (B) Gravity spectral curve obtained from 1° X 1° sub-area window of the Bouguer gravity anomaly map of the World Gravity Model 2012 (WGM 2012) shown in Figure 5 and used to estimate depths to density boundaries.

However, we are reluctant to interpret this depth as indicating the depth to Moho because many studies have concluded that magnetic data are of limited use in imaging anomalies below the Curie Point Depth (Haggerty, 1978; Salem et al., 2014). We

interpret the 11.8 km depth as the boundary between the upper and lower crust. Previous studies considered the depth corresponding to high wavenumbers as corresponding to near surface random noise (e.g. Tselentis et al., 1988). However, we point to that the 2.7 km depth is in agreement with the depth to the base of the Afar basalts that is determined from geological observations.

4.4.2.2 Depth to the Density Sources

To determine the depths to density interfaces beneath the Dobi graben and surroundings, we applied the spectral analysis technique first implemented by Spector and Grant (1970) and widely used thereafter by numerous researchers (e.g., Dorman and Lewis, 1970; Karner and Watts, 1993; Tselentis et al., 1988) to the Bouguer gravity anomaly data. We calculated the 2D spectrum for a 1° × 1° (~110 km × ~110 km) window centered on the Dobi graben with 50% extension of the grid in all directions to minimize Gibb's phenomena. We used the same statistical analysis described above for used for the aeromagnetic data.

The 2D spectral curve in Figure 8B suggests the presence of density boundaries at depths of ~22.5 km, ~11.1 km, and 3.4 km corresponding to low (~0.05 – 0.13 radian/km), intermediate (0.13 – 0.33 radian/km) and high (~0.33 – 0.50 radian/km) wavenumbers, respectively. The standard deviation and statistical error for these boundaries are 3.03 and 2.19 for the depth of 22.5 km, 3.78 and 3.34 for the depth of 11.1 km and 2.67 and 2.83 for the depth of 3.4 km. We interpret the ~22.5 km depth to represent the depth to the Moho which is in good agreement with the depth of ~23 obtained by Reed et al. (2014) from a receiver function study for station AD15 within the

Dobi graben (Green star in Fig. 2). We interpret the ~11.1 km depth as the boundary between the upper and lower crust. This is in good agreement with the thickness of ~11 km estimated by Makris and Ginzurg (1987) for the upper crust of the AD from active-source seismic refraction study. It is also in good agreement with the depth of ~10.5 km obtained by Lewi et al. (2016) for the boundary between the upper and lower crust beneath the Tendaho graben from spectral analysis of high-resolution ground gravity data. The ~3.4 km depth is within the spectrum random noise and it a bit deeper than the depth to the base of the Afar basalts as has been determined from geological observations. Hence, we leave this depth un-interpreted.

4.5 Two-dimension (2D) Forward Modelling of Ground Magnetic and Satellite Gravity Data

4.5.1 Constraints from Previous Studies

A common problem in most mathematically-based geological models using geophysical data arises from the non-uniqueness of the models created, especially when using gravity and magnetic data. This leads to the impression that no single geophysical model can stand as being the most geologically accurate than the other models (Saltus and Blakely, 2011). Saltus and Blakely (2011) stressed the importance of integrating a p*rior* knowledge and the implementation of different techniques to lessen the non-uniqueness of the gravity and magnetic models.

We have employed different geological and geophysical information to constrain the 2D model we produced for the Dobi graben and surroundings. (1) We used the surface geology along the model's profile, especially the exposure of the Afar basalts and

the graben sediment fill, as a first order constraint. We also used the thicknesses of these units estimated from geological observations as initial constraint for the model. (2) We used the magnetic susceptibility values from Bridges et al. (2012) as initial values in the modeling of the ground magnetic data, but we adjusted these values during the modeling process to achieve the best fit between the observed and the calculated magnetic anomalies. (3) Since there are no direct density measurement within the Dobi graben and surroundings, we used the Nafe and Drake (1957) method to determine the average density values for different units in the 2D model from the V_p values measured by the active-source seismic refraction study of Berckhemer et al. (1975) and Markis & Ginzurgm (1987) which covered the Dobi graben and surroundings (Blue line in Fig. 2). (a) the V_p value of the graben sediment fill is 3.5 km/s and this converts to a density of 2.29 gm/cm^3. (b) the V_p value of the upper crust is 6.2 km/s and this translates to a density of 2.71 gm/cm^3. (c) the V_p value of the lower crust is 6.6 km/s and this gives a density value of 2.96 gm/cm^3. (d) The V_p value of the SCLM is 7.5 gm/cm^3 and this produces and density of 3.2 gm/cm3. We compared the density values we obtained with the average density values used in previous gravity models developed for the Tendaho graben (Bridges et al., 2012; Lewi et al., 2016) and we found them to be within 10%. (4) We used results from the active-source seismic refraction studies of Berckhemer et al. (1975) and Markis & Ginzurgm (1987) (together with our results from the spectral analysis of the aeromagnetic and the satellite gravity data) to constrain the depth to the boundary between the upper crust and lower crust in the 2D model. (5) We constrained the depth to the Moho in the 2D model using results from the receiver function study from the two broadband stations found along the model profile (Station AD15 and AD18

in Fig. 2; Reed et al. (2012). As mentioned earlier, we found the Moho depth we obtained from the spectral analysis of the satellite gravity data in good agreement with that obtained by Reed et al. (2014) for station AD15 from the receiver function study.

4.5.2 The Two-dimensional Magnetic and Gravity Modeling

The 2D model we developed for the Dobi graben and surroundings, together with the observed and the calculated magnetic susceptibility and Bouguer gravity anomaly values and an idealized near-surface cross section, are shown in Figure 9. The length of the model is ~24 km and it is oriented NE-SW, approximately orthogonal to the strike direction of the normal faults within the Dobi graben (Fig. 2). The model starts at the Unda Gamarri horsts and extends northeastward into the Gumma - Kambourta graben (Fig. 2). The model consists of six elements; graben sediment fill, Afar basalts, upper crust, lower crust with and without zones where melt and mafic dikes are possibly present, and SCLM. The magnetic susceptibility and density values for these model elements are listed in Table 1. The RMSE between the observed and the calculated anomalies of the model is 2.632 nT for the ground magnetic anomalies (Fig. 9A) and 0.388 mGal for the Bouguer gravity anomalies (Fig. 9B). The graben sediment fill are found within the Dobi and the Gumma– Kambourta grabens. We modeled these sediments with two layers ranging in thickness between zero at the graben's border faults to ~0.6 km close to the center of the Dobi graben (Fig. 9D). We modeled the sediment in both grabens with uniform density value of 2.280 gm/cm^3 (Table 1). However, we assigned a lower magnetic susceptibility value (1.257E-05 SI) to the sediment filling the Gumma – Kambourta graben that those filling the Dobi graben (3.280E-03 SI) (Table 2).

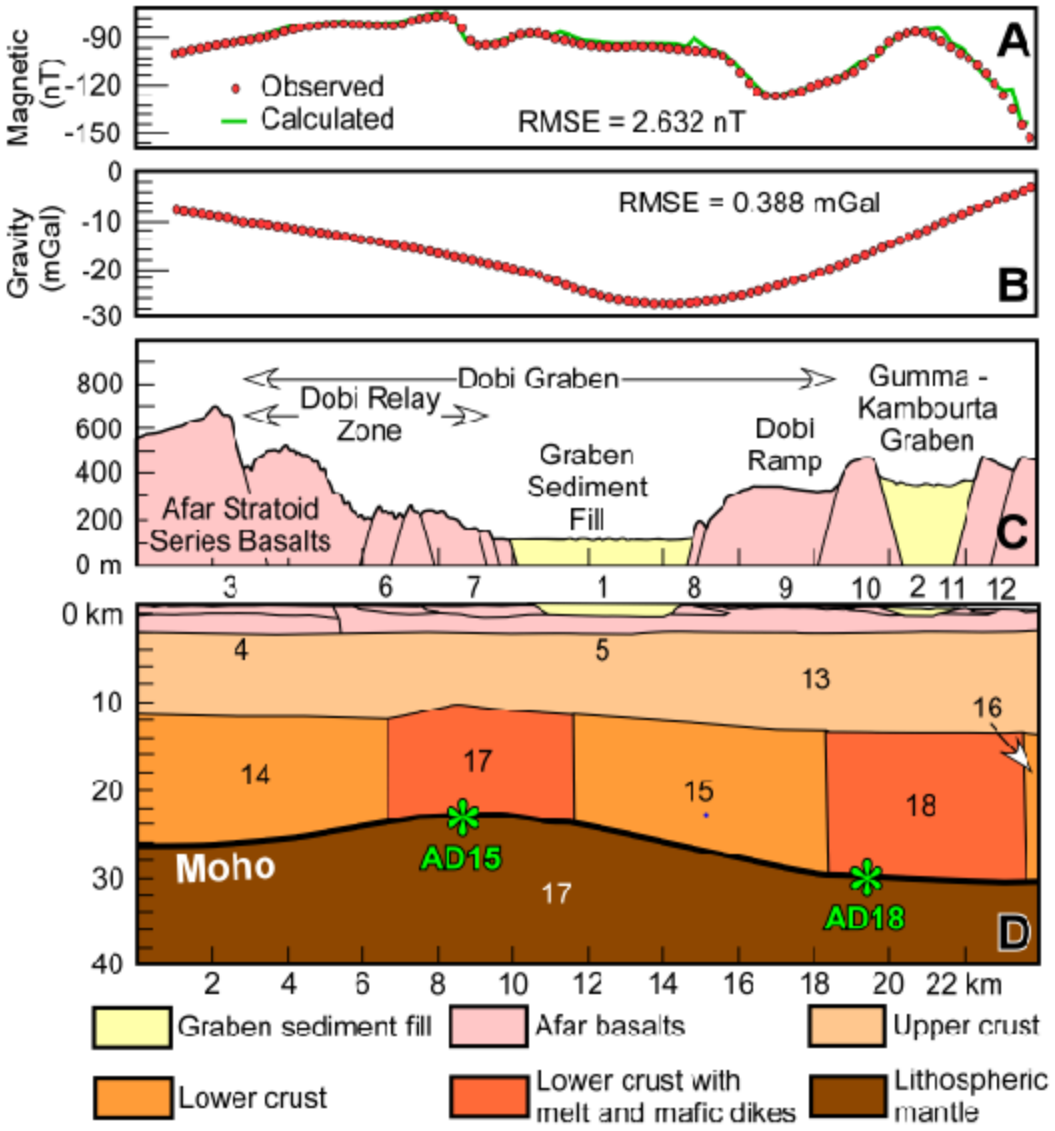

Figure 9: Two-dimensional (2D) forward magnetic and gravity model of the upper lithospheric structure beneath the Dobi and Gumma – Kambourta grabens. See Figure 2 for the location of the model. (A) Observed (from the high resolution ground magnetic data) and calculated magnetic anomalies. (B) Observed (from the satellite gravity data) and calculated Bouguer gravity anomalies. (C) Near-surface schematic cross-section along the same baseline of the 2D model. (D) Upper lithosphere cross-section interpreting the above magnetic and gravity observations. See Table 1 for the values of magnetic susceptibility and density of different polygons of the 2D model. The green stars represent the estimated Moho depth from the receiver function study of Reed et al. (2014).

Table 1: Magnetic susceptibility and density values used in for the development of the two-dimensional (2D) magnetic and gravity model shown in Figure 9.

Polygon #	**Possible unit**	**Magnetics (SI)**	Density (Kg/m^3)
1	Sediment	3.280E-03	2280
2		1.257E-05	2280
3	Stratoid Basalt	2.497E-02	2750
4		4.260E-03	2750
5		2.657E-02	2750
6		2.382E-03	2750
7		4.009E-03	2750
8		9.554E-03	2750
9		1.257E-05	2750
10		1.257E-05	2750
11		1.257E-05	2750
12		1.257E-05	2750
13	Upper Crust	1.106E-03	2700
14	Lower Crust	2.300E-03	2962
15		1.232E-03	2960
16		4.901E-03	2960
17	Melt material	1.300E-01	2820
18		1.400E-01	2830
19	SCLM	0.000E+00	3180

The magnetic susceptibility value we assigned to the sediment filling the Gumma – Kambourta graben is consistent with that expected for lacustrine, evaporate and eolian sediment. However, the magnetic susceptibility value we assigned to the sediment filling the Dobi graben is higher than what is expected for lacustrine, evaporate and eolian sediment. We attribute this to possibly the presence of higher proportion of the weathering products of the Afar basalts within the sediment filling the Dobi graben.

We modeled the Afar basalts with 10 polygons forming a sub-horizontal layer with an average thickness of ~2 km and this layer reaches a depth of ~2.5 km beneath the

Dobi graben. This is because of the down-dropping of the hanging-wall of the graben (Fig. 9C and D). We assigned a density value of 2.75 gm/cm^3 for all polygons representing the Afar basalts but we used different magnetic susceptibility values ranging between1.257E-05 SI and 2.657E-02 SI for these polygons (Table 2). This variation in magnetic susceptibility is possibly due to lithological variations, disproportional presence of lateritic horizons, degree of chemical weathering, which alters the spatial distribution of magnetic minerals (Su et al., 2015). Additionally, the variation in the magnetic susceptibility in the Afar basalts can also be due to the commonly variable content of magnetite within different basaltic flows (Beccaluya et al., 2009). Following, we give one example to highlight the possible effect of the presence of different lithologies on the variability of magnetic susceptibility values used in our model. Our 2D model adopts lower magnetic susceptibility values for polygons within the Dobi relay zone (Table 1, Fig. 9C and D). This is possibly due to the presence of trachytic lava flows within this part of the Dobi graben.

We modeled the upper crust with a uniform layer with depths ranging between ~10 km and ~12 km (Fig. 9D). This is consistent with results from our spectral analysis of the aeromagnetic and satellite gravity data (Fig. 8), results from active-source seismic refraction studies (Berckhemer et al., 1975; Makris and Ginzburg, 1987), and spectral analysis of high-resolution ground gravity data (Lewi et al., 2016). We assigned a density value of 2.70 gm/cm^3 and a magnetic susceptibility value of 1.106E-03 SI for the upper crust. The upper crust beneath the Dobi graben and surroundings could possibly represent the crystalline rocks of the Arabian-Nubian Shield topped with Mesozoic sedimentary rocks. These rock types are exposed in the Ethiopian and Somalian plateaus to the west

and south, respectively of the AD, as well as in the Danakil block in the northeastern section of the AD (Beyene and Abdelsalam, 2005).

We modeled the lower crust with 5 polygons to represent lateral variation presented by zones of melt and mafic dikes (Fig. 9D). Our 2D model adopted a depth of ~22 km for the Moho beneath the Dobi graben and a depth of ~30 km for the Moho beneath the Gumma – Kamboura graben (Fig. 9D). This is consistent with the Moho depth results from receiver function study (Reed et al., 2012; Green stars in Fig. 9D). We used a density value of ~2.96 gm/cm^{3}and magnetic susceptibility values ranging between 1.232E-03 SI and 4.901E-03 SI for the part of the lower crust, which is not modified by melt and mafic dikes (Table 2; Fig. 9D). However, in the 2D model we used lower density values (2.82 gm/cm^3 and 2.83 gm/cm^3) and higher magnetic susceptibility values (1.300E-01 SI and 1.400E-01 SI) for the zones of the lower crust where melt and mafic dikes are present (Table 2; Fig. 9D). In our 2D model, we used higher magnetic susceptibility values for these zones to account for the magnetic maxima observed over the Dobi relay zone and the Gumma–Kambourta graben (Fig. 9A and C). The location of the proposed zones where melt is present is consistent with the high V_p/V_s ratios determined by Reed et a. (2012) from receiver function study for stations AD15 and AD18 (Green stars in Fig. 9D). The higher magnetic susceptibility values within these zones imply the presence of more mafic material (such as mafic dikes) compared to the surrounding lower crust. This is presumably due to that part of the melt had solidified as dikes due to temperature and pressure changes after it risen into the lower crust. Thus, the magnetization does not have to be necessary lower because these zones are warm. This is because the magnetization of minerals does not linearly die off with temperature. Rather,

it stays the same until it reaches the Curie point temperature and then it loses its magnetization. Hence, we interpret these zones as portions of the lower crust were melt is present and have been intruded by mafic dikes.

4.5.3 Sensitivity Analysis and Model Validation

4.5.3.1 Principle and General Procedures

In order to determine the validity of our 2D model (Fig. 9D), we performed two types of sensitivity analyses. First, we considered magnetic susceptibility and density values different from those we used in the final 2D model. We performed this analysis to evaluate whether the new magnetic susceptibility and density values will increase or decrease the RMSE between the observed and the calculated anomalies. For this, we varied the magnetic susceptibility and density values between -25% (lower limit) and +25% (upper limit) of the values we used in the final 2D model using 5% increments. Second, we considered depths to the boundaries between various elements of the model different from those we used in the final 2D model and evaluated the resulting changes in the RMSE between the observed and the calculated anomalies.

4.5.3.2 Variations in Magnetic Susceptibility Values

The magnetic susceptibility values we used in the final 2D model (Fig. 9D) are listed in Table 1. The changes in these values when they are varied at an increment of 5% within -25% (lower limit) and +25% (upper limit) are listed in Appendices 1. The changes in RMSE between the observed and the calculated anomalies when the magnetic susceptibility values are varied from those used in the final 2D model are listed in

Appendices 2. The comparison between the observed and the calculated magnetic anomalies obtained when the lower and the upper limits of the magnetic susceptibility values are used for each element of the model instead of those used in the final 2D model is shown in Figure 10A-E. The plot of the RMSE for each element of the 2D model when the lower and the upper limits of the magnetic susceptibility values are used is shown in Figure 10F. Our analysis showed that our 2D model is not significantly sensitive to variation in the magnetic susceptibility values assigned to the graben sediment fill (Appendices 2, Fig. 10A and F). Varying the magnetic susceptibility values to the lower and the upper limit changes the RMSE to 2.78 nT and 1.805 nT, respectively (Appendices 2; Figure 10F). This is similar to the RMSE of 2.632 nT obtained for the final 2D model. However, we found our 2D model to be relatively sensitive to magnetic susceptibility value variations in the Afar basalts (Appendices 2, Fig. 10B and F). For example, changing the magnetic susceptibility value to the lower limit will result in increasing the RMSE from 2.632 nT to 5.684 nT (Appendices 2, Fig. 10F). Also, changing the magnetic susceptibility value to the upper limit will increase the RMSE to 6.765 nT (Appendices 2; Fig. 10F). Hence, our sensitivity analysis supports that the magnetic susceptibility values we used for the graben sediment fill and the Afar basalts in the final 2D model represent the best choice to achieve the best fit between the observed and the calculated magnetic anomalies.

Our 2D model is not sensitive to variations in the magnetic susceptibility values of the upper crust (Appendices 2, Fig. 10C and F). Changing the magnetic susceptibility values to the lower and the upper limits will change the RMSE to 2.445 nT and 2.453 nT, respectively (Appendices 2, Fig. 10F).

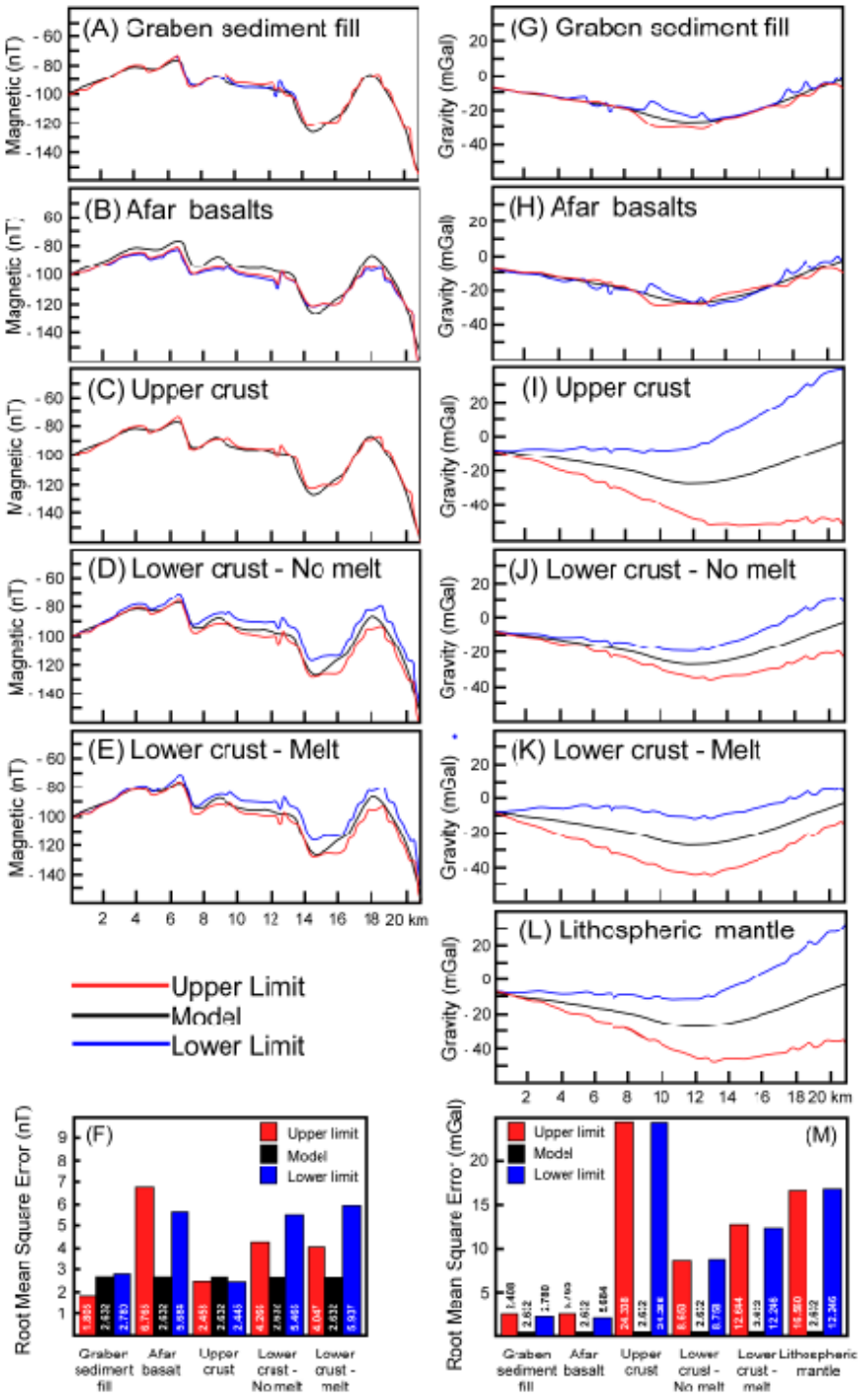

Figure 10: (A-E) Comparison between the observed and the calculated magnetic anomalies obtained when the lower (-25%) and upper (+25%) limits of the magnetic susceptibility values are used for each element of the model instead of those used in the final two-dimensional (2D) model shown in Figure 9D. (F) Plot of

the Root Mean Square Error (RMSE) between the observed and the calculated magnetic anomalies when the lower and the upper limits of the magnetic susceptibility values of each element of the 2D model are used. (G-L) Comparison between the observed and the calculated Bouguer gravity anomalies obtained when the lower and upper limits of the density values are used for each element of the model instead of those used in the final 2D model. (M) Plot of the RMSE between the observed and the calculated Bouguer gravity anomalies when the lower and the upper limits of the density values of each element of the 2D model are used. See Appendices 1-4 for the magnetic susceptibility and density values used and the accompanying the RMSE.

These RMSE values are not significantly different from the RMSE of 2.632 nT of the final 2D model. However, we found our model to be sensitive to variation in the magnetic susceptibility values in the lower crust including the regions that we modeled as containing melt and mafic dikes (Appendices 2, Fig. 10D-F). For example, varying the magnetic susceptibility values of the polygons representing the lower crust where there is no melt or mafic dikes to the lower and upper limits will increase the RMSE to 5.466 and 4.266, respectively (Appendices 2; Fig. 10F). Also, changing the magnetic susceptibility values of the polygons representing the lower crust where melt and mafic dikes are present will increase the RMSE to 5.937 and 4.047, respectively (Appendices 2; Fig. 10F). Hence, our sensitivity analysis support that the magnetic susceptibility values we used in the final model for the upper and the lower crust including regions where there is melt and mafic dikes represent the best choice to achieve the best fit between the observed and the calculated magnetic anomalies.

4.5.3.3 Variations in Density Values

The density values we used in the final 2D model (Fig. 9D) are listed in Table 1. The changes in these values when they are varied at an increment of 5% within -25% (lower limit) and +25% (upper limit) are listed in Appendices 3. The changes in RMSE between the observed and the calculated anomalies when the density values are varied from those used in the final 2D model are listed in Appendices 4. The comparison between the observed and the calculated Bouguer gravity anomalies obtained when the lower and the upper limits of the density values are used for each element of the 2D model instead of those used in the final model is shown in Figure 10G-L. The plot of the RMSE for each element of the 2D model when the lower and the upper limits of the density values are used is shown in Figure 10M.

Our 2D model is slightly sensitive to density variation in the polygons representing the graben sediment fill and the Afar basalts (Appendices 4, Fig. 10G, H and M). Varying the density values of the graben sediment fill to the lower (-25%) and the upper (+25%) limits of the density value used in the final 2D model result in increasing the RMSE to 2.149 mGal and 1.805 mGal, respectively (Appendices 4; Fig. 10M). Varying the density values of the Afar basalts to the lower and the upper limits of the density values used in the final 2D model will increase the RMSE to 1.984 mGal and 2.408 mGal (Appendices 4; Fig. 10M). These changes represent slight increase in the RMSE from the value of 0.388 mGal obtained in the final 2D model.

Our 2D model is highly sensitive to density variation in the upper crust, lower crust (especially in the zones modeled with melt and mafic dikes) and the SCLM (Appendices 4; Fig. 10I-M). Changing the density values to the lower limit for the upper crust will

increase the RMSE to 24.265 mGal (Appendices 4; Fig. 10M). Similar density value changes for the lower crust with and without melt and mafic dikes will increase the RMSE to 8.758 mGal and 12.246 mGal, respectively (Appendices 4; Fig. 10M). Increasing the density value to the upper limit for the upper crust will increase the RMSE to 24.338 mGal (Appendices 4; Fig. 10M). Increasing the density value to the upper limit for the lower crust with and without melt and mafic dikes will increase the RMSE to 8.653 mGal and 12.644 mGal, respectively (Appendices 4; Fig. 10M). Finally, increasing the density value to the upper limit for the SCLM will result in increasing the RMSE to 16.560 mGal (Appendices 4; Fig. 10M). Hence, our sensitivity analysis supports that the density values we used for the upper crust, lower crust without and with melt and mafic dikes, and SCLM in the final 2D model represent the best choice to achieve the best fit between the observed and the calculated Bouguer gravity anomalies.

4.5.3.4 Changes in the Depth of Boundaries

In our final 2D model, the depth to the boundary between the upper and the lower crust and the depth to the Moho are well constrained from active-source seismic refraction and receiver function studies (Berckhemer et al., 1975; Makris and Ginzburg, 1987; Reed et al., 2014). These boundaries are further constrained by our spectral analysis of the aeromagnetic and the satellite gravity data.

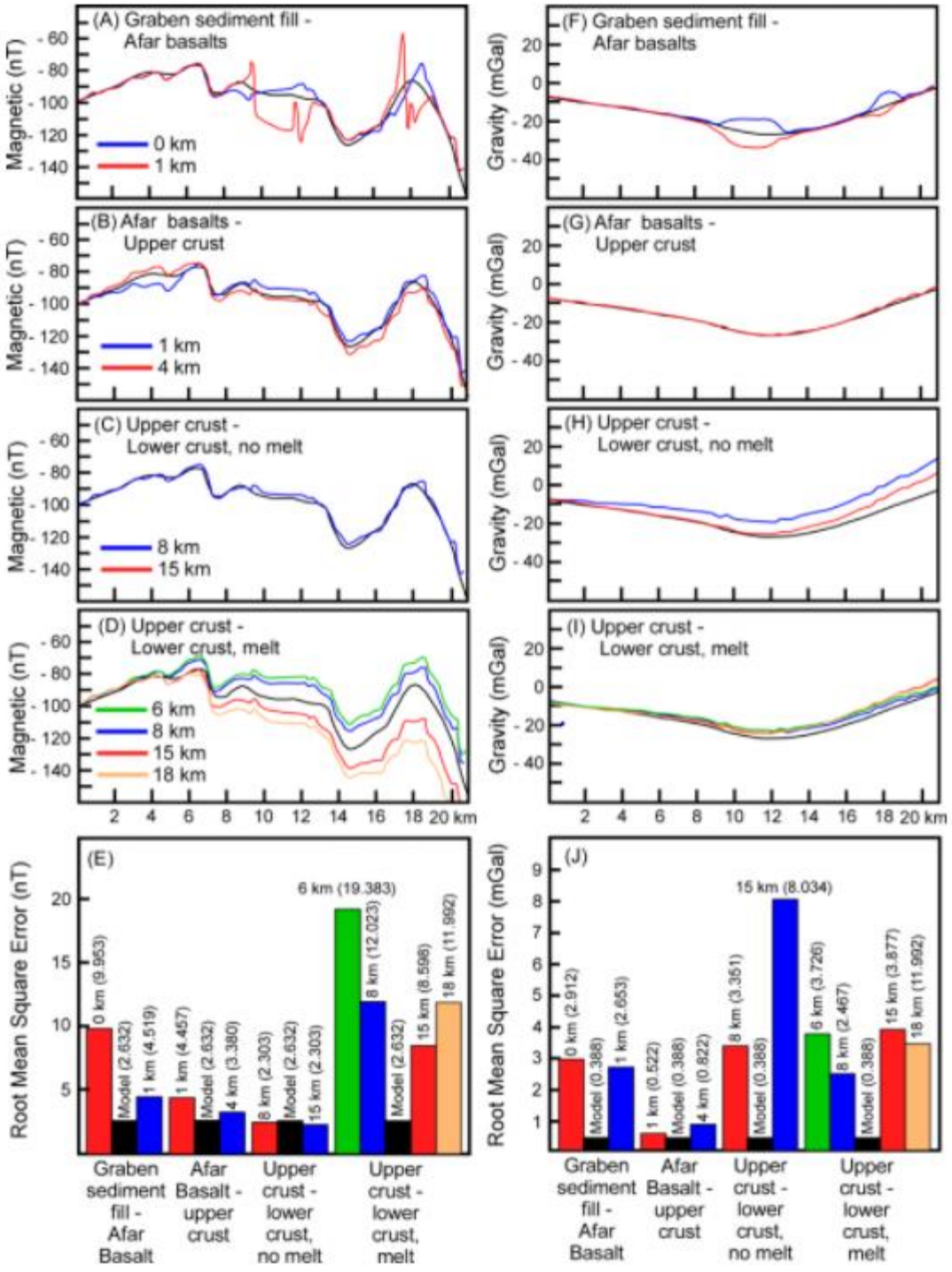

Figure 11: (A-D) Comparison between the observed and the calculated magnetic anomalies when the depths to different boundaries between various elements of the two-dimensional (2D) model shown in Figure 9D are varied. (E) Plot of the Root Mean Square Error (RMSE) between the observed and the

calculated magnetic susceptibility values when the depths to different boundaries between various elements of the 2D model are varied. (F-I) Comparison between the observed and the calculated Bouguer gravity anomalies when the depths to different boundaries between various elements of the 2D model shown in Figure 9D are varied. (J) Plot of the RMSE between the observed and the calculated Bouguer gravity values when the depths to the boundaries between various elements of the 2D model are varied. See Appendices 5 for depths used and the accompanying RMSE.

The changes in the calculated magnetic anomalies following varying the depth of these boundaries are shown in Figure 11A-D. The changes in the RMSE between the observed and the calculated magnetic susceptibility values following varying the depth of these boundaries are listed in Appendices 5 and illustrated in Figure 11E. The changes in the calculated Bouguer gravity anomalies following varying the depth of these boundaries are shown in Figure 11F-I. The changes in the RMSE between the observed and the calculated Bouguer gravity anomalies following varying the depth of these boundaries are listed in Appendices 5 and illustrated in Figure 11J.

Our 2D model proposes that the graben sediment fill is within the Dobi and Gumma – Kambouta grabens (Fig. 9D). The thickness of these sediment increases for zero at the graben's border faults to a maximum thickness of 0.6 km close to the center of the Dobi graben. Adopting a uniform sediment thickness of 0.2 km for the entire Dobi and Gumma-Kambourta grabens (fixing the boundary between the graben sediment fill and the Afar basalts at zero km level) will result in increasing the RMSE between the observed and the calculated magnetic anomalies to 9.953 nT and between the observed and the calculated Bouguer gravity anomalies to 2.912 mGal (Appendices 5; Fig. 11A, E,

F and J). Increasing the thickness of the graben sediment fill to 1 km will increase the RMSE to 4.519 nT and 2.653 mGal (Appendices 5; Fig. 11A, E, F and J).

Our 2D model shows the boundary between the Afar basalts and the upper crust to be at ~2 km and this boundary becomes slightly deeper (~2.5 km) beneath the Dobi graben because of the down dropping of the hanging-wall of the graben (Fig. 9D). Changing this boundary to a uniform depth of 1 km will result in slight increase in the RMSE between the observed and calculated magnetic anomalies from 2.632 nT to 4.457 nT (Appendices 5; Fig. 11B and E). However, this change will result in an insignificant increase (from 0.388 mGal to 0.522 mGal) in the RMSE between the observed and the calculated Bouguer gravity anomalies (Appendices 5; Fig. 11G and J). Also, changing the depth of this boundary to 4 km will cause the RMSE to increase to 3.38 nT and 0.822 mGal (Appendices 5; Fig. 11B, G, E and J).

Our 2D model shows the boundary between the upper and lower crust to be at depth between ~10 km and ~12 km. We found that the variation in the depth of this boundary (away from regions in the lower crust that we modelled as containing melt and mafic dikes) doesn't cause significant changes in the RMSE between the observed and the calculated magnetic anomalies. For example, shallowing the depth of this boundary to 8 km or deepening it to 15 km will result in changing the RMSE to 2.480 nT and 2.303 nT, respectively (Appendices 5; Fig. 11C and E). This is slightly different from the RMSE of 2.632 nT in our final 2D model (Fig. 11E). In contrast, we found that changing the depth of the boundary between the upper and lower crust (away from the regions in the lower crust that we modelled as containing melt and mafic dikes) will result in significant increase in the RMSE between the observed and calculated Bouguer gravity

anomalies. Changing the depth of this boundary to 8 km and 15 km will result in increasing the RMSE to 3.351 mGal and 8.034 mGal, respectively (Appendices 5; Fig. 11H and J).

Our sensitivity analysis found that the calculated magnetic anomalies are much more sensitive than the calculated Bouguer gravity anomalies to variation of the depth to the lower crust where melt and mafic dikes are present (Appendices 5; Fig. 11D, E, I and J). Using shallower depth (6 km and 8 km) for this boundary (which implies the presence of melt and mafic dikes in the upper crust) results in increasing the RMSE between the observed and the calculated magnetic anomalies to 19.383 nT and 12.023 nT, respectively (Appendices 5; Fig. 11D and E). Considering deeper depth (15 km and 18 km) will result in increasing the RMSE to 8.598 nT and 11.992 nT, respectively (Appendices 5; Fig. 11D and E). Changing the depth of this boundary to 6 km, 8 km, 15 km and 18 km will result in changing the RMSE between the observed and the calculated Bouguer gravity anomalies to 3.726 mGal, 2.467 mGal, 3.877 mGal, and 3.408 mGal, respectively (Appendices 5; Fig. 11I and J). Therefore, our sensitivity analysis results indicate that the presence of melt and mafic dikes is more likely to be restricted to the lower crust (Fig. 9D).

4.6 Discussion

4.6.1 Presence of Melt in the Lower Crust

Our 2D model proposes the existence of two zones in the lower crust with melt and mafic dikes. These zones are beneath the Dobi relay zone and the Gumma – Kambourta graben (Fig. 9D). Although the Dobi graben is associated with a Bouguer

gravity minimum (Fig. 9B), the magnetic data indicate two regions of magnetic maxima (Fig. 9A). Our 2D model shows the regions withmelt and mafic dikes in the lower crust to have relatively lower density values (2.83 gm/cm^3) compared to the surrounding lower crust. However, Our 2D model shows this region melt and mafic dikes with significantly higher magnetic susceptibility values (0.13 SI and 0.14 SI (Table 1).

The presence of melt has been previously suggested by the high V_p/V_s ratios as determined by receiver function studies (Reed et al., 2014). Reed et al. (2014) determined that the V_p/V_s ratio for station AD15 (which falls within our suggested zone of melt and mafic dikes beneath the Dobi relay zone; Fig. 9C and D) to be ~2.01 and this value corresponds to the presence of ~9% melt. In addition, Reed et al. (2014) determined that the V_p/V_s ratio for station AD18 (which falls within our suggested zone of melt and mafic dikes beneath the Gumma – Kambourta graben; Fig. 9C and D) to be ~1.89 and this value corresponds to the presence of ~5.1% melt.

The existence of such zones of melt within the lower crust is consistent with observations from other segments of the EARS. Stuart et al. (2006) determined V_p/V_s ratios greater than 2.0 for the northern Main Ethiopian Rift and suggested that such high values is because of the presence of melt. Tiberi et al. (2005) inverted regional gravity data to suggest the existence of a magmatically under-plated lower crust beneath the Ethiopian plateau and portions of the Main Ethiopian Rift and further suggested that this material might be the source of some of the melt within the EARS crust.

Bridges et al. (2012) concluded that there is a region where melt is present beneath the Tendaho graben, which is located southwest of the Dobi graben (Fig. 1B). Also, Lewi et al. (2016) suggested the presence of melt in the lower crust beneath the

center of the Tendaho graben. The presence of melt in the crust beneath the Tendaho graben is not unexpected because it is much wider and it contains hot springs and witnessed recent magmatic activities. The existence of zones of melt within the lower crust beneath the Dobi and Gumma – Kambourta grabens where these regions do not have known recent magmatism suggests the possibility of volcanic activity in the future.

4.6.2 Crustal Thickness

Previous receiver function studies have proposed the presence of a thinned crust beneath the AD in association with the ascendance of a mantle plume. Our spectral analysis of the aeromagnetic and satellite gravity data found magnetic and density boundaries at depths of 22.9 and 22.5 km, respectively (Fig. 8A and B). We interpreted the depth of 22.5 km from the spectral analysis of the satellite gravity data to represent the Moho beneath the Dobi graben (Figs. 8A and B). This depth is in agreement with results from receiver function studies of one station within the Dobi graben where the Moho depth is found to be ~23 km (Reed et al., 2014; Station AD15 in Fig. 2). Reed et al. (2014) also found a Moho depth of ~30 km beneath station AD18 that is located on the southwestern escarpment of the Gumma – Kambourta graben. This depth agrees with the depths determined by our 2D model (Fig. 9D).

4.6.3 Possible Crustal Evolution and its Tectonic Implications

Jacques et al. (2011) attributed the crustal stretching in the Dobi graben to faulting and block tilting in the upper crust that accompany elastic stress release. The 1989 swarm of intermediate magnitude ($5.7 < Ms < 6.3$) earthquakes indicates that this mechanical

stretching persists to the ~15 km seismogenic zone depth (Jacques et al., 2011). Noir et al. (1997) analyzed the 1989 earthquakes sequence near the Dobi graben to show that the earthquakes occurred from buildup of tensile stress and explained the origin of the sequence in terms of changes in the Coulomb stresses due to the diffusion of fluids. Assistance of movement along these faults through high fluid pressure to overcome frictional drag is further supported by our observations that, in many places, travertine deposits are found along these faults.

Our 2D model shows that the crust beneath the graben is thinner and that the lower crust hosts zones of melt and mafic dikes. This suggests that crustal stretching within the Dobi graben beneath the seismogenic zone depth (~15 km) is accommodated in a ductile manner. Hence, it can be suggested that crustal stretching in the Dobi graben beneath the seismogenic zone depth is assisted by the presence of melt as well as by intrusion of mafic dikes.

The concept of magma-assisted rifting was introduced by Ebinger and Casey (2001) to explain the observed transfer of extension from the border faults of the Main Ethiopian Rift to the rift floor. Such magma-assisted rifting is currently taking place in the central part of the Red Sea rift within the AD as evidenced by the Dabbahu diking event (Wright et al., 2016). Our proposition for the evolution of the Dobi graben that involves decoupling of the extension across the seismogenic zone depth of ~15 km that separates mechanical stretching above it and ductile flow below it (assisted by melt and intrusion of mafic dikes), is in good agreement with the magma-assisted rifting model.

4.7 Conclusions

Results from our analysis using high-resolution ground magnetic data across the Dobi graben and surroundings aided by aeromagnetic and satellite gravity data suggest the presence of narrow (~5 km wide) zones of melt and mafic dikes within the lower crust centered beneath the Dobi relay zone and the Gumma – Kambourta graben. Our results also suggest the presence of thinner crust (~22 km) beneath the Dobi graben as well as a boundary between the upper and lower crust at ~10 km to ~12 km. This boundary is within the ~15 km depth to the seismogenic zone that was estimated from earthquake events within the Dobi graben. We propose a model that advocates for decoupling of extension beneath the Dobi graben in which the crust above the seismogenic zone is extending by mechanical stretching whereas the crust below the seismogenic zone is extending by ductile flow aided by the presence of melt and intrusion of mafic dikes. This is in good agreement with the magma-assisted model proposed for different segments of the EARS and is currently observed in the central part of the Red Sea rift within the AD.

4.8 Acknowledgments

The acquisition of the ground magnetic data was supported by Statoil award number 4501505097l. We thank colleagues from Oklahoma State University and Addis Ababa University for providing insight and expertise that greatly assisted this research and for comments that greatly improved the manuscript. We thank Dr. John Armitage of the Institute de Physique du Globe de Paris and an anonymous reviewer for detailed and constructive reviews. We thank Dr. Damien Delvaux for editorial handling of the

manuscript. This is Oklahoma State University Boone Pickens School of Geology contribution # 2018-xx.

4.9 References

Abbate, E., Passerini, P., Zan, L., 1995. Strike-slip faults in a rift area: A transect in the Afar Triangle, East Africa. Tectonophysics 241, 67-97, doi:10.1016/0040-1951(94)00136-W.

Acton, G.D., Tessema, A., Jackson, M., Bilham, R., 2000. The tectonic and geomagnetic significance of paleomagnetic observations from volcanic rocks from central Afar, Africa. Earth and Planetary Science Letters 180, 225–241, https://doi.org/10.1016/S0012-821X(00)00173-4.

Askari, A., 2014. Edge detection of gravity anomaly sources via the tilt angle, total horizontal

derivative, total horizontal derivative of the tilt angle and new normalized total horizontal derivative. Scholas Journal Of Engineering and Technology 2(6B), 842-846.

Ayalew, D., Ebinger, C., Bourdon, E., Wolfenden, E., Yirgu, G., Grassineau, N., 2006. Temporal compositional variation of syn-rift rhyolites along the western margin of the southern Red Sea and northern Main Ethiopian rift. In: The Afar Volcanic Province within the East African Rift System, edited by, Yirgu, G., Ebinger, C. Maguire, P. K. H. Geological Society, London 259, 121–130, http://doi.org/10.1144/GSL.SP.2006.259.01.10.

Balmino, G., N. Vales, S. Bonvalot, and A. Briais., 2011. Spherical harmonic modelling to ultra-high degree of Bouguer and isostatic anomalies, Journal of Geodesy 86, 499-520, doi:10.1007/s00190-011-0533-4.

Barberi, F. and Varet, J., 1977. Volcanism of Afar: smallscale plate tectonics implications. Geological Society of America Bulletin 88, 1251–1266, http://doi.org/10.1130/0016-7606

Bastow, I.D., Nyblade, A.A., Stuart, G.W., Rooney, T.O., Benoit, M.H., 2008. Rifting at the edge of the African low velocity anomaly. Geochemistry Geophysics Geosystems, 9, 12022, doi:10.1029/2008GC002107.

Beccaluva, L., Bianchini, G., Natali, C., Siena, F. 2009. Continental flood basalts and mantle plume: a case study of the northern Ethiopian Plateau. Journal of Petrology, 50, 1377-1403.

Benoit, M.H., Nyblade, A.A., VanDecar, J.C., 2006. Upper mantle P-wave speed variations beneath Ethiopia and the origin of the Afar hotspot. Geology, 34, 329–332, doi:10.1130/G22281.1.

Berckhemer, H., Baier, B., Harteisen, H., Behle, A., Burkhardt, H., Gebrande, H., Makris, J., Menzel, H., Miller, H., Vees, R. 1975. Deep seismic soundings in the Afar region and on the highland of Ethiopia. In: Pilger, A. & Ro¨sler, A. (eds) Afar Depression of Ethiopia, Vol. I. Schweizerbart, Stuttgart, 89–107.

Beyene, A., Abdelsalam, M. G., 2005. Tectonics of the Afar Depression: A review and synthesis. Journal of African Earth Sciences 41, p. 41-59, doi.org/10.1016/j.jafrearsci.2005.03.003.

Bilham, R., Bendick, R., Larson, K., Mohr, P., Braun, J., Tesfaye, S., Asfaw, L., 1999. Secular and tidal strain across the Main Ethiopian Rift, Geophys. Res. Lett., 26, 2789–2792.

Blakely, R.J., Simpson, R.W., 1986. Approximating edges of source bodies from magnetic
or gravity anomalies. Geophysics 51, 1494–1498, https://doi.org/10.1190/1.1442197.

Bridges, D. L., Mickus, K., Gao, S. S., Abdelsalam, M. G., Alemu, A., 2012. Magnetic stripes of
a transitional continental rift in Afar. Geology 40, 203–206, http://doi.org/10.1130/G32697.1.

Buck, W., 2004. Consequences of asthenospheric variability on continental rifting, in Rheology and Deformation of the Lithosphere at Continental Margins, edited by G. Karner et al., pp. 1–30, Columbia Univ. Press, New York.

Buck, W., 2006. The role of magma in the development of the Afro-Arabian Rift System, in The Structure and Evolution of the East African Rift System in the Afar Volcanic Province, edited by G. Yirgu, C. J. Ebinger, and P. K. H. Maguire, Geological Society London Special Publication, 259, 43–54.

Chiozzi, P., Matsushima, J., Okubo, Y., Pasquale, V., Verdoya, M., 2005. Curie point depth from sprectral snalysis of magnetic data in central-southern Europe. Physics of the Earth and Planetary Interiors 152, 267-276.

Cooper, G., Cowan, D., 2004. Filtering using variable order vertical derivatives. Computers and Geosciences 30, 455–459, doi.org/10.1016/j.cageo.2004.03.001.

Cordell, L., 1979. Gravimetric expression of graben faulting in Santa Fe country and the Espanola Basin, New Mexico. New Mexico Geol. Soc. Guidebook, 30th Field Conf, pp. 59–64.

Courtillot, V., Galdeano, A., Mouel, J.L.L., 1980. Propagation of an accreting plate boundary: A discussion of new aeromagnetic data in the Gulf of Tadjurah and southern Afar. Earth and Planetary Science Letters 47, 144–160, doi.org/10.1016/0012-821X(80)90113-2.

Daniels, K., Bastow, I.D., Keir, D., Sparks, R.S.J., Menand, T., 2013. Thermal models of dyke intrusion during development of continent–ocean transition. Earth and Planetary Science Letters 385 145-153, doi: 10.1016/j.epsl.2013.09.018.

Daly, E., Keir, D., Ebinger, C., Stuart, G., Bastow, I., Ayele, A., 2008. Crustal tomographic imaging of a transitional continental rift: the Ethiopian Rift, Geophysical Journal International, 172(3),1033–1048, doi:10.1111/j.1365-246X.2007.03682.x.

Dorman, L., Lewis, B., 1970. Experimental isostasy, 1, Theory of the determination of the Earth's isostatic response to a concentrated load. Journal of Geophysical Research, 75, 3357–3365. doi: 10.1029/JB075i017p03357.

Dugda, M., Nyblade, A., Julia, J., Langston, C., Ammon, C. ,Simiyu, S., 2005. Crustal structure in Ethiopia and Kenya from receiver function analysis. Journal of Geophysical Research 110, doi.org/10.1029/2004JB003065

Dugda, M., Nyblade, A., 2006. New constraints on crustal structure in eastern Afar from the analysis of receiver functions and surface wave dispersion in Djibouti. The

Geological Society of London 259, 239-251, doi.org/10.1144/GSL.SP.2006.259.01.19.

Ebinger, C. J., Casey, M., 2001. Continental breakup in magmatic provinces: an Ethiopian example. Geology 29, 527–530, doi: 10.1130/0091-7613(2001)029[0527:CBIMPA]2.0.CO;2.

Haggerty, S., 1978. Mineralogical constraints on Curie isotherms in deep crustal magnetic anomalies. Geophysical Research Letters 5, 105-108.

Hammond, J. O. S., Kendall, J. M., Stuart, G. W., Keir, D., Ebinger, C., Ayele, A. & Belachew, M., 2011. The nature of the crust beneath the Afar triple junction: evidence from receiver functions. Geochemistry, Geophysics, Geosystems 12, 1525–2027.

Hayward, N. J., Ebinger, C. J., 1996. Variations in the along-axis segmentation of the Afar Rift system. Tectonics 15, 244-257, doi: 10.1029/95TC02292.

Hofstetter, R., Beyth, M., 2003. The Afar Depression: Interpretation of the 1960-2000 earthquakes. Geophysical Journal International 155, 715-732, doi: 10.1046/j.1365-246X.2003.02080.x.

Jacobsen, 1987. A case for upward continuation as a standard separation filter for potential-field maps. Geophysics 52, 1138 – 1148, doi:10.1190/1.1442378.

Jacques, E., Kidane, T., Tapponnier, P., Manighetti, I., Gaudemer, Y., Meyer, B., Ruegg, J. C., Audin, L., Armijo, R., 2011. Normal Faulting during the August 1989 Earthquakes in Central Afar: Sequential Triggering and Propagation of Rupture

along the Dobi Graben. Bulletin of the Seismological Society of America 101(3), 994-1023, doi: 10.1785/120080317.

Jakovlev, A., Rümpker, G., Schmeling, H., Koulakov, I., Lindenfeld, M., Wallner, H., 2013. Seismic images of magmatic rifting beneath the western branch of the East African rift. Geochemistry, Geophysics, Geosystems 14, 4906-4920, doi:10.1002/2013GC004939.

Karner, G., Watts, A., 1983. Gravity anomalies and flexure of the lithosphere at mountain ranges. Journal of Geophysical Research 88, 10,449-10,477.

Keir, D., Pagli, C., Bastow, I. D.,Ayele, A., 2011. The magma-assisted removal of Arabia in Afar: evidence from dike injection in the Ethiopian rift captured using InSAR and seismicity. Tectonics 30, TC2008, doi: 10.1029/2010TC002785.

Kendall, J. M., Pilidou, S., Keir, D., Bastow, I., Stuart, G., Ayele, A., 2006. Mantle upwellings, melt migration and the rifting of Africa: Insights from seismic anisotropy, in The Structure and Evolution of the East African Rift System in the Afar Volcanic Province, edited by Yirgu, G., Ebinger, C., and Maguire, P.K.H., Geological Society of London Special Publication 259, 271–293.

Kendall, J.M., Stuart, G.W., Ebinger, C., Bastow, I.D., Keir, D., 2005. Magma-assisted rifting in Ethiopia. Nature 433, 146-148, doi: 10.1038/nature03161.

Keranen, K., Klemperer, S., Gloaguen, R., EAGLE Working Group, 2004. Three-dimensional seismic imaging of a protoridge axis in the main Ethiopian rift. Geology 32, 949–952, doi: 10.1130/G20737.1.

Kidane, T., Courtillot, V., Manighetti, I., Audin, L., Lahitte, P., Quidelleur, X., Gillot, P.Y., Gallet, Y., Carlut, J., and Haile, T., 2003. New paleomagnetic and

geochronologic results from Ethiopian Afar: Block rotations linked to rift overlap and propagation and determination of a ~2 Ma reference pole for stable Africa. Journal of Geophysical Research 108, (B2), 2102, doi: 10.1029/2001JB000645.

Kogan, L., Fisseha, S., Bendick, R., Reilinger, R., McClusky, S., King, R., Solomon, T., 2012. Lithospheric strength and strain localization in continental extension from observations of the East African Rift. Journal of Geophysical Research, 117, B03402, doi: 10.1029/2011JB008516, 2012.

Lewi. E., Keir, D., Birhanu, Y., Blundy, J., Stuart, G., Wright, T, Calais, E., 2016. Use of a high-precision gravity survey to understand the formation of oceanic crust and the role of melt at the southern Red Sea rift in Afar, Ethiopia, in Magma-dominated rifting in the Afar triple junction, edited by Wright T., Ayele A., Ferguson, J., Kidane, T., Vye-Brown, C., Geological Society of London, Special Publications 420, 165-180, https://doi.org/10.1144/SP420.13.

Mackenzie, G., Thybo, H., Maguire, P., 2005. Crustal velocity structure across the Main Ethiopian Rift: Results from 2-dimensional wide-angle seismic modelling, Geophysical Journal International, 162, 994–1006, doi:10.1111/j.1365-246X.2005.02710.x.

Makris, J. and Ginzburg, A., 1987. The Afar depression: transition between continental rifting and sea-floor spreading. Tectonophysics 141, 199–214, https://doi.org/10.1016/0040-1951(87)90186-7.

Mammo, T., 2004. Mapping the crust-mantle boundary beneath the Afar Depression. Gondwana Research 7, 855-861, doi: 10.1016/S1342-937X(05)71069-8.

Manighetti, I., Tapponier, P., Courtillot, V., Gallet, Y., Jacques, E., Gillot, P.Y., 2001. Strain transfer between disconnected, propagating rifts in Afar. Journal of Geophysical Research 106, 13613-13665, doi: 10.1029/2000JB900454.

Marson, I., Klingele, E., 1993. Advantages of using the vertical gradient of gravity for 3-D interpretation. Geophysics 58, 1588–1595, https://doi.org/10.1190/1.1443374.

McKenzie, D. P., Davies, D., Molnar, P., 1970. Plate tectonics of the Red Sea and East Africa. Nature 226, 243–248, doi: 10.1038/226243a0.

Nafe, J. E., Drake, C. L. 1957. Variation with depth in shallow and deep water marine sediments of porosity, density and the velocities of compressional and shear waves. Geophysics 22, 523–552.

Reed, C. A., Almadani, S., Gao, S., Elsheikh, A.A. , Cherir, S. , Abdelsalam, M.G., Thurmond, A.K., Liu, K.H., 2014. Receiver function constraints on crustal seismic velocities and partial melting beneath the Red Sea rift and adjacent regions, Afar Depression. Journal of Geophysics. Research 119, 2138-2152, Doi:10.1002/2013JB010719.

Rooney, T., T. Furman, G. Yirgu;D. Ayalew, 2005. Structure of the Ethiopian lithosphere: Xenolith evidence in the Main Ethiopian Rift, Geochem. Cosmochim. Acta 69, 3889–3910, doi:10.1016/j.gca.2005.03.043.

Rooney, T. O., Herzberg, C., Bastow, I. D., 2012. Elevated mantle temperature beneath East Africa, Geology, 40(1), 27–30.

Rooney, T. O., Mohr, P., Dosso, L., Hall, C., 2013. Geochemical evidence of mantle reservoir evolution during progressive rifting along the western Afar margin, Geochim. Cosmochim. Acta, 102, 65–88, doi:10.1016/j.gca.2012.08.019.

Rooney, T., Lavigne, A., Svoboda, C., Girard, G., Yirgu, G., Dereje Ayalew, D., John Kappelman, J., 2016. The making of an underplate: Pyroxenites from the Ethiopian lithosphere. Chemical Geology, doi:10.1016/j.chemgeo.2016.09.011.

Ruegg, J. C., 1975. Main results about the crustal and upper mantle structure of the Djibouti region (T.F.A.I), in Pilger., A., and Rösler, A., eds., Afar depression of Ethiopia: Stuttgart, E. Schweizerbart'sche Verlagsbuchhandlung, p. 120-134.

Salem, A., Williams, S., Fairhead, J.D., Ravat, D., Smith, R., 2007. Tilt-depth method: A simple depth estimation method using first-order magnetic derivatives. The Leading Edge 26, 1502-1505, https://doi.org/10.1190/1.2821934.

Salem, A., Green, C., Ravat, D., Singh, K., East, P., Fairhead, D., Mogren, S., and Biegert, E., 2014. Depth to Curie temperature across the central Red Sea from magnetic data using the de-fractal method. Tectonophysics 624-625, 75-86.

Saltus, R., and Blakely, R., 2011. Unique geologic insights from "non-unique" gravity and magnetic interpretation. GSA Today, v. 21, no. 12, doi: 10.1130/G136A.1.

Sigmundsson, F., 1992. Tectonic implication of the 1989 Afar earthquake sequence, Geophysical Research Letter 19, 877-880, doi:10.1029/92GL00686.

Stab, M., Bellahsen, N., Pik, R., Quidelleur, X., Ayalew, D., Leroy, S., 2016. Modes of rifting in magma-rich settings: tectono-magmatic evolution of Central Afar. Tectonics, 35(1), 2-38, doi:10.1002/2015TC003893.

Su, N., Yang, S., Wang, X., Bi, L., Yang, C., 2015. Magnetic parameters indicate the intensity of chemical weathering developed on igneous rocks in China. Catena, 133, 328–341, doi.org/10.1016/j.catena.2015.06.003

Tanaka, A., Okubo, Y., Matsubayashi, O., 1999. CPD based on spectrum analysis of the magnetic anomaly data in East and Southeast Asia. Tectonophysics 306, 461–470, doi:10.1016/s0040-1951(99)00072-4.

Tapponnier, P., Armijo, R., Manighetti, I., Courtillot, V., 1990. Bookshelf faulting and horizontal block rotations between overlapping rifts in Southern Afar: Geophysical Research Letters 17, 1-4, doi: 10.1029/GL017i001p00001.

Tesfaye, S., 2005. Fault population investigation and estimating magnitude of extension in Guma Graben, Central Afar, Ethiopia. Journal of African Earth Sciences 41,437–444, https://doi.org/10.1016/j.jafrearsci.2005.05.002.

Tiberi, C., Ebinger, C., Ballu, V., Stuart, G., Oluma, B., 2005. Inverse models of gravity data from the Red Sea–Aden–East African rifts triple junction zone. Geophysical Journal International 163, 775–787.

Trifonova, P., Zhelev, Z., Petrova, T., Bojadgieva, K., 2009. Curie depth points of Bulgarian territory inferred from geomagnetic observations and its correlation with regional thermal structure. Tectonophysics 473, 362-374.

Tselentis, G., Drakopoulos, J., Dimitriadias, K., 1988. A spectral approach to Moho depths estimation from gravity measurements in Epirus (NW Greece). Journal of Physics of the Earth 36, 255–266, http://doi.org/10.4294/jpe1952.36.255.

Varet, J., 1978. Geology of Central and Southern Afar (Ethiopia and Djibouti Republic) F. Gasse for Chapter IV on Sedimentary Formation. Eds. CNRS, France, Paris, p. 118.

Wölbern, I., Rümpker, G., Link, K., Sodoudi, F., 2012. Melt infiltration of the lower lithosphere beneath the Tanzania craton and the Albertine rift inferred from S

receiver functions. Geochemistry, Geophysics, Geosystems 13, doi: 10.1029/2012GC004167.

Wolfenden, E., Ebinger, C., Yirgu, G., Renne, P. R., Kelley, S. P., 2005. Evolution of a volcanic rifted margin: southern Red Sea, Ethiopia. Geological Society of America Bulletin 117, 846-864.

Wright, T., Ebinger, C., Biggs, J., Ayele, A., Yirgu, G., Keir, D., Stork, A., 2006. Magma-maintained rift segmentation at continental rupture in the 2005. Afar diking episode. Nature 442, 291-294, doi: 10.1038/nature04978.

Zeng, H., Xu, D., Tan, H., 2007. A model study for estimating optimum upward-continuation height for gravity separation with application to a Bouguer gravity anomaly over a mineral deposit, Jilin province, northeast China. Geophysics 72, I45–I50, doi: 10.1190/1.2719497.

APPENDICES

PAPER I

Appendices **1**

The total deviation of the scattered values from the trend that defined the size distribution analyses has been statistically identified. The statistical deviations could be measured as the summed square of residuals and is usually labeled as SSE.

$$SSE = \sum_{i=1}^{n} w_i(y_i - \hat{y}_i)^2 \qquad \text{eqn. 1}$$

A value closer to 0 indicates that the model has a minimum random error component, and that the fit will be more useful to give a meaningful displacement-length relationship characterization in a given traced fault population. This statistic characterization measures how successful the fit is in explaining the variation of the data commonly referred to as R-square. R-square is then defined as the ratio of the sum of squares of the regression (SSR) and the total sum of squares (SST). SSR is defined as

$$SSR = \sum_{i=1}^{n} w_i(\hat{y}_i - \bar{y})^2 \qquad \text{eqn. 2}$$

SST is also called the sum of squares about the mean, and is defined as

$$SST = \sum_{i=1}^{n} w_i(y_i - \bar{y})^2 \qquad \text{eqn. 3}$$

However, SST = SSR + SSE. Given these definitions, R-square is expressed as

$$R^2 = \frac{SSR}{SST} = 1 - \frac{SSE}{SST} \qquad \text{eqn. 4}$$

R-square ranges between 0 and 1, with a value closer to 1 implicates greater percentage of variance is considered in by the model. For example, an R-square value of 0.6534 can be interpreted as the fit explains 65.34% of the total variation occurrence in the traced fault population about the average.

SAS Program

```
PROC IMPORT OUT= WORK.FaultPop1
            DATAFILE= "C:\Users\DELL\Desktop\Fault Population.xlsx"
            DBMS=EXCEL REPLACE;
     RANGE="Sheet1$";
     GETNAMES=YES;
     MIXED=NO;
     SCANTEXT=YES;
     USEDATE=YES;
     SCANTIME=YES;
RUN;

PROC IMPORT OUT= WORK. FaultPop2
            DATAFILE= "C:\Users\DELL\Desktop\ Fault Population.xlsx"
            DBMS=EXCEL REPLACE;
     RANGE="Sheet2$";
     GETNAMES=YES;
     MIXED=NO;
     SCANTEXT=YES;
     USEDATE=YES;
     SCANTIME=YES;
RUN;

PROC IMPORT OUT= WORK. FaultPop3
            DATAFILE= "C:\Users\DELL\Desktop\ Fault Population.xlsx"
            DBMS=EXCEL REPLACE;
     RANGE="Sheet3$";
     GETNAMES=YES;
     MIXED=NO;
     SCANTEXT=YES;
     USEDATE=YES;
     SCANTIME=YES;
RUN;

PROC IMPORT OUT= WORK. FaultPop4
            DATAFILE= "C:\Users\DELL\Desktop\ Fault Population.xlsx"
            DBMS=EXCEL REPLACE;
     RANGE="Sheet4$";
     GETNAMES=YES;
     MIXED=NO;
     SCANTEXT=YES;
     USEDATE=YES;
     SCANTIME=YES;
RUN;

PROC IMPORT OUT= WORK. FaultPop5
            DATAFILE= "C:\Users\DELL\Desktop\ Fault Population.xlsx"
            DBMS=EXCEL REPLACE;
     RANGE="Sheet5$";
     GETNAMES=YES;
     MIXED=NO;
     SCANTEXT=YES;
     USEDATE=YES;
     SCANTIME=YES;
RUN;
```

```
PROC IMPORT OUT= WORK. FaultPop6
            DATAFILE= "C:\Users\DELL\Desktop\ Fault Population.xlsx"
            DBMS=EXCEL REPLACE;
     RANGE="Sheet6$";
     GETNAMES=YES;
     MIXED=NO;
     SCANTEXT=YES;
     USEDATE=YES;
     SCANTIME=YES;
RUN;


ods pdf file=" FaultPopfile on regression" ;


proc reg data= FaultPop1;
title'Derale';
    model   DMax= Length
                  ;
   ;
run;
quit;

title;



proc reg data= FaultPop2;
title'Dobi relay zone';
    model   DMax= Length
                  ;
   ;
run;
quit;

title;



proc reg data= FaultPop3;
title'Dobi Extensional Imbrication';
    model   DMax= Length
                  ;
   ;
run;
quit;

title;



proc reg data= FaultPop4;
title'Termenation zone';
    model   DMax= Length
                  ;
```

```
   ;
run;
quit;
title;

proc reg data= FaultPop5;
title'Henale';
    model   DMax= Length
                ;
   ;
run;
quit;
title;


proc reg data= FaultPop6;
title'High ramp linkage zone';
    model   DMax= Length
                ;
   ;
run;
quit;
ods pdf close;

title;


ods pdf file=" FaultPop1  file on regression" ;


proc reg data= FaultPop1
plots(only label)=(RSTUDENTBYPREDICTED COOKSD DFFITS DFBETAS);
title'Derale';
    model   DMax= Length
                ;
   ;
run;
quit;

title;



proc reg data= FaultPop2
plots(only label)=(RSTUDENTBYPREDICTED COOKSD DFFITS DFBETAS);
title'Dobi relay zone';
    model   DMax= Length
                ;
   ;
run;
quit;

title;
```

```
proc reg data= FaultPop3
plots(only label)=(RSTUDENTBYPREDICTED COOKSD DFFITS DFBETAS) ;
title'Dobi Extensional Imbrication';
    model   DMax= Length
                ;
   ;
run;
quit;

title;



proc reg data= FaultPop4
plots(only label)=(RSTUDENTBYPREDICTED COOKSD DFFITS DFBETAS) ;
title'Termenation zone';
    model   DMax= Length
                ;
   ;
run;
quit;
title;

proc reg data= FaultPop5
plots(only label)=(RSTUDENTBYPREDICTED COOKSD DFFITS DFBETAS) ;
title'Henale';
    model   DMax= Length
                ;
   ;
run;
quit;
title;


proc reg data= FaultPop6
plots(only label)=(RSTUDENTBYPREDICTED COOKSD DFFITS DFBETAS);
title'High ramp linkage zone';
    model   DMax= Length
                ;
   ;
run;
quit;
ods pdf close;

title;


data dobiRelay;
set dobiRelayNew;
if _n_ not in (23,24,40,65,98,121);
run;

data zelalem8;
set zelalem2;
if _n_ not in (1,3,4,5);
run;
```

```
proc reg data=Zelalem8;
title'dobi Relay modified';
    model   DMax= Length
                  ;
   ;
run;
quit;
title;


data zelalem9;
set zelalem3;
title'Dobi Extensional Imbrication'
if _n_ not in (2,3,4,5,6,8,9,10,16,52);
run;

title;
```

Appendices **2**

All faults

The REG Procedure
Model: MODEL1
Dependent Variable: DMax DMax

Number of Observations Read	953
Number of Observations Used	953

Analysis of Variance					
Source	DF	Sum of Squares	Mean Square	F Value	Pr > F
Model	1	5686595	5686595	1340.77	<.0001
Error	951	4033475	4241.29905		
Corrected Total	952	9720070			

Root MSE	65.12526	R-Square	0.5850
Dependent Mean	77.63559	Adj R-Sq	0.5846
Coeff Var	83.88582		

Parameter Estimates						
Variable	Label	DF	Parameter Estimate	Standard Error	t Value	Pr > |t|
Intercept	Intercept	1	19.15772	2.64594	7.24	<.0001
Length	Length	1	0.02785	0.00076057	36.62	<.0001

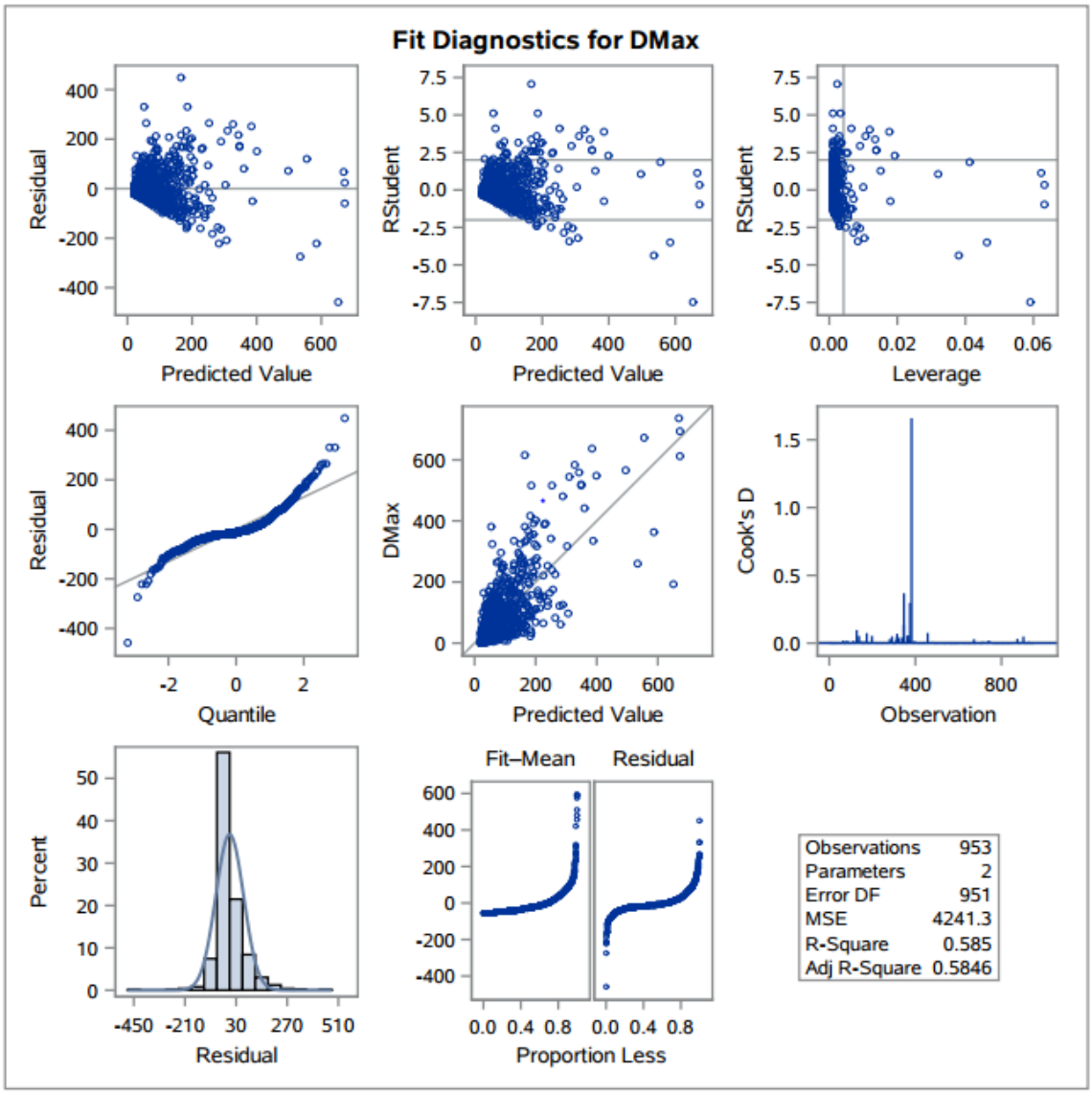
Fit Diagnostics for DMax
Residual
Predicted Value
RStudent
Predicted Value
RStudent
Leverage
Residual
Quantile
DMax
Predicted Value
Cook's D
Observation
Percent
Residual
Fit–Mean
Residual
Proportion Less
Observations 953
Parameters 2
Error DF 951
MSE 4241.3
R-Square 0.585
Adj R-Square 0.5846

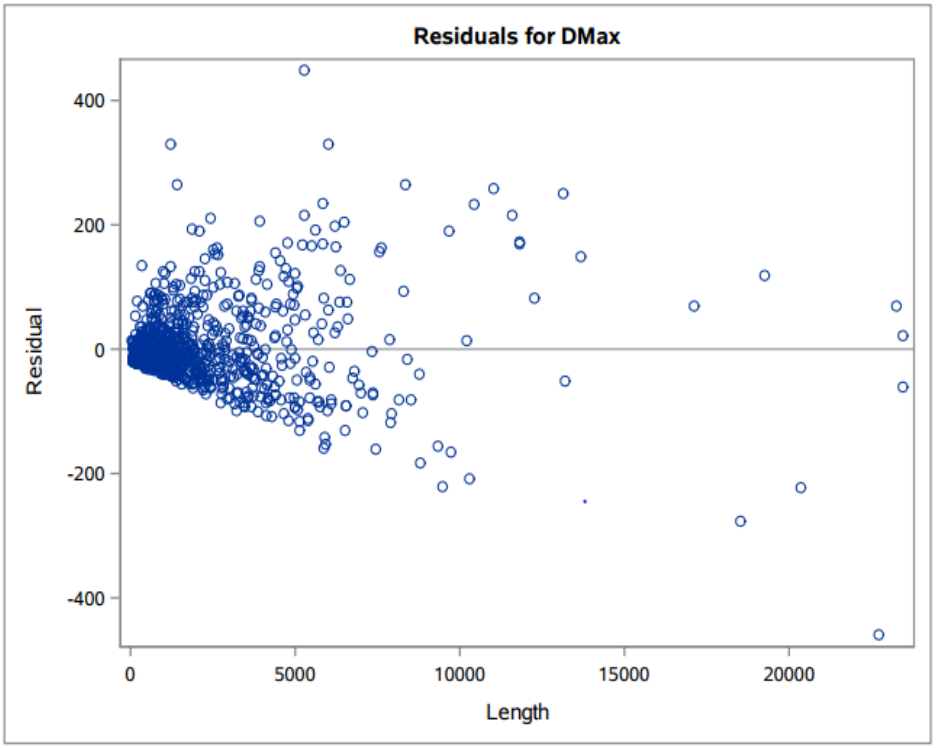
Residuals for DMax
Residual
400
200
0
-200
-400
0
5000
10000
15000
20000
Length

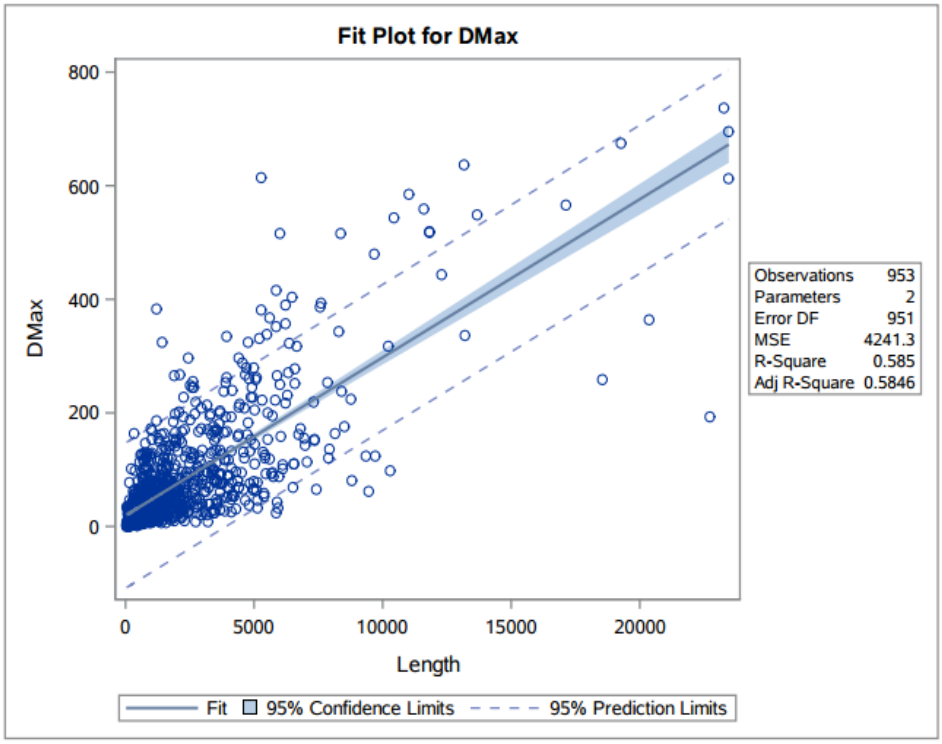
Fit Plot for DMax
DMax
800
600
400
200
0
0
5000
10000
15000
20000
Length
Observations 953
Parameters 2
Error DF 951
MSE 4241.3
R-Square 0.585
Adj R-Square 0.5846
Fit
95% Confidence Limits
95% Prediction Limits

Both Tips

The REG Procedure
Model: MODEL1
Dependent Variable: DMax DMax

Number of Observations Read	66
Number of Observations Used	66

Analysis of Variance					
Source	DF	Sum of Squares	Mean Square	F Value	Pr > F
Model	1	87272	87272	108.14	<.0001
Error	64	51651	807.04178		
Corrected Total	65	138923			

Root MSE	28.40848	R-Square	0.6282
Dependent Mean	39.70013	Adj R-Sq	0.6224
Coeff Var	71.55765		

Parameter Estimates						
Variable	Label	DF	Parameter Estimate	Standard Error	t Value	Pr > |t|
Intercept	Intercept	1	3.13761	4.95883	0.63	0.5292
Length	Length	1	0.01658	0.00159	10.40	<.0001

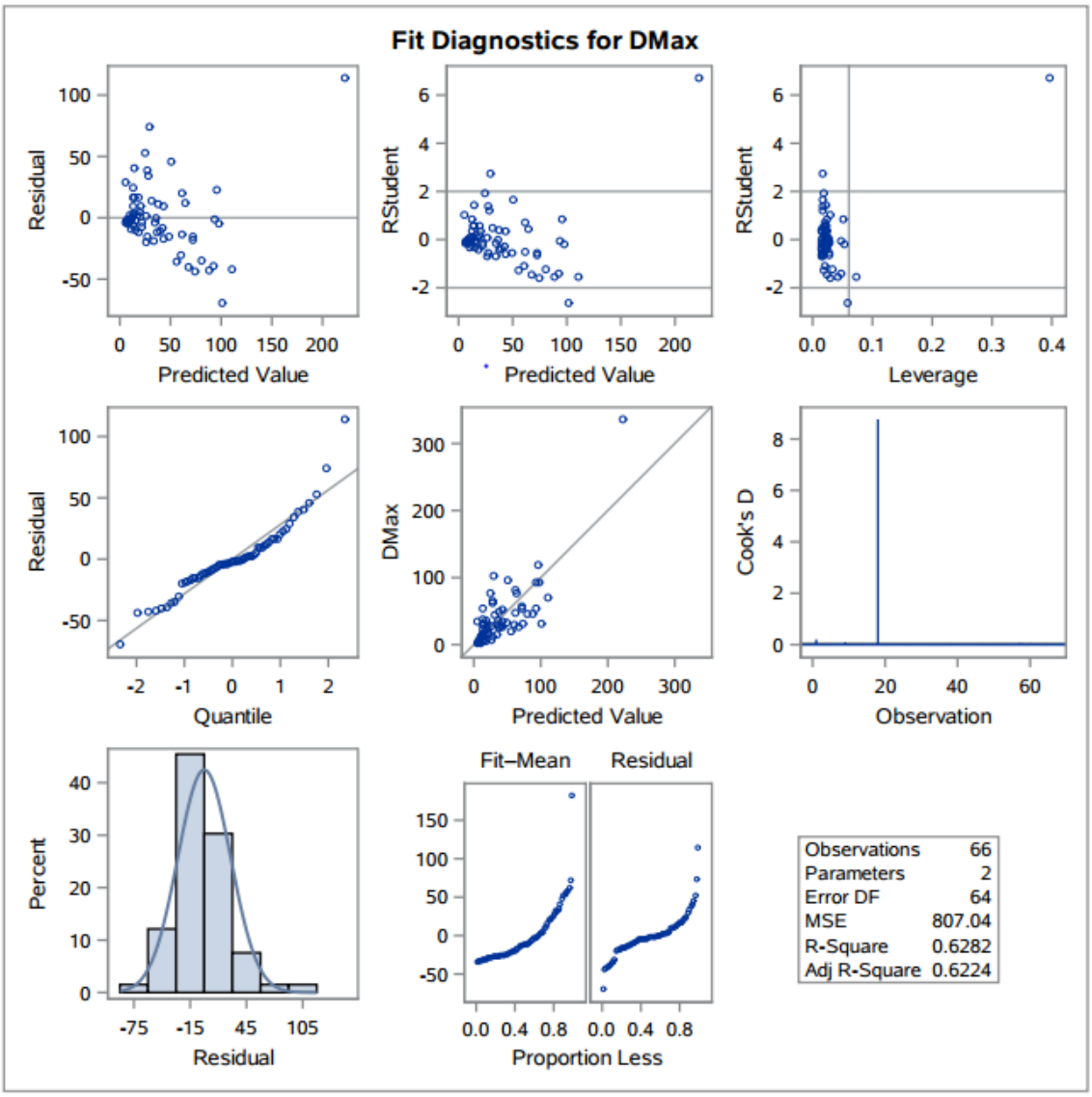
Fit Diagnostics for DMax
Residual
Predicted Value
RStudent
Predicted Value
RStudent
Leverage
Residual
Quantile
DMax
Predicted Value
Cook's D
Observation
Percent
Residual
Fit–Mean
Residual
Proportion Less
Observations 66
Parameters 2
Error DF 64
MSE 807.04
R-Square 0.6282
Adj R-Square 0.6224

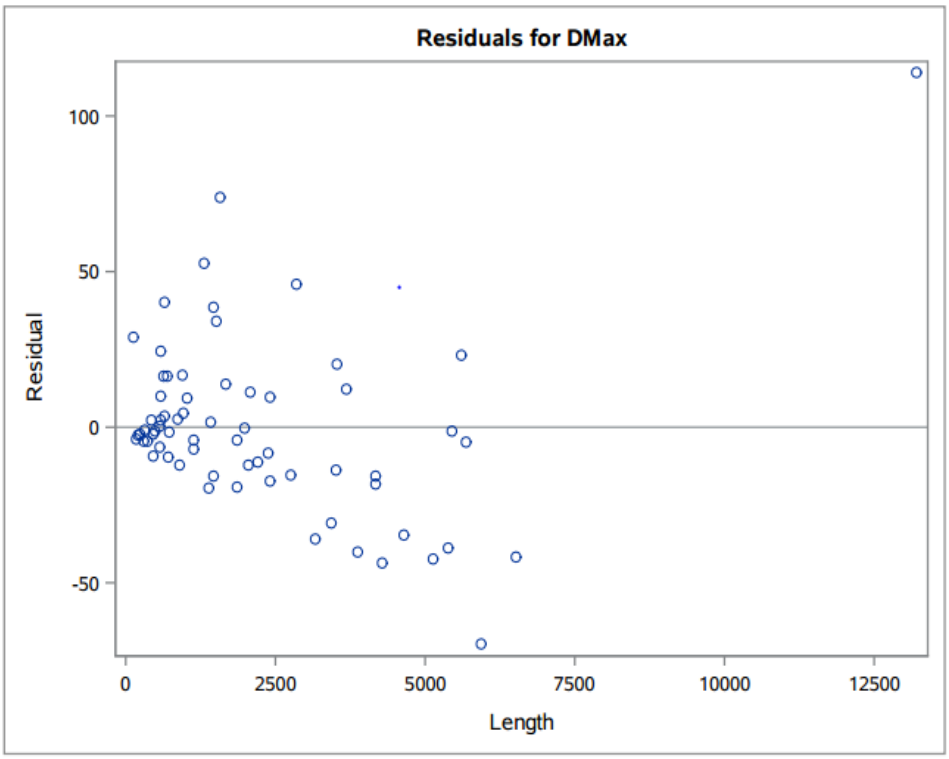
Residuals for DMax
Residual
100
50
0
-50
0
2500
5000
7500
10000
12500
Length

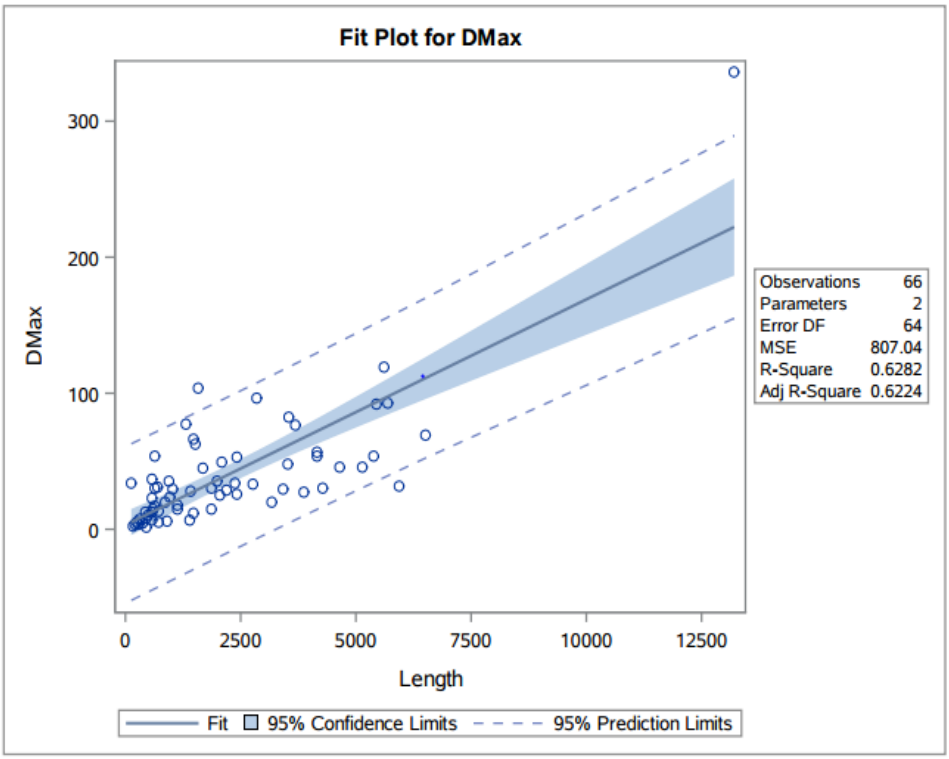
Fit Plot for DMax
DMax
300
200
100
0
0
2500
5000
7500
10000
12500
Length
Observations 66
Parameters 2
Error DF 64
MSE 807.04
R-Square 0.6282
Adj R-Square 0.6224
Fit
95% Confidence Limits
95% Prediction Limits

Breach

The REG Procedure
Model: MODEL1
Dependent Variable: DMax DMax

Number of Observations Read	137
Number of Observations Used	137

Analysis of Variance					
Source	DF	Sum of Squares	Mean Square	F Value	Pr > F
Model	1	392138	392138	101.28	<.0001
Error	135	522688	3871.76195		
Corrected Total	136	914826			

Root MSE	62.22348	R-Square	0.4286
Dependent Mean	67.94225	Adj R-Sq	0.4244
Coeff Var	91.58291		

Parameter Estimates						
Variable	Label	DF	Parameter Estimate	Standard Error	t Value	Pr > |t|
Intercept	Intercept	1	15.35816	7.45399	2.06	0.0413
Length	Length	1	0.05532	0.00550	10.06	<.0001

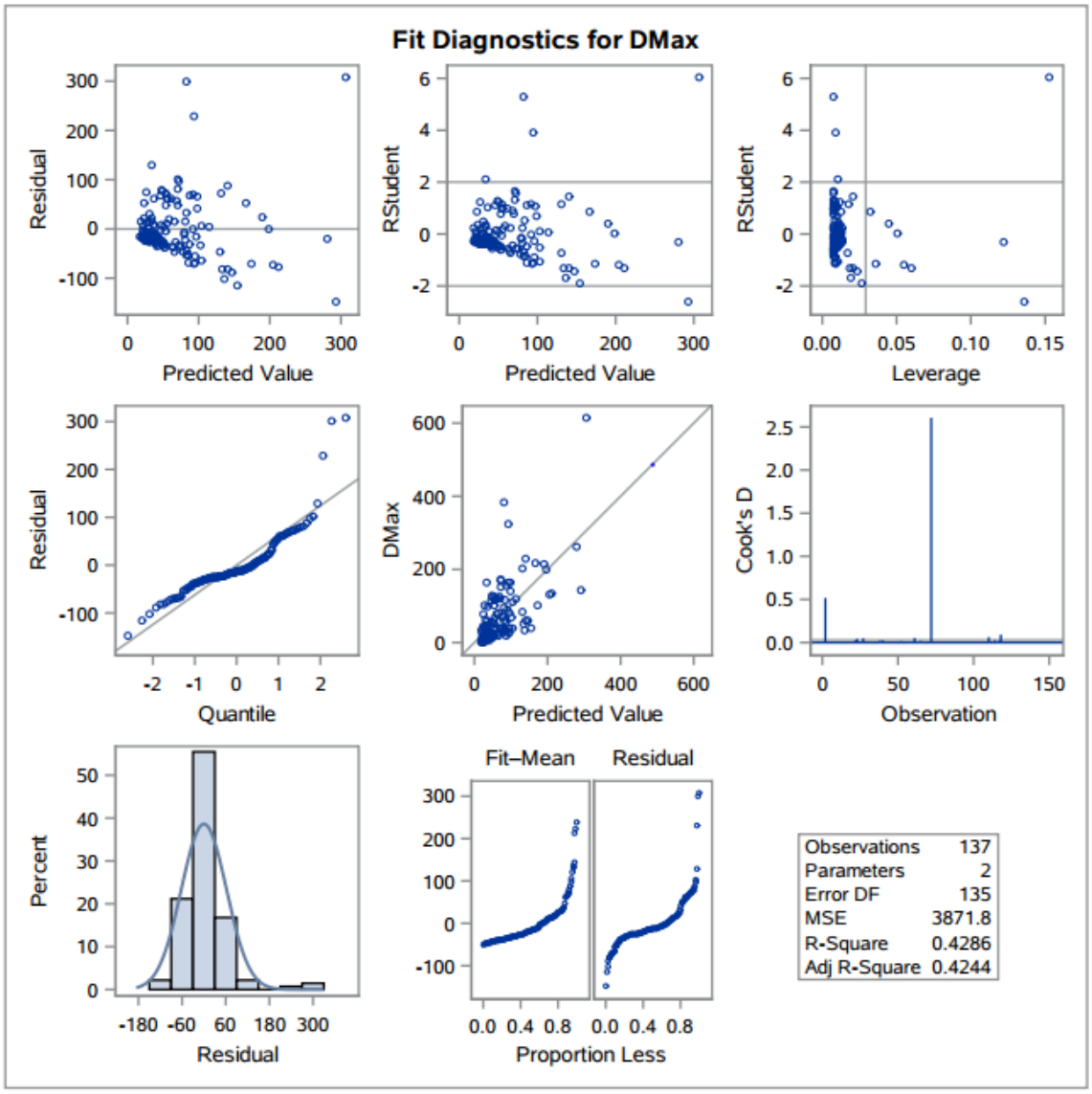
Fit Diagnostics for DMax
Residual
Predicted Value
RStudent
Predicted Value
RStudent
Leverage
Residual
Quantile
DMax
Predicted Value
Cook's D
Observation
Percent
Residual
Fit–Mean
Residual
Proportion Less
Observations 137
Parameters 2
Error DF 135
MSE 3871.8
R-Square 0.4286
Adj R-Square 0.4244

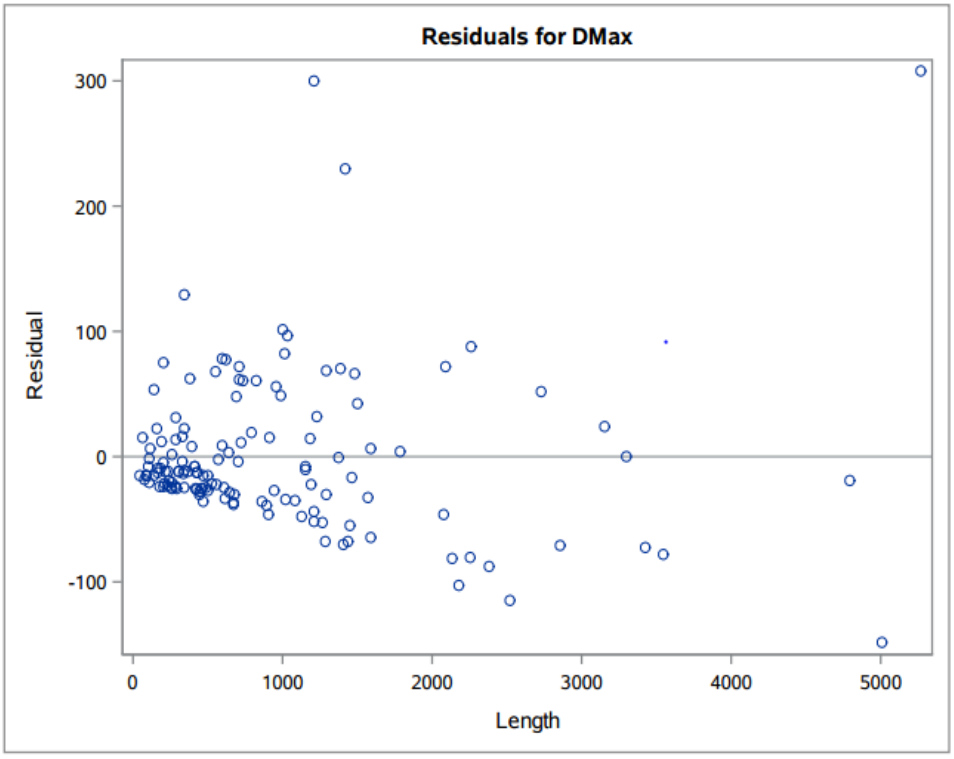
Residuals for DMax
Residual
300
200
100
0
-100
0
1000
2000
3000
4000
5000
Length

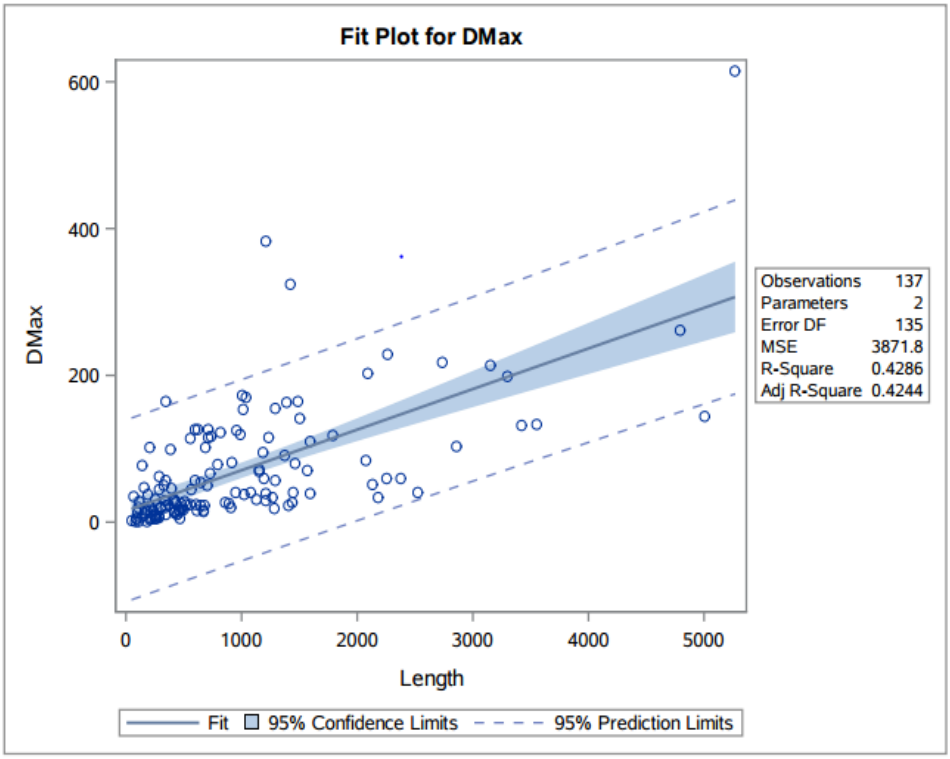
Fit Plot for DMax
DMax
600
400
200
0
0
1000
2000
3000
4000
5000
Length
Observations 137
Parameters 2
Error DF 135
MSE 3871.8
R-Square 0.4286
Adj R-Square 0.4244
Fit
95% Confidence Limits
95% Prediction Limits

Half Restricted

The REG Procedure
Model: MODEL1
Dependent Variable: DMax DMax

Number of Observations Read	810
Number of Observations Used	810

Analysis of Variance					
Source	DF	Sum of Squares	Mean Square	F Value	Pr > F
Model	1	5578623	5578623	1249.57	<.0001
Error	808	3607249	4464.41687		
Corrected Total	809	9185872			

Root MSE	66.81629	R-Square	0.6073
Dependent Mean	83.47006	Adj R-Sq	0.6068
Coeff Var	80.04821		

Parameter Estimates						
Variable	Label	DF	Parameter Estimate	Standard Error	t Value	Pr > |t|
Intercept	Intercept	1	22.76356	2.90875	7.83	<.0001
Length	Length	1	0.02894	0.00081874	35.35	<.0001

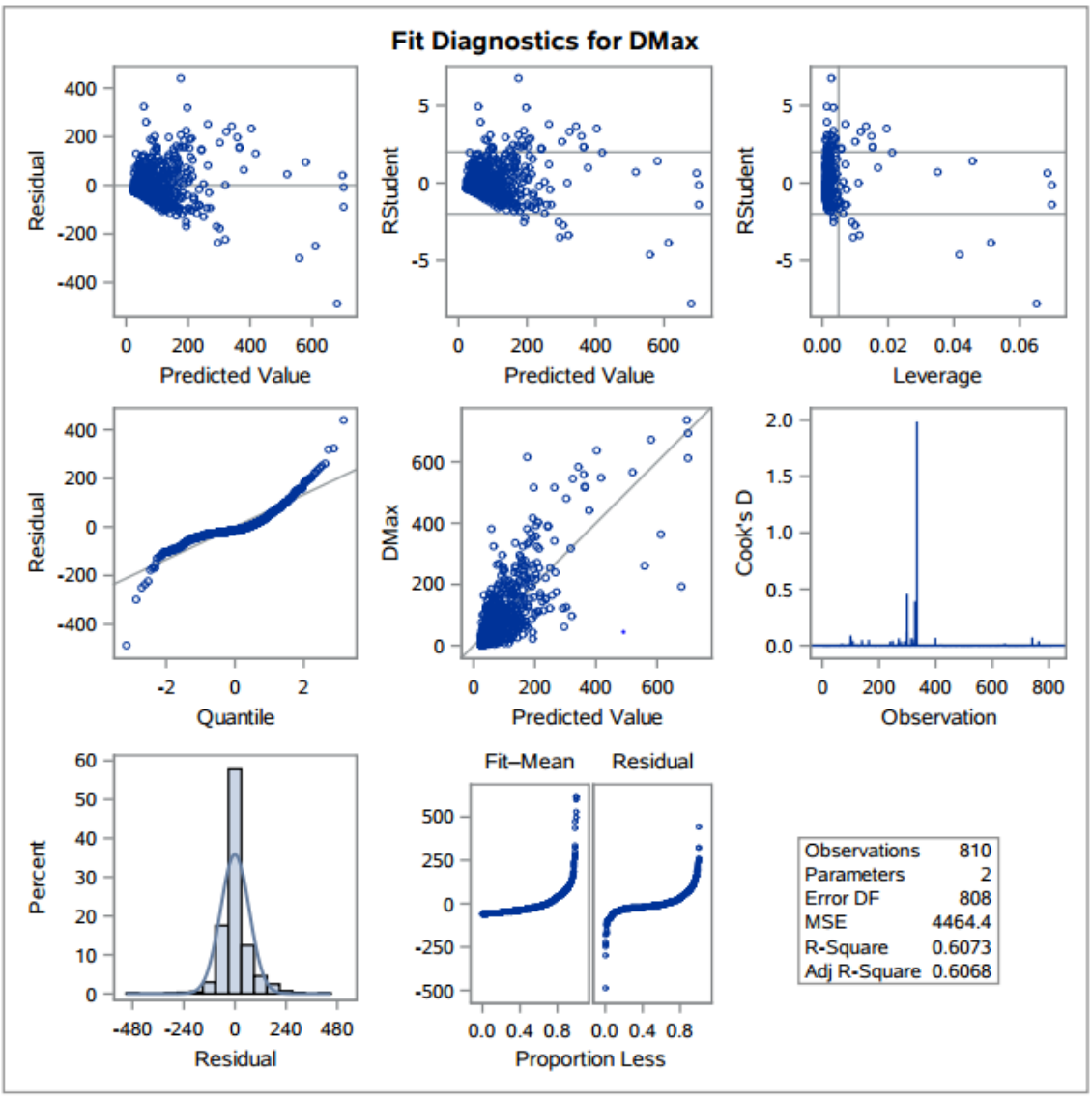
Fit Diagnostics for DMax
Residual
Predicted Value
RStudent
Predicted Value
RStudent
Leverage
Residual
Quantile
DMax
Predicted Value
Cook's D
Observation
Percent
Residual
Fit–Mean
Residual
Proportion Less
Observations 810
Parameters 2
Error DF 808
MSE 4464.4
R-Square 0.6073
Adj R-Square 0.6068

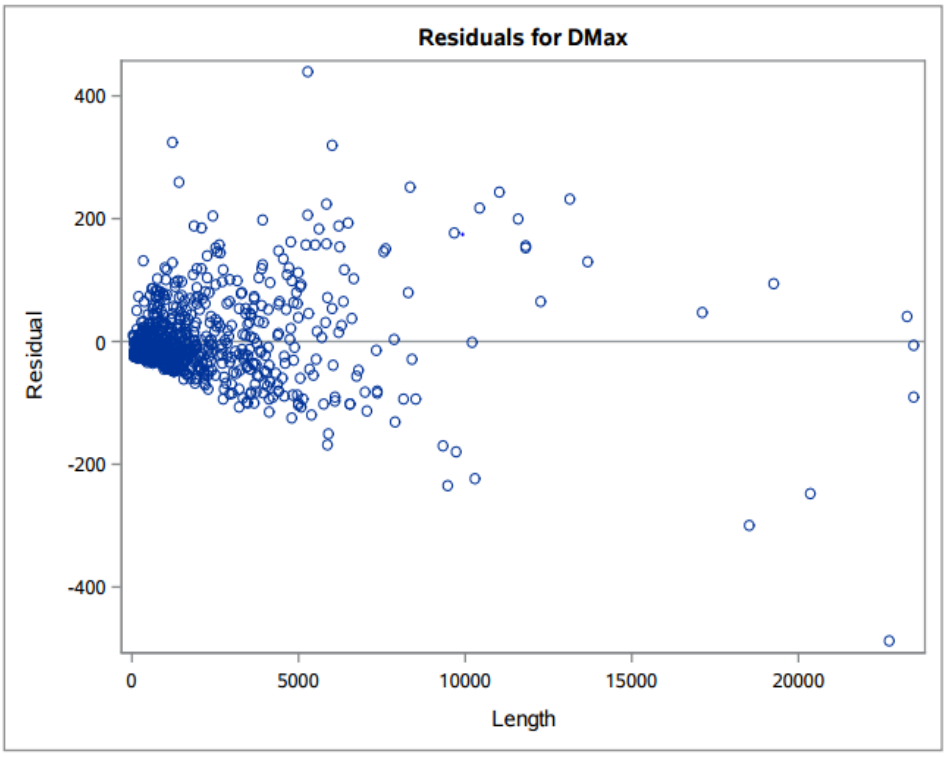
Residuals for DMax
Residual
400
200
0
-200
-400
0
5000
10000
15000
20000
Length

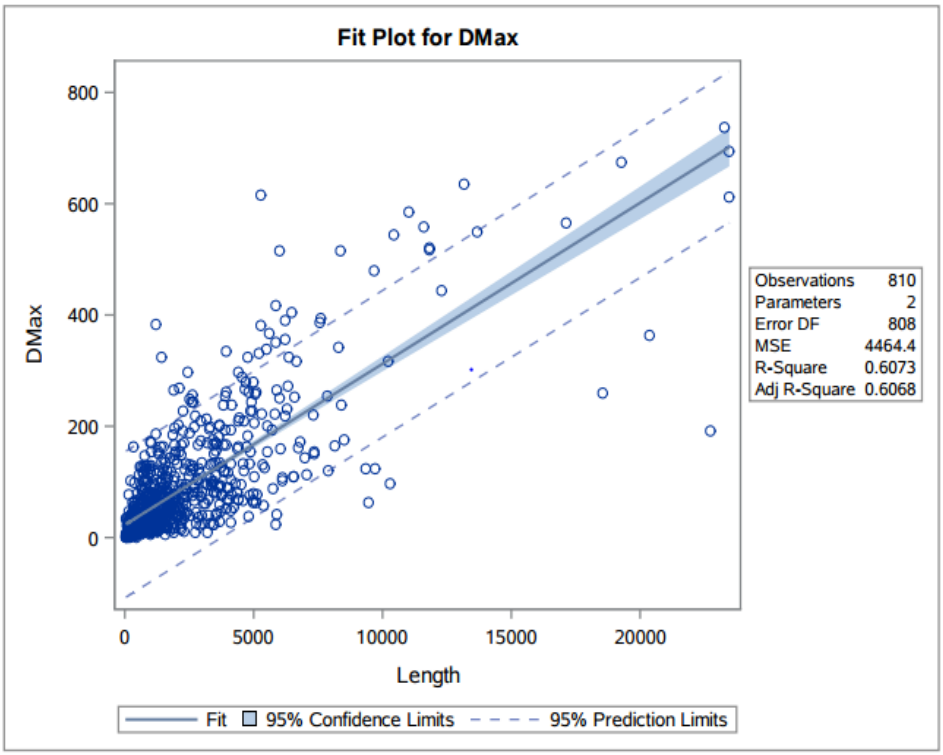
Fit Plot for DMax
DMax
800
600
400
200
0
0
5000
10000
15000
20000
Length
Observations 810
Parameters 2
Error DF 808
MSE 4464.4
R-Square 0.6073
Adj R-Square 0.6068
Fit
95% Confidence Limits
95% Prediction Limits

Tapering Northwest

The REG Procedure
Model: MODEL1
Dependent Variable: DMax DMax

Number of Observations Read	287
Number of Observations Used	287

Analysis of Variance					
Source	DF	Sum of Squares	Mean Square	F Value	Pr > F
Model	1	2555114	2555114	534.05	<.0001
Error	285	1363546	4784.37024		
Corrected Total	286	3918659			

Root MSE	69.16914	R-Square	0.6520
Dependent Mean	85.74444	Adj R-Sq	0.6508
Coeff Var	80.66895		

Parameter Estimates						
Variable	Label	DF	Parameter Estimate	Standard Error	t Value	Pr > |t|
Intercept	Intercept	1	12.71053	5.16313	2.46	0.0144
Length	Length	1	0.02565	0.00111	23.11	<.0001

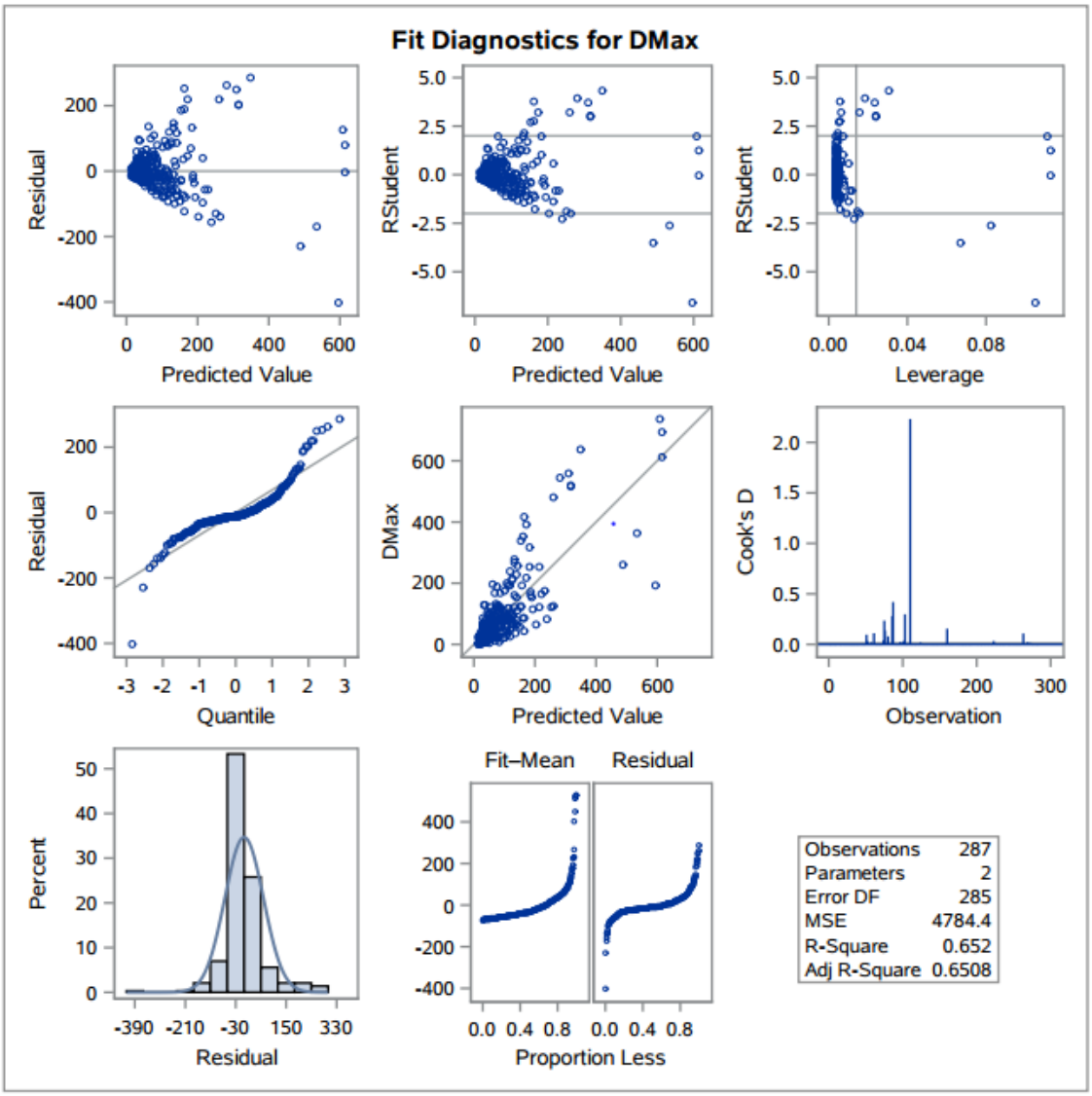
Fit Diagnostics for DMax
Residual
Predicted Value
RStudent
Predicted Value
RStudent
Leverage
Residual
Quantile
DMax
Predicted Value
Cook's D
Observation
Percent
Residual
Fit–Mean
Residual
Proportion Less
Observations 287
Parameters 2
Error DF 285
MSE 4784.4
R-Square 0.652
Adj R-Square 0.6508

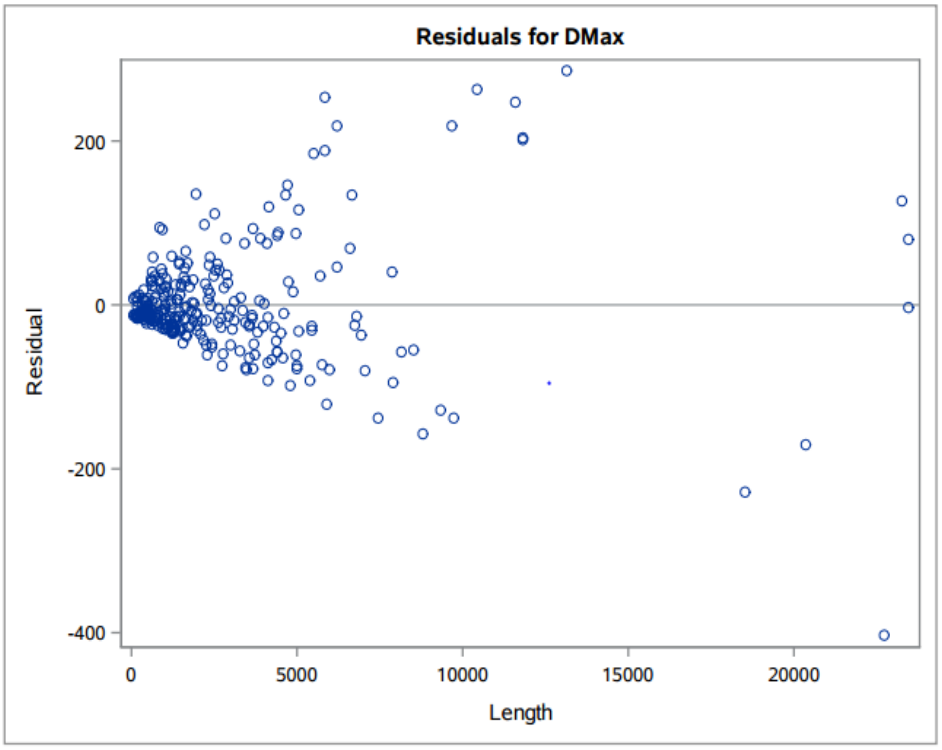
Residuals for DMax
Residual
200
0
-200
-400
0
5000
10000
15000
20000
Length

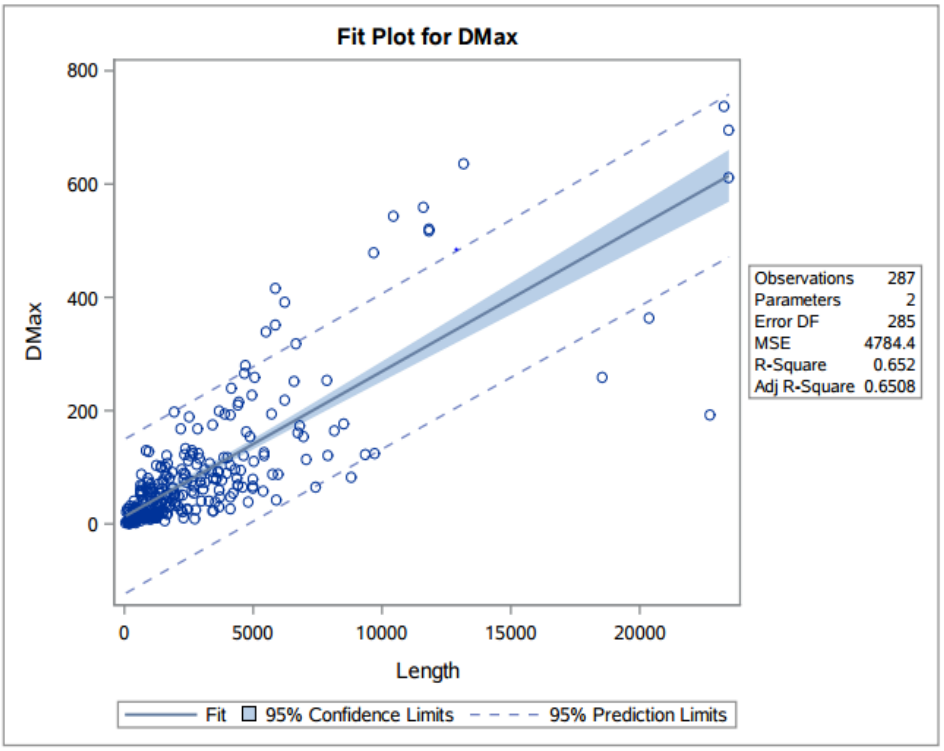
Fit Plot for DMax
DMax
800
600
400
200
0
0
5000
10000
15000
20000
Length
Observations 287
Parameters 2
Error DF 285
MSE 4784.4
R-Square 0.652
Adj R-Square 0.6508
Fit
95% Confidence Limits
95% Prediction Limits

Tapering Southeast

The REG Procedure
Model: MODEL1
Dependent Variable: DMax DMax

Number of Observations Read	463
Number of Observations Used	463

Analysis of Variance					
Source	DF	Sum of Squares	Mean Square	F Value	Pr > F
Model	1	3015500	3015500	868.54	<.0001
Error	461	1600549	3471.90604		
Corrected Total	462	4616049			

Root MSE	58.92288	R-Square	0.6533
Dependent Mean	80.88503	Adj R-Sq	0.6525
Coeff Var	72.84770		

Parameter Estimates						
Variable	Label	DF	Parameter Estimate	Standard Error	t Value	Pr > |t|
Intercept	Intercept	1	14.74783	3.54046	4.17	<.0001
Length	Length	1	0.03372	0.00114	29.47	<.0001

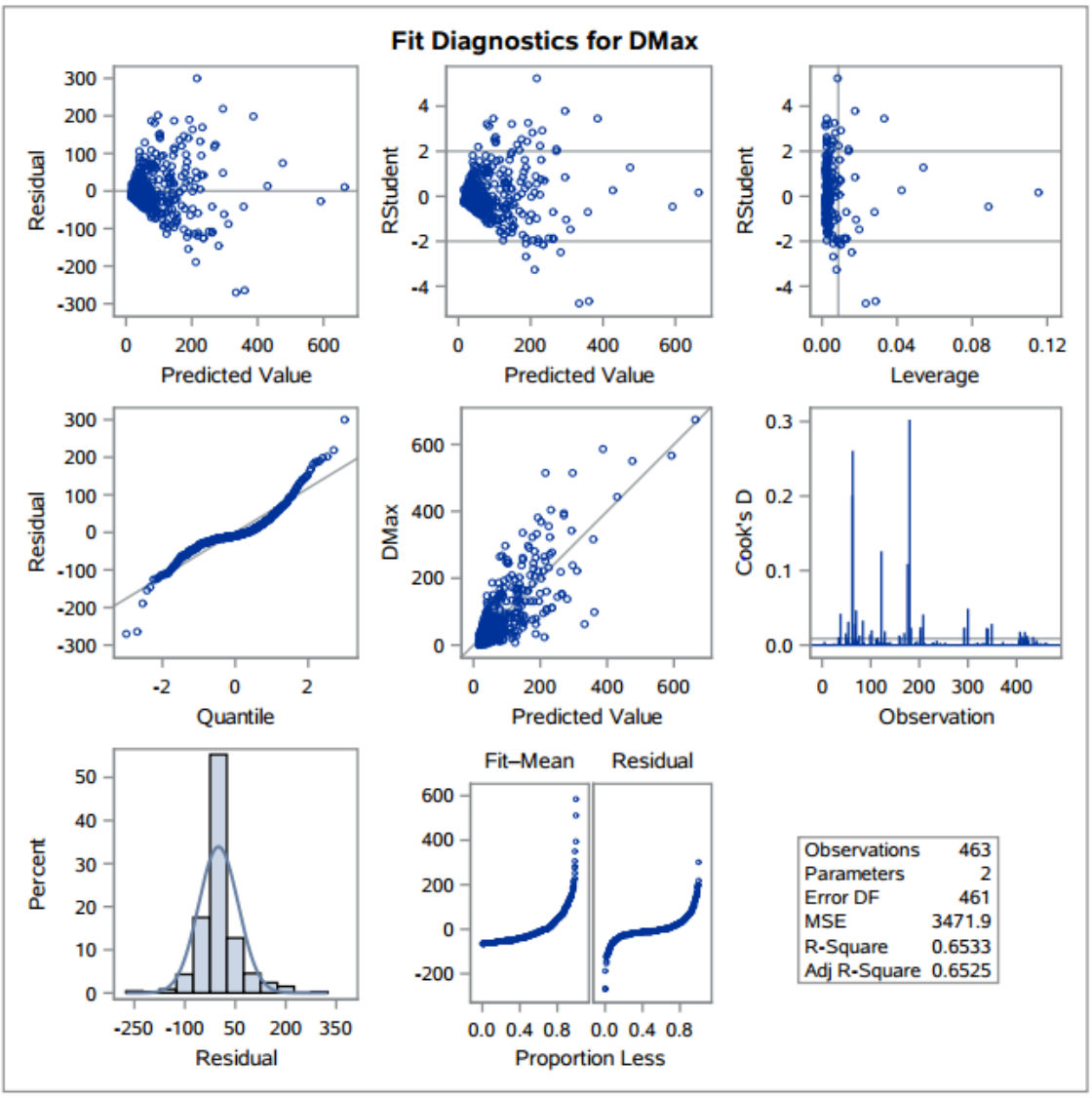
Fit Diagnostics for DMax
Residual
Predicted Value
RStudent
Predicted Value
RStudent
Leverage
Residual
Quantile
DMax
Predicted Value
Cook's D
Observation
Percent
Residual
Fit–Mean
Residual
Proportion Less
Observations 463
Parameters 2
Error DF 461
MSE 3471.9
R-Square 0.6533
Adj R-Square 0.6525

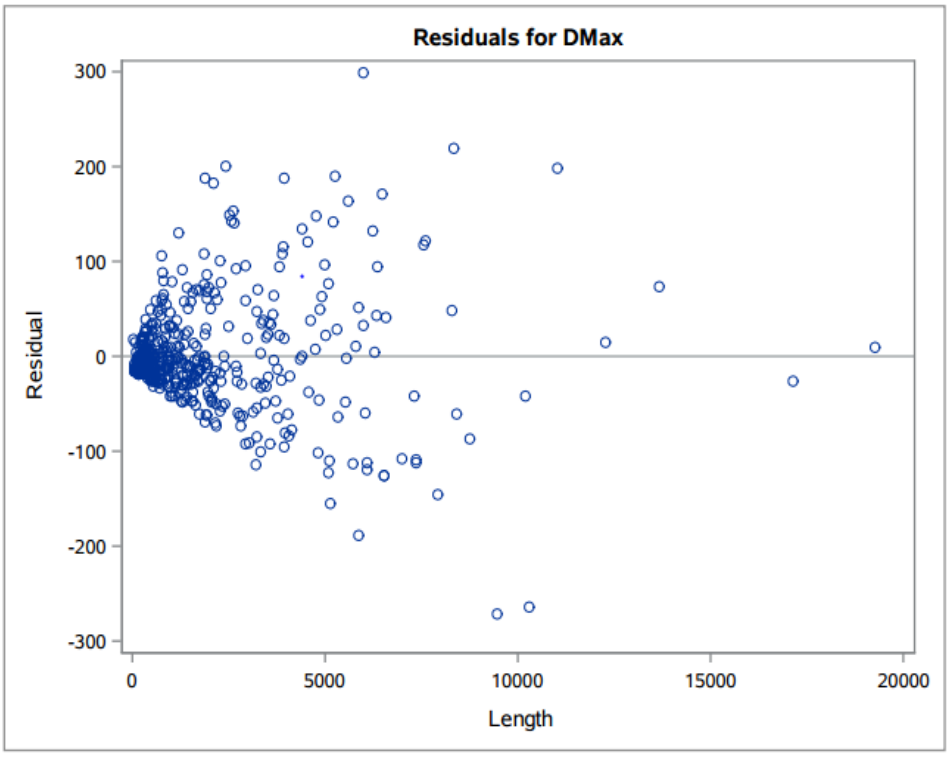
Residuals for DMax
Residual
300
200
100
0
-100
-200
-300
0
5000
10000
15000
20000
Length

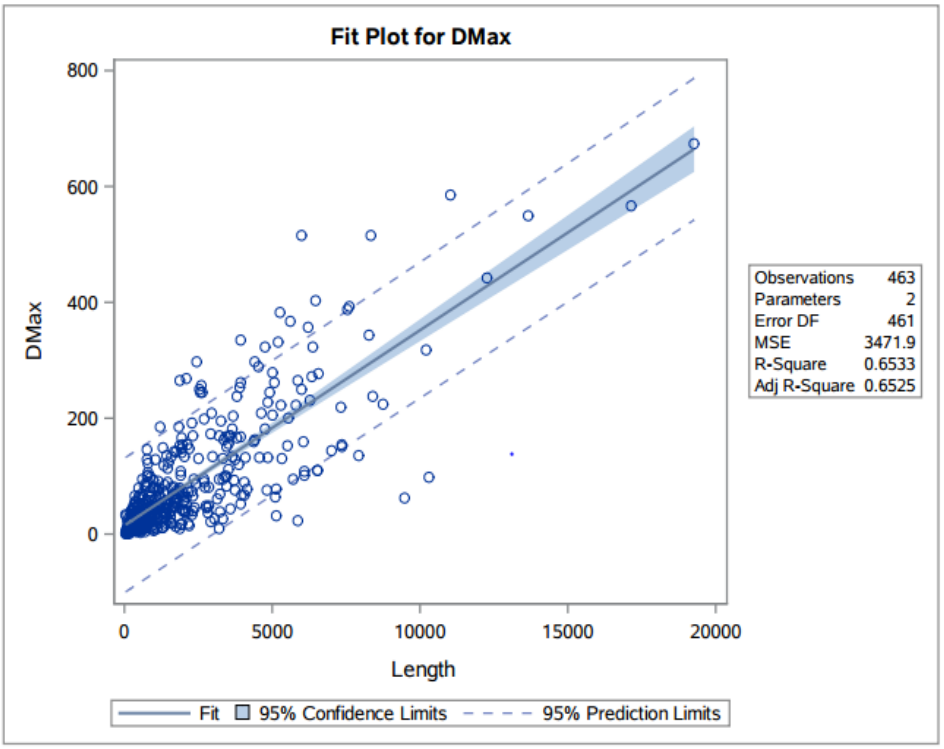
Fit Plot for DMax
DMax
800
600
400
200
0
0
5000
10000
15000
20000
Length
Observations 463
Parameters 2
Error DF 461
MSE 3471.9
R-Square 0.6533
Adj R-Square 0.6525
Fit
95% Confidence Limits
95% Prediction Limits

Tip Restricted

The REG Procedure
Model: MODEL1
Dependent Variable: DMax DMax

Number of Observations Read	79
Number of Observations Used	79

Analysis of Variance					
Source	DF	Sum of Squares	Mean Square	F Value	Pr > F
Model	1	110463	110463	89.45	<.0001
Error	77	95083	1234.84331		
Corrected Total	78	205546			

Root MSE	35.14034	R-Square	0.5374
Dependent Mean	49.73158	Adj R-Sq	0.5314
Coeff Var	70.66001		

Parameter Estimates						
Variable	Label	DF	Parameter Estimate	Standard Error	t Value	Pr > |t|
Intercept	Intercept	1	11.92597	5.62213	2.12	0.0371
Length	Length	1	0.01848	0.00195	9.46	<.0001

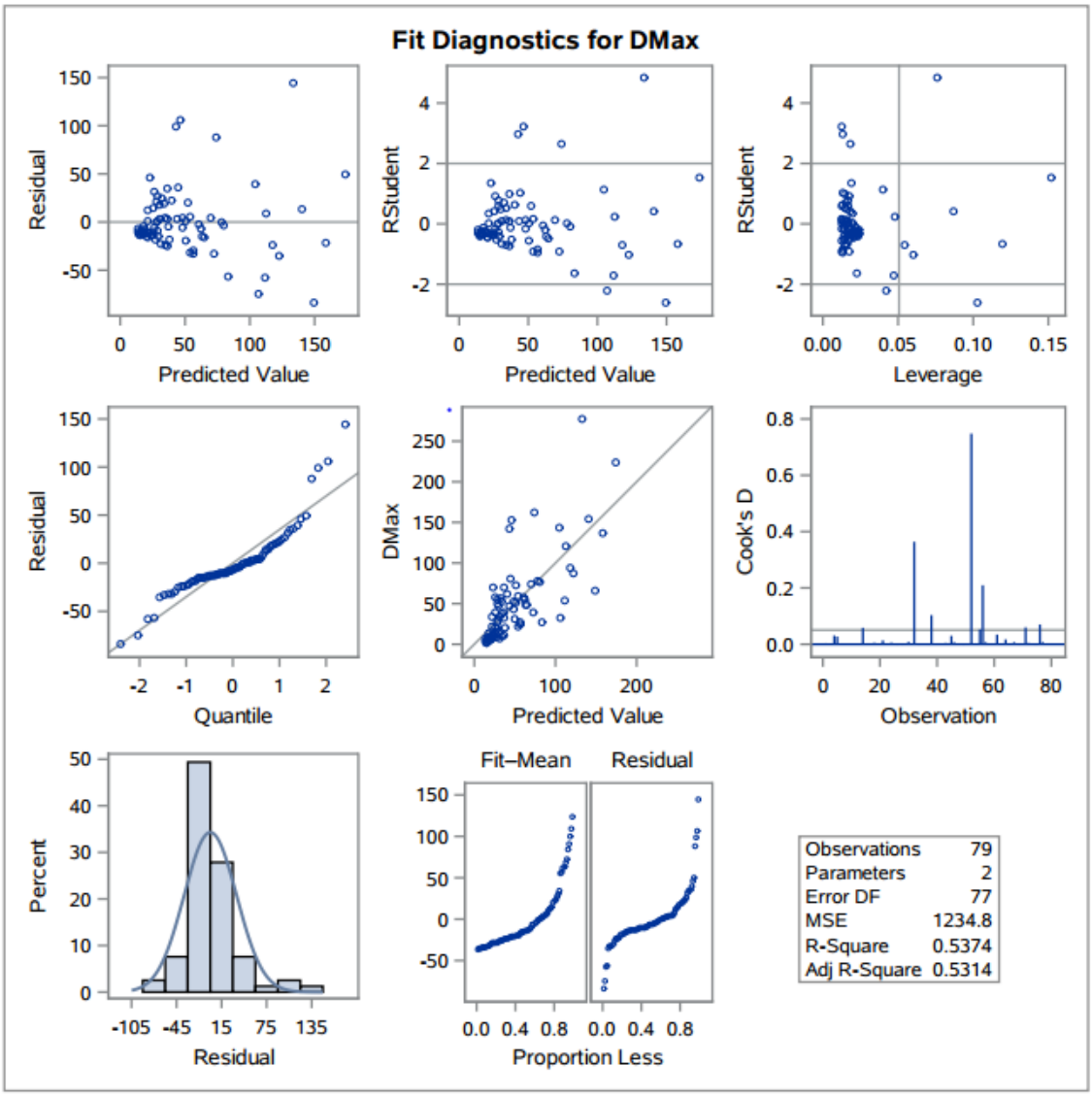
Fit Diagnostics for DMax
Residual
Predicted Value
RStudent
Predicted Value
RStudent
Leverage
Residual
Quantile
DMax
Predicted Value
Cook's D
Observation
Percent
Residual
Fit–Mean
Residual
Proportion Less
Observations 79
Parameters 2
Error DF 77
MSE 1234.8
R-Square 0.5374
Adj R-Square 0.5314

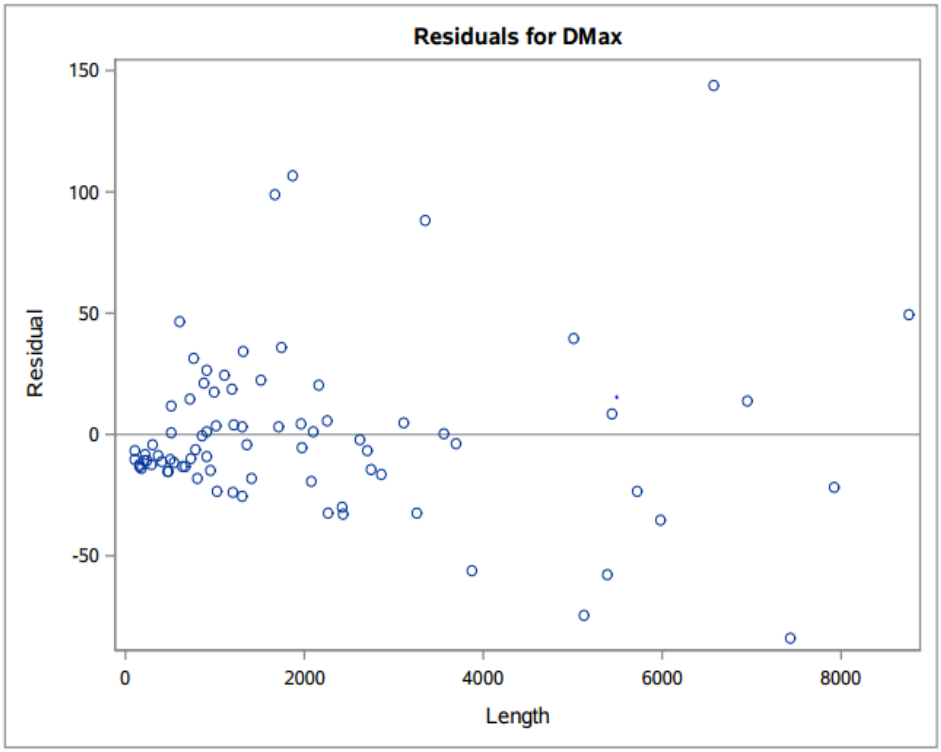
Residuals for DMax
Residual
150
100
50
0
-50
0
2000
4000
6000
8000
Length

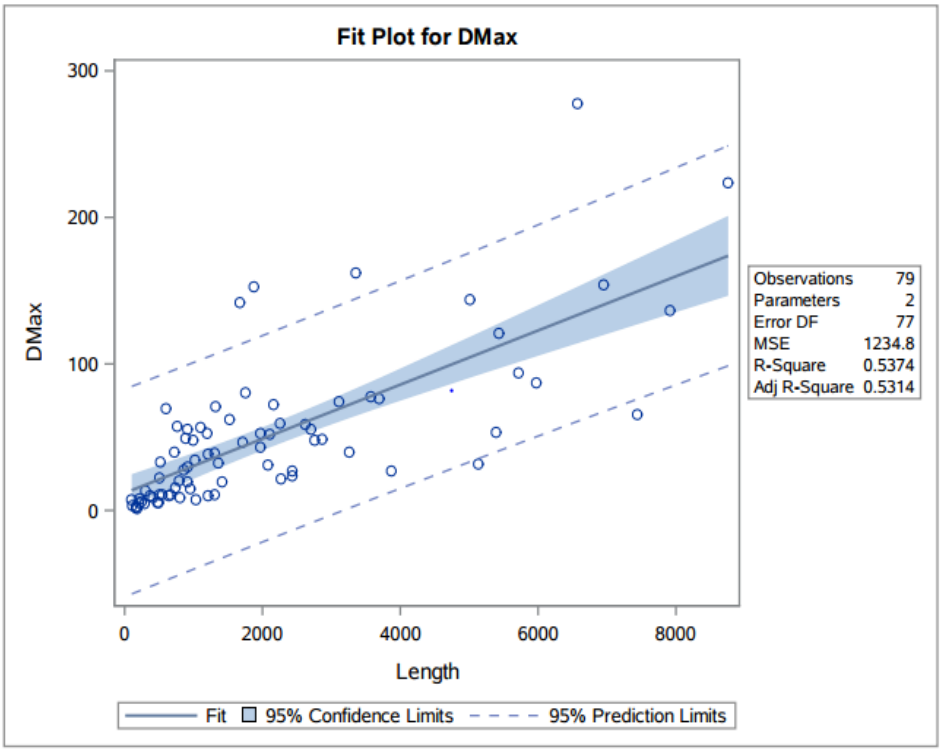
Fit Plot for DMax
DMax
300
200
100
0
0
2000
4000
6000
8000
Length
Observations 79
Parameters 2
Error DF 77
MSE 1234.8
R-Square 0.5374
Adj R-Square 0.5314
Fit
95% Confidence Limits
95% Prediction Limits

Tip Unrestricted

The REG Procedure
Model: MODEL1
Dependent Variable: DMax DMax

Number of Observations Read	60
Number of Observations Used	60

Analysis of Variance					
Source	DF	Sum of Squares	Mean Square	F Value	Pr > F
Model	1	90694	90694	116.41	<.0001
Error	58	45186	779.06742		
Corrected Total	59	135880			

Root MSE	27.91178	R-Square	0.6675
Dependent Mean	38.80547	Adj R-Sq	0.6617
Coeff Var	71.92743		

Parameter Estimates						
Variable	Label	DF	Parameter Estimate	Standard Error	t Value	Pr > |t|
Intercept	Intercept	1	0.99194	5.02664	0.20	0.8443
Length	Length	1	0.01748	0.00162	10.79	<.0001

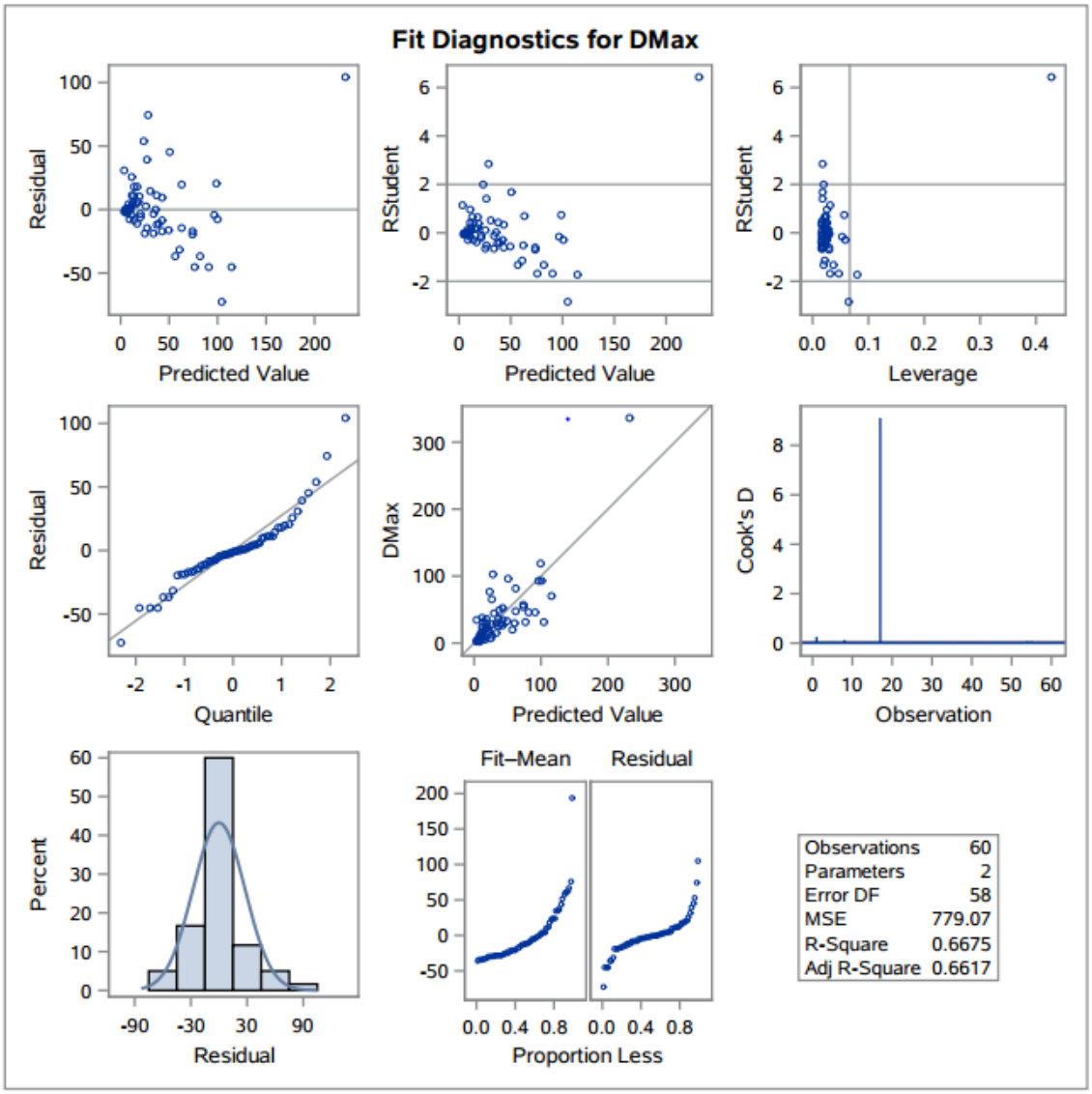
Fit Diagnostics for DMax
Residual
Predicted Value
RStudent
Predicted Value
RStudent
Leverage
Residual
Quantile
DMax
Predicted Value
Cook's D
Observation
Percent
Residual
Fit–Mean
Residual
Proportion Less
Observations 60
Parameters 2
Error DF 58
MSE 779.07
R-Square 0.6675
Adj R-Square 0.6617

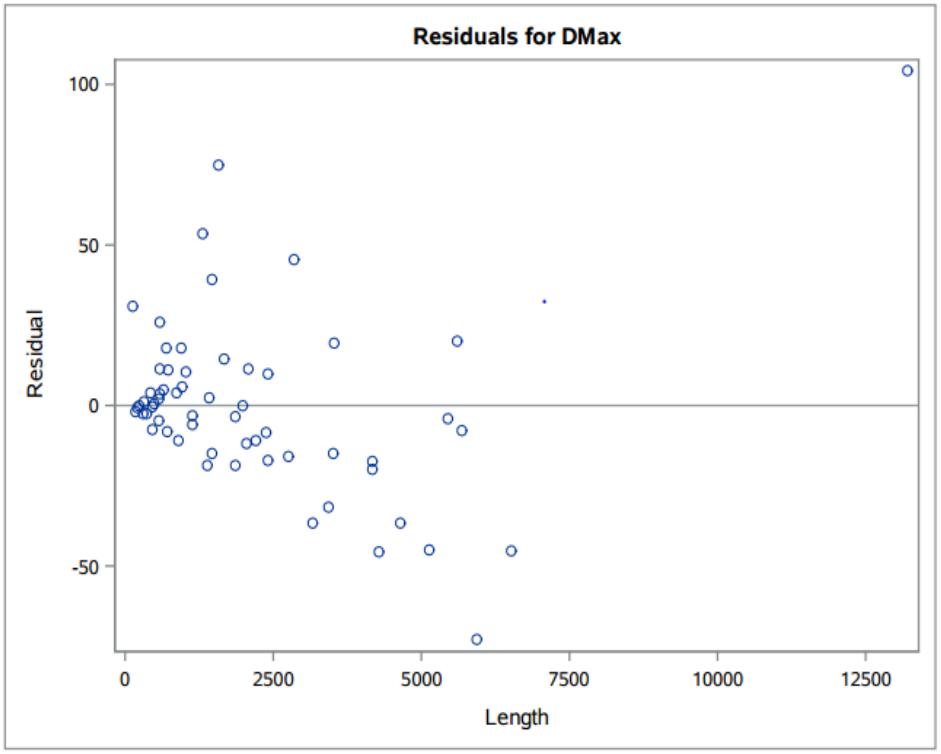
Residuals for DMax
Residual
100
50
0
-50
0
2500
5000
7500
10000
12500
Length

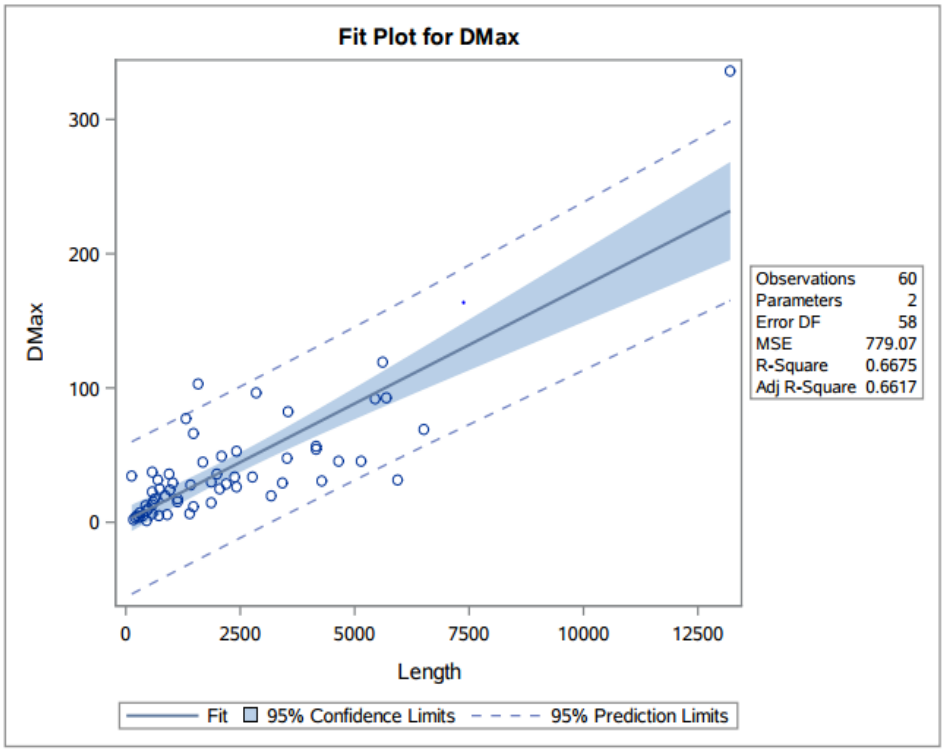
Fit Plot for DMax
DMax
300
200
100
0
0
2500
5000
7500
10000
12500
Length
Observations 60
Parameters 2
Error DF 58
MSE 779.07
R-Square 0.6675
Adj R-Square 0.6617
Fit
95% Confidence Limits
95% Prediction Limits

Appendices **3**

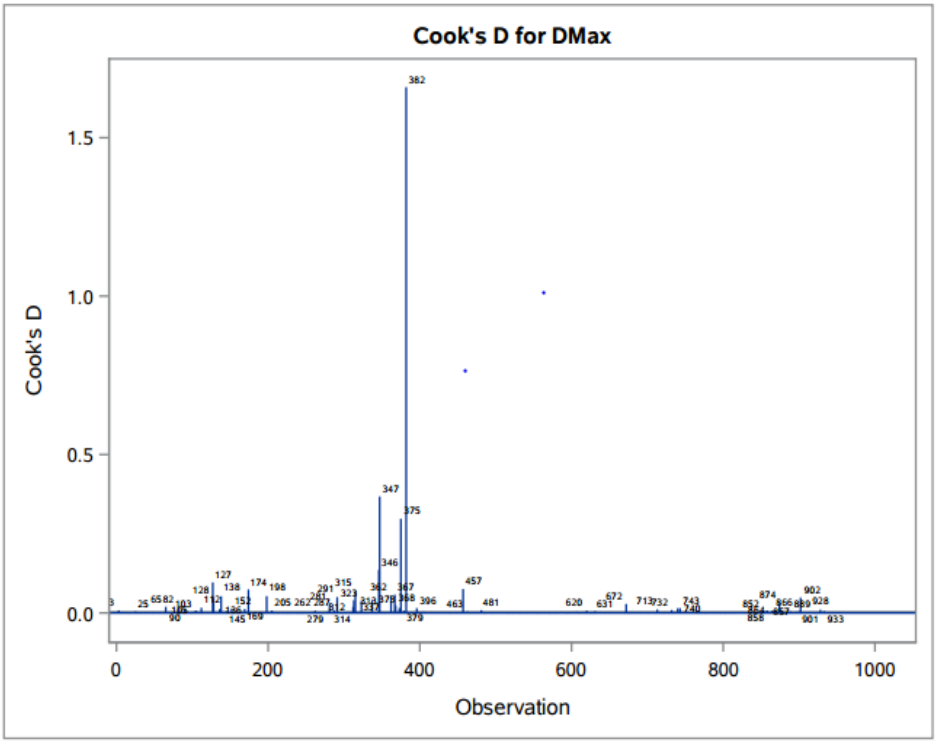

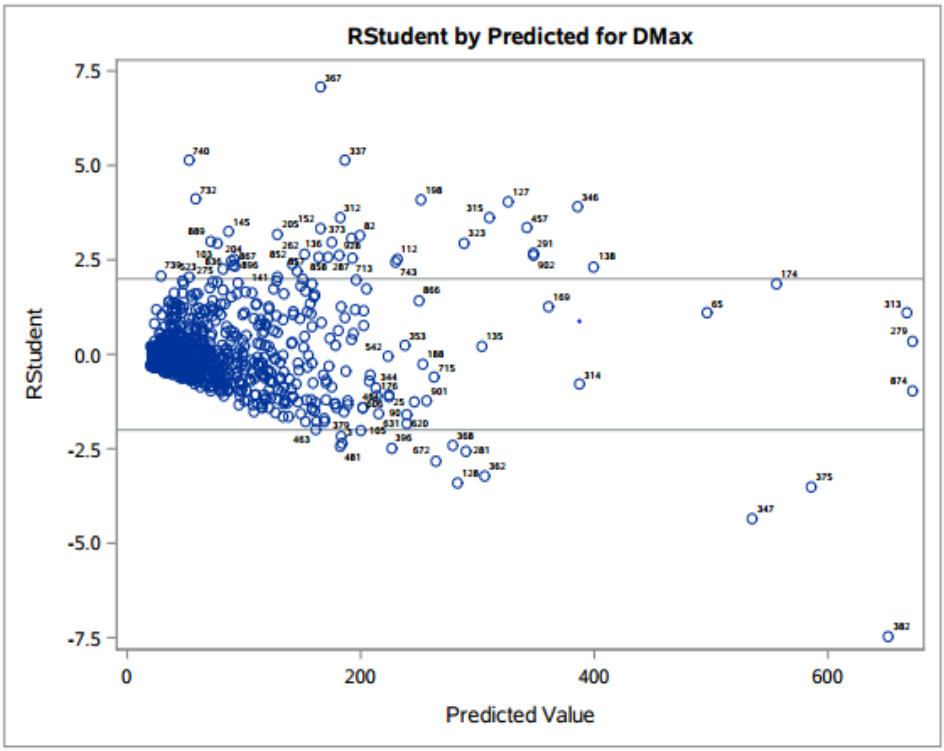

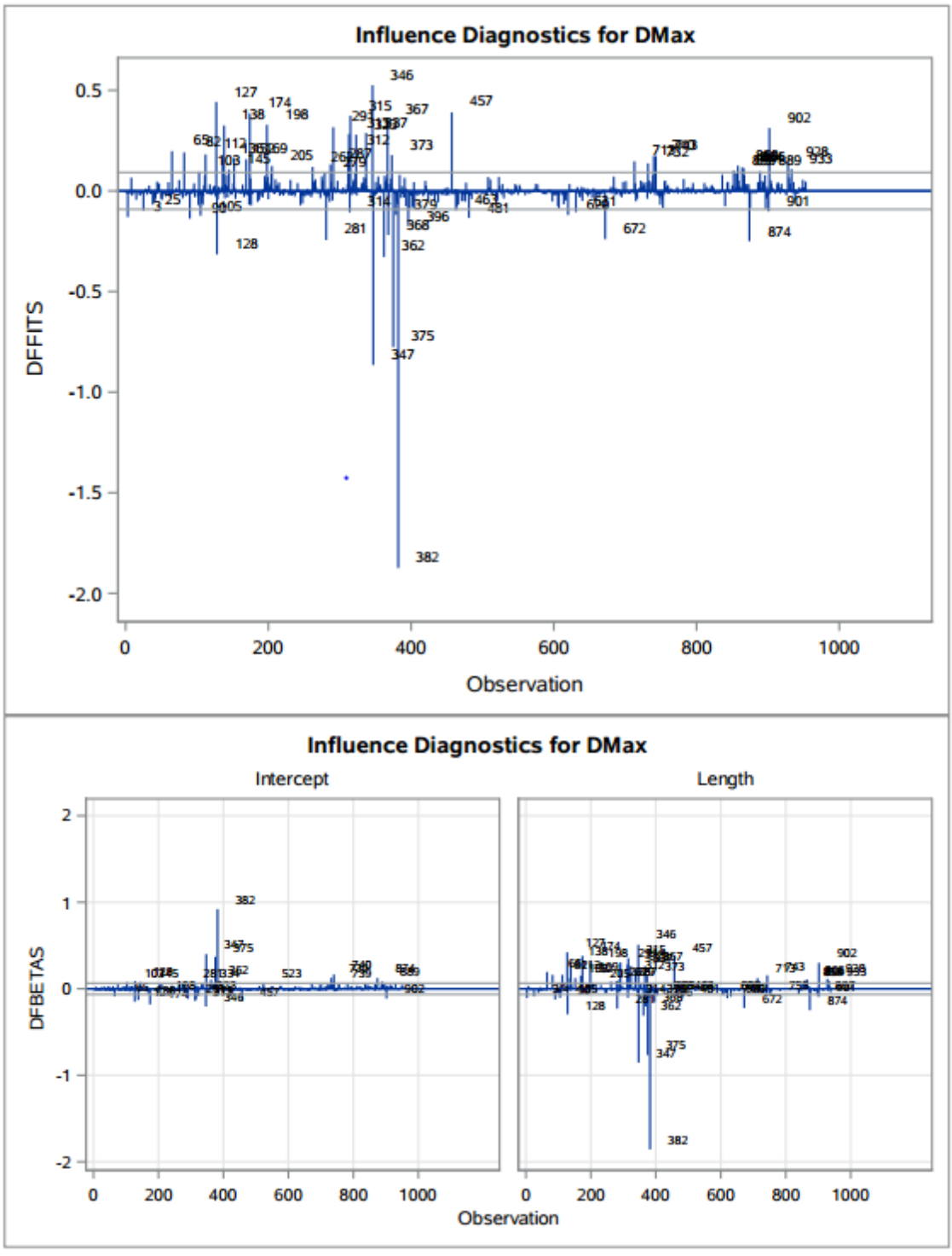
Influence Diagnostics for DMax
DFFITS
Observation
Influence Diagnostics for DMax
Intercept
Length
DFBETAS
Observation

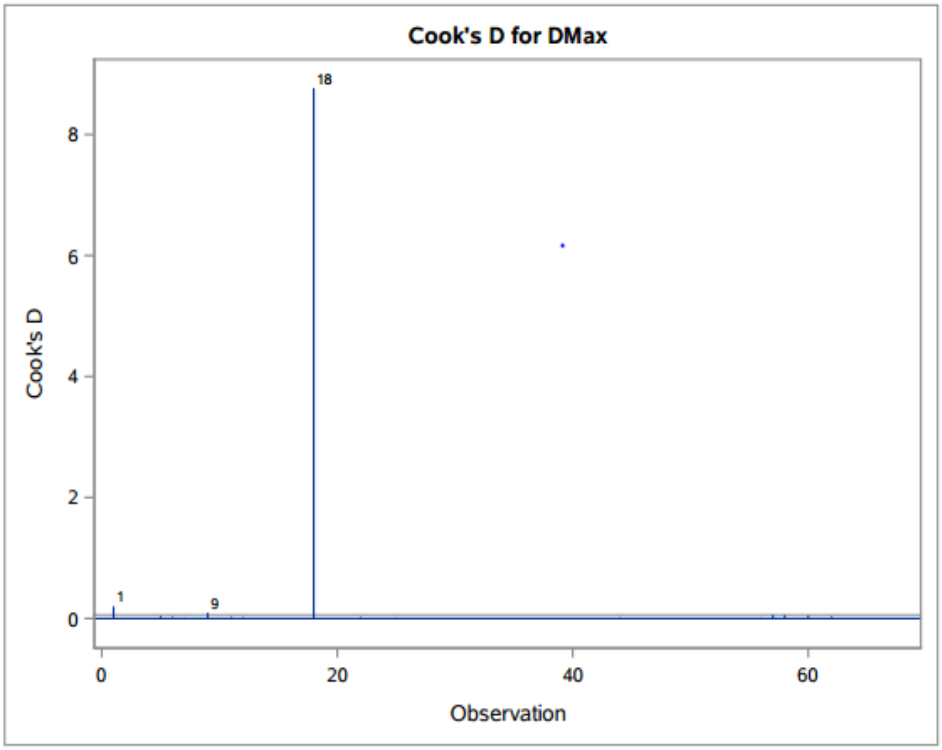
Cook's D for DMax
Cook's D
Observation
18
1
9
0
2
4
6
8
0
20
40
60

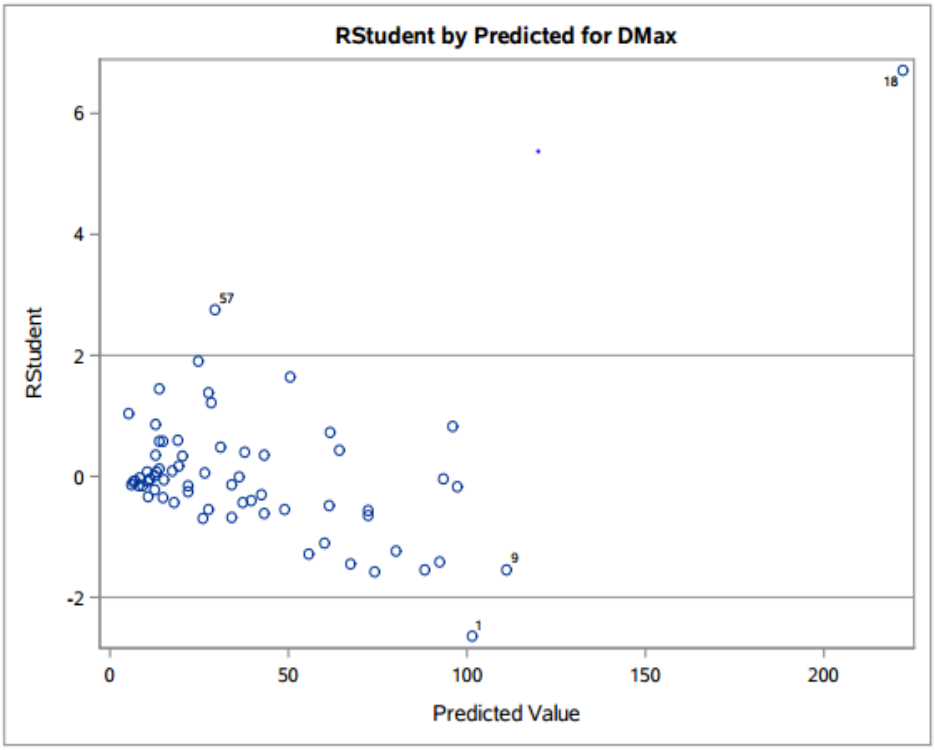
RStudent by Predicted for DMax
RStudent
Predicted Value
18
57
9
1
-2
0
2
4
6
0
50
100
150
200

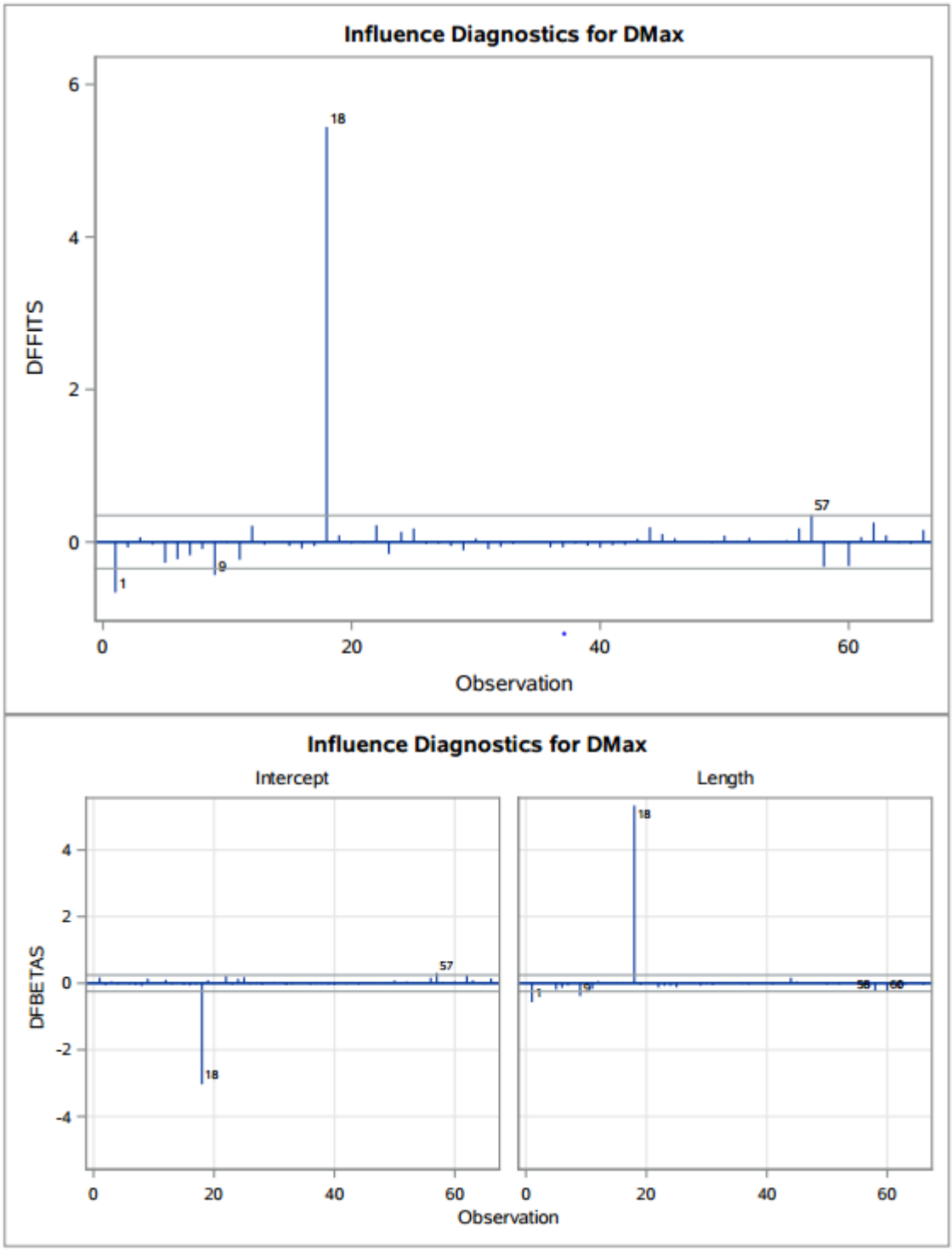
Influence Diagnostics for DMax
DFFITS
6
4
2
0
18
57
9
1
0
20
40
60
Observation
Influence Diagnostics for DMax
Intercept
Length
DFBETAS
4
2
0
-2
-4
57
18
18
1
9
58
60
0
20
40
60
Observation

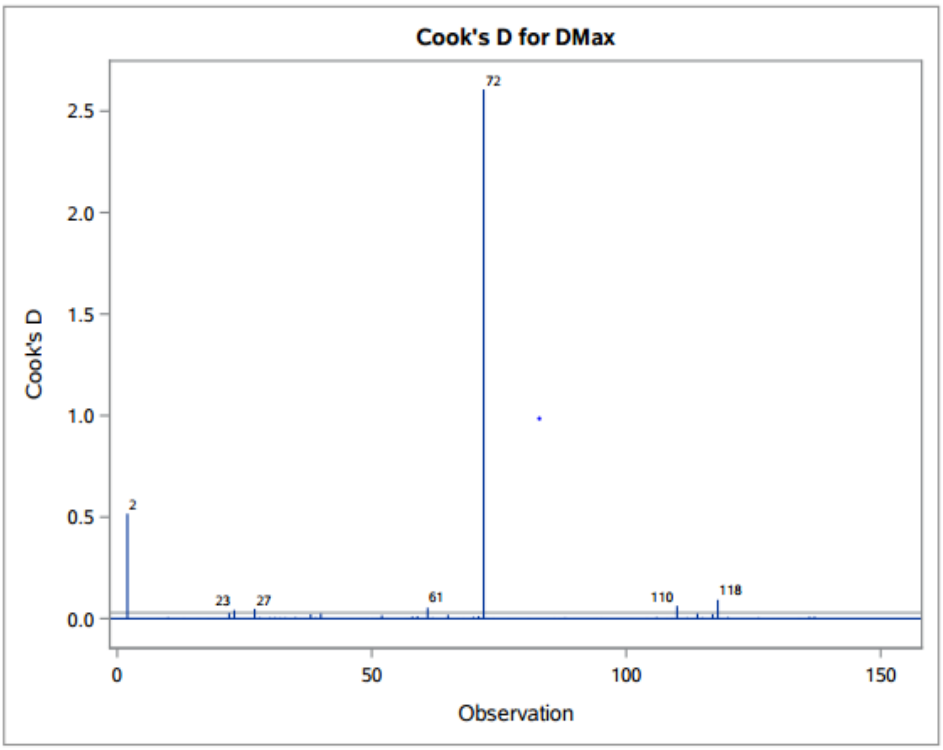
Cook's D for DMax
Cook's D
Observation
72
2
23
27
61
110
118
0.0
0.5
1.0
1.5
2.0
2.5
0
50
100
150

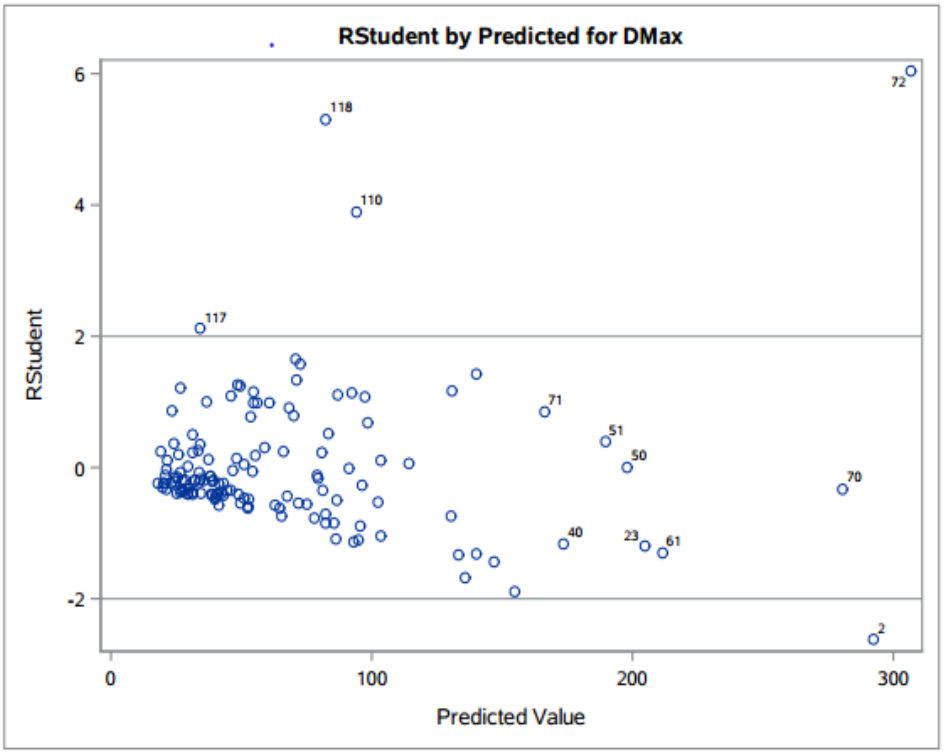
RStudent by Predicted for DMax
RStudent
Predicted Value
72
118
110
117
71
51
50
70
40
23
61
2
6
4
2
0
-2
0
100
200
300

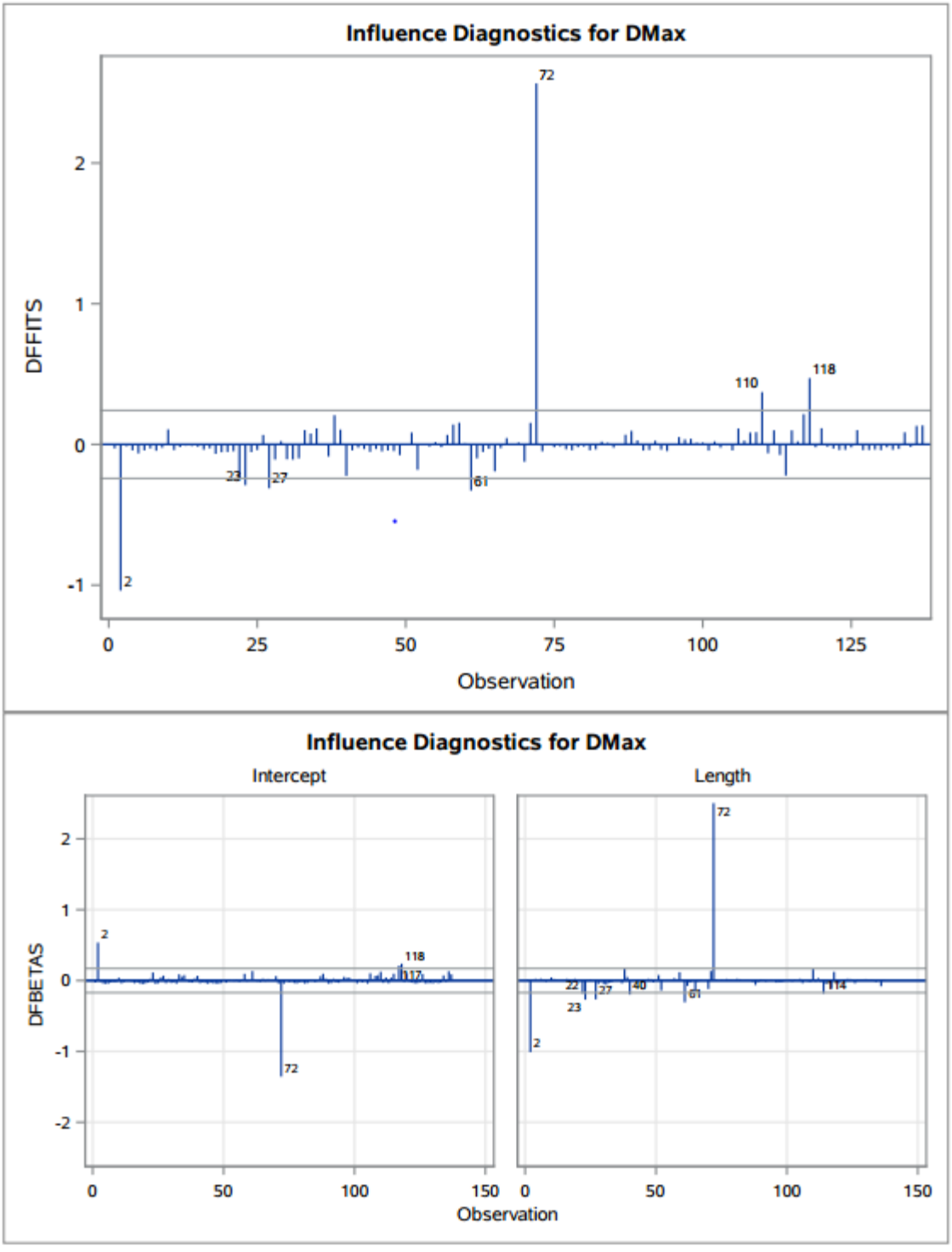
Influence Diagnostics for DMax
DFFITS
Observation
72
110
118
23
27
61
2
Influence Diagnostics for DMax
Intercept
Length
DFBETAS
Observation
2
118
117
72
22
27
40
61
23
114

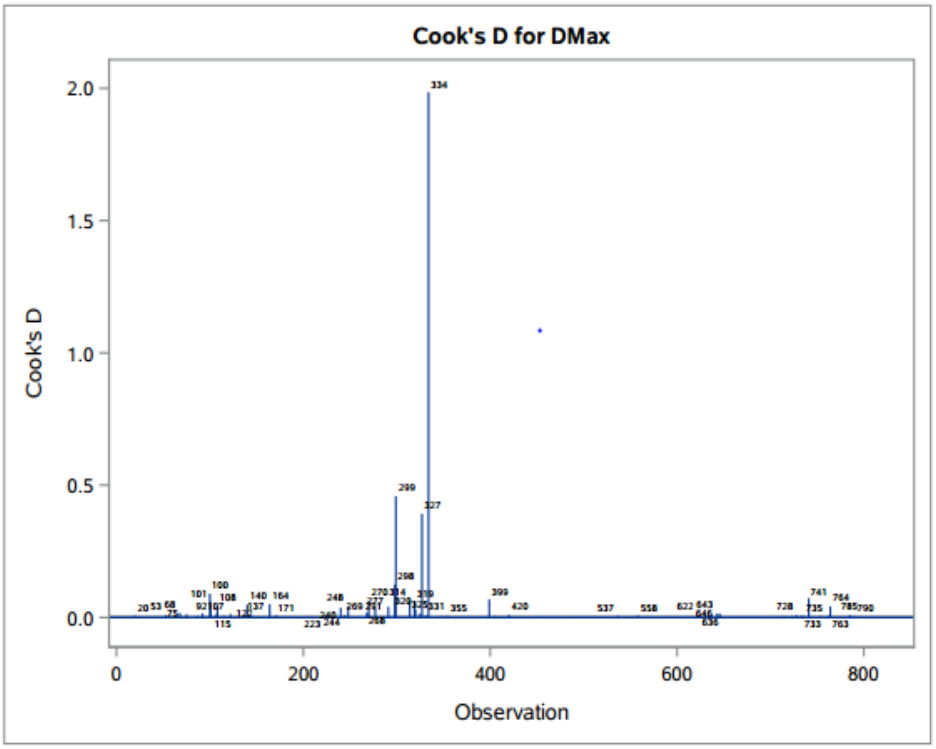
Cook's D for DMax
Cook's D
Observation
0.0
0.5
1.0
1.5
2.0
0
200
400
600
800

+

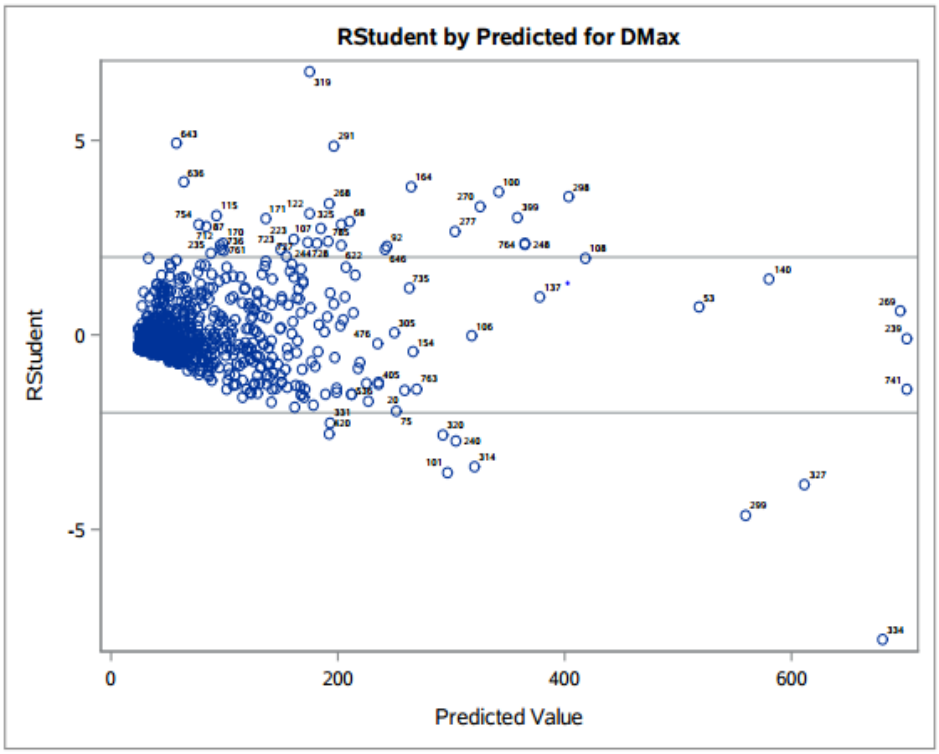
RStudent by Predicted for DMax
RStudent
Predicted Value
5
0
-5
0
200
400
600

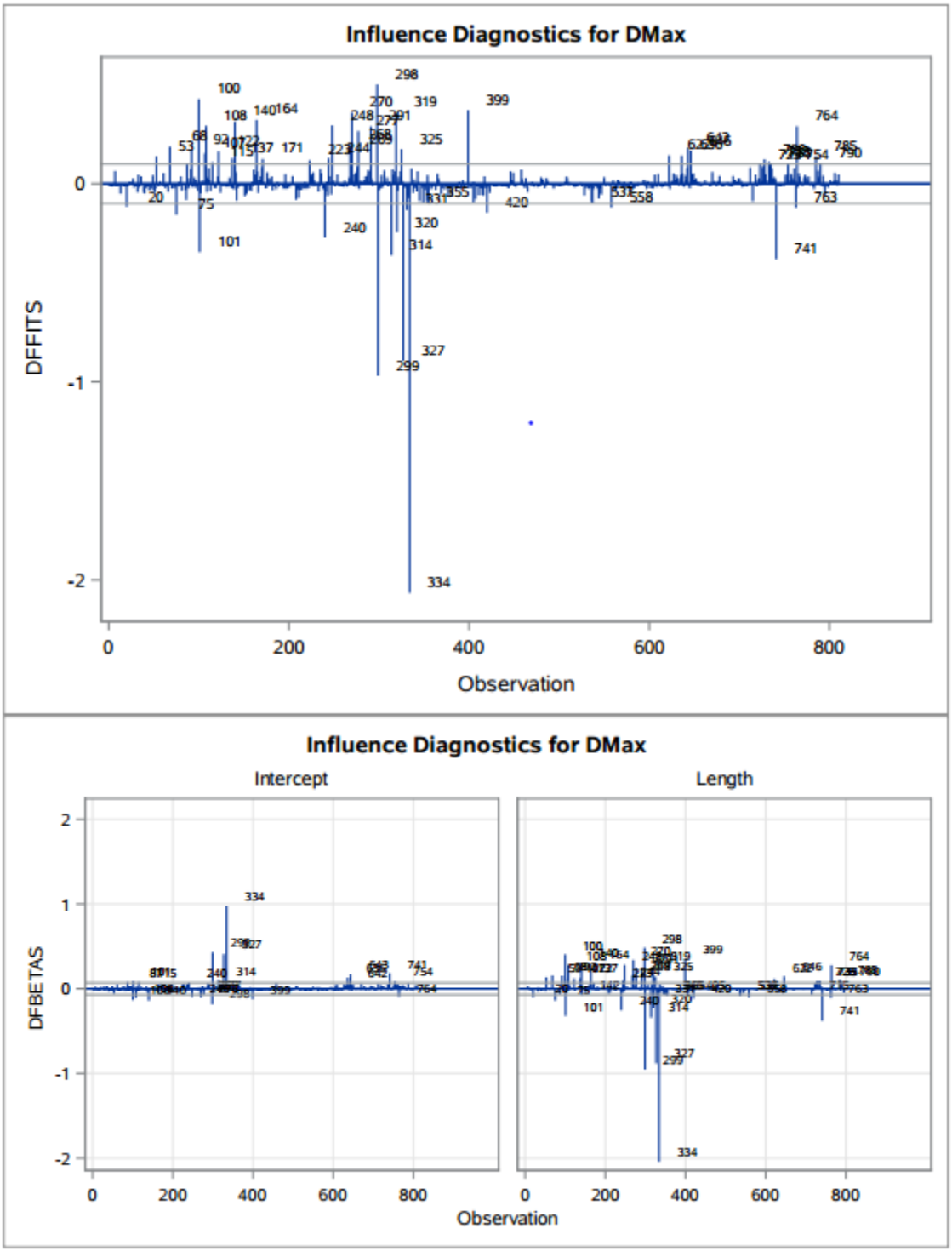
Influence Diagnostics for DMax
DFFITS
Observation
0
200
400
600
800
0
-1
-2
Influence Diagnostics for DMax
Intercept
Length
DFBETAS
Observation
2
1
0
-1
-2
0
200
400
600
800

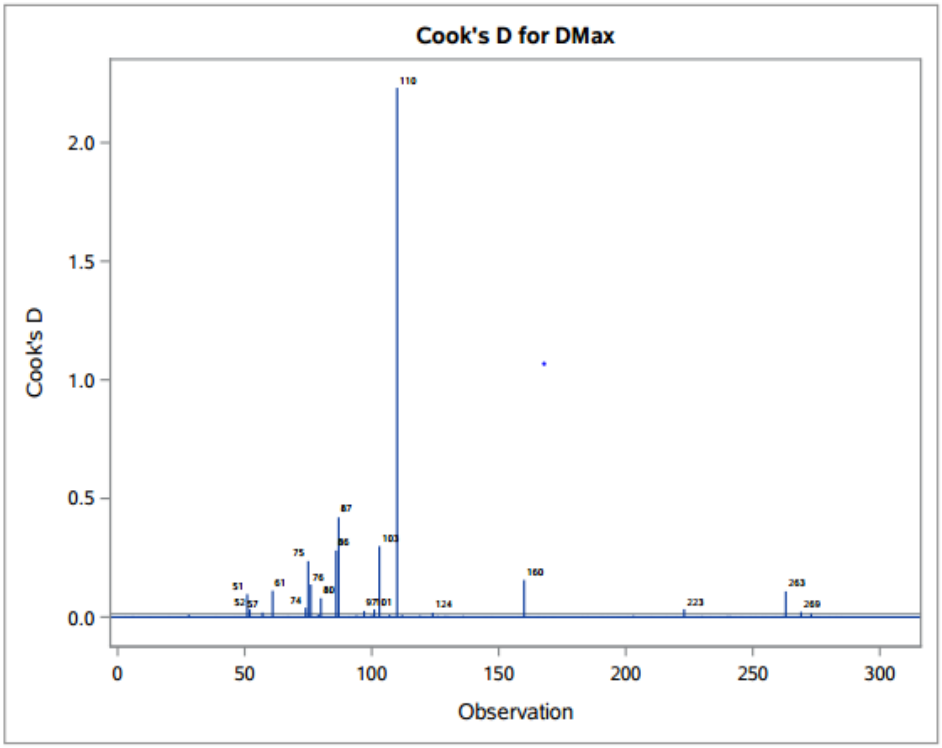
Cook's D for DMax
Cook's D
Observation
0.0
0.5
1.0
1.5
2.0
0
50
100
150
200
250
300
110
87
86
103
75
76
61
51
52
57
74
80
97
101
124
160
223
263
269

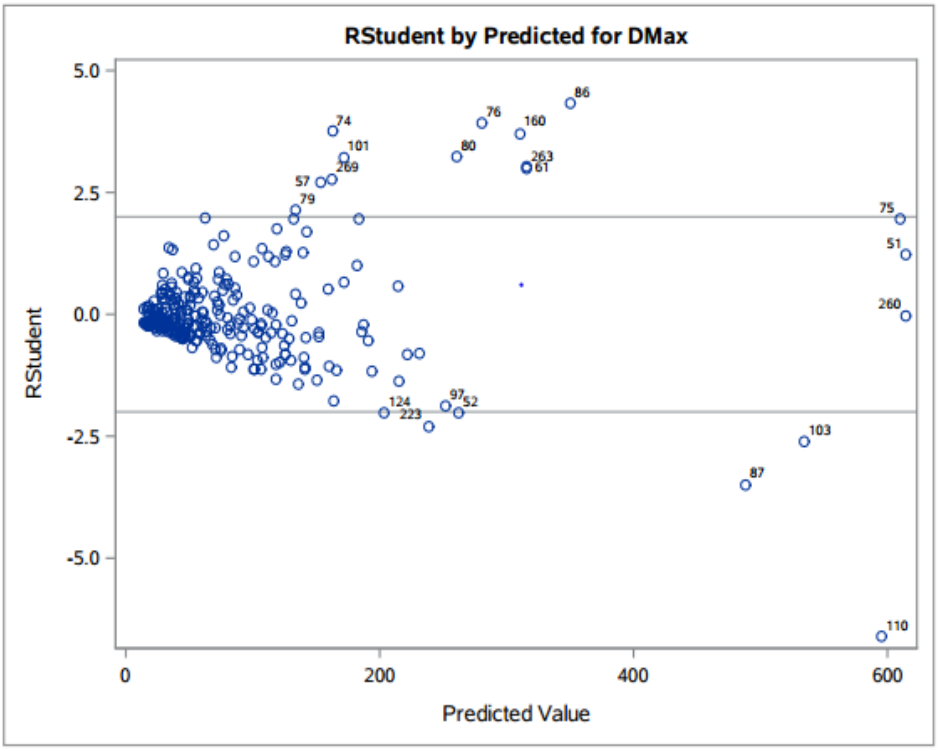
RStudent by Predicted for DMax
RStudent
Predicted Value
5.0
2.5
0.0
-2.5
-5.0
0
200
400
600
86
74
76
160
101
80
263
269
61
57
79
75
51
260
124
223
97
52
103
87
110

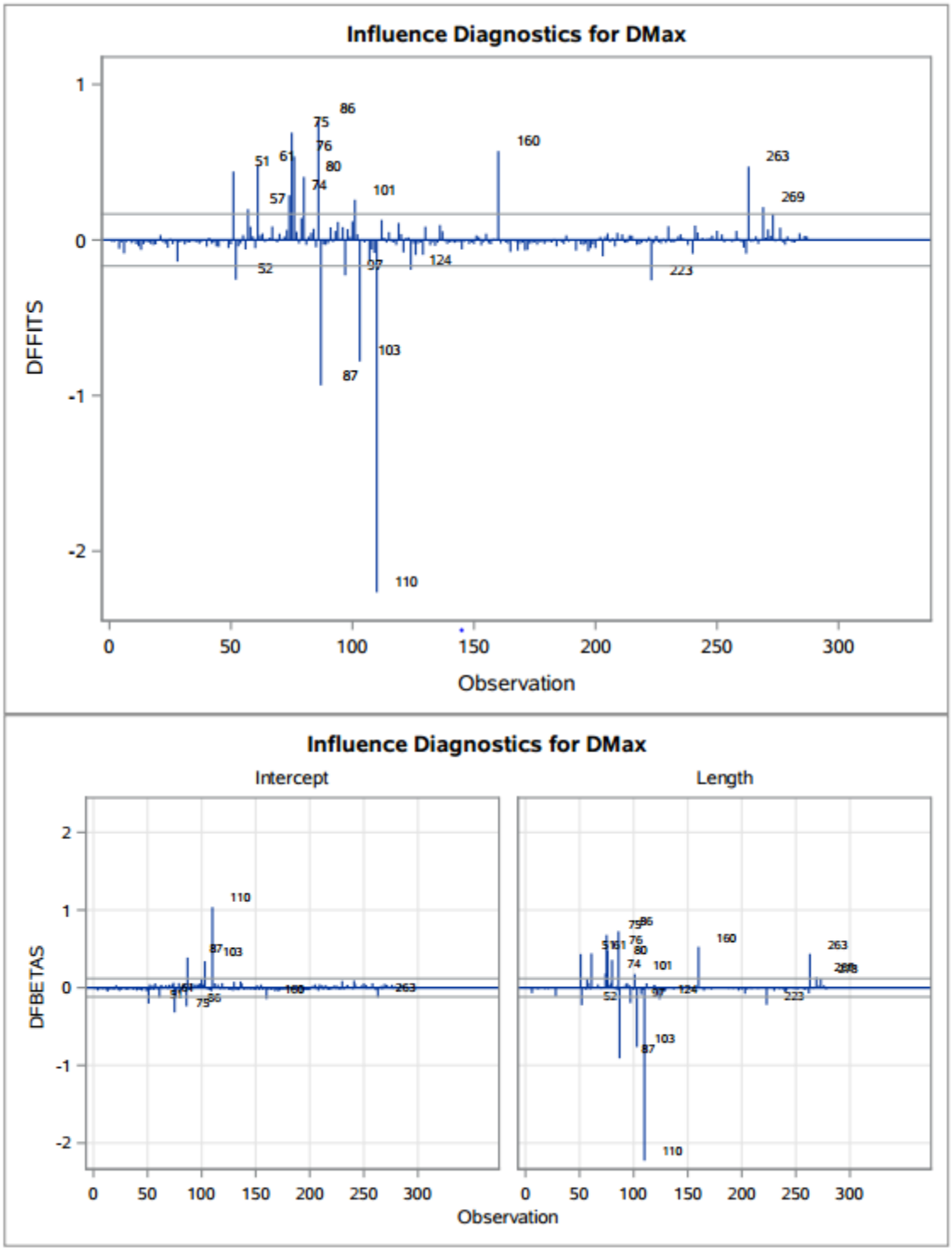
Influence Diagnostics for DMax
DFFITS
Observation
Influence Diagnostics for DMax
Intercept
Length
DFBETAS
Observation

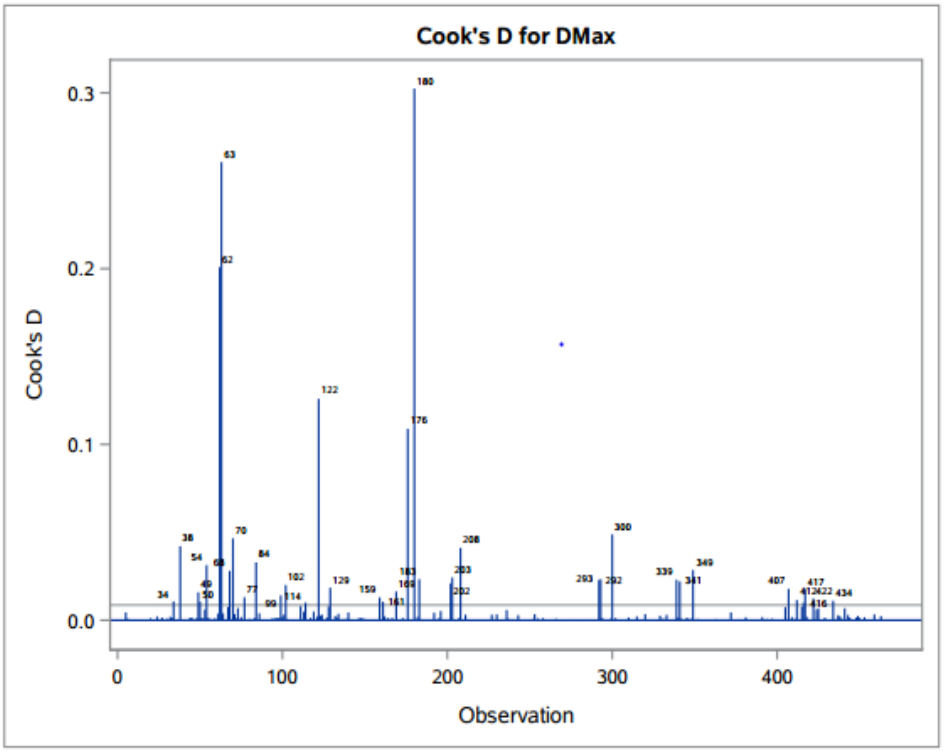
Cook's D for DMax
Cook's D
Observation
0.0
0.1
0.2
0.3
0
100
200
300
400

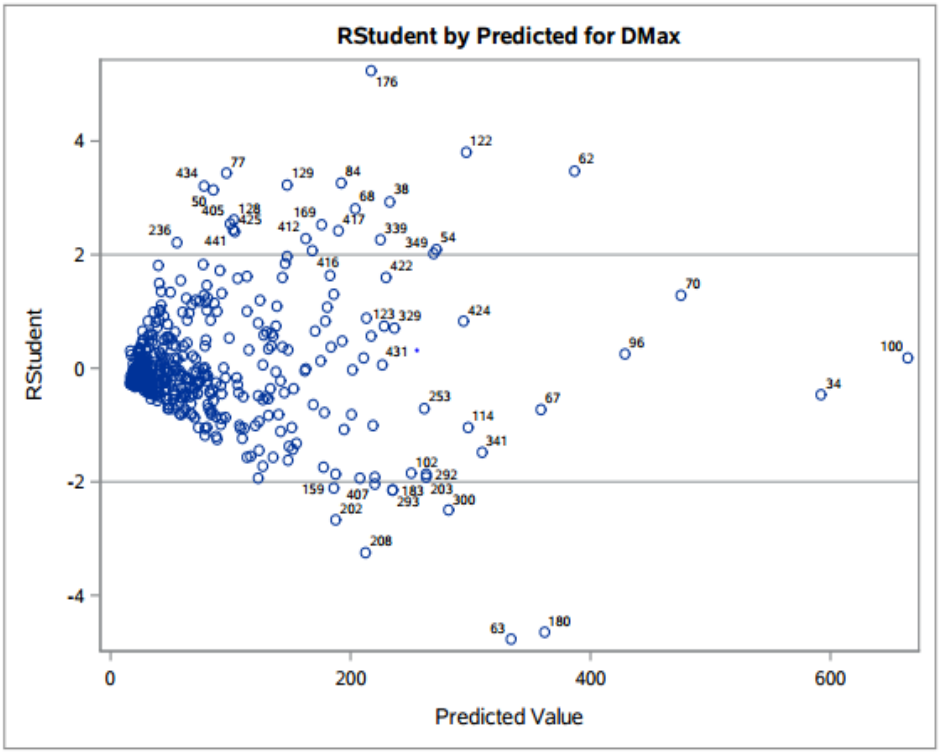
RStudent by Predicted for DMax
RStudent
Predicted Value
-4
-2
0
2
4
0
200
400
600

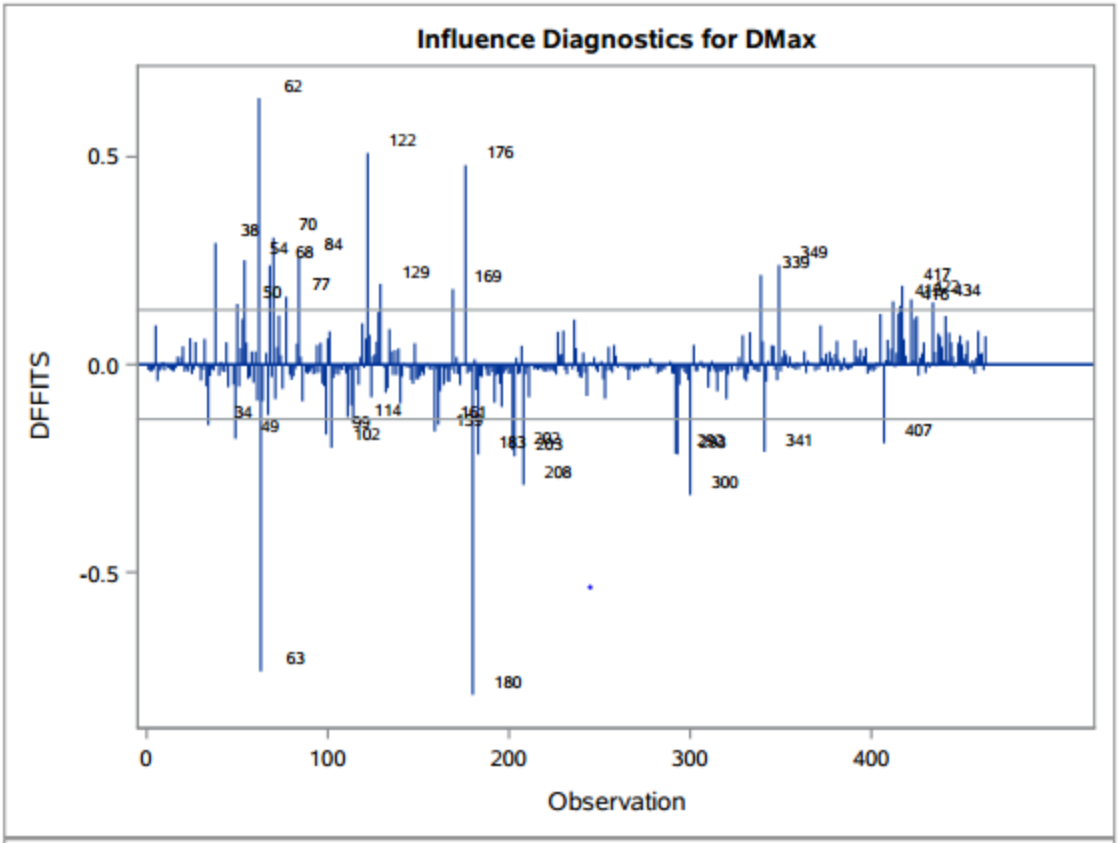
Influence Diagnostics for DMax
DFFITS
0.5
0.0
-0.5
0
100
200
300
400
Observation
62
122
176
38
70
54
68
84
129
169
77
50
339
349
417
434
34
49
114
102
341
407
208
300
63
180

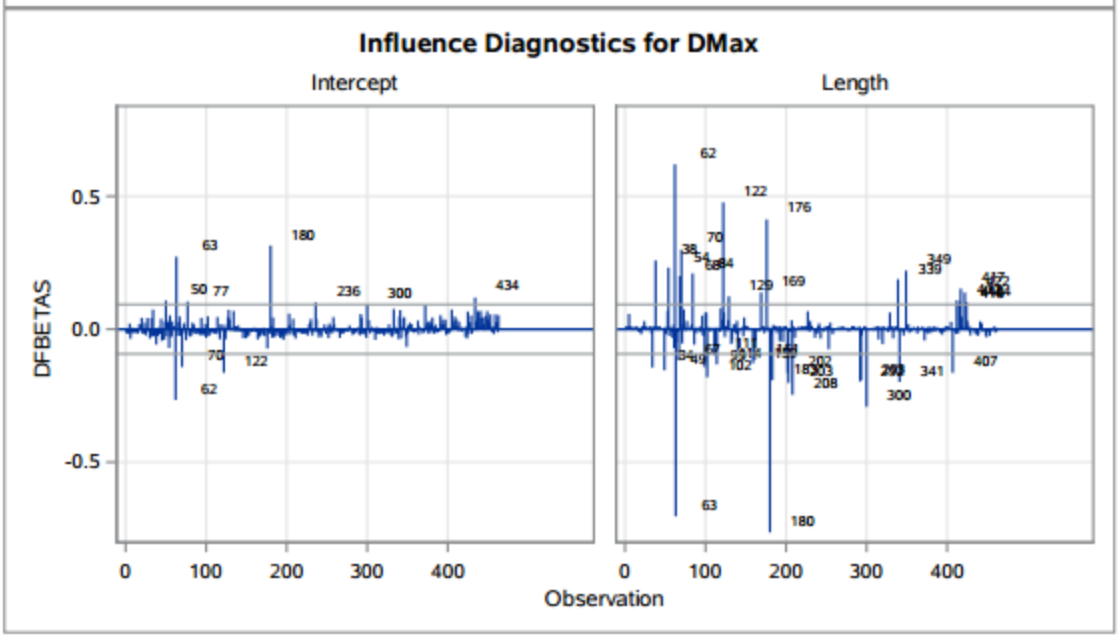
Influence Diagnostics for DMax
Intercept
Length
DFBETAS
0.5
0.0
-0.5
0
100
200
300
400
Observation
63
180
50
77
236
300
434
70
122
62
341
407
208
63
180

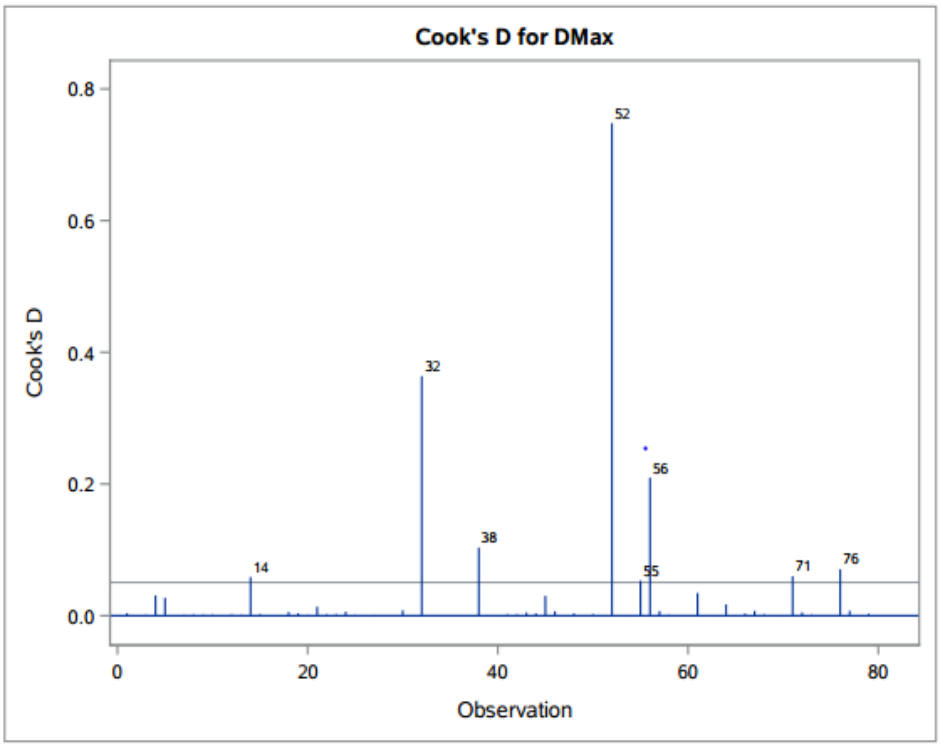
Cook's D for DMax
Cook's D
0.8
0.6
0.4
0.2
0.0
52
32
56
38
14
55
71
76
0
20
40
60
80
Observation

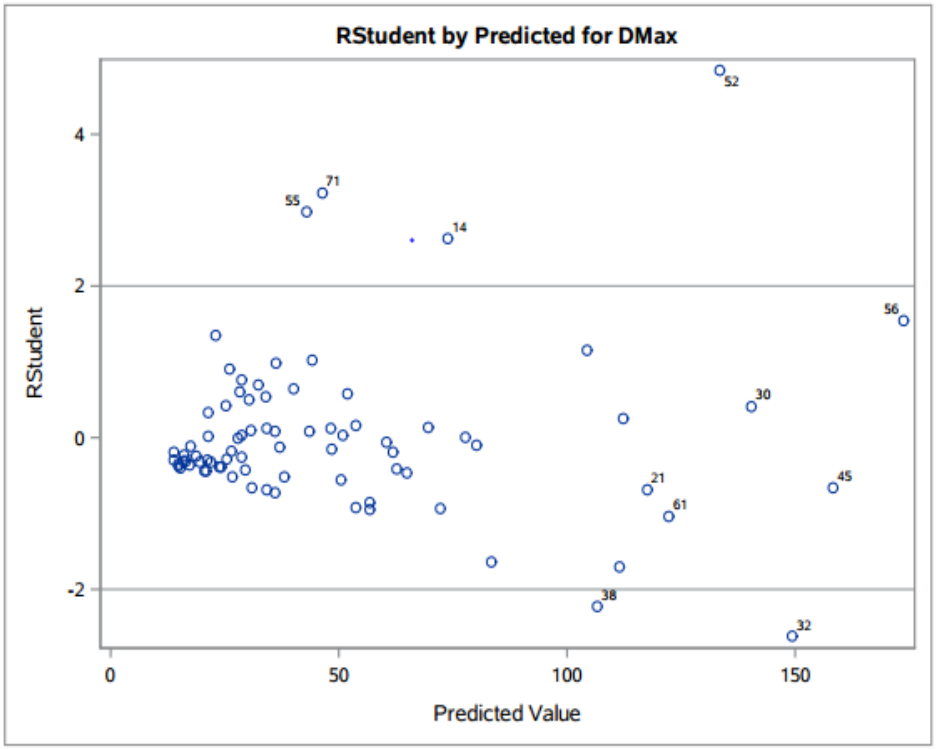
RStudent by Predicted for DMax
RStudent
4
2
0
-2
52
71
55
14
56
30
21
61
45
38
32
0
50
100
150
Predicted Value

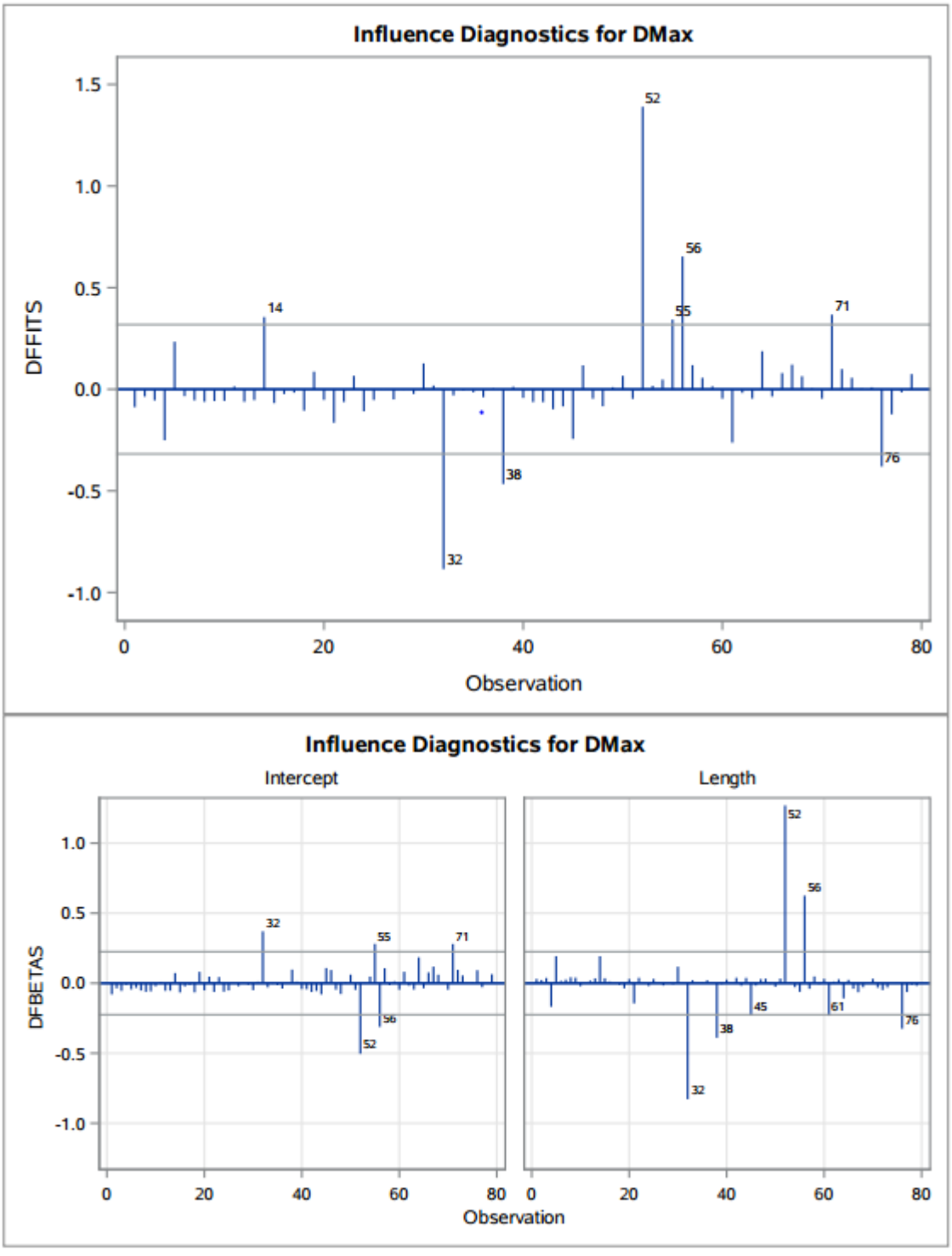
Influence Diagnostics for DMax
DFFITS
1.5
1.0
0.5
0.0
-0.5
-1.0
52
56
14
55
71
38
76
32
0
20
40
60
80
Observation
Influence Diagnostics for DMax
Intercept
Length
DFBETAS
1.0
0.5
0.0
-0.5
-1.0
32
55
71
56
52
52
56
45
38
61
76
32
0
20
40
60
80
Observation

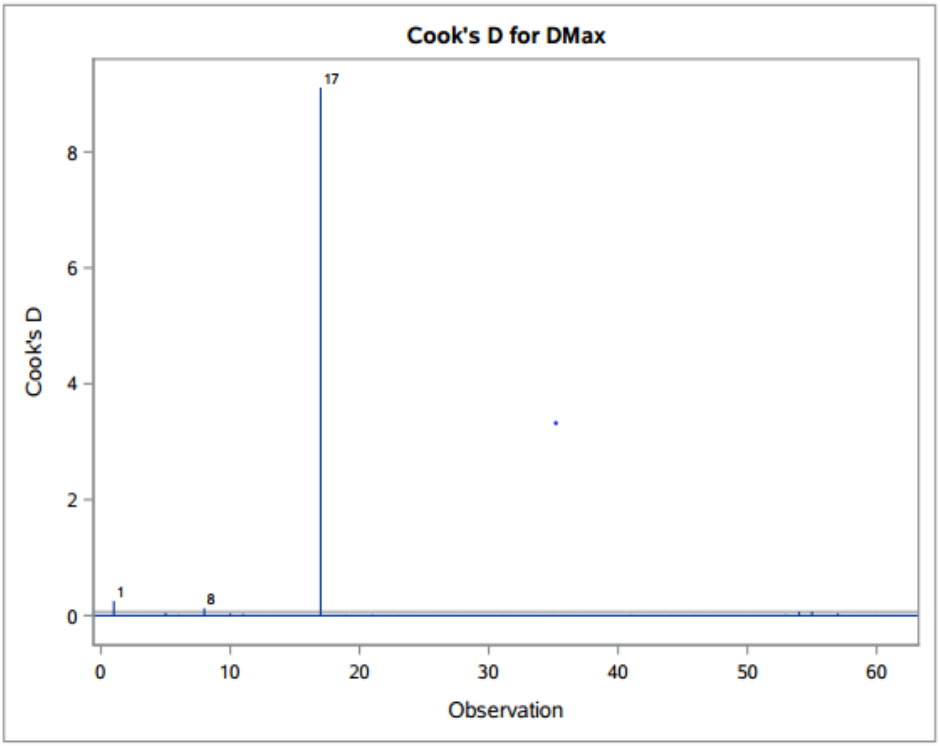
Cook's D for DMax
Cook's D
Observation
17
1
8
0
2
4
6
8
0
10
20
30
40
50
60

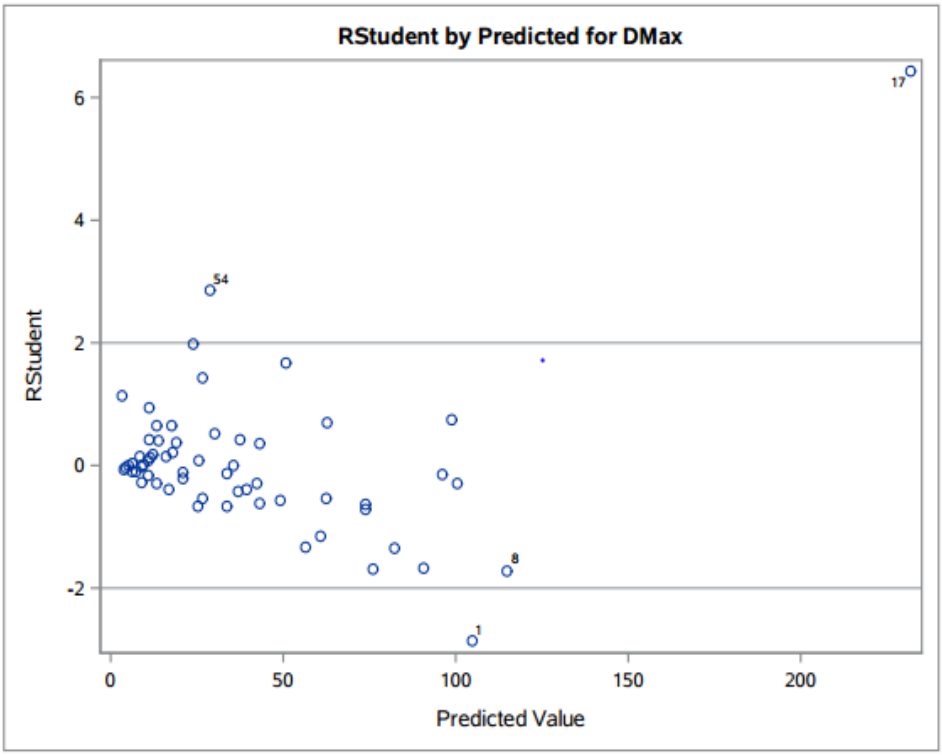
RStudent by Predicted for DMax
RStudent
Predicted Value
17
54
8
1
6
4
2
0
-2
0
50
100
150
200

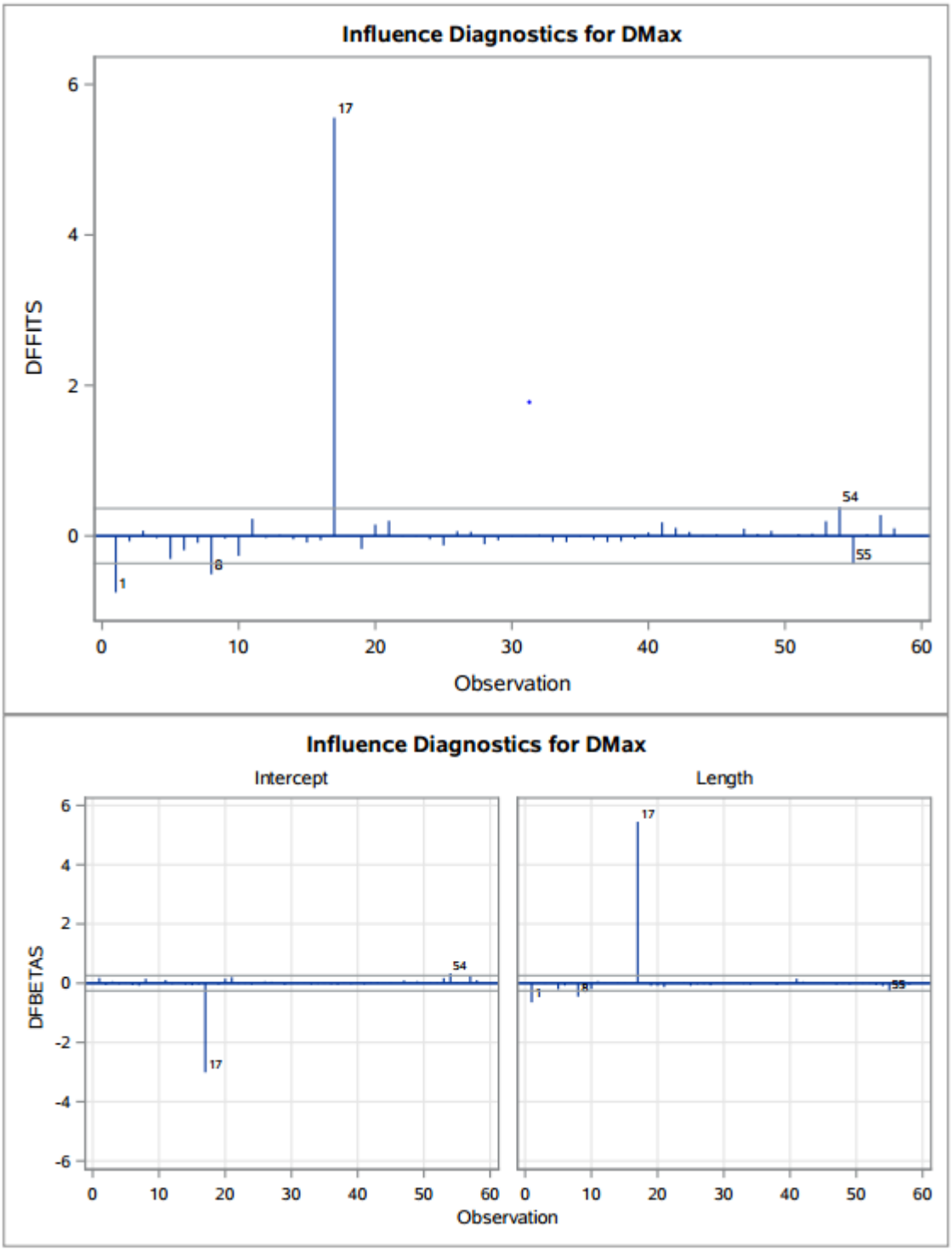
Influence Diagnostics for DMax
DFFITS
Observation
17
54
55
8
1
Influence Diagnostics for DMax
Intercept
Length
DFBETAS
Observation

PAPER II

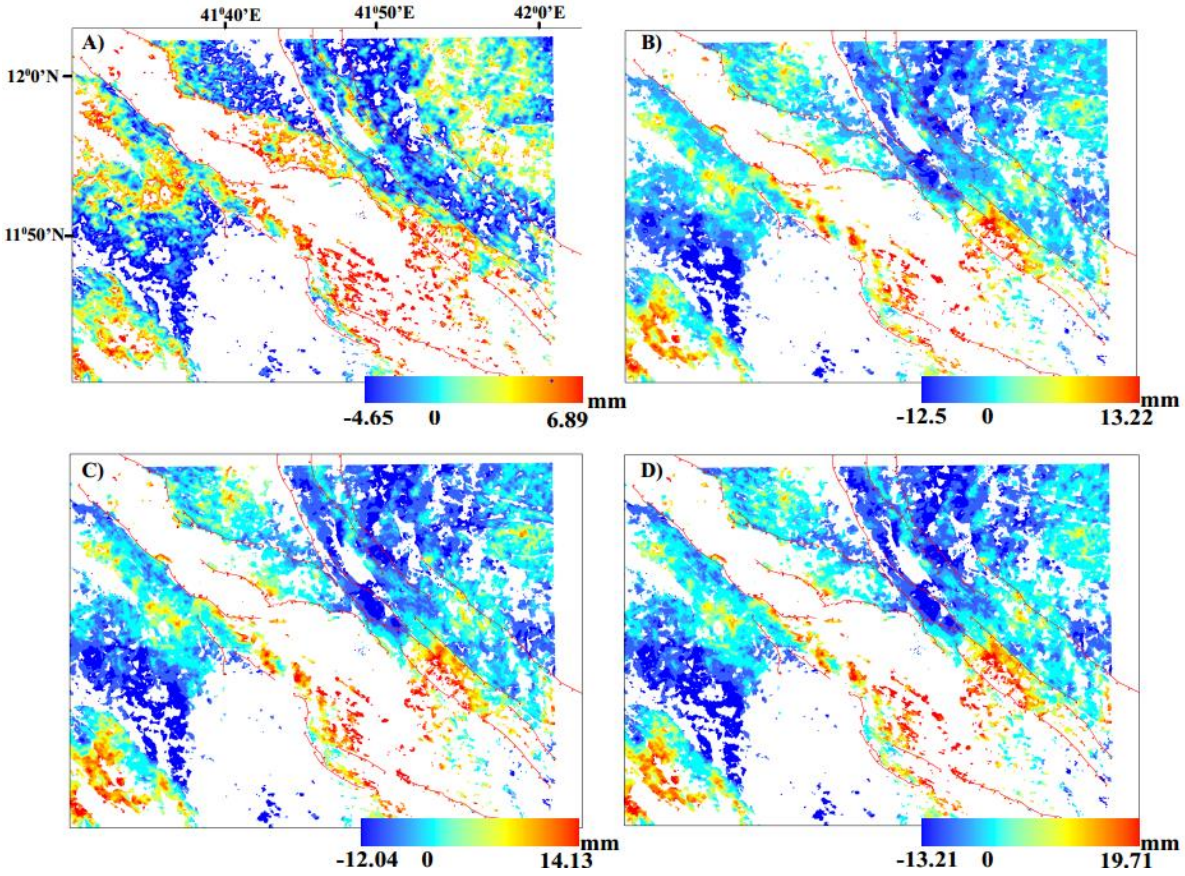

Appendices **1:** SBA time series displacement map acquired on A) October 30, 2007; B) November 18, 2008; C) December 23, 2008; D) January 27, 2009.

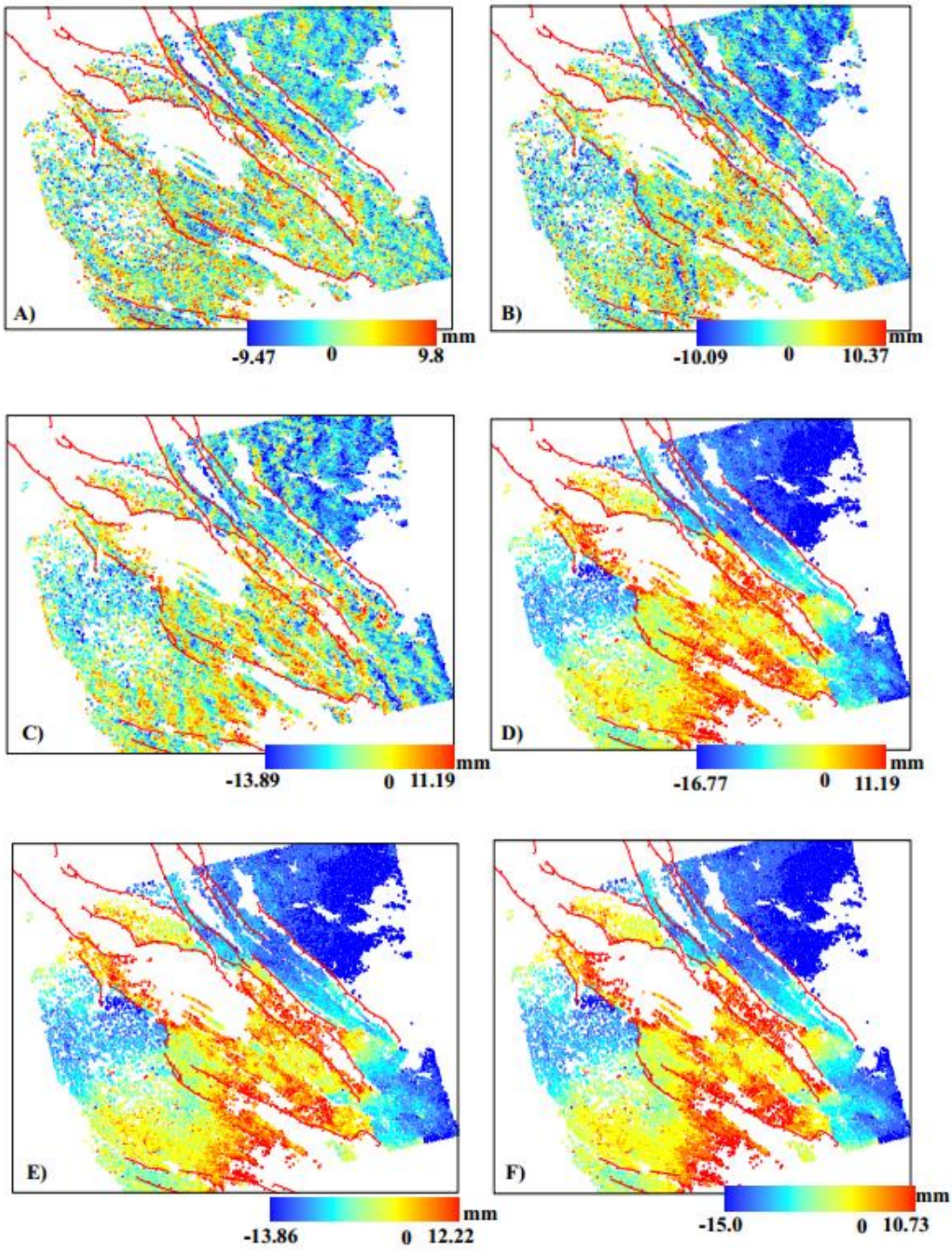
A)
mm
-9.47
0
9.8
B)
mm
-10.09
0
10.37
C)
mm
-13.89
0
11.19
D)
mm
-16.77
0
11.19
E)
mm
-13.86
0
12.22
F)
mm
-15.0
0
10.73

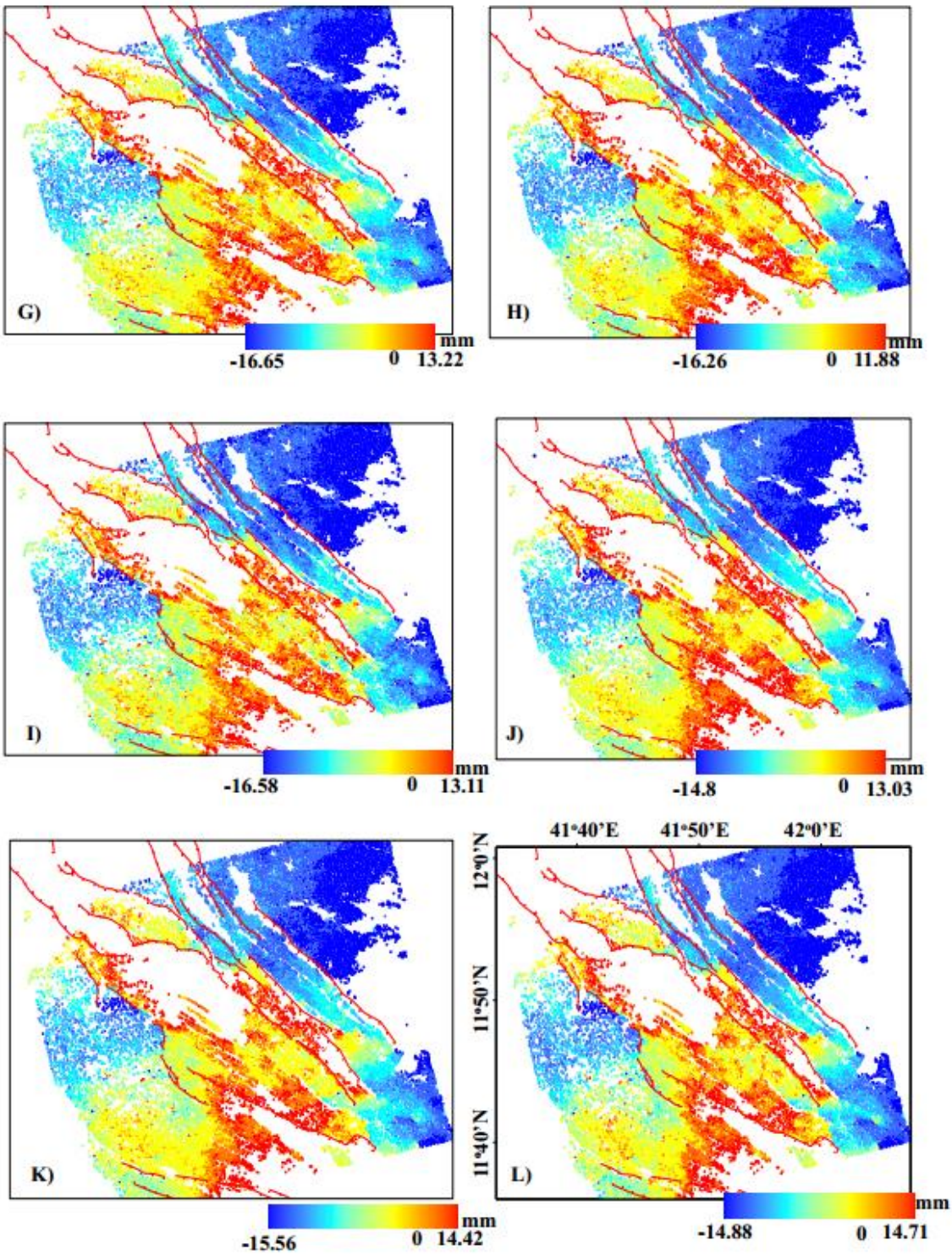

Appendices **2:** QPS time series displacement map acquired on A) August 3, 2007; B) September 7, 2007; C) October 12, 2008; D) December 5, 2008; E) January 9, 2009; F) February 13, 2009; G) March 20, 2009; H) April 24, 2009; I) July 3, 2009; J) August 7, 2009; K) September 11, 2009; and L) October 16, 2009.

Appendices **3:** Temporal and small baseline for persistent scaterrer (PS) technique

Coherence Precision reference = 0.75

Average Ps Number Accuracy = 200

Date[25-NOV-2003][20031125_09078_slc] MEAN BASELINE [152.018 m]
PRECISION [Velocity = 0.498051 mm/year Height = 0.00208616 m]

Date[09-MAR-2004][20040309_10581_slc] MEAN BASELINE [-360.907 m]
PRECISION [Velocity = 0.504219 mm/year Height = 0.00208423 m]

Date[18-MAY-2004][20040518_11583_slc] MEAN BASELINE [-111.15 m]
PRECISION [Velocity = 0.515824 mm/year Height = 0.002079 m]

Date[31-AUG-2004][20040831_13086_slc] MEAN BASELINE [-67.1979 m]
PRECISION [Velocity = 0.543056 mm/year Height = 0.00206184 m]

Date[05-OCT-2004][20041005_13587_slc] MEAN BASELINE [-405.787 m]
PRECISION [Velocity = 0.555719 mm/year Height = 0.00205252 m]

Date[09-NOV-2004][20041109_14088_slc] MEAN BASELINE [469.37 m]
PRECISION [Velocity = 0.57329 mm/year Height = 0.00204032 m]

Date[14-DEC-2004][20041214_14589_slc] MEAN BASELINE [480.345 m]
PRECISION [Velocity = 0.596584 mm/year Height = 0.00202515 m]

Date[03-MAY-2005][20050503_16593_slc] MEAN BASELINE [-888.869 m]
PRECISION [Velocity = 0.73482 mm/year Height = 0.00194411 m]

Date[05-FEB-2007][20070205_25797_slc] MEAN BASELINE [42.4019 m]
PRECISION [Velocity = 1.12615 mm/year Height = 0.00360552 m]

Date[12-MAR-2007][20070312_26298_slc] MEAN BASELINE [-235.165 m] PRECISION [Velocity = 1.05345 mm/year Height = 0.00362827 m]

Date[16-APR-2007][20070416_26799_slc] MEAN BASELINE [-10.6447 m] PRECISION [Velocity = 0.989304 mm/year Height = 0.00362852 m]

Date[21-MAY-2007][20070522_27300_slc] MEAN BASELINE [93.5357 m] PRECISION [Velocity = 0.929431 mm/year Height = 0.00360212 m]

Date[25-JUN-2007][20070625_27801_slc] MEAN BASELINE [-19.8566 m] PRECISION [Velocity = 0.872211 mm/year Height = 0.00355075 m]

Date[30-JUL-2007][20070730_28302_slc] MEAN BASELINE [101.297 m] PRECISION [Velocity = 0.817292 mm/year Height = 0.00348077 m]

Date[21-AUG-2007][20070821_28617_slc] MEAN BASELINE [127.873 m] PRECISION [Velocity = 0.912818 mm/year Height = 0.00308104 m]

Date[03-SEP-2007][20070903_28803_slc] MEAN BASELINE [10.0582 m] PRECISION [Velocity = 0.771225 mm/year Height = 0.003415 m]

Date[08-OCT-2007][20071008_29304_slc] MEAN BASELINE [86.5506 m] PRECISION [Velocity = 0.735419 mm/year Height = 0.0033637 m]

Date[30-OCT-2007][20071030_29619_slc] MEAN BASELINE [28.839 m] PRECISION [Velocity = 0.812564 mm/year Height = 0.00292483 m]

Date[12-NOV-2007][20071112_29805_slc] MEAN BASELINE [-86.4138 m] PRECISION [Velocity = 0.704168 mm/year Height = 0.00331195 m]

Date[05-JAN-2008][20080105_30578_slc] MEAN BASELINE [0 m] PRECISION [Velocity = 0.678421 mm/year Height = 0.00298577 m]

Date[21-JAN-2008][20080121_30807_slc] MEAN BASELINE [154.195 m] PRECISION [Velocity = 0.655641 mm/year Height = 0.00322656 m]

Date[25-FEB-2008][20080225_31308_slc] MEAN BASELINE [187.878 m]
PRECISION [Velocity = 0.634041 mm/year Height = 0.00317493 m]

Date[09-JUN-2008][20080609_32811_slc] MEAN BASELINE [-103.843 m]
PRECISION [Velocity = 0.57028 mm/year Height = 0.00300017 m]

Date[14-JUL-2008][20080714_33312_slc] MEAN BASELINE [-216.721 m]
PRECISION [Velocity = 0.551067 mm/year Height = 0.00294252 m]

Date[18-NOV-2008][20081118_35130_slc] MEAN BASELINE [120.407 m]
PRECISION [Velocity = 0.535156 mm/year Height = 0.00230805 m]

Date[23-DEC-2008][20081223_35631_slc] MEAN BASELINE [185.358 m]
PRECISION [Velocity = 0.524314 mm/year Height = 0.00228082 m]

Date[27-JAN-2009][20090127_36132_slc] MEAN BASELINE [268.206 m]
PRECISION [Velocity = 0.520702 mm/year Height = 0.00227174 m]

Reference Date[03-SEP-2007][20070903_28803_slc] PRECISION [Velocity = 0.771225 mm/year Height = 0.003415 m]

Slave file [05-FEB-2007] [20070205_25797_slc] Normal Baseline = -88.828 m

Slave file [12-MAR-2007] [20070312_26298_slc] Normal Baseline = 227.893 m

Slave file [16-APR-2007] [20070416_26799_slc] Normal Baseline = 97.5791 m

Slave file [21-MAY-2007] [20070522_27300_slc] Normal Baseline = -76.8034 m

Slave file [25-JUN-2007] [20070625_27801_slc] Normal Baseline = 45.2256 m

Slave file [30-JUL-2007] [20070730_28302_slc] Normal Baseline = -92.0626 m

Slave file [08-OCT-2007] [20071008_29304_slc] Normal Baseline = -108.296 m

Slave file [12-NOV-2007] [20071112_29805_slc] Normal Baseline = 93.9221 m

Slave file [21-JAN-2008] [20080121_30807_slc] Normal Baseline = -139.217 m

Slave file [25-FEB-2008] [20080225_31308_slc] Normal Baseline = -173.202 m

Slave file [09-JUN-2008] [20080609_32811_slc] Normal Baseline = 113.143 m

Slave file [14-JUL-2008] [20080714_33312_slc] Normal Baseline = 221.345 m

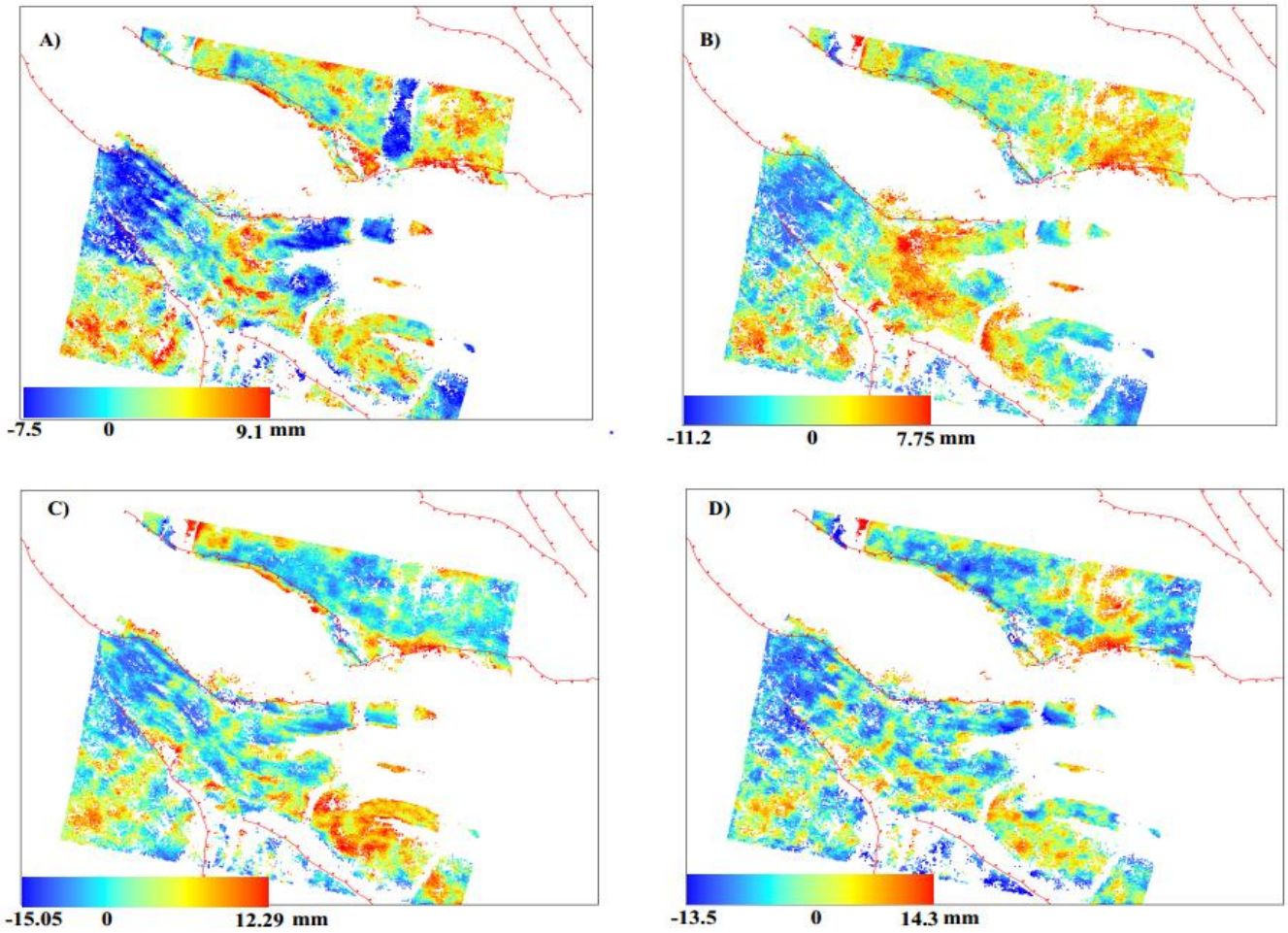
A)
-7.5
0
9.1 mm
B)
-11.2
0
7.75 mm
C)
-15.05
0
12.29 mm
D)
-13.5
0
14.3 mm

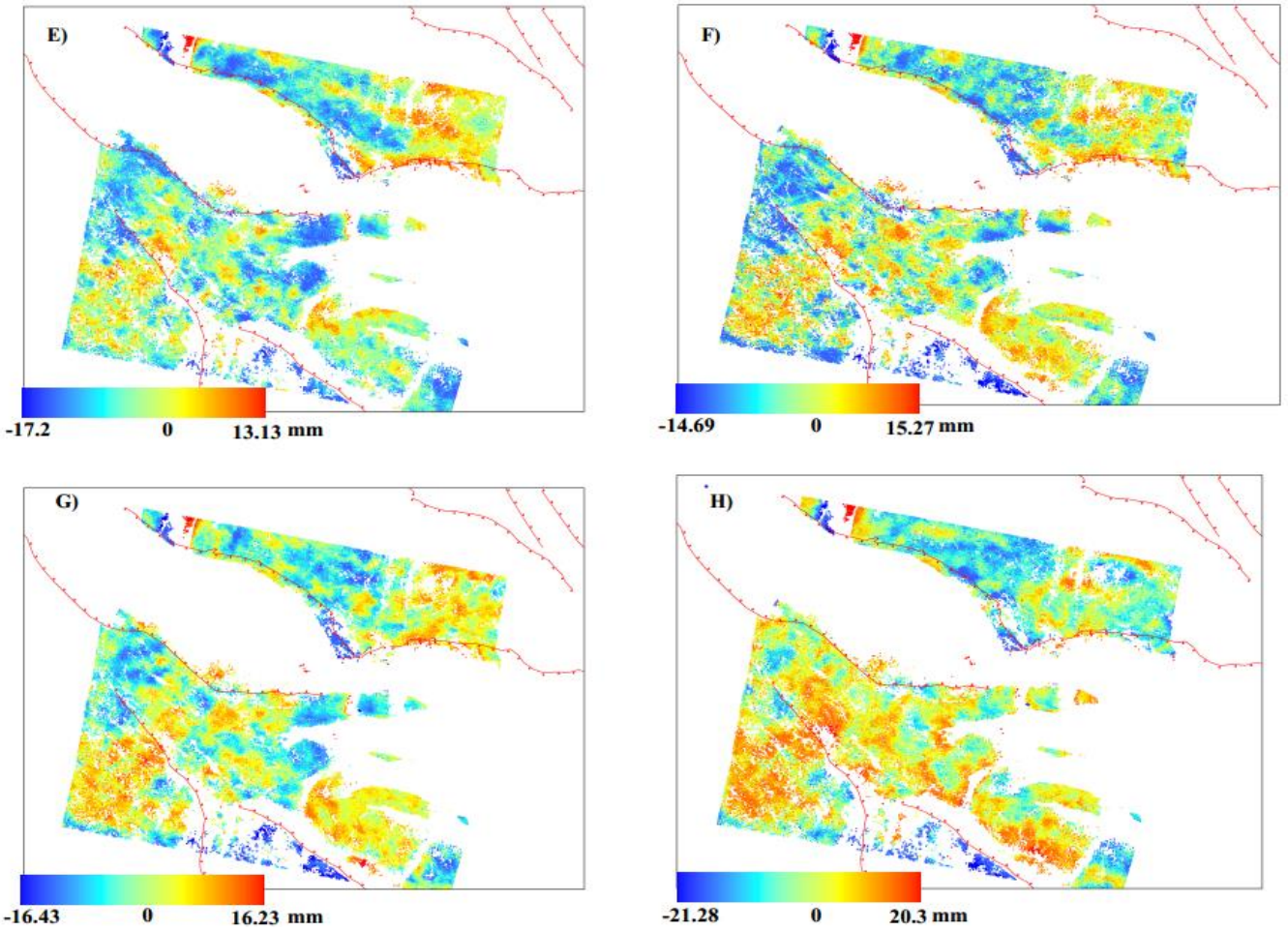
E)
-17.2
0
13.13 mm
F)
-14.69
0
15.27 mm
G)
-16.43
0
16.23 mm
H)
-21.28
0
20.3 mm

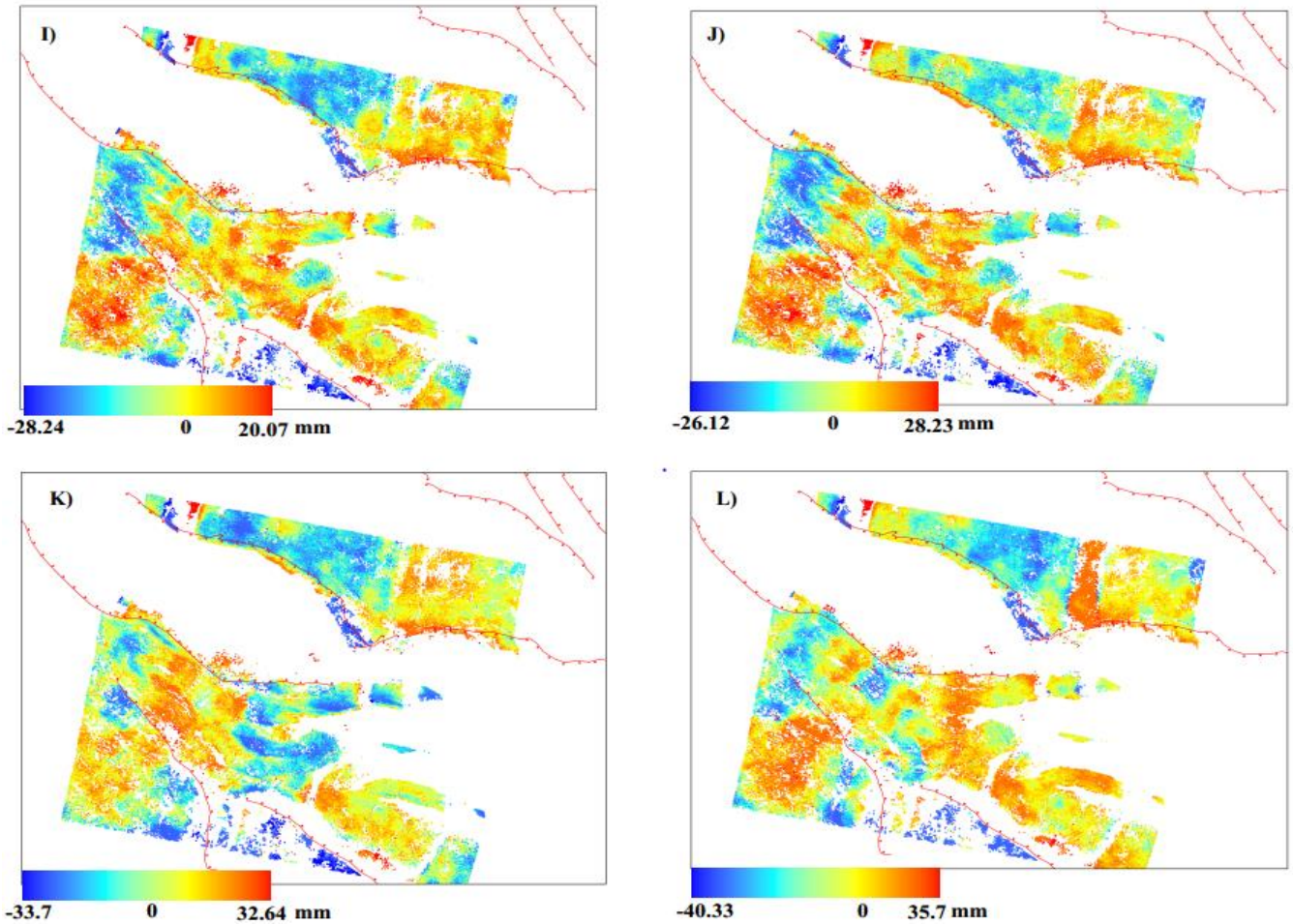

Appendices **4: Persistent Scaterer (**PS) time series displacement map acquired on A) March 3, 2007; B) April 16, 2007; C) May 21, 2008; D) June 25, 2008; E) July 20, 2009; F) September 3, 2009; G) October 8, 2009; H) November 12, 2009; I) January 21, 2009; J) February 25, 2009; K) June 9, 2009; and L) July 14, 2009.

Appendices **1**: Magnetic susceptibility values resulting from varying the magnetic susceptibility values used for different element in the two-dimensional (2D) magnetic and gravity model in Figure 9 within -25% (lower limit) and +25% (upper limit) at 5% increment.

		Lower Limits					**Final model**					**Upper Limits**
Polygon #	**Model unit**	**SI value varied by -25%**	**SI value varied by -20%**	**SI value varied by -15%**	**SI value varied by -10%**	**SI value varied by -5%**	**Magnetics (SI)**	**SI value varied by +5%**	**SI value varied by 10%**	**SI value varied by +15%**	**SI value varied by +20%**	**SI value varied by +25%**
1	Sediment	2.460E-03	2.624E-03	2.788E-03	2.952E-03	3.263E-03	**3.280E-03**	3.296E-03	3.608E-03	3.772E-03	3.936E-03	4.100E-03
2		9.428E-06	1.006E-05	1.068E-05	1.131E-05	1.251E-05	**1.257E-05**	1.263E-05	1.383E-05	1.446E-05	1.508E-05	1.571E-05
3	Stratoid Basalt	1.873E-02	1.998E-02	2.122E-02	2.247E-02	2.484E-02	**2.497E-02**	2.509E-02	2.747E-02	2.871E-02	2.996E-02	3.121E-02
4		3.195E-03	3.408E-03	3.621E-03	3.834E-03	4.239E-03	**4.260E-03**	4.281E-03	4.686E-03	4.899E-03	5.112E-03	5.325E-03
5		1.992E-02	2.125E-02	2.258E-02	2.391E-02	2.643E-02	**2.657E-02**	2.670E-02	2.922E-02	3.055E-02	3.188E-02	3.321E-02
6		1.037E-03	1.106E-03	1.175E-03	1.244E-03	1.375E-03	**2.382E-03**	1.389E-03	1.521E-03	1.590E-03	1.659E-03	1.728E-03
7		3.007E-03	3.207E-03	3.407E-03	3.608E-03	3.989E-03	**4.009E-03**	4.029E-03	4.410E-03	4.610E-03	4.810E-03	5.011E-03
8		7.166E-03	7.643E-03	8.121E-03	8.599E-03	9.506E-03	**9.554E-03**	9.602E-03	1.051E-02	1.099E-02	1.147E-02	1.194E-02
9		9.428E-05	1.006E-05	1.068E-05	1.131E-05	1.251E-05	**1.257E-05**	1.263E-05	1.383E-05	1.446E-05	1.508E-05	1.571E-05
10		9.428E-06	1.006E-05	1.068E-05	1.131E-05	1.251E-05	**1.257E-05**	1.263E-05	1.383E-05	1.446E-05	1.508E-05	1.571E-05
11		9.428E-06	1.006E-05	1.068E-05	1.131E-05	1.251E-05	**1.257E-05**	1.263E-05	1.383E-05	1.446E-05	1.508E-05	1.571E-05
12		9.428E-06	1.006E-05	1.068E-05	1.131E-05	1.251E-05	**1.257E-05**	1.263E-05	1.383E-05	1.446E-05	1.508E-05	1.571E-05
13	Upper Crust	8.294E-04	8.847E-04	9.400E-04	9.953E-04	1.100E-03	**1.106E-03**	1.111E-03	1.216E-03	1.272E-03	1.327E-03	1.382E-03
14	Lower Crust	1.725E-03	1.840E-03	1.955E-03	2.070E-03	2.288E-03	**2.300E-03**	2.311E-03	2.530E-03	2.645E-03	2.760E-03	2.875E-03
15		9.236E-04	9.852E-04	1.047E-03	1.108E-03	1.225E-03	**1.232E-03**	1.238E-03	1.355E-03	1.416E-03	1.478E-03	1.539E-03
16		3.676E-03	3.921E-03	4.166E-03	4.411E-03	4.876E-03	**4.901E-03**	4.925E-03	5.391E-03	5.636E-03	5.881E-03	6.126E-03
17	Melt material	9.750E-02	1.040E-01	1.105E-01	1.170E-01	1.293E-01	**1.300E-01**	1.306E-01	1.430E-01	1.495E-01	1.560E-01	1.625E-01
18		1.050E-01	1.120E-01	1.190E-01	1.400E-01	1.393E-01	**1.400E-01**	1.407E-01	1.540E-01	1.610E-01	1.680E-01	1.750E-01
19	SCLM	0.000E+00	0.000E+00	0.000E+00	0.000E+00	0.000E+00	**0.000E+00**	0.000E+00	0.000E+00	0.000E+00	0.000E+00	0.000E+00

Appendices **2**: Variation in Root Mean Square Error (RMSE) between the observed and calculated magnetic anomalies when varying the magnetic susceptibility values from those used in the final two-dimensional (2D) model in Figure 9 by an increment of 5% within -25% (lower limit) and +25% (upper limit).

Final Model		**Lower Limits**	Difference between the observed and the calculated magnetic anomalies (nT)							**Upper Limits**
Magnetics (SI)	**Model Unit**	SI value varied by -25%	SI value varied by -20%	SI value varied by -15%	SI value varied by -10%	SI value varied by -5%	SI value varied by +5%	SI value varied by 10%	SI value varied by +15%	SI value varied by +20%	SI value varied by +25%
3.280E-03	**Sediment**	2.78	1.762	1.378	1.004	0.653	0.445	0.742	1.102	1.48	1.805
1.257E-05											
2.497E-02	**Stratoid Basalt**	**5.684**	4.631	3.646	2.803	2.235	2.295	3.638	4.622	5.675	**6.765**
4.260E-03											
2.657E-02											
2.382E-03											
4.009E-03											
9.554E-03											
1.257E-05											
1.257E-05											
1.257E-05											
1.257E-05											
1.106E-03	**Upper Crust**	2.445	2.446	2.447	2.448	2.449	2.449	2.451	2.451	2.452	2.453
2.300E-03	**Lower Crust**	**5.466**	**4.674**	**4.222**	2.83	2.259	2.207	2.386	2.888	3.537	**4.266**
1.232E-03											
4.901E-03											
1.300E-01	**Melt material**	**5.937**	5.106	4.346	3.13	2.439	2.321	2.693	3.13	3.351	**4.047**
1.400E-01											
All Layers		4.331	3.732	3.199	2.563	2.453	2.466	2.999	3.492	4.068	4.695

Appendices **3**: Density values resulting from varying the density values used for different element in the two-dimensional (2D) magnetic and gravity model in Figure 9 within -25% (lower limit) and +25% (upper limit) at 5% increment.

		Lower Limits					**Final Model**					**Upper Limits**
Polygon #	Model unit	Density varied by -25%	Density varied by -20%	Density varied by -15%	Density varied by -10%	Density varied by -5%	Density (Kg/m3)	Density varied by +5%	Density varied by 10%	Density varied by +15%	Density varied by +20%	Density varied by +25%
1	Sediment	1710	1824	1938	2052	2166	**2280**	2394	2508	2622	2736	2850
2		1710	1824	1938	2052	2166	**2280**	2394	2508	2622	2736	2850
3	Stratoid Basalt	2062.5	2200	2337.5	2475	2612.5	**2750**	2887.5	3025	3162.5	3300	3437.5
4		2062.5	2200	2337.5	2475	2612.5	**2750**	2887.5	3025	3162.5	3300	3437.5
5		2062.5	2200	2337.5	2475	2612.5	**2750**	2887.5	3025	3162.5	3300	3437.5
6		2062.5	2200	2337.5	2475	2612.5	**2750**	2887.5	3025	3162.5	3300	3437.5
7		2062.5	2200	2337.5	2475	2612.5	**2750**	2887.5	3025	3162.5	3300	3437.5
8		2062.5	2200	2337.5	2475	2612.5	**2750**	2887.5	3025	3162.5	3300	3437.5
9		2062.5	2200	2337.5	2475	2612.5	**2750**	2887.5	3025	3162.5	3300	3437.5
10		2062.5	2200	2337.5	2475	2612.5	**2750**	2887.5	3025	3162.5	3300	3437.5
11		2062.5	2200	2337.5	2475	2612.5	**2750**	2887.5	3025	3162.5	3300	3437.5
12		2062.5	2200	2337.5	2475	2612.5	**2750**	2887.5	3025	3162.5	3300	3437.5
13	Upper Crust	2025	2160	2295	2430	2565	**2700**	2835	2970	3105	3240	3375
14	Lower Crust	2221.5	2369.6	2517.7	2665.8	2813.9	**2962**	3110.1	3258.2	3406.3	3554.4	3702.5
15		2220	2368	2516	2664	2812	**2960**	3108	3256	3404	3552	3700
16		2220	2368	2516	2664	2812	**2960**	3108	3256	3404	3552	3700
17	Melt material	2115	2256	2397	2538	2679	**2820**	2961	3102	3243	3384	3525
18		2122.5	2264	2405.5	2547	2688.5	**2830**	2971.5	3113	3254.5	3396	3537.5
19	SCLM	2385	2544	2703	2862	3021	**3180**	3339	3498	3657	3816	3975

Appendices **4**: Variation in the Root Mean Square Error (RMSE) between the observed and calculated Bouguer gravity anomalies when varying the density values from those used in the final two-dimensional (2D) magnetic and gravity model in Figure 9 by an increment of 5% within -25% (lower limit) and +25% (upper limit).

Final Model	Model Unit	Lower Limits	RMSE between the observed and the calculated gravity anomalies (mGal)								Upper Limits
Density (Kg/m^3)		Density varied by -25%	Density varied by -20%	Density varied by -15%	Density varied by -10%	Density varied by -5%	Density varied by +5%	Density varied by 10%	Density varied by +15%	Density varied by +20%	Density varied by +25%
2280	Sediment	2.149	1.762	1.378	1.004	0.653	0.445	0.742	1.102	1.48	1.805
2750	Stratoid	1.984	1.586	1.204	0.866	0.634	0.88	1.223	1.604	2.002	2.408
2700	**Upper Crust**	**24.265**	**19.38**	**14.446**	**9.607**	**4.783**	**4.989**	**9.815**	**14.653**	**19.495**	**24.338**
2960	Lower crust	**8.758**	**7.122**	**5.384**	3.655	1.957	1.759	3.447	**5.175**	**6.912**	**8.653**
2820	Melt material	**12.246**	**9.926**	**7.429**	4.939	2.477	2.688	**5.155**	**7.646**	**10.144**	**12.644**
3180	SCLM	**16.722**	**13.444**	**10.118**	**6.797**	3.494	3.286	**6.586**	**9.907**	**13.232**	**16.56**
	All layers	2.952	2.395	1.84	1.294	0.773	0.736	1.086	1.626	2.178	2.735

Appendices 5: Variation of the thickness and depth to different elements of the two-dimensional (2D) magnetic and gravity model showing in Figure 9 and the resulting Root Mean Square Error (RMSE) between the observed and calculated magnetic and Bouguer gravity anomalies.

Model Unit	**Boundary Condition**	**Density (Kg/m^3)**	**Magnetics (SI)**	**Sensitivity depth (Km)**	**RMSE (mGal)**	**RMSE (nI)**
Sediment	Lower Limit	2280	3.28E-03	0	2.912	**9.953**
Sediment	Upper Limit	2280	3.28E-03	1	2.653	4.519
Stratoid	Lower Limit	2750	2.66E-02	1	0.522	4.457
Stratoid	Upper Limit	2750	2.66E-02	4	0.822	3.38
Upper Crust/Lower Crust	Lower Limit	*2700/2960	1.11E-03	8	3.351	2.483
Upper Crust/Lower Crust	Upper Limit	*2700/2960	1.11E-03	15	**8.034**	2.303
Melt Material /Upper Crust	Lower Limit	*2820/2700	1.30E-01	6	3.726	**19.383**
Melt Material /Upper Crust	Lower Limit2	*2820/2700	1.30E-01	8	2.467	**12.023**
Melt Material /Lower Crust	Upper Limit	*2820/2960	1.30E-01	15	3.877	**8.598**
Melt Material /Lower Crust	Upper Limit2	*2820/2960	1.30E-01	18	3.408	**11.992**

VITA

ZELALEM S DEMISSIE
Candidate for the Degree of

Doctor of Philosophy

Thesis: **SURFACE AND CRUSTAL DEFORMATION MECHANISM OF THE DOBI GRABEN AND SURROUNDING AREA IN THE AFAR DEPRESSION, ETHIOPIA**

Major Field: **GEOLOGY**

Biographical:

Education:

Completed the requirements for the Doctor of Philosophy in Geology at Oklahoma State University, Stillwater, Oklahoma in December, 2018.
Completed the requirements for the Master of Science in **Remote Sensing and GIS** (Geology) from Addis Ababa University, Addis Ababa, 2005.
Completed the requirements for the Bachelor of Science (Honors) in Geology and Geophysics at Addis Ababa University, Addis Ababa, Ethiopia, 2000.

Experience:
2016 to present: Geospatial and GIS Consultant to the World Bank,
2012-May 2016: Teaching, Research Assistant, Boone Pickens School of Geology 2009-2011: Teaching, Research Assistant, Department of Geology, Kent State University, Ohio.
2006-2009: Geologist and GIS expert; GS Info Solution PLC., Ethiopia
2001-2006: Project Geologist; National Mining Corporation, Addis Ababa, Ethiopia

Professional Memberships:
Society of Exploration Geophysicists (SEG)
American Geophysical Union (AGU)
American Association of Petroleum Geologists (AAPG)
Geological Society of America (GSA)